

THESIS

LARAMIDE TRANSPRESSION AND OBLIQUE THRUSTING IN THE
NORTHEASTERN FRONT RANGE, COLORADO: 3D KINEMATICS OF THE
LIVERMORE EMBAYMENT

Submitted By

Scott M. Larson

Department of Geosciences

In partial fulfillment of the requirements

for the degree of Master of Science

Colorado State University

Fort Collins, Colorado

Spring 2009

COLORADO STATE UNIVERSITY

November 11th, 2008

WE HEREBY RECOMMEND THAT THE THESIS PREPARED UNDER OUR SUPERVISION BY SCOTT M. LARSON ENTITLED “LARAMIDE TRANSPRESSION AND OBLIQUE THRUSTING IN THE NORTHEASTERN FRONT RANGE, COLORADO: 3D KINEMATICS OF THE LIVERMORE EMBAYMENT” BE ACCEPTED AS FULFILLING IN PART REQUIREMENTS FOR THE DEGREE OF MASTER OF SCIENCE.

Committee on Graduate Work

Adviser

Department Head

ABSTRACT OF THESIS

LARAMIDE TRANSPRESSION AND OBLIQUE THRUSTING IN THE NORTHEASTERN FRONT RANGE, COLORADO: 3D KINEMATICS OF THE LIVERMORE EMBAYMENT

Basement-involved foreland orogens commonly contain anastomosing networks of bifurcating basement arches flanked by arch-bounding thrusts which commonly alternate flanks and vergence directions along strike. Transition zones, where thrust vergence reverses along the strike of an arch, exhibit three-dimensional structural complexities due to diverse trends and geometries of secondary faults and folds. The role of diversely-oriented, secondary structures in accommodating three-dimensional strain across transition zones is the fundamental problem driving this investigation.

This investigation analyzed the kinematics and three-dimensional geometry of the Livermore Embayment, a transition zone which accommodated the reversal in the tectonic vergence of thrusts bounding the northeastern Front Range and southeastern Laramie Range. The Livermore Embayment is a rhomb-shaped embayment of the lower Fountain Fm. bounded by the North Livermore, West Livermore and Livermore faults and the N- and NE-trending Grayback, Roberts, and Horseshoe monoclines. Minor fault data (n=3326) from 72 locations and joint attitudes (n=1087) from 19 locations were collected from the Proterozoic basement and upper Paleozoic and Mesozoic sedimentary strata. Kinematic data, bedding attitude data (n=1048), time- and depth-structure contour maps from proprietary seismic data, and depths of formation tops from >100 wells were used to constrain 18 balanced cross sections and a 3D structural model.

Compton ideal σ_1 analysis of minor fault data shows regional Laramide σ_1 was subhorizontal and unidirectional at 085° , refuting previous hypotheses for the area invoking a dominance of vertical motions during Laramide deformation. Variable σ_1 trends at individual locations provide evidence for strain partitioning and vertical axis rotation within E-, and NE-trending transpressional structures. Relative-timing relationships of faults to joints and a 058° trend of master joints suggest a late-Laramide timing of extensional fracturing. An average trend of 149° for cross joints are consistent with a mid- to late-Miocene timing of normal faulting in the western Front Range.

The proximity of the Livermore Embayment to the Proterozoic Skin Gulch Shear Zone (SGSZ) and the abrupt changes in trend and geometry of secondary structures to parallel the ENE-trend of the SGSZ are suggestive of regional fault reactivation. Kinematic data, paleomagnetic data, 2D structural modeling, and 3D block balancing all suggests the Livermore Embayment is a transpressional, right-lateral shear zone accommodating a transition between oppositely-vergent, conjugate Laramide thrusts. The Livermore Embayment itself is the product of localized transpression and highly-oblique thrusting on subvertical pre-existing faults, with the lateral translation of fault blocks limiting crustal thickening on neo-formed Laramide thrusts.

Scott Michael Larson
Department of Geosciences
Colorado State University
Fort Collins, CO 80523
Spring 2009

ACKNOWLEDGMENTS

This research was supported by Edward M. Warner, Chevron, and a research assistantship from ConocoPhillips. Midland Valley Exploration provided discounted training and graciously donated the use of 2DMove and 3DMove. Stan Mollerstuen provided unpublished structure contour maps and 2D seismic data which constrained the geometry of the Round Butte Thrust and the adjacent portion of the Denver Basin.

I would like to sincerely thank my adviser Eric Erslev for his guidance and patient instruction during my graduate studies at CSU. Eric, your energy, passion and enthusiasm for rigorously testing geologic hypotheses has been an inspiration to me. Thank you.

Thanks go to my thesis committee members, Dr. Jerry Magloughlin and Dr. Wayne Charlie. I would also like to thank faculty members, staff and my fellow graduate students for their friendship, tutelage and camaraderie. Thanks to my professors at Montana State University-Bozeman, especially Dr. David Lageson, whose entertaining and stimulating lectures inspired a business major to pursue a degree in geology.

The data presented in this thesis could not have been collected without the permission of many public and private landowners. I would like to personally thank Larimer County Parks and Open Lands, the City of Fort Collins, the Maxwell Ranch, Eldon Ackerman, The Roberts Family, Larry Peterson, and the Colorado Lien Company.

I would like to thank my family and friends for their support. My wife Rebecca deserves significant credit for both her sacrifices and the emotional and financial support she has given me during my studies. I couldn't have done it without you.

TABLE OF CONTENTS

	Page
Title Page.....	i
Signature Page.....	ii
Abstract of Thesis.....	iii
Acknowledgements.....	v
Table of Contents.....	vi
1. INTRODUCTION.....	1
2. PREVIOUS WORK.....	10
Plate Dynamics of Basement-Involved Foreland Orogens.....	10
Plate Tectonic Mechanisms.....	12
Laramide Kinematic Models.....	15
Kinematic Analyses of Minor Faults.....	19
Previous Structural Interpretations of the Northeastern Front Range.....	21
3. STRATIGRAPHIC SUMMARY.....	28
Precambrian.....	28
Paleozoic.....	31
Mesozoic.....	32
Cenozoic.....	35
4. METHODS OF DATA COLLECTION AND ANALYSES AND DISCUSSION OF OBSERVATIONS AND KINEMATIC DATA.....	37
Fault Data Collection Methods and Shear Sense Determination.....	37
Fracture and Bedding Data Collection Methods.....	39
Methods of the Initial Kinematic Analysis of Minor Fault Data.....	39
Methods of the Initial Analysis of Joint Data.....	41
Geologic Observations.....	41
Southeastern Granite Quadrangle.....	50
Table Mountain Quadrangle.....	54
Virginia Dale Quadrangle.....	61
Livermore Quadrangle.....	61
Livermore Mountain Quadrangle.....	72
Laporte Quadrangle.....	78
Horsetooth Reservoir Quadrangle.....	80
Conclusions.....	85
5. DETAILED ANALYSES OF MINOR FAULT AND JOINT DATA.....	88
Minor Fault Slickenlines and Ideal σ_1 Axes.....	88
Discussion and Interpretations of Minor Fault Data.....	100
Joint Data and Analysis Methods.....	101
Discussion and Interpretations of Joint Data.....	106

TABLE OF CONTENTS (CONT.)

	Page
6. TWO-DIMENSIONAL STRUCTURAL INTERPRETATIONS AND ANALYSES.....	108
Motivations for 2D Structural Interpretations and Analyses.....	108
Methods of Cross Section Construction.....	108
Motivation for Mutliple Structural Restoration Methods.....	109
Two-Dimensional Structural Interpretations.....	111
Conclusions.....	133
7. THREE-DIMENSIONAL STRUCTURAL INTERPRETATIONS AND ANALYSES.....	135
Motivations for 3D Structural Interpretations and Analyses.....	135
Methods of 3D Model Construction.....	135
Observations.....	141
Structural Interpretations.....	143
Interpretations of Orogen Scale Processes.....	156
8. CONCLUSIONS.....	157
Questions for Future Research.....	159
References Cited.....	161
Appendix One: Complete Minor Fault Analyses.....	175
Appendix Two: Joint Data Analyses.....	186
Appendix Three: Bedding Attitude Data.....	189

Chapter 1

Introduction

Basement-involved foreland orogens, including the Laramide Orogen of western North America, the Tien Shan of central Asia, and the Sierras Pampeanas of western Argentina, document upper crustal strain in intra-plate regions thousands of kilometers from convergent plate boundaries (Jordan and Allmendinger, 1986; Nikishin, 1993; Dickinson and Snyder, 1978). Although many competing hypotheses exist for causal plate geometries and their kinematic linkage to intra-plate strain, gross upper crustal geometries are relatively uncontested (Erslev, 2005).

The first-order features of basement-involved foreland orogens include: 1) an anastomosing network of asymmetric basement arches; 2) lens-shaped (in map view), symmetric to asymmetric (section view) foreland basins containing synorogenic strata; and 3) basin- and arch-bounding thrusts which commonly alternate arch flanks and vergence directions along strike (Erslev, 2005) (Fig. 1.1). First-order basement arches generally contain smaller, second-order faults and anticlines on their crests, forelimbs and backlimbs (Fig. 1.2). The transition zones between the culminations of basement arches of differing trends and thrust vergences typically exhibit three-dimensional structural complexities due to diverse trends and geometries of second-order faults and folds. The poor understanding of the role that diversely-oriented second-order structures play in

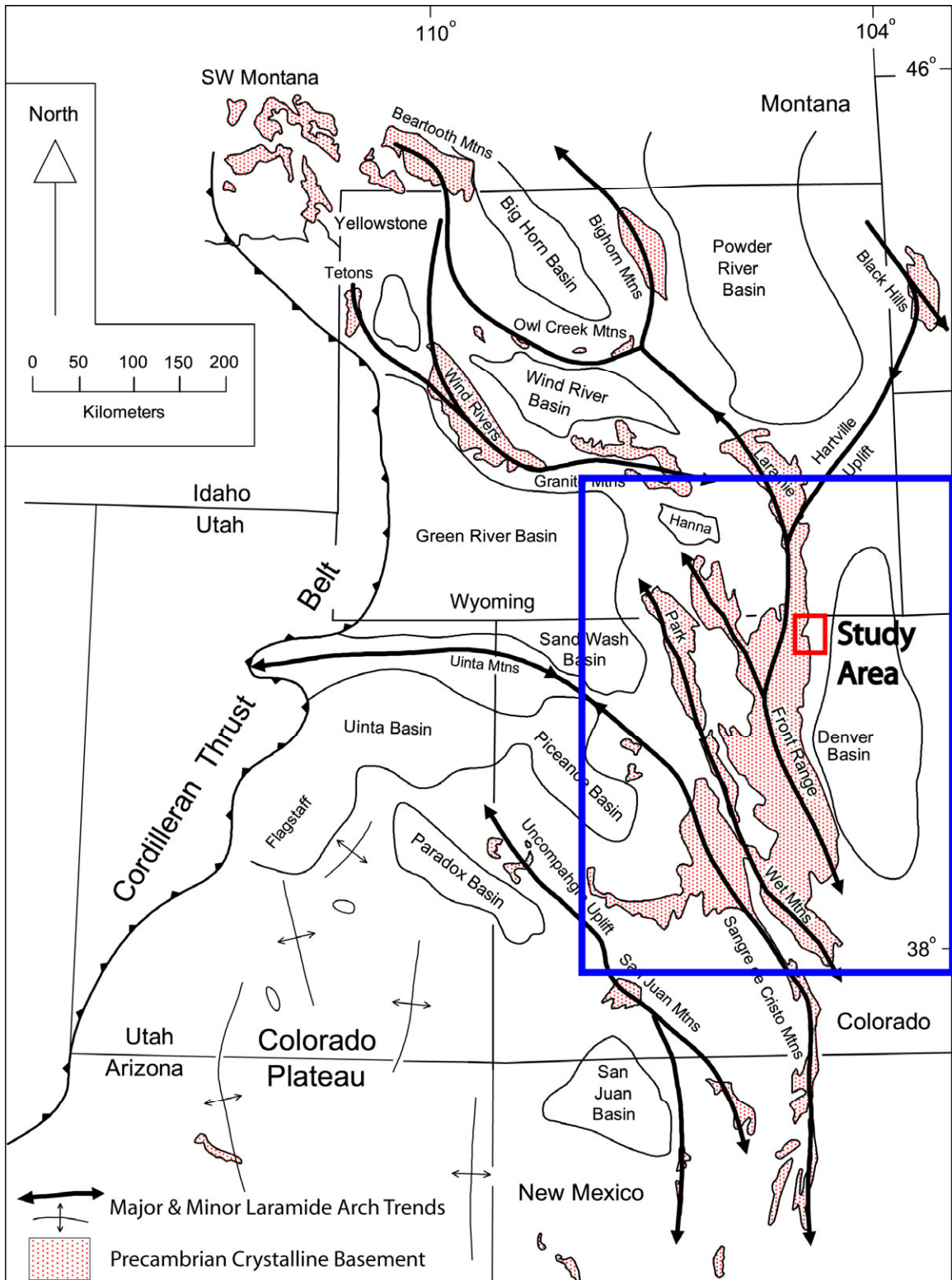


Fig. 1.1. Map of the Rocky Mountains showing exposed Precambrian basement rocks, Laramide basins, trends of major and minor Laramide arches (Erslev, 2005). Red and blue boxes show extents of study area and Fig. 1.3.

accommodating strain in three dimensions across transition zones between oppositely-vergent thrusts is the fundamental problem driving this investigation.

The following questions address the major structural problems regarding our understanding of complex transition zones between oppositely-vergent thrusts.

- What are the modes of deformation within transitional zones? Hypotheses include: a) trishear fault-propagation folding; b) fault-bend folding; c) oblique-slip reactivation of pre-existing basement faults; d) folding of crystalline basement; and e) flexural slip on bedding-parallel detachments.
- What are the kinematics of transitional zones between oppositely-vergent thrusts? Hypotheses include: a) unidirectional, subhorizontal shortening on two laterally propagating, ideal faults; b) multidirectional, subhorizontal slip.
- What is the detailed geometry of the complex transition zone? Specifically, is the transition in thrust vergence accommodated by a) single, or multiple tear or transfer fault(s); b) abrupt changes in shortening along-strike; c) gradual lateral changes of fault offset; d) gradually plunging folds; e) smoothly distributed internal strain?

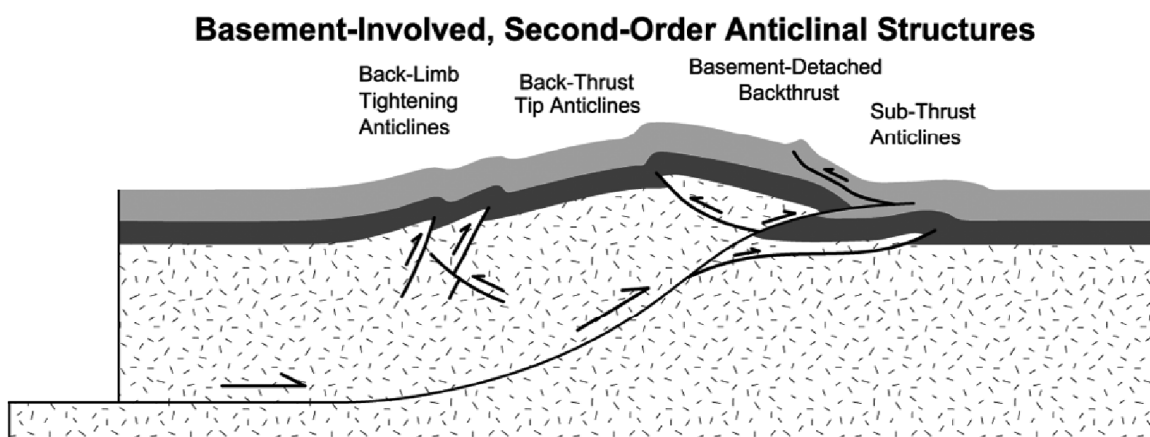


Fig. 1.2. A restorable, geometric model of first-order basement arches and associated second-order fault-related folds (Erslev, 2005).

- What controls the diverse trends and geometries of the second-order structures in complex transitional zones? Hypotheses include: a) reactivation of inherited structures; b) 3D strain compatibility requirements; c) strain relay causing local variation in strain amounts across multiple faults; and d) strain partitioning causing localized multidirectional shortening.
- What kinds of brittle deformation mechanisms occur in second-order structures? Mechanisms include: a) shear fracturing, b) extensional fracturing, c) frictional sliding, and d) pressure solution.
- What is the timing of deformation mechanisms relative to one another and the orogeny? Timing relative to the orogeny includes: a) pre-orogenic, b) syn-orogenic, and c) post-orogenic.

This investigation analyzes the kinematics, 3D geometry and the modes and mechanisms of deformation in a transitional zone which accommodated an abrupt reversal in the tectonic vergence of first-order, arch-bounding thrusts within the northeastern Front Range and southeastern Laramie Range of the western U.S.A. (Fig. 1.3). The 950 km² study area extends for over 30 km along the strike of the eastern Front Range / Laramie Range Arch and western Denver Basin in northern Colorado and southeastern Wyoming (Fig. 1.3). The area encompasses the transition from the backlimb of the northern Front Range to the forelimb of the southern Laramie Range (Fig. 1.3). The trends and geometries of second-order structures change abruptly along the strike of the arch, requiring the study area to be divided in southern, central and northern structural domains (Fig. 1.4).

The eastern half of the southern domain contains the Bellvue Dome and the Douglass Lake, Campbell Valley, and Wellington anticlines; a series of N-trending, highly-asymmetric anticlines with steeply-dipping west forelimbs and shallowly-dipping east backlimbs (Fig. 1.4). The more deeply-exposed, western half of the southern domain contains the Hewlett, Dilky Ranch, North Fork, and Bellvue Faults, a series of N- and NNW-striking, ENE-dipping, reverse faults (Fig. 1.4). The boundary between the

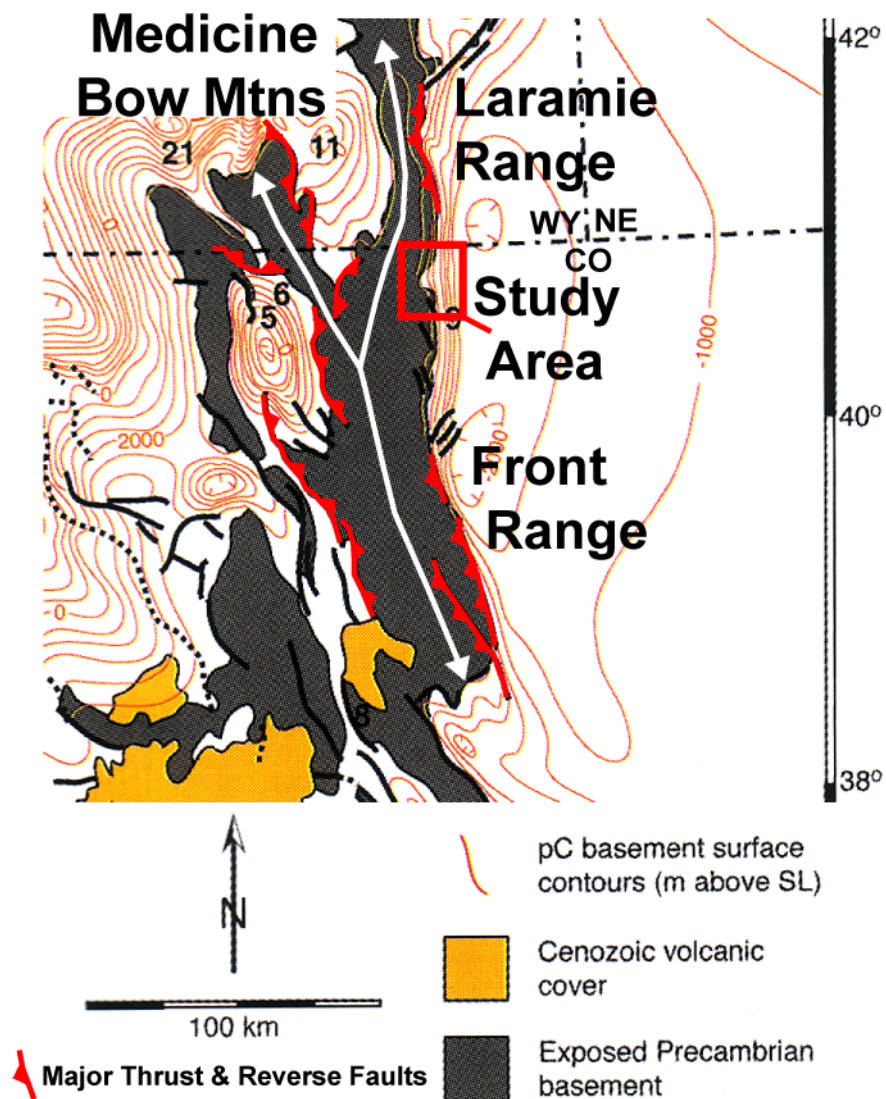


Fig. 1.3. Map of major Laramide features and structure contours of the top of Precambrian basement (Bump, 2003). Red box shows extent of Fig. 1.4.

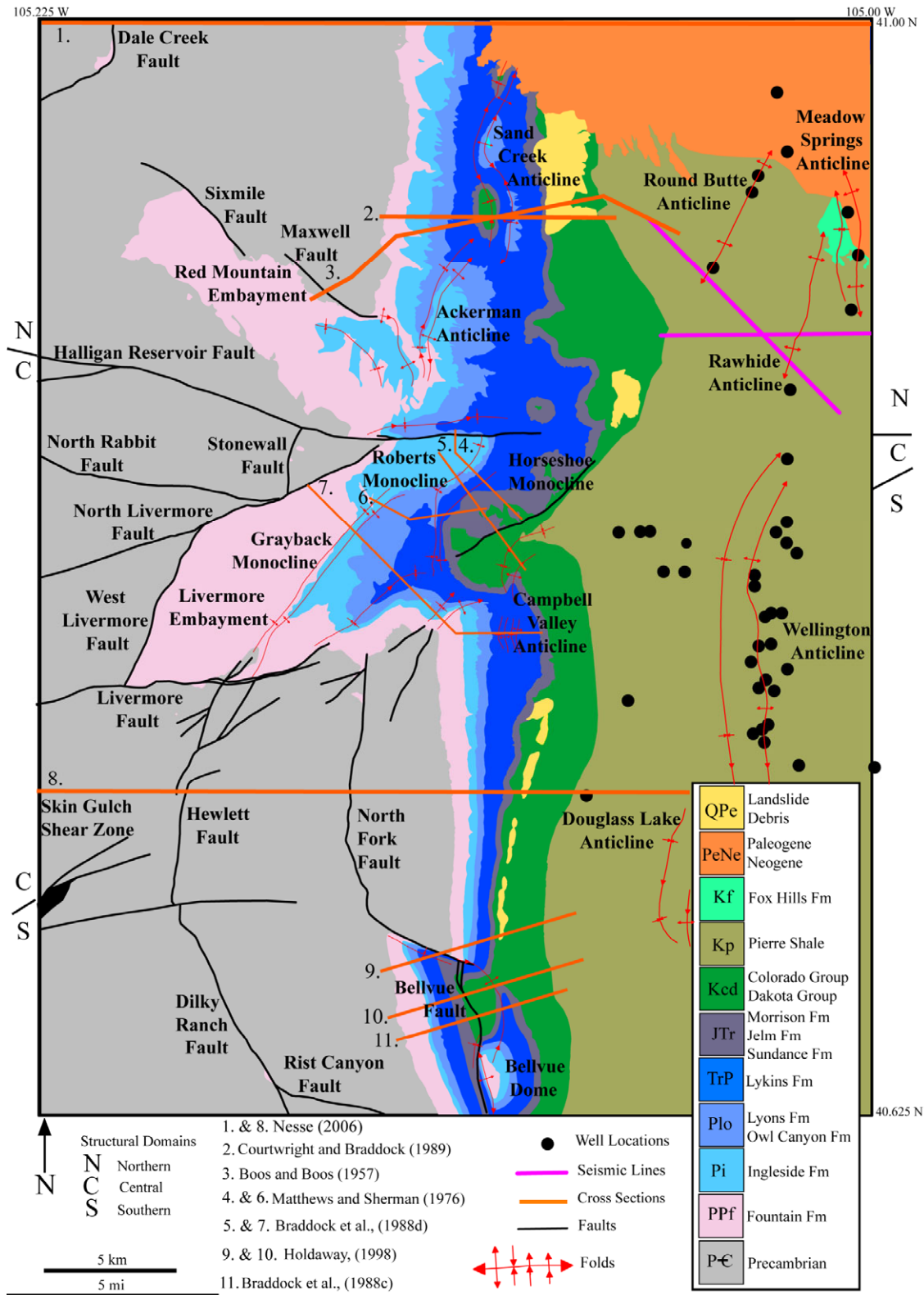


Fig. 1.4. Bedrock geologic map and previously published cross sections of the study area (Braddock et al., 1988a-d; 1989b; Courtwright and Braddock, 1989).

southern and central domains is the Skin Gulch Shear Zone, a major NE-trending Proterozoic shear zone that extends across the northern Front Range (Abbott, 1976; Braddock et al., 1988a; Nesse and Braddock, 1989; Selverstone et al., 2000).

The central domain is bounded on the south by the Skin Gulch Shear Zone and the Livermore Fault and to the north by the Halligan Reservoir Fault (Fig. 1.4). The Livermore and Halligan Reservoir Faults are two major E-W trending, subvertical faults which span the northern Front Range Arch (Tweto, 1979; Egger and Braddock, 1988; Shaver et al., 1988; Braddock et al., 1989b, 1989c). The central domain is dominated by the Livermore Embayment, a rhomb-shaped, fault-bounded, subhorizontal embayment of the lower Fountain Formation (Fig. 1.4). The Livermore Embayment is bounded to the N, W and S by the North Livermore, West Livermore and Livermore faults, respectively. To the east, the Livermore Embayment is flanked by the N- and NE-trending Grayback, Roberts, and Horseshoe Monoclines (Fig. 1.4).

The northern domain lies between the Halligan Reservoir Fault and the Colorado-Wyoming border (Fig. 1.4). The northern domain contains the Ackerman, Sand Creek, Meadow Springs and Rawhide Anticlines. All are north-trending, asymmetric anticlines with steeply-dipping, western forelimbs and shallowly-dipping, eastern backlimbs (Fig. 1.4). Although the Round Butte Anticline is the northeastern continuation of the Horseshoe Monocline, it is a highly-asymmetric, east-vergent anticline with a subvertical to overturned forelimb and a shallow backlimb (Fig. 1.4). The western portion of northern domain consists of the Red Mountain Embayment, a southeast plunging structural trough bounded to the northeast by the northwest-striking Sixmile and Maxwell faults (Fig. 1.4). The northwestern corner of the northern domain contains isolated

outcrops of the Fountain Formation preserved west of the sinuous, north- and northeast-striking Dale Creek Fault (Fig. 1.4).

The study area is an ideal location to test hypotheses regarding the consequences of vergence reversals of first-order, arch-bounding thrusts. The E-dipping Never Summer Thrust and the W-dipping Laramie Thrust are both low angle faults which place basement rocks on the Pierre Shale (O'Neill, 1981; Allmendinger et al., 1982; Brewer et al., 1982, Johnson and Smithson, 1985). The trends and geometries of the second-order structures are diverse whereas the first-order arch trend is linear. The area is well-exposed at multiple structural levels, excellently mapped (Abbott, 1976; Scott and Cobban, 1986; Braddock et al., 1988a-d, 1989a-c; Nesse and Braddock, 1989; Punongbayan et al., 1989; Courtwright and Braddock, 1989; Houston, and Marlatt, 1997; Ver Ploeg et al., 2000), and contains abundant subsurface data from oil wells (COGCC, 2006; WYOGCC, 2006) and 2D seismic data (Mollerstuen, pers. comm., 2006). The Laramide fault geometries (Erslev and Rogers, 1993) and local kinematics (Holdaway, 1998; Erslev et al., 2004a) of the adjacent area to the south are very well constrained. Quartzarenite-rich formations of the late Paleozoic and Mesozoic are ideal for preserving minor faults formed during the Laramide Orogeny, as these strata post-date the mid-Pennsylvanian Ancestral Rockies Orogeny (Kluth and Coney, 1981; Kluth, 1986; Ye et al., 1996).

The investigation integrated published geologic map data, proprietary seismic and public well data, new minor and major fault data, fracture, bedding and observational data into a geospatial database using ArcGIS. Detailed analyses of minor fault data using in house software programs tested hypotheses of strain partitioning, local stress refraction, vertical-axis rotations, and oblique-slip of reactivated basement faults. 2D and

3D quantitative analyses and restorations of fault blocks were used to test hypotheses of along-strike variations of fault-slip, strain relay, vertical-axis rotations and regional detachment of strata using 2DMove and 3DMove software packages from Midland Valley Exploration (MVE, 2006a; 2006b).

This investigation is of specific importance to our understanding of the structural geology of the Colorado Front Range as the structures of study area were first discussed as demonstrating the dominance of vertical tectonics during the Laramide Orogeny (Matthews and Sherman, 1976; Matthews and Work, 1978).

The importance of understanding the geometry of fault-bounded basement arches cannot be understated as they are the structural traps coring the supergiant oil fields of Saudi Arabia (Nicholson and Groshong, 2006). Although first-order basement arches are typically breached by erosion, second-order anticlines can form substantial structural traps for hydrocarbons. An investigation of second-order structures could reveal the mode(s), mechanism(s), and relative timing of deformation, providing a better understanding of fractured reservoirs. A detailed regional analysis across a reversal of thrust vergence could provide the ability to predict the location, extent and 3D closure of second-order structures cored by blind faults. In addition, ability to predict the locations of blind faults with little to no surface expression in tectonically-active foreland orogens may improve seismic risk assessment.

Chapter 2

Previous Work

Plate Dynamics of Basement-Involved Foreland Orogens

Our present understanding of basement-involved foreland orogenesis has been enhanced from the recognition of amagmatic zones of intra-plate deformation in the northern and central Andes coinciding with segments of anomalously low-angle subduction of the Nazca plate (Coney and Reynolds, 1977; Dickinson and Snyder, 1978). Jordan and Allmendinger (1986) recognized the similar geometries of the Valle Fértil and Wind River faults, and found the Sierras Pampeanas to be analogous to the Laramide Orogeny (Fig. 2.1). Jordan et al. (1983), and Jordan and Allmendinger (1986) examined the surface geometries, focal mechanisms and depths of seismicity in the Sierras Pampeanas and concluded regional contraction is accommodated by listric thrusts soling into a subhorizontal, lower crustal detachment. The correlations between styles of contractional deformation, magmatic activity and slab subduction angles placed the Laramide Orogeny within a global tectonic context.

Modern research has focused on the parameters which control flat-slab subduction (Ramos et al., 2002; Gutscher et al., 2000, 2002; van Hunen, 2002). Observations of steep-slab subduction of 5 - 10 Ma oceanic crust and the flat-slab subduction of 30-45 Ma oceanic crust along the Nazca-South American plate boundary pose problems for hypotheses invoking the age and density of oceanic crust as the primary control on

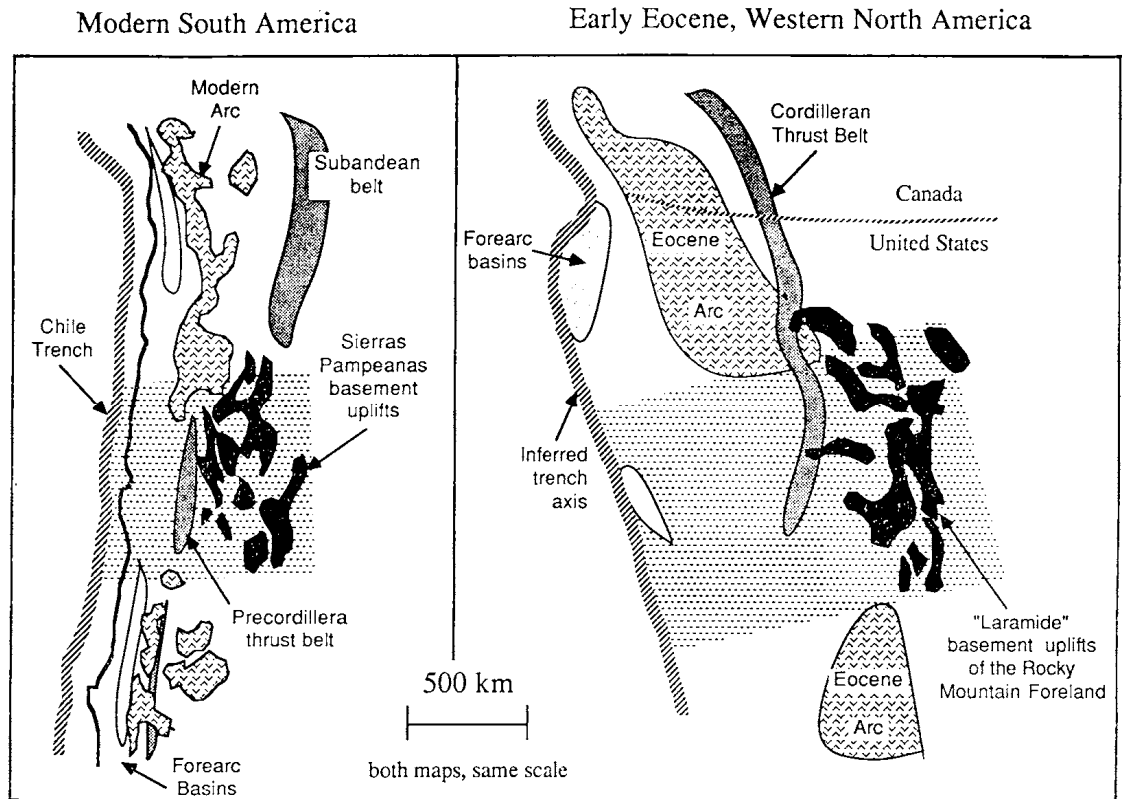


Fig. 2.1. Tectonic maps of the Sierras Pampeanas and the Laramide Orogeny (Jordan and Allmendinger, 1986).

the subduction angle (Cloos, 1993; Gutscher, 2002). Alternating segments of “normal” and “flat-slab” subduction also suggests the 3-4 cm/yr absolute velocity of the South American Plate is not overriding it faster than it can sink as hypothesized by Cross and Pilger (1982). Cahill and Isacks (1992) suggested the curving boundary of the Peruvian “flat slab” segment may have an effect on the angle of the subducted slab. However, the convergent plate boundaries of the central Chilean and Laramide “flat slab” segments are remarkably straight, suggesting plate boundary curvature has also little effect on subducted slab angle. Smalley and Isacks (1987) linked deformation in the Sierras Pampeanas to subduction of the thickened oceanic crust of the Juan Fernandez Ridge, establishing oceanic crustal thickness as a key control of subduction angle. Low heat flow of “flat slab” segments suggests a shallow slab of cool, thick oceanic crust insulates the

overriding plate from the asthenospheric wedge and also acts as a heat sink (Henry and Pollack, 1988; Gutscher, 2002). Increased seismic energy released and greater depths of aftershocks on “flat slab” segments suggests cooling increases the depth, area and degree of coupling within the seismogenic zone between converging plates (Fig. 2.2) (Gutscher, 2002). Ramos et al. (2002) suggested the eastward sweeping of magmatism associated with migration of the asthenospheric wedge heats and thermally weakens the lower crust, facilitating the development of a subhorizontal detachment within the lower crust.

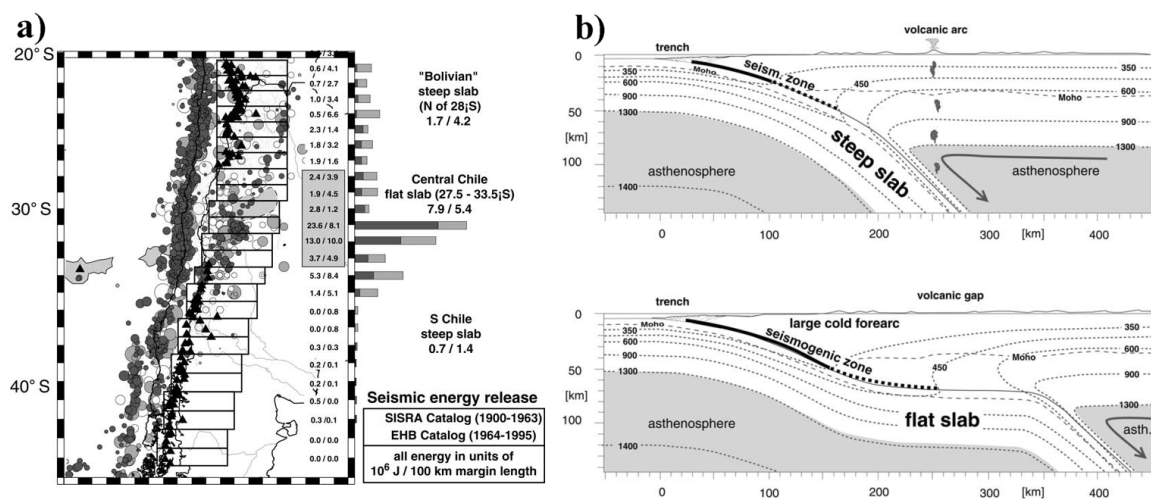


Fig. 2.2. Illustrations of a) the seismic energy released across 1° latitude segments of the Central Chilean “Flat Slab” margin, and b) the effect of subduction style on thermal structure of subduction zones (Gutscher, 2002).

Plate Tectonic Mechanisms

The tectonic mechanism(s) providing the kinematic link between stress generated by “flat slab” subduction and focused, upper-crustal deformation in intra-plate settings remains enigmatic and controversial (Erslev, 2005). Hypotheses proposed to explain intra-plate crustal strain include: a) reverse faults cutting the entire lithosphere (McQueen and Beaumont, 1989); b) subcrustal traction and shear (Bird, 1988; 1998); c) mid-crustal injection of ductile crust and detachment (McQuarrie and Chase, 2000); d) pure shear

thickening of the mantle lithosphere (Egan and Urquart, 1994); e) lithospheric buckling (Tikoff and Maxson, 2001); and f) crustal buckling and lower crustal detachment (Lowell, 1983; Oldow, 1990; Erslev, 1993) (Fig. 2.3).

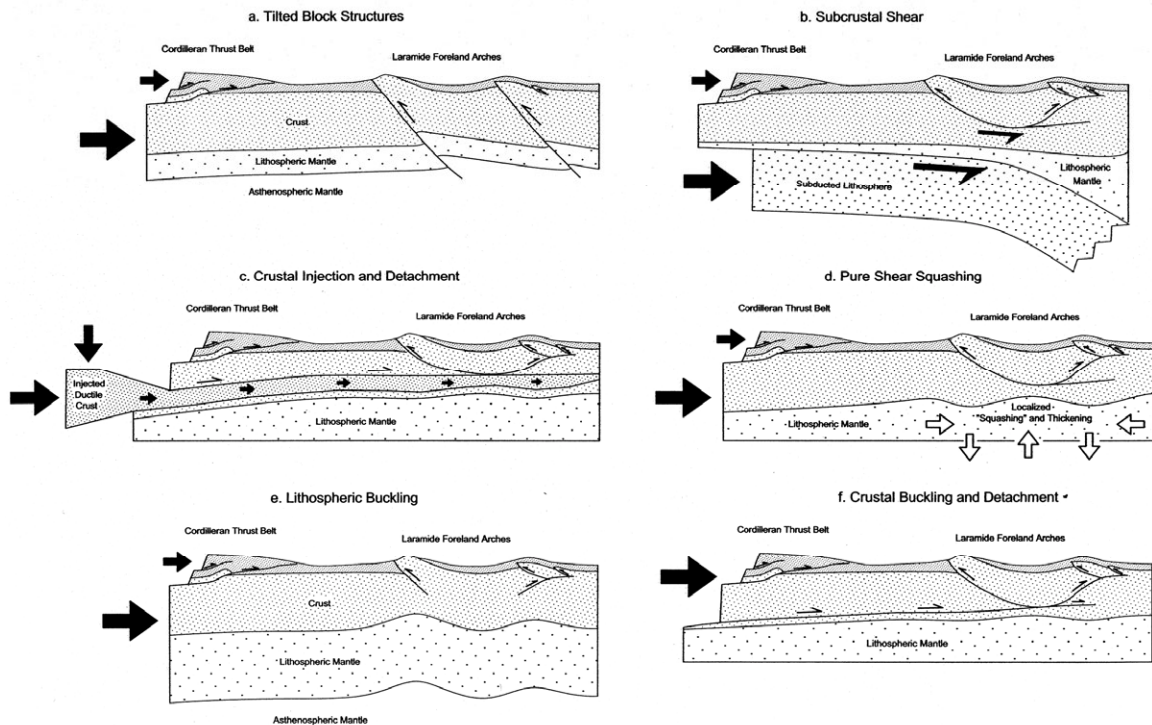


Fig. 2.3. Schematic, lithosphere-scale cross sections illustrating kinematic hypotheses which link upper crustal deformation to tectonic processes (Erslev, 2005).

The McQueen and Beaumont (1989) model of reverse faults cutting the lithosphere predicts upper mantle seismicity and offsets in the moho and gravity highs in the backlimbs of basement arches associated with elevated upper mantle. The Egan and Urquart (1994) model of pure shear thickening of the crust and upper mantle predicts a mirror image antithetic topography of the Moho on similar wavelengths as basement arches and gravity highs beneath arches and lows beneath basins. The Tikoff and Maxson (2001) model of lithospheric buckling predicts a synthetic Moho topography on similar wavelengths as basement arches and symmetric gravity highs and lows beneath arches

and basins, respectively. Their lithospheric buckling model also predicts normal faulting by outer arc extension along the crests of arches and substantial deformation within basins due to synclinal tightening. Bird's (1988, 1998) model of subcrustal shearing predicts a thin mantle lithosphere across the Laramide foreland which thickens eastward due to underplating of sheared mantle lithosphere. The McQuarrie and Chase (2000) model of crustal injection predicts the emplacement of a tabular body of ductile lower crust on a mid-crustal detachment to account for the high elevation of Colorado Plateau and Rocky Mountain region. Several workers have proposed a model which invoking end-loading of the lithosphere at a subduction zone forming a lower crustal subhorizontal detachment and causing buckling of the crust (Lowell, 1983; Oldow, 1989; Erslev, 1993).

Modeling of the structural geometry of the lithosphere constrained by gravity data collected in profiles perpendicular to the Wind River and Sweetwater Arches required crustal thickening on listric thrusts which soled into a lower crustal detachment and left the Moho undisturbed (Hurich and Smithson, 1982; Sharry et al., 1986; Hall and Chase, 1989). Regional maps of crustal thickness estimates taken from seismic refraction and attribute analyses of seismic waves generated by distant earthquakes show a relatively planar Moho (Snelson et al., 1998; Dueker, 2001; Li et al., 2002), despite 5-10 km of structural relief on the top of the Precambrian basement (Keefer and Love, 1963). Karlstrom et al. (2002) hypothesized that crustal thickness variations across the Laramide foreland are more closely related to the tectonic fabric generated during the assembly of the crust in the Archean and Early Proterozoic Eons. The latest Miocene to Present timing of uplift across the Colorado Plateau, Rocky Mountain and western Great Plains

regions are constrained by Miocene basalts (Sahagian et al., 2002) and sedimentological data supporting a post-depositional tilting of the Ogallala group (McMillan et al., 2002).

A subplanar Moho across the Laramide Foreland casts doubt on hypotheses invoking reverse faulting of the entire lithosphere, lithospheric buckling and pure-shear squashing of the ductile lower crust (Keller et al., 1998; Snelson et al., 1998). The correlation between the age and thickness of the lithosphere across the Rocky Mountain Foreland suggests the Laramide Orogeny appears to not have altered the structure of the lower crust and upper mantle lithosphere (Keller et al., 1998; Snelson et al., 1998). These observations question ideas of shortening of the lithosphere by the transmission of subcrustal shear and tectonic underplating of sheared mantle lithosphere. Mass balance and material constraints as well as inconsistencies in the timing of regional uplift challenge hypotheses invoking the injection of ductile lower crust across the Laramide Foreland. Hypotheses of end-loading of the lithosphere forming a subhorizontal, lower crustal detachment and buckling the upper crust honor observational data for the Rocky Mountain foreland and the Sierras Pampeanas of Argentina (Jordan and Allmendinger, 1986; Gutscher et al., 2000; Gutscher, 2002; Ramos et al., 2002; Erslev, 2005).

Laramide Kinematic Models

Why do first-order Laramide arches have such diverse trends and geometries of across the Rocky Mountain Foreland? This fundamental question has spawned a dizzying number of hypotheses linking multimodal trends of upper crustal deformation to plate kinematics. Early controversies of Laramide kinematics arose in the 1960s as geologists debated the relative dominance of horizontal and vertical motions, separating into two antagonistic schools of thought, informally known as the “horizontal tectonics” and the

“vertical tectonics” schools. In the late 1970s and early 1980s unambiguous evidence of “horizontal tectonics” was provided by wells which drilled through kilometers of Precambrian hanging wall rock before encountering Phanerozoic footwall strata (Gries, 1983a; 1983b) and seismic data imaging low-angle thrusts beneath the Wind River and Laramie Ranges (Smithson et al., 1979; Brewer et al., 1982; Johnson and Smithson, 1985). Constraints of material balance and the mechanical behavior of crystalline basement rocks questioned the validity of interpretations invoking subvertical, planar and concave-down, primary faults (Erslev, 1986; Stone, 2006).

Modern debates of Laramide kinematics have focused on hypotheses linking plate kinematics to the diverse trends of Laramide arches and faults. Laramide arch trends vary from N-S (Sangre De Cristo, Front Range Arches), NE-SW (Hartville Arch), NW-SE (Wind River, Black Hills Arches), and E-W (Unita, Owl Creek, and Sweetwater Arches) (Fig. 1.1). The diverse trends of basement arches, as well as the patterns and timing of regional basin development and proposed right-lateral slip on N-striking faults in New Mexico, were the basis for hypotheses of a counterclockwise rotation of Laramide compressive stress (Gries, 1983b; 1990; Chapin and Cather, 1981; Karlstrom and Daniel, 1993; Cather et al., 2006) (Fig. 2.4). Bird (1988, 1998) hypothesized a 15° clockwise rotation of Laramide compression generated by a 15° difference in the motion of the Kula and Farallon plates relative to the North American plate. Geochemical data from alkalic igneous rocks of the Pacific Northwest suggest the Kula/Farallon plate boundary was located near the U.S. - Canada border during the Eocene (Breitsprecher et al., 2003). This casts doubt on ideas of multiple stages of shortening due to different vectors of motion of the Farallon and Kula plates during “flat-slab” subduction.

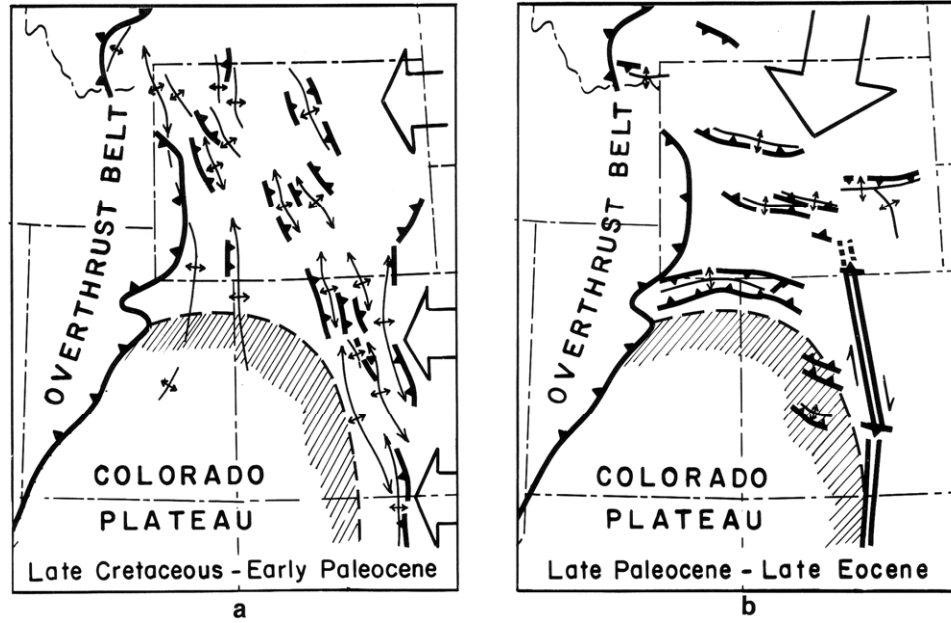


Fig. 2.4. Multi-directional model of deformation showing predicted compression directions during a) early and b) late Laramide time (Gries, 1983b).

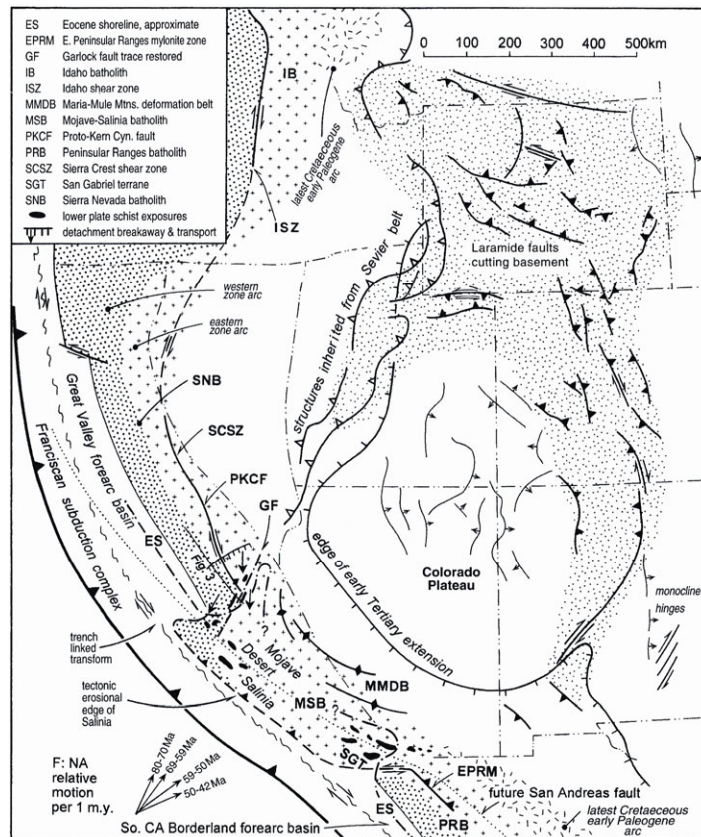


Fig. 2.5. Multi-directional model of Laramide deformation showing a clockwise rotation of compression directions during late Cretaceous to Paleogene (Saleeby, 2003).

Saleeby (2003) recognized that the subbatholith mantle lithosphere of the southern Sierra Nevada batholith is not present in southern California, where it is supplanted by the Rand Schist, a schist similar in age and assemblages to schists of the Franciscan Complex (Fig. 2.5). Saleeby (2003) hypothesized that late Cretaceous subcrustal shear removed subbatholith material and the Rand Schist was formed by tectonic underplating during the subduction of a thick, buoyant oceanic plateau; hypothesized to be the Farallon counterpart to the Hess-Shatsky igneous province. Saleeby (2003) hypothesized that end-loading of the North American plate during the subduction of this plateau drove deformation and a 30° clockwise rotation of stresses.

Palynological dating of syn-Laramide strata suggests arch development began in the late Cenomanian in southwestern Montana and progressed southward and eastward during the late Cretaceous and early Paleogene (Fig. 2.6) (Perry et al., 1992; Perry and Flores, 1997). The temporal progression and spatial continuity of arch development shows a late Cretaceous counterclockwise rotation in the direction of thrusting (Fig. 2.6).

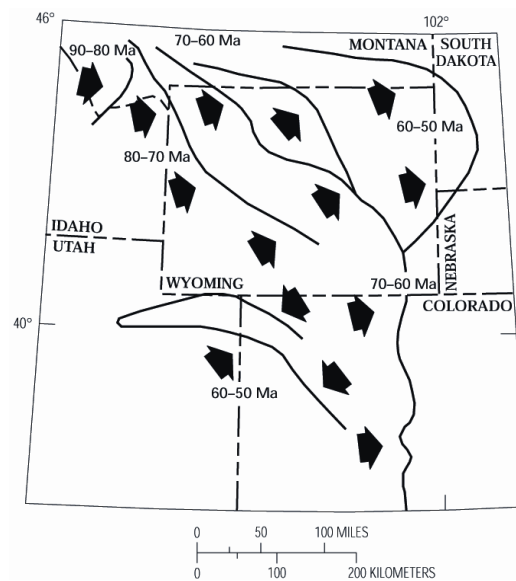


Fig. 2.6. Map showing sequence of inception and migration direction of Laramide deformation in the northern Rocky Mountain Foreland (Perry et al., 1992).

Kinematic Analyses of Minor Faults

The analysis of minor fault data is a powerful tool for testing and rejecting kinematic hypotheses for the Laramide Foreland (Varga, 1993; Molzer and Erslev, 1995; Erslev et al., 2004; Erslev, 2005; Erslev and Larson, 2006; Neely and Erslev, in review). The kinematic analyses of minor fault data, with constraints imposed by mass balance and subsurface data have been pivotal in documenting the dominance of horizontal shortening across the Laramide foreland, refuting hypotheses invoking vertical tectonics. Minor fault analysis has provided strong evidence for unidirectional shortening along the northeastern and eastern margins of the Laramide orogen generating dip-slip thrusting subperpendicular to the Front Range, Bighorn and Beartooth arches (Erslev and Larson, 2006; Neely and Erslev, in review), as well as highly-oblique thrusting along the Casper and Owl Creek arches (Molzer and Erslev, 1995) (Fig. 2.7). However minor fault data collected in the eastern Uinta Arch, White River Arch, San Juan basin, and north central New Mexico have documented multidirectional shortening within the interior and southeastern margin of the orogen (Gregson and Erslev, 1997; Erslev, 2001, Ruf and Erslev, 2005). Regionally-divergent trends of unidirectional shortening have resulted in hypotheses of stress reorientation and strain partitioning (Varga, 1993). Erslev (1993) suggested oblique-slip on lateral ramps, dip-slip on frontal ramps and the transfer of slip between arches during the northeastward propagation of a lower crustal detachment to explain the regional variability of trends and vergence directions (Bolay-Koenig and Erslev, 2003; Erslev, 2005).

Minor fault analyses have helped kindle a recent controversy regarding the amount of Laramide right-lateral strike-slip on the N-striking, Picuris-Pecos Fault System

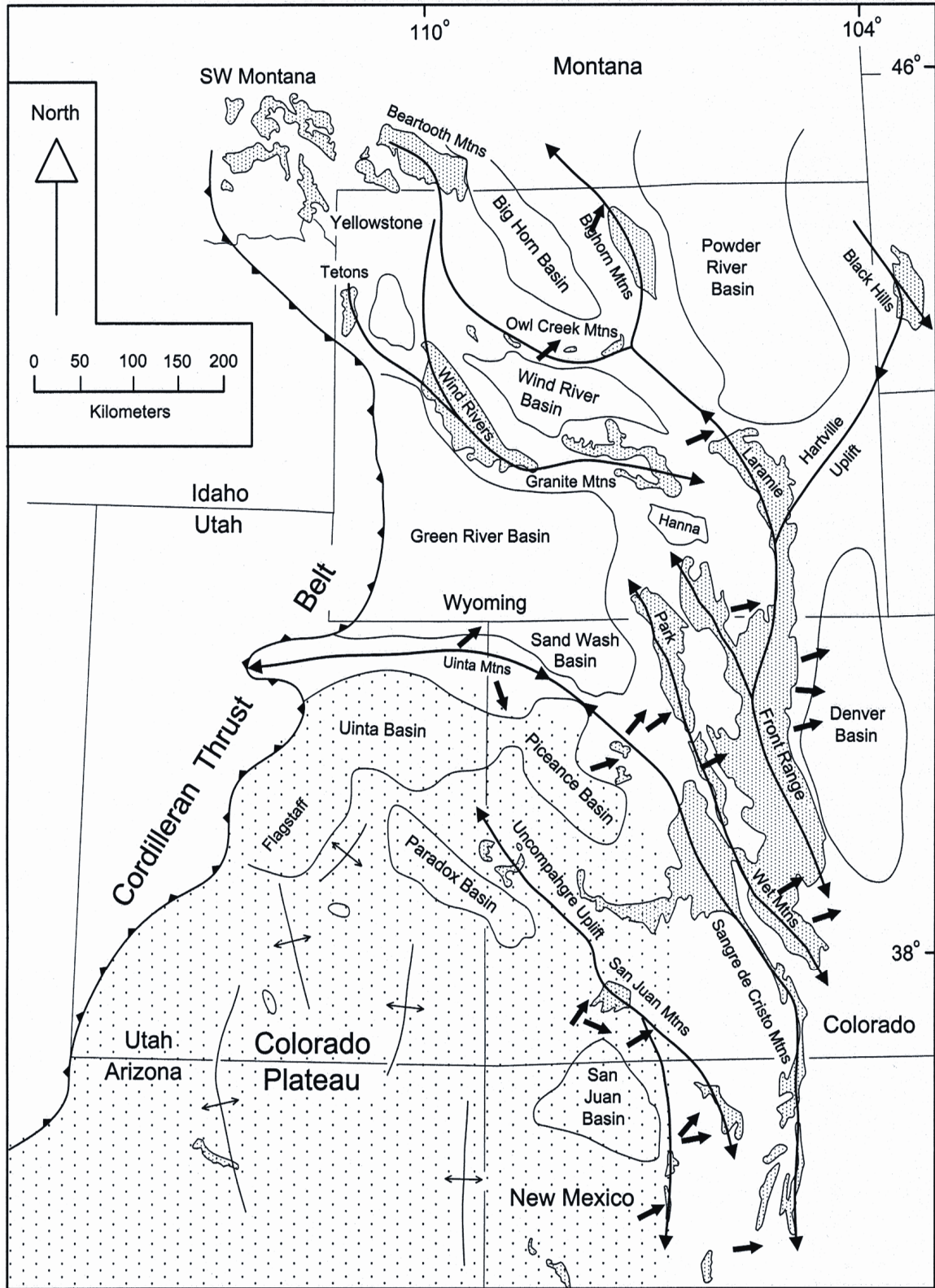


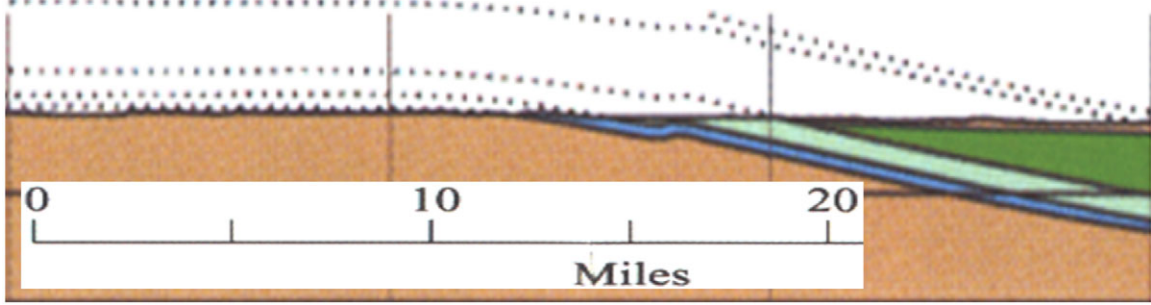
Fig. 2.7. Tectonic map of Laramide Foreland. Arrows indicate average shortening directions from published and unpublished minor fault data (Erslev, 2005).

in northern New Mexico. Several workers have proposed hypotheses invoking tens of km of right-lateral slip on the Picuris-Pecos Fault System during the Laramide Orogeny to explain the 38 km of right-lateral offset observed in aeromagnetic maps (Chapin and Cather, 1981; Karlstrom and Daniel, 1993; Cather, 1999; Cather et al., 2006). Minor faults document a dominance of E-W shortening with lesser N-S shortening and regional extension (Erslev, 2001; Fankhauser and Erslev, 2004, Erslev et al., 2004b). The implications of fault analyses motivated paleomagnetic analyses of carbonate dikes within the Deer Creek breccia and $^{40}\text{Ar}/^{39}\text{Ar}$ dating of the Deer Creek breccia (Fankhauser and Erslev, 2004; Wawrzyniec et al., 2007). Paleomagnetic analyses revealed a well-defined magnetization of late Paleozoic age and $^{40}\text{Ar}/^{39}\text{Ar}$ dates of K-feldspars ranged from 854 ± 1 Ma to 1082 ± 2 Ma. These results suggest a late Precambrian timing of deformation of the PPFS and pose problems for hypotheses invoking counterclockwise rotations of stress and tens of km of right-lateral strike-slip in the southern Rockies during the Laramide Orogeny (Cather, 1999; Cather et al., 2006).

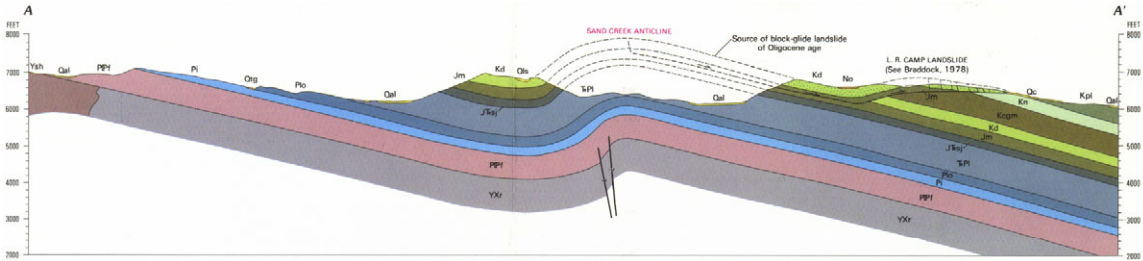
Previous Structural Interpretations of the Northeastern Front Range

The first geologic mapping and structural interpretation of the northeastern Front Range was done in the late 1860's and early 1870's by the Hayden Survey. Hayden's (1874, 1877) cross sections through the SSE-plunging, asymmetric anticlines and NNW-striking faults of the northeastern Front Range showed vertical faults offsetting the E-dipping Pennsylvanian nonconformity and overlying strata. Ziegler (1917) first recognized that missing strata near Morrison, Colorado was the result of reverse slip on the Golden Fault. Ziegler's (1917) cross section through the Big Thompson Anticline shows the asymmetric fold as cored by a blind, subplanar ENE-dipping reverse fault.

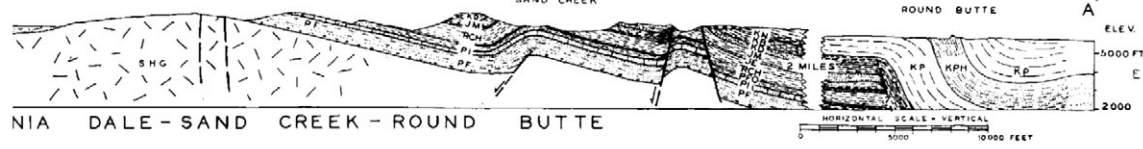
1. Nesse (2006)



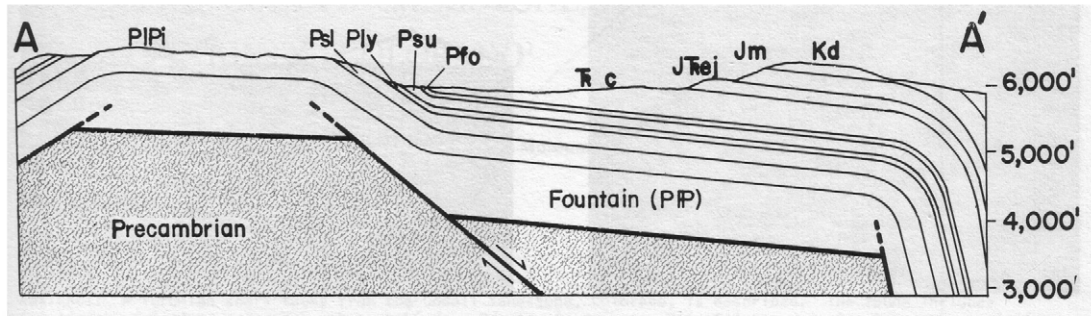
2. Courtwright and Braddock (2006)



3. Boos and Boos (1957)



4. Matthews and Sherman (1976)



5. Braddock et al. (1988d)

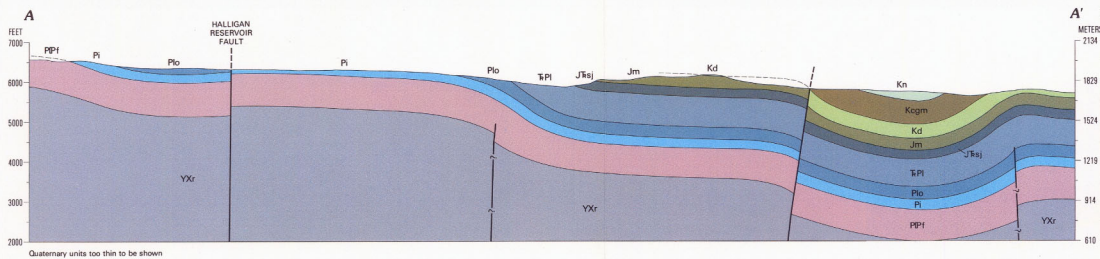
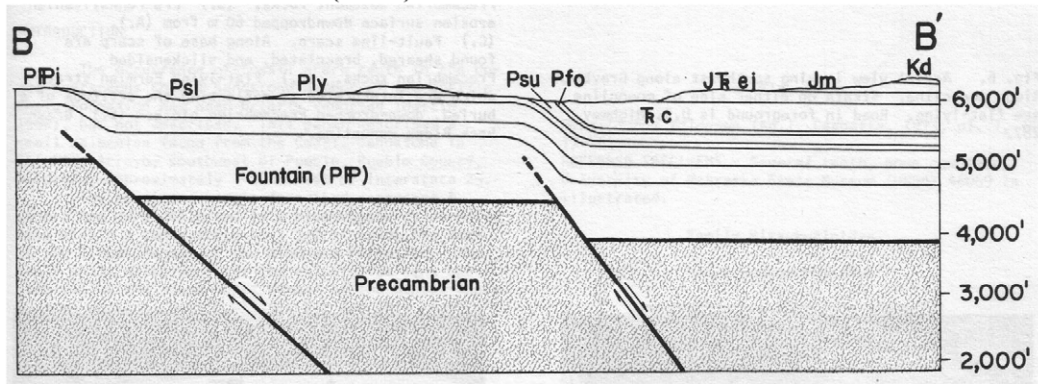


Fig. 2.8. Previous cross sections through the study area. Locations of sections lines in Fig. 1.4. Scale varies between sections but all have no vertical exaggeration.

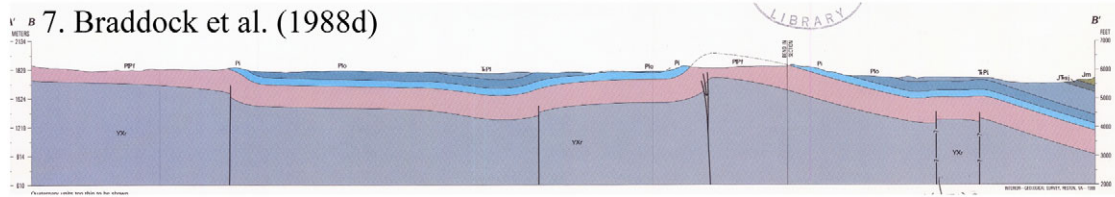
Boos and Boos (1957) first mapped the study area in detail and coined the term “Livermore Graben” to describe the Livermore Embayment. They proposed the North and West Livermore Faults were “strike-faulted,” or largely strike-slip. Boos and Boos (1957) were puzzled by the diversity in trends of folds and faults and suggested Laramide kinematics were locally complex by stating “no simple compressive forces could produce the discordantly arranged folds and faults of the Sand Creek Belt.” Boos and Boos (1957) mapped the Precambrian basement in detail and interpreted local Laramide faults and folds as the product of the reactivation of inherited faults. Boos and Boos’s (1957) early interpretations of the Round Butte Fault and the Sand Creek Anticline invoked normal-fault-related folding (Figs. 1.4, 2.8). However, in an unpublished 1960 report to the Pure Oil Co., C.M. Boos reinterpreted the Round Butte Fault Zone as a splay of NW-dipping reverse faults to explain repeated sections of Permian strata encountered in the Texaco Warren Livestock #1 well.

Matthews and Sherman (1976) published cross sections and the first 3D structural interpretations of the Livermore area. This model invoked basement blocks bound by planar, variably-striking, dip-slip normal faults (Figs. 1.4, 2.8d, 2.9a). They suggested the variable trends of the monoclinical fold axes were evidence arguing against regional horizontal compression driving Laramide deformation in the Livermore area. Matthews and Work (1978) included the Livermore area in their interpretation of the structural geology of the Northeastern Front Range. They hypothesized regional Laramide tectonism resulted in the differential amounts of subvertical uplift of basement blocks bound by planar, variably-striking, moderate to high-angle normal and reverse faults.

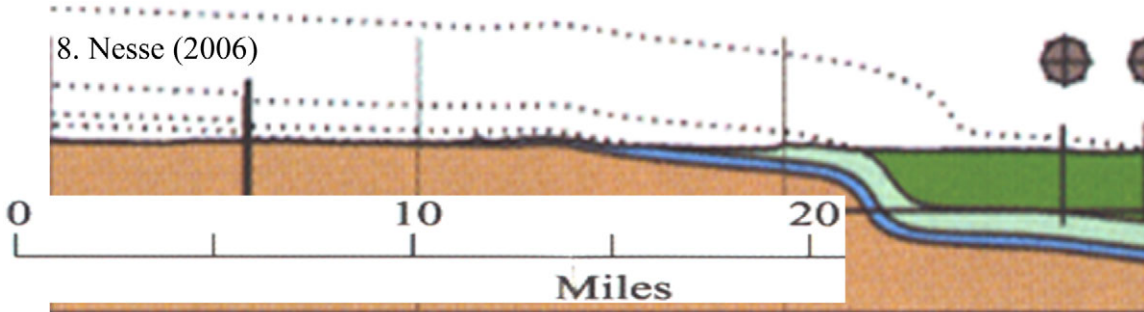
6. Matthews and Sherman (1976)



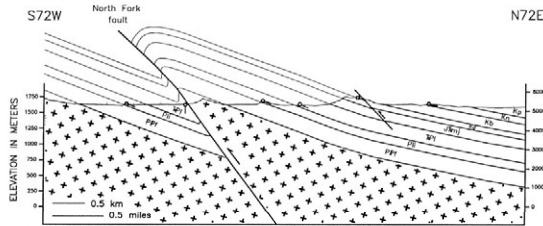
7. Braddock et al. (1988d)



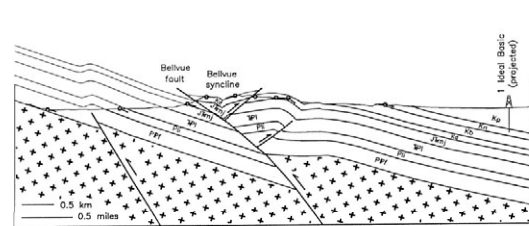
8. Nesse (2006)



9. Holdaway (1998)



11. Holdaway (1998)



10. Braddock et al. (1988c)

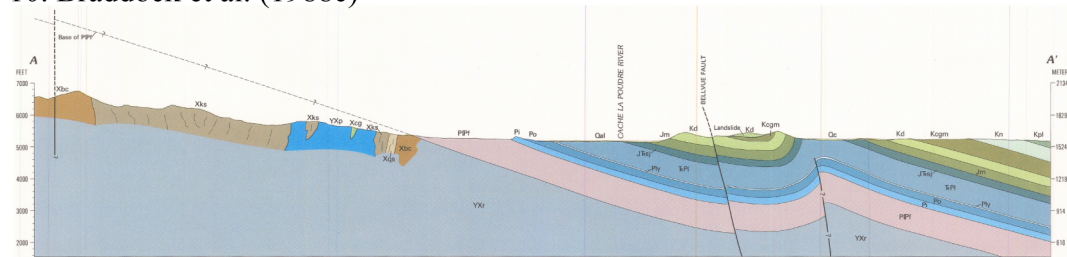


Fig. 2.9. Previous cross sections through the study area. Locations of sections lines in Fig. 1.4. Scale varies between sections but all have no vertical exaggeration.

Cross sections included with the published USGS geologic maps (Braddock et al. 1988a-d; 1989a-b; Courtwright and Braddock, 1989) invoke dip-slip motion on planar to concave-down, subvertical faults, basement folding near faults and parallel folding of the sedimentary strata (Figs. 1.4, 2.8e, 2.8e, 2.9b, 2.9f).

The excavation of exposed NNW-striking faults in the northeastern Front Range near Fort Collins has yielded dips ranging from 20° to 70° NE (Erslev and Rogers, 1993). Surveying of basement foliations and fold axes and trenching of the Milner Mountain fault suggested a maximum of 20° of basement folding was limited to 100 m of the fault, which dips 60° NE (Erslev and Rogers, 1993). A local gravity survey across the Milner Mountain fault constrained the fault dip to 50° ± 10° E (Narr, 1994).

Erslev and Gregson (1996) first utilized the kinematic analyses of minor fault data to test hypotheses of Laramide deformation in the northeastern Front Range. Erslev and Gregson (1996) documented unidirectional, horizontal shortening oriented approximately 080° in the Horsetooth Reservoir area west of Fort Collins, Colorado. They documented a southeastward deflection of stress from the upper hinge to the forelimb of Grayback Monocline, a major NE-striking monocline in the Livermore Embayment. They hypothesized that the clockwise deflection of stress could be due to stress refraction by strain partitioning, fault reactivation, or clockwise, vertical axis rotations by right-lateral strike-slip (Erslev and Gregson, 1996).

Holdaway (1998) analyzed minor fault data collected from the Northeastern Front Range immediately west of Fort Collins, Colorado, and documented that regional Laramide stress and strain was unidirectional and oriented at 079°. This orientation of Laramide stress resulted in dip-slip and oblique-slip on the right-stepping, *en echelon*

ENE-dipping reverse faults which flank the northeastern Front Range immediately south of the study area (Figs. 1.4, 2.9d, 2.9e). Paleomagnetic analyses of Permian strata in the hangingwall and footwall of the ENE-dipping Long Gulch Fault showed no vertical axis rotations, suggesting dip-slip on ENE-dipping reverse faults. Paleomagnetic analyses of Permian strata in the NE-trending Grayback Monocline tested hypotheses of stress refraction and rigid-body, vertical axis rotations in the highly-faulted forelimb of the fold. Holdaway's (1998) paleomagnetic analyses of the Grayback Monocline documented clockwise, vertical axis rotations of 15-40° in the Ingleside fm (GBM2, Fig. 2.10).

Tetreault et al. (2008) performed detailed paleomagnetic analyses at various locations within the forelimb of the Grayback Monocline and confirmed that maximum rotations occurred within most steeply dipping strata within the forelimb. They suggest the Grayback Monocline was formed by transpressional trishear fault-propagation-folding occurred above a reactivated, NW-dipping, right-lateral / reverse fault (Fig. 2.10).

Nesse's (2006) regional cross sections through the study area invoked fault-bend and fault-propagation-folding of the Pennsylvanian nonconformity and dip-slip on ENE-dipping reverse faults (Figs. 1.4, 2.8a, 2.9c). His crustal-scale cross section through the northern Front Range invokes fault-bend folding of the backlimb of an anticline above a planar, ENE-dipping thrust fault to explain the Precambrian basement thrust upon Cretaceous strata on the western flank and the homoclinal, 25-30° ENE dips of the Pennsylvanian nonconformity and strata on the eastern flank of the Front Range.

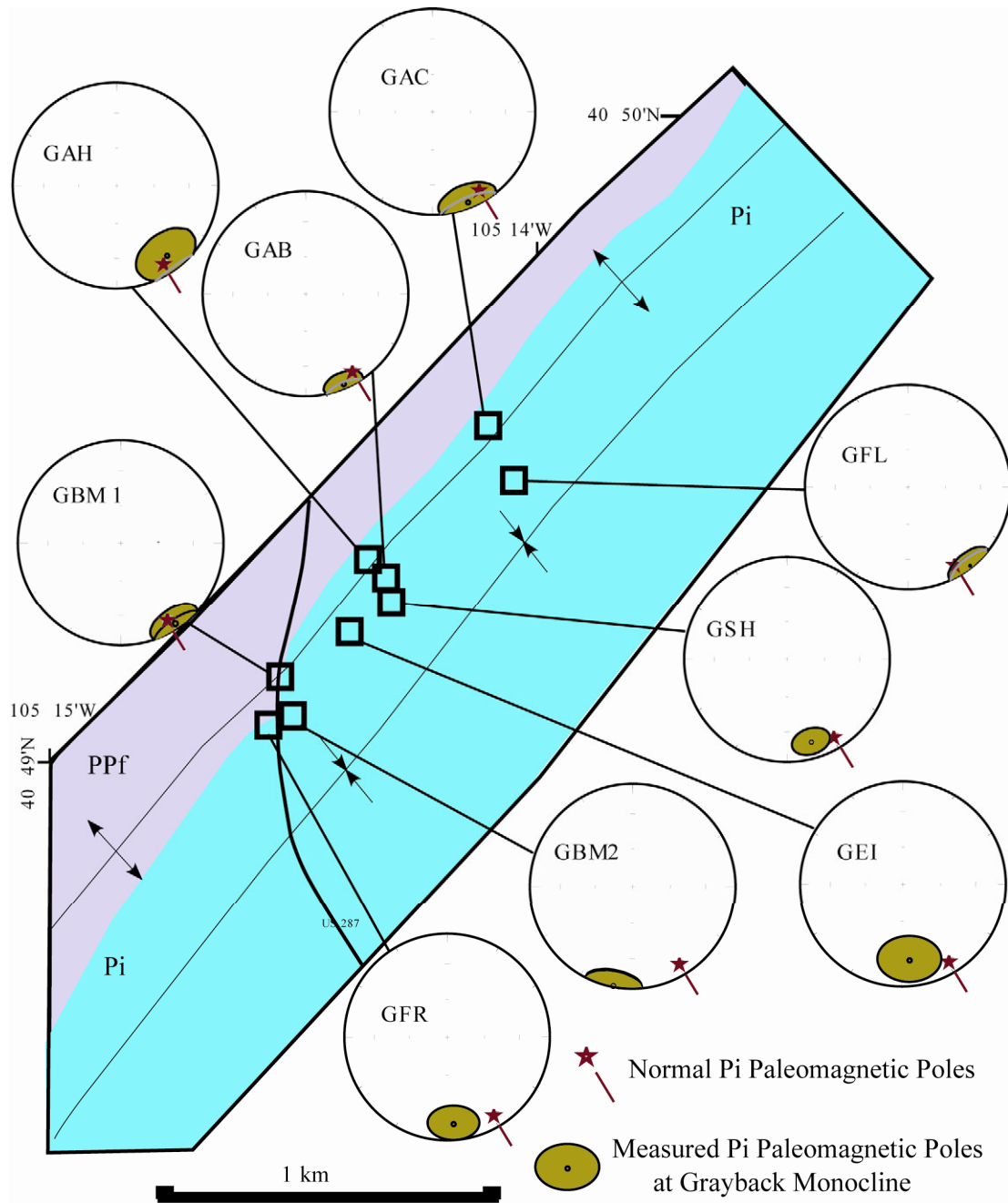


Fig. 2.10. Paleomagnetic data from Grayback Monocline (adapted from Tetreault et al., 2008).

Chapter 3

Stratigraphic Summary

The northeastern Front Range contains rocks ranging in age from early Proterozoic to late Miocene (Peterman et al., 1968; De Paolo, 1981; Courtwright and Braddock, 1989) (Figure 3.1). Devonian kimberlite intrusions northwest of the study area contain lower Paleozoic sediments, providing evidence that early Paleozoic strata once covered the study area (McCallum and Mabarak, 1976; Smith, 1977). Regional uplift and erosion associated with the Pennsylvanian Ancestral Rockies Orogeny removed early Paleozoic strata and formed the subplanar Pennsylvanian nonconformity upon which upper Paleozoic and Mesozoic strata were deposited (Kluth, 1997). Thicknesses of upper Paleozoic and Mesozoic strata change gradually across the study area (Braddock et al., 1988c; 1988d; 1989a; Courtwright and Braddock, 1989) other than areas where Laramide deformation has tectonically thinned or thickened strata.

Precambrian

The oldest Precambrian rocks in the northeastern Front Range are the Early Proterozoic metasedimentary and metavolcanic schists, gneisses, and amphibolites which were metamorphosed as massive arc terranes were accreted onto the Wyoming Craton within the southeast-dipping subduction zone known as the Cheyenne Belt (Houston, 1993; Chamberlain, 1998). The minimum ages of the metasedimentary and metavolcanic rocks are constrained by the 1.79 Ga U-Pb age of the granitic and pegmatitic plutons that

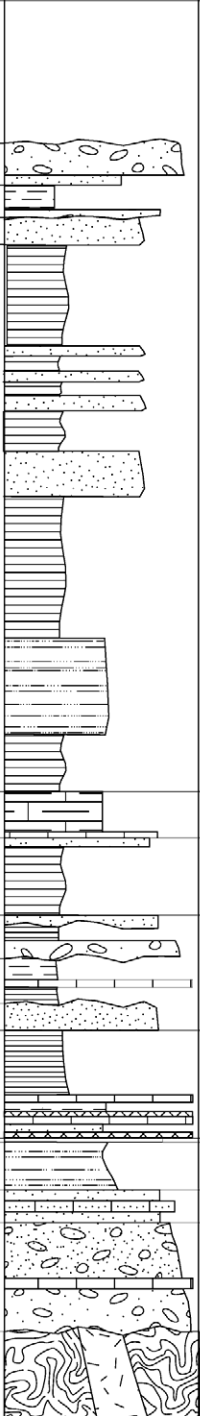
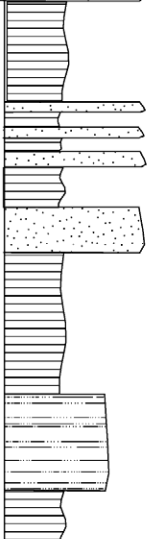
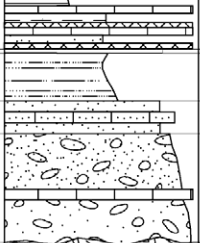
ERA	PERIOD	FORMATION	THICKNESS ft	LITHOLOGY	MAP SYMBOL				
CENOZOIC	Holocene Pleistocene	Alluvium, Colluvium, Landslide Deposits, & Terrace Gravels	0' - ?		Qal, Qc, Qls, Qtg				
	Miocene Oligocene	Ogallala / Arikaree	300' - 350'		No, Na				
		White River Group	0' - 240'		PeW				
		Fox Hills	450'		Kfh				
MESOZOIC	Cretaceous	Pierre Shale	> 4435'		Kp				
						Niobrara	290' - 350'	Kn	
						Benton Group	495' - 570'	Kegm	
						Dakota Group	245' - 320'	Kd	
						Jurassic	Morrison	300' - 330'	Jm
							Sundance / Jelm	152' - 200'	JTrsj
	Triassic	Lykins	700' - 800'	TrPl					
	PALEOZOIC	Permian	Lyons	3' - 30'		Plo Pi			
			Owl Canyon	200' - 350'					
			Ingleside	200' - 240'					
Penn.		Fountain	650' - 800'	PPf					
Middle and Early Proterozoic Crystalline Basement					XYu				

Fig. 3.1. Generalized stratigraphic column of the Northeastern Front Range.
Braddock et al. (1988a, 1988c, 1988d) and Courtwright and Braddock (1989).

were intruded concordantly and subsequently deformed during the Medicine Bow Orogeny (Braddock et al., 1988; Chamberlain, 1998). The ENE-trending Cheyenne Belt formed a diffuse zone of deformation as arc terranes were thrust upon the rifted transitional crust of the southern Wyoming craton (Houston, 1993; Chamberlain, 1998).

The Precambrian of the study area is dominated by two middle Proterozoic plutonic complexes, the 1.43 Ga Sherman Granite (Zielinski et al., 1981), and the 1.42 Ga Silver Plume Granite (Peterman et al., 1968). These middle Proterozoic granites were subsequently locally mylonitized along the NE-trending Moose Mountain, Skin Gulch and Poudre River Shear Zones (Braddock et al., 1988a; Punongbayan, 1989; Selverstone et al., 1997). The Skin Gulch Shear Zone lies in the southeastern study area and parallels the NE-trending magnetic low which spans the northern Front Range (Fig. 3.2).

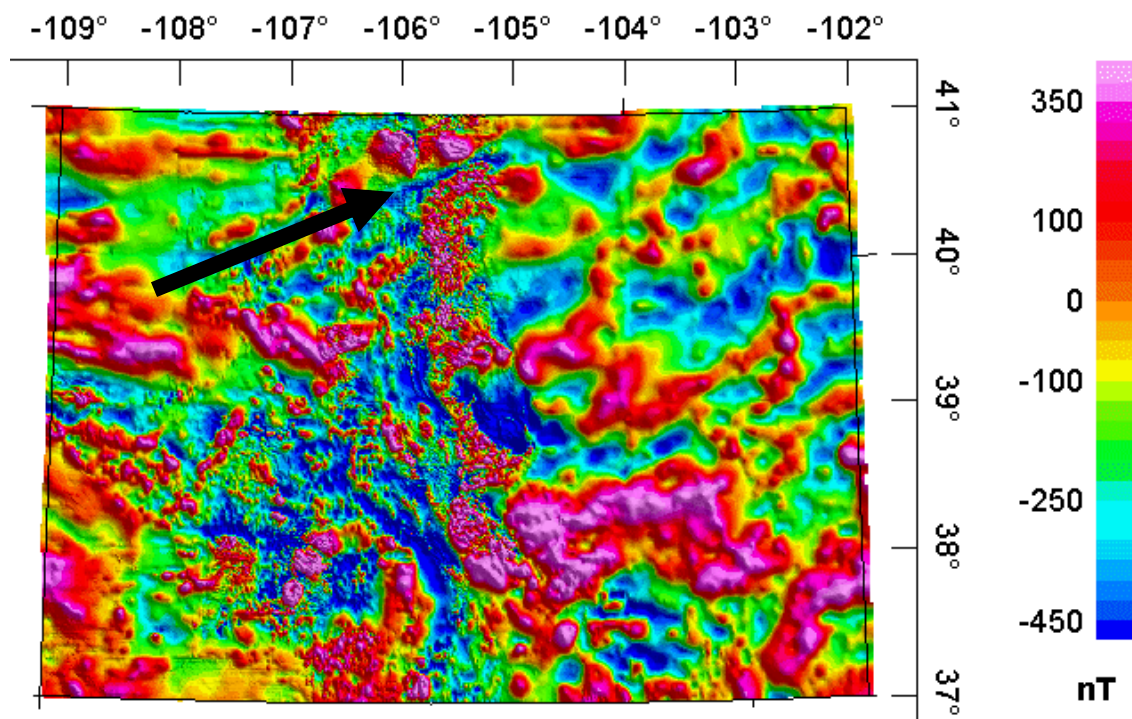


Fig. 3.2. Aeromagnetic map of Colorado. Arrow marks the NE-trending magnetic low of metamorphic rocks and middle Proterozoic shear zones. Image from the USGS (<http://pubs.usgs.gov/of/2000/ofr-00-0044/colorado.htm>).

Paleozoic

Massive blocks of lower Paleozoic strata are present in the Devonian-Silurian kimberlite diatremes of the State-Line Diamond District (McCallum and Mabarak, 1976; Smith, 1977). This suggests the northeastern Front Range contained lower Paleozoic sedimentary strata, similar to those preserved near Glenwood Springs, CO, prior to the Pennsylvanian Ancestral Rockies Orogeny (Kluth, 1997). Erosion of the Frontrangia uplift removed lower Paleozoic strata and formed the subplanar, middle Pennsylvanian nonconformity upon which the Fountain Formation was deposited (Kluth, 1997).

The Fountain Formation is a reddish-brown, coarse-grained arkosic sandstone and conglomerate interbedded with maroon siltstone, shale and limestone. The Fountain Formation was deposited during the late Pennsylvanian and Early Permian and ranges in thickness from 198 to 244 m (Braddock et al., 1988). The Fountain Formation is typically non-resistant to erosion and poorly exposed but to the north it becomes more calcareous, forming prominent hogbacks. The Fountain Formation preserves minor faults in streamcuts and roadcuts where sandstone and limestone beds dip $>10^\circ$.

The lower Permian Ingleside Formation is a pink, medium- to fine-grained quartzarenite which gradationally changes to gray, massive limestone and ranges in thickness from 61 to 73 m (Braddock et al., 1988a, Courtwright and Braddock, 1989). The variable lithologies of the Ingleside Formation were interpreted by Rhoads (1987) as the product of the depositional environment fluctuating from a near-shore beach to a shallow marine environment. Silica-cemented quartzarenite and limey sandstone of the Ingleside Fm preserve slickenlined cataclasite on minor fault surfaces. However, calcite fibers on faults in sandy limestone and limestone are seldom preserved, except in areas

with high erosion rates. Slickenlines on bedding planes suggest bedding parallel detachment is common as sandstone and limestone differ in their mechanical behavior.

The lower Permian Owl Canyon Formation is a dark, reddish-brown to maroon siltstone, shale and fine-grained sandstone which ranges in thickness from 61 to 107 m (Braddock et al., 1988, Courtwright and Braddock, 1989). The Owl Canyon Formation is generally poorly-exposed, forming strike valleys between Ingleside and Lyons hogbacks. Silica-cemented sandstone and siltstone beds preserve slickensided minor faults where dipping $>10^\circ$. Discrete, mesoscopic anticlines in the backlimbs of folds suggest faulting and folding was a product of flexural slip on the thinly-bedded strata.

The lower Permian Lyons Formation is a tan to pinkish-gray, medium-grained, well-sorted quartzarenite with planar and trough crossbedding (Braddock et al., 1988, Courtwright and Braddock, 1989). It ranges in thickness across the study area from 10 m in the south to <1 m near the Wyoming border. The Lyons Formation forms a prominent hogback where thicker than a meter and contains abundant slickensided minor faults.

Mesozoic

The upper Permian and lower Triassic Lykins Formation is dominantly a reddish-brown and maroon siltstone but also contains sandstone, shale, limestone and two prominent gypsum beds near its base. It ranges in thickness from 227 to 244 m (Braddock et al., 1988; Courtwright and Braddock, 1989). The Lykins Formation is poorly exposed throughout the study area, forming the prominent strike valley between the Lyons and Dakota hogbacks. The heavily-fractured and karsted gypsum beds of the lower Lykins Formation are well exposed in the backlimb of the Sand Creek Anticline. The Lykins formation contains few minor faults and dramatically varies in thickness within folds.

The upper Triassic Jelm Formation is a pink to orange-pink, fine- to medium-grained, calcareous, crossbedded eolian sandstone which unconformably rests on the Lykins Formation and ranges in thickness from 27 to 44 m (Braddock et al., 1988, Courtwright and Braddock, 1989). The upper and middle Jurassic Sundance Formation consists of gray to tan, fine- to medium-grained, well-sorted eolian sandstone, is 26 m thick and rests unconformably upon the Jelm Formation (Braddock et al., 1988, Courtwright and Braddock, 1989). The Jelm and Sundance Formations are typically partially to poorly exposed, covered by vegetation and landslide debris of the overlying Lytle Formation. Minor faults in the porous eolian sandstones are prominent as shear bands of silicic cataclasite are more resistant to erosion than unfaulted sandstone.

The upper Jurassic Morrison Formation contains greenish-gray and reddish-brown claystone with weakly resistant beds of micrite and gray, fine-grained sandstone and ranges in thickness from 101 to 110 m (Braddock et al., 1988, Courtwright and Braddock, 1989). It is typically poorly exposed and masked by Dakota Group landslides but minor faults in the brittle micritic limestone bed are exposed on steep slopes and roadcuts. The abundant claystone allows the unit to change thickness dramatically within folds and acts as a detachment for glide-block landslides of the lower Dakota Group (Braddock, 1978).

The lower Cretaceous Dakota Group forms the easternmost sandstone hogbacks of the Front Range foothills. The Lytle Formation is a yellowish-brown, massive coarse-grained sandstone and conglomerate with interbedded shales, bound by unconformities, and ranges in thickness from 24 to 34 m (Braddock et al., 1988; Courtwright and Braddock, 1989). The Lytle and Plainview formations form the higher, western hogback of the Dakota Group. The Plainview Formation is a buff-gray to tan, fine-grained

quartzarenite with lesser siltstone and shale and ranges in thickness from 11 to 26 m (Braddock et al., 1988; Courtwright and Braddock, 1989). The Lytle and Plainview formations preserve abundant minor faults where silica-cemented and dipping $>10^\circ$.

The Skull Creek Formation is a black to gray shale with thin siltstone and sandstone beds, and ranges in thickness from 23 to 46 m (Braddock et al., 1988; Courtwright and Braddock, 1989; Graham and Ethridge, 1995). The unit is not resistant to erosion, forming strike valleys between hogbacks and is the detachment for upper Dakota Group glide-block landslides (Braddock, 1978).

The Fort Collins Formation overlies the Skull Creek Formation in an upward coarsening gradational contact and is 8 to 13 m of grayish-tan, bioturbated, fine-grained sandstone (Graham and Ethridge, 1995). The Horsetooth Formation is grayish-tan, medium-grained massive sandstone ranging in thickness from 0 to 12 m. It was deposited in valleys in the Fort Collins Formation during a relative lowstand in local baselevel (Dolson et al., 1991). The Fort Collins and Horsetooth formations collectively form the lower, eastern Dakota hogback and contained the greatest abundance of slickensided minor fault data collected across the entire study area.

The upper Cretaceous Benton Group contains the Greenhorn Limestone, Codell Sandstone, and the Mowry, Graneros and Carlile Shales and ranges in thickness from 151 to 174 m (Braddock et al., 1988; Courtwright and Braddock, 1989). The Benton Group, with the exception of the upper Codell Sandstone, is poorly exposed across the study area and dramatically changes thickness within folds.

The upper Cretaceous Niobrara Formation contains the Smoky Hill Shale and the Fort Hays Limestone members (Braddock et al., 1988; Courtwright and Braddock, 1989).

The Smoky Hill Shale is 84 m of gray calcareous shale, marl and shaley limestone. The Fort Hays limestone is 5 m of massive gray micrite and forms a low relief hogback which denotes the base of the Niobrara Formation.

The upper Cretaceous Pierre Shale is largely composed of olive-gray shale and siltstone with several sandstone members. Collectively the 10 members of the Pierre Shale are approximately 1350 m thick in the northern Front Range (Scott and Cobban, 1978; Courtwright and Braddock, 1989). A complete section is preserved in the northeastern study area where it is overlain by the Fox Hills Formation (Scott and Cobban, 1986).

An incomplete exposure of tan, medium-grained sandstone of the upper Cretaceous Fox Hills Formation lies in the northeastern study area (Scott and Cobban, 1986). Complete sections of the unit averaged 137 m in thickness (Nibbelink, 1983).

Cenozoic

The Oligocene Chadron and Brule formations of the White River Group lie in an angular unconformity on the east-dipping Mesozoic strata in the northern study area. The Chadron Formation is a coarse-grained arkosic sandstone and conglomerate interbedded with mudstone and the Brule formation is dominated by massive mudstone (Courtwright and Braddock, 1989). The thickness of the White River Group has not been precisely measured but is about 75 m thick in a paleovalley eroded into Mesozoic strata near the Colorado-Wyoming border (Courtwright and Braddock, 1989).

The Miocene Arikaree Formation is a light-brown to light-gray siltstone and fine-grained sandstone which ranges in thickness from 0 to 15 m and is exposed in the steep slopes below the cliffs capping the Gangplank (Courtwright and Braddock, 1989).

The Ogallala Formation is a resistant, olive-gray, coarse-grained sandstone and conglomerate, approximately 91 m thick (Courtwright and Braddock, 1989). The Ogallala Formation laps onto the Precambrian basement of the Laramie Range in southern Wyoming and crops out to the east of the study area, forming the High Plains (Ver Ploeg et al., 2000). The Ogallala Formation once formed a much more extensive alluvial apron shed eastward from Laramide arches during regional uplift associated with the Rio Grande Rift in the late Miocene (Raynolds, 1997; McMillan et al., 2002).

Chapter 4

Methods of Data Collection and Analyses and Discussion of Observations and Kinematic Data

The primary objective of this research was to constrain Laramide kinematics through the determination of the directions of strain and stress axes across the study area. Local and regional stress and strain directions can be determined through the analysis of mesoscopic, slickensided minor faults (Angelier, 1984; 1990). Several techniques exist for the analysis of minor fault data which consist of fault plane strike and dip, the trend and plunge of slickenlines and fault shear sense (Compton, 1966; Angelier, 1990). The analysis of minor faulting will be used to test the various hypotheses of Laramide kinematics proposed for the area.

Fault Data Collection Methods and Shear Sense Determination

Minor fault (n=3326) and shear plane data (n=55) were collected from 72 stations within the Precambrian basement and upper Paleozoic and Mesozoic sedimentary strata of the northeastern Front Range of Colorado and Wyoming. While a majority of fault data was collected from shallowly-dipping Phanerozoic strata ($<35^\circ$), some data were collected from basement fault zones and adjacent steeply-dipping strata. Shear sense of minor faults were determined using the RM and RO criteria of Petit (1987) (Fig. 4.1a). One fault plane and slickenline measurement was collected from each fault with the exception of a large thrust fault at Grayback Monocline (station 3.12e, Fig. 4.18).

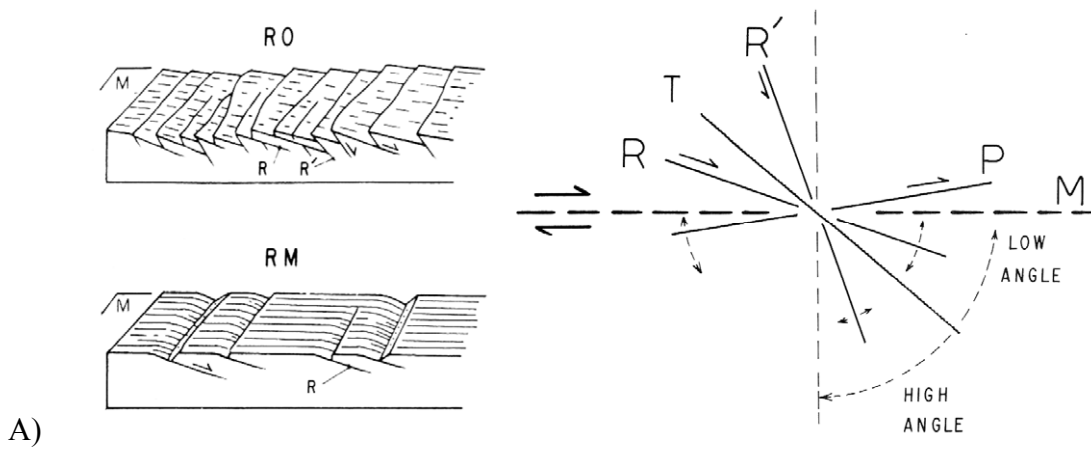


Fig. 4.1. A) Block diagrams of RO, RM type faults and the orientations of synthetic Riedel (R) shears, P-shears (P), antithetic Riedel (R') shears, and tensile (T) fractures (Petit, 1987). B) RO and RM fabrics on a thrust fault. C) RO and RM fabrics on a left-lateral strike-slip fault.

Fracture and Bedding Data Collection Methods

Extensional fracture, or joint, data (n= 1087) were collected from 19 data stations in the sandstone beds of the Fountain, Ingleside, Owl Canyon, and Lykins formations and the Dakota Group as well as the gypsum beds of the lower Lykins Formation. Joint data are summarized in Appendix B. The relative timing of jointing was recorded where abutting or cross-cutting relationships of joints and minor faults were obvious.

Bedding attitude data (n=576) were recorded from Pennsylvanian to Cretaceous strata, and additional data (n= 472), digitized from USGS geologic maps (Braddock et al., 1988a-d; 1989a-d; Courtwright and Braddock, 1989) are also included in Appendix C.

Methods of the Initial Kinematic Analysis of Minor Fault Data

Kinematic analysis methods employed in this study were eigenvector analysis of slickenlines attitudes and the ideal σ_1 method of Compton (1966) to quantify clustering of stress and strain axes about an average orientation. Eigenvector analysis of slickenlines was chosen as slickenlines represent the slip directions during deformation. The results of strain analysis were compared to stress analysis results. The ideal σ_1 method of Compton (1966) calculates an ideal σ_1 direction assuming σ_1 is on the plane perpendicular to a slickenlined fault and contains the slickenline, and that an angle α lies between the slickenline and the σ_1 axis. This provides two possible orientations of σ_1 , of which only one is consistent with the observed shear sense. The Compton (1966) ideal σ_1 method assumes faulting occurs on ideal planes without the influence a mechanical anisotropy, like bedding planes. Contoured stereoplots of ideal σ_1 axes can be used to distinguish single vs. multiple compression directions and vertical axis rotation (Erslev et al., 2004a). The ideal σ_1 method has been used for the conjugate minor faults common in the

Phanerozoic strata of the Front Range and Laramide foreland (Erslev et al., 2004a). Holdaway (1998) has shown that ideal conjugate minor fault planes faults in Permian through Cretaceous strata were formed by Laramide compression and have not been reactivated by subsequent tectonism. The stress inversion methods of Angelier (1984; 1990) were not utilized as Holdaway (1998) has shown the Compton (1966) ideal σ_1 method of stress analysis is best suited for ideal conjugate minor faults.

Raw minor fault data were entered into the Select spreadsheet which can be used to test whether slickenlines fall upon the fault plane and adjust accordingly. Slickenline trends on high-angle faults (<45° dip) were corrected using plunge and plunge direction. Slickenline plunges on low-angle faults (>45° dip) were corrected using trend. SELECT (Erslev, 1998) calculated the rake angles of slickenlines using corrected fault plane and slickenline attitudes. Rake angles were used to correct erroneous shear senses as strike-slip faults cannot have rake angles between 45° and 135° and thrust and normal faults must have rake angles between 45° and 135°. SELECT created files of the attitudes of fault planes, slickenlines, and ideal σ_1 compression axes using reasonable α angles ranging from 15° - 33° (Byerlee, 1978). Fault data were analyzed in ORIENT (Vollmer, 1991), creating stereoplots of fault planes, slickenlines, ideal σ_1 axes and generating eigenvectors and eigenvalues of the average trend and plunge of slickenlines and ideal σ_1 axes for each fault data station. Eigenvector and Eigenvalues of ideal σ_1 axes were recorded for the “best-fit” α angle ($\pm 1^\circ$) which provided the highest first eigenvalue, and for the ideal σ_1 axes with an $\alpha=25^\circ$ (Byerlee, 1978), as published in Erslev and Larson (2006). Roseplots of the trends of ideal σ_1 axes were created using 10° smoothing and scaled based on the size of the data set using LDIS 2.0 (Erslev, 1998).

Appendix A contains the results of all stress and strain analyses and the geographic coordinates, formation, and bedding attitude for all fault data stations.

Methods of the Initial Analysis of Joint Data

Joint attitude data were separated, based on abutting relationships observed at each data station, into J1 and J2 files and SELECT was used to create J1 and J2 fracture planes files. Each J1 and J2 fracture planes file was analyzed in ORIENT, calculating eigenvectors and eigenvectors of poles to planes and creating stereoplots of fracture planes. Fracture attitudes were rotated about a horizontal axis parallel to the strike of bedding which restored bedding to horizontal and the attitudes of poles to joint planes were recorded. Roseplots of joint strikes were created using 10° smoothing and scaled based on the size of the data set using LDIS (Erslev, 1998). Minor fault data were collected adjacent to joint data stations to determine the orientations of local minor fault planes, estimate Laramide stress and strain, and observe relative timing relationships.

Geologic Observations

Brief summaries of the geometry and orientation of structures, field observations, and fault and fracture data are presented in a north to south progression, and followed by a brief discussion of the data and observations. The study area was divided into areas based on the 1:24 000 scale geologic maps published by the USGS (Figs. 4.2 - 4.9). Where large numbers of minor fault and fracture data were collected from closely spaced data stations, the geologic maps were further divided into subareas. The maps include stereoplots of fault and fracture planes, slickenlines, ideal σ_1 axes and bedding and smoothed roseplots of ideal σ_1 trends, joint and strike-slip fault strikes, whose sizes are proportional to data set (Figs. 4.10 – 4.26).

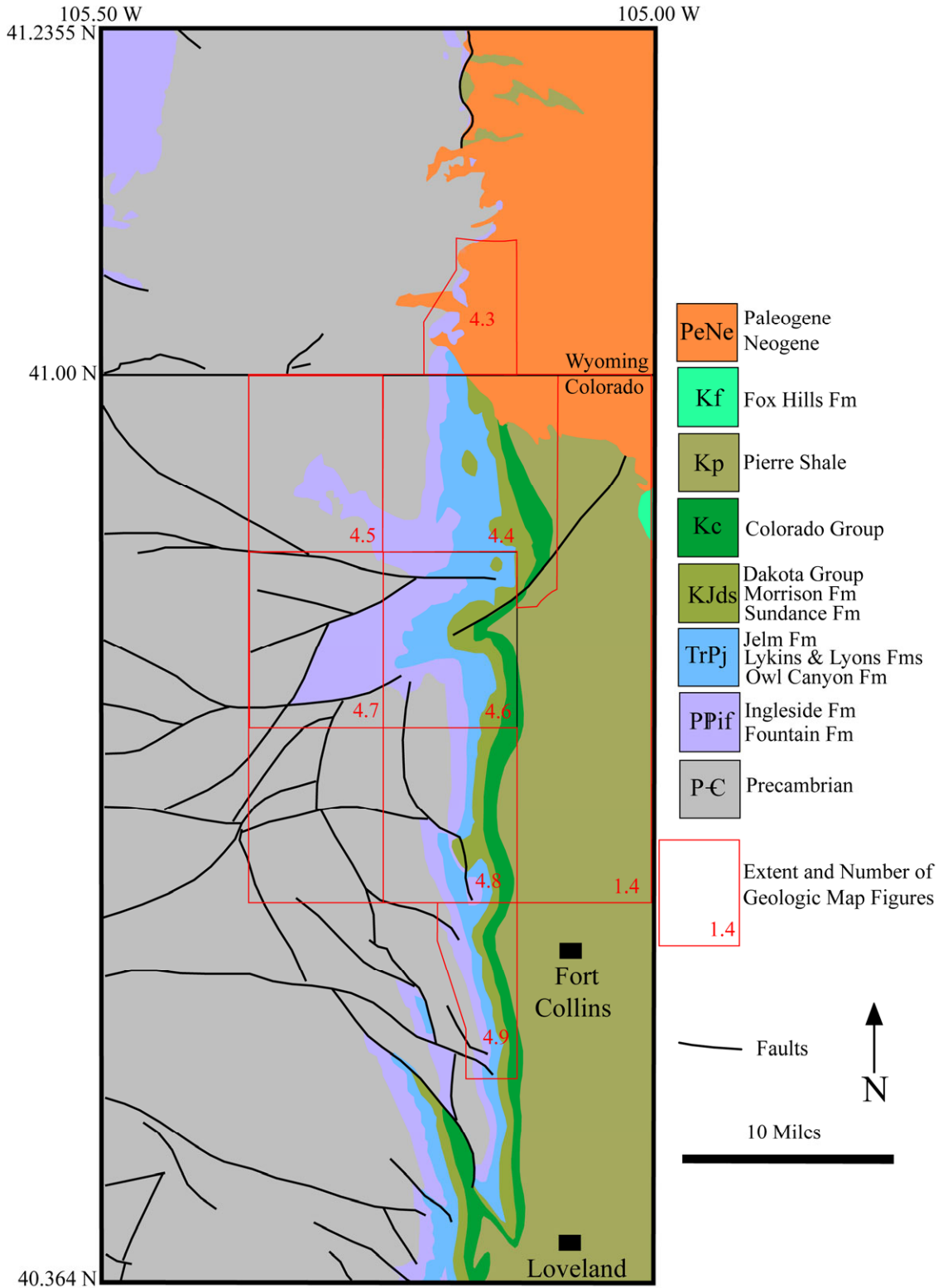


Fig. 4.2. Simplified bedrock geologic map of the northeastern Front Range and southern Laramie Range. Red boxes show the extent of larger scale geologic maps. Figure adapted from Tweto (1979) and Love and Christiansen (1985).

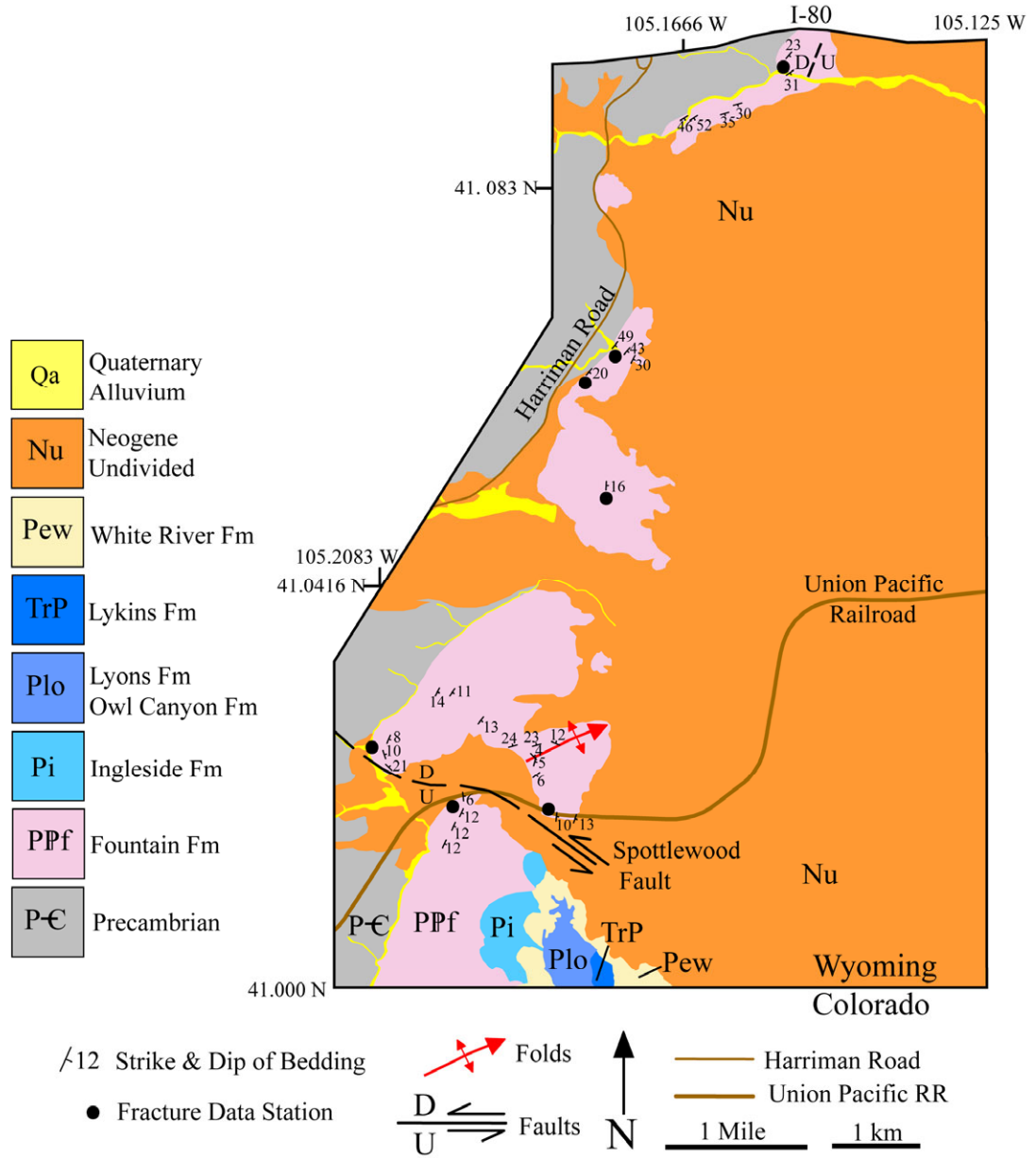


Fig. 4.3. Geologic map of the southeastern Granite quadrangle, adapted from Houston and Marlatt (1997) and Ver Ploeg et al. (2000).

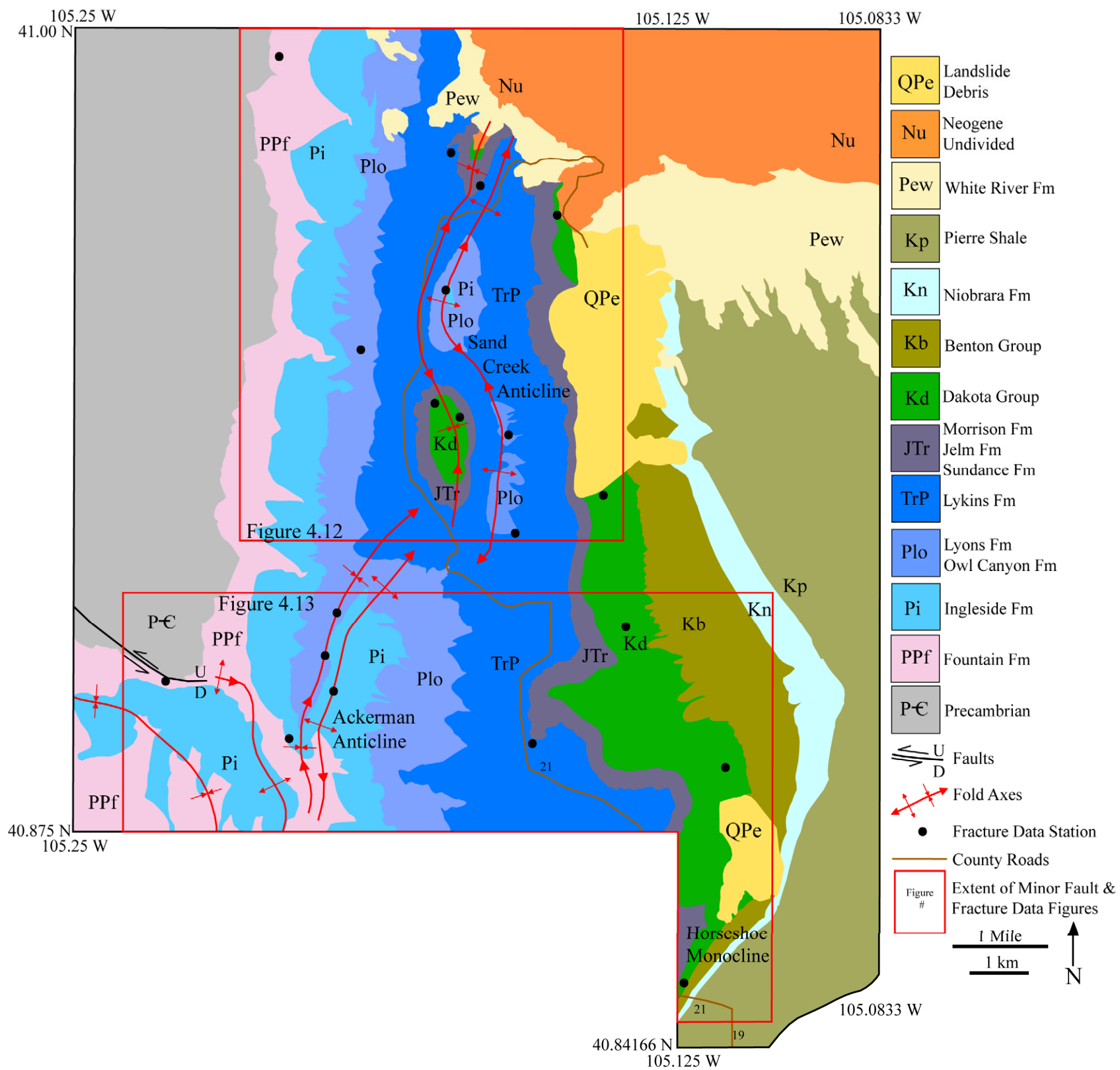


Fig. 4.4. Bedrock Geologic Map of the Table Mountain Quadrangle. Adapted from Courtwright and Braddock (1989).

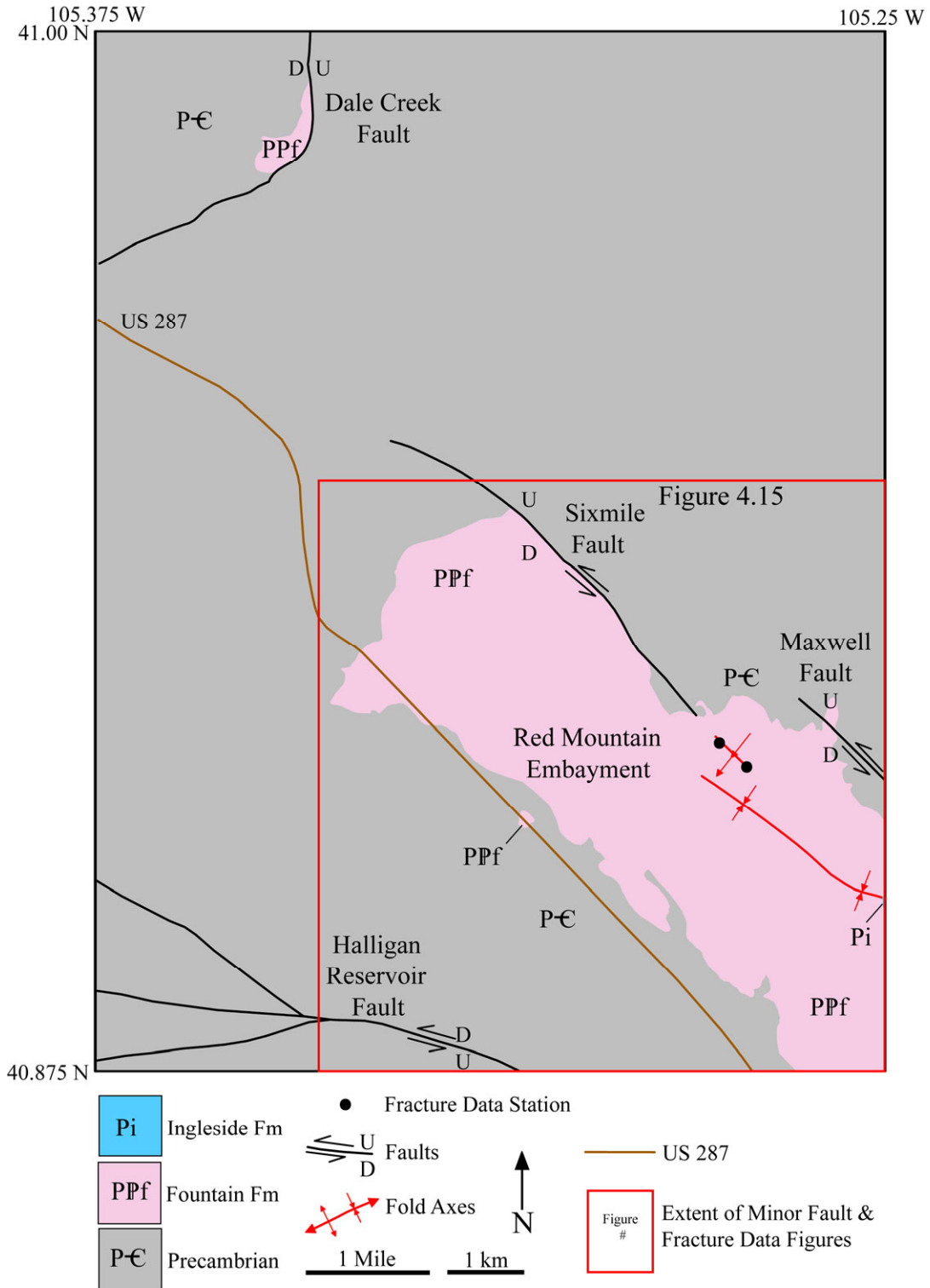


Fig. 4.5. Bedrock geologic map of the Virginia Dale quadrangle. Adapted from Braddock et al. (1989b).

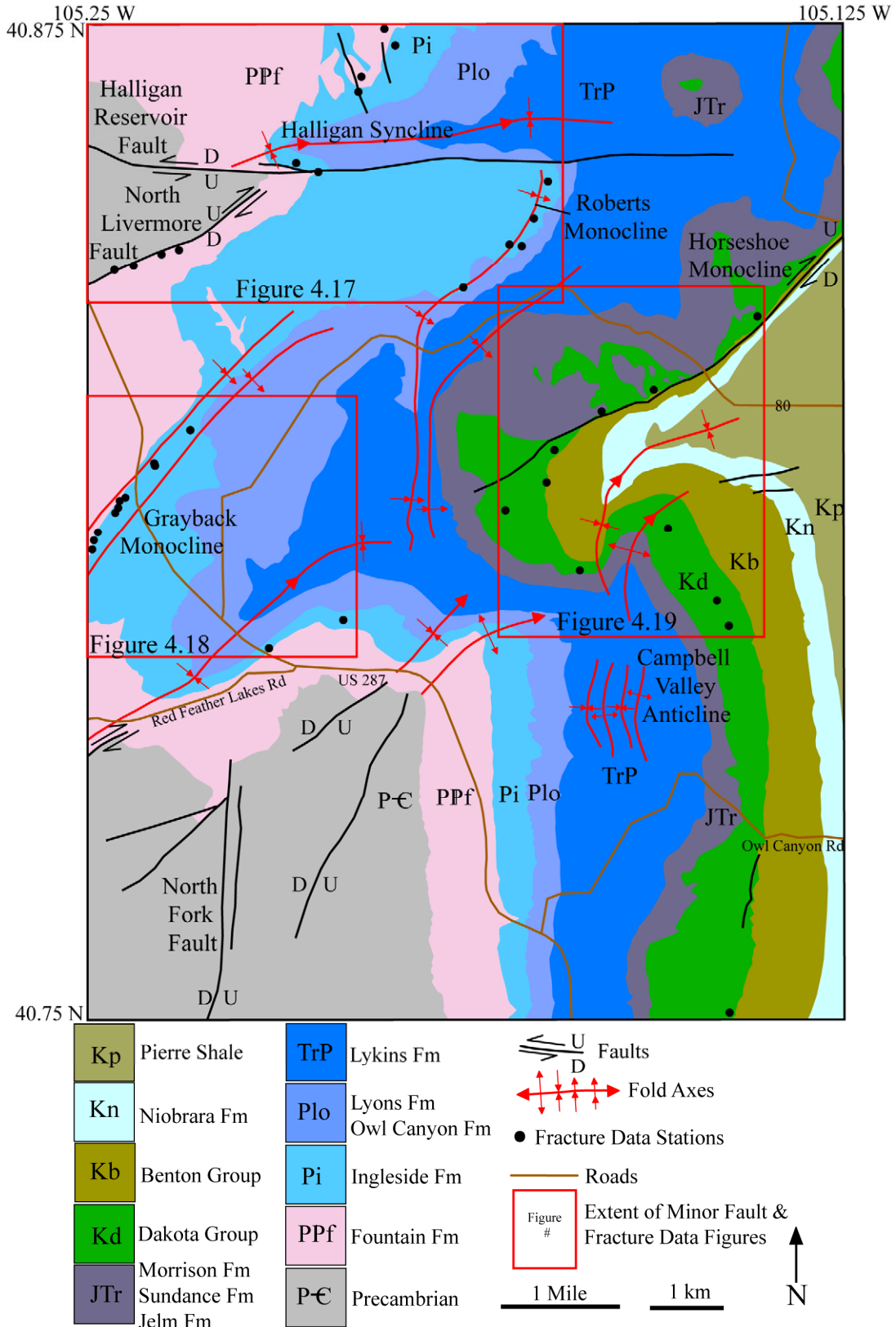


Fig. 4.6. Bedrock geologic map of the Livermore quadrangle.
Adapted from Braddock et al. (1988d).

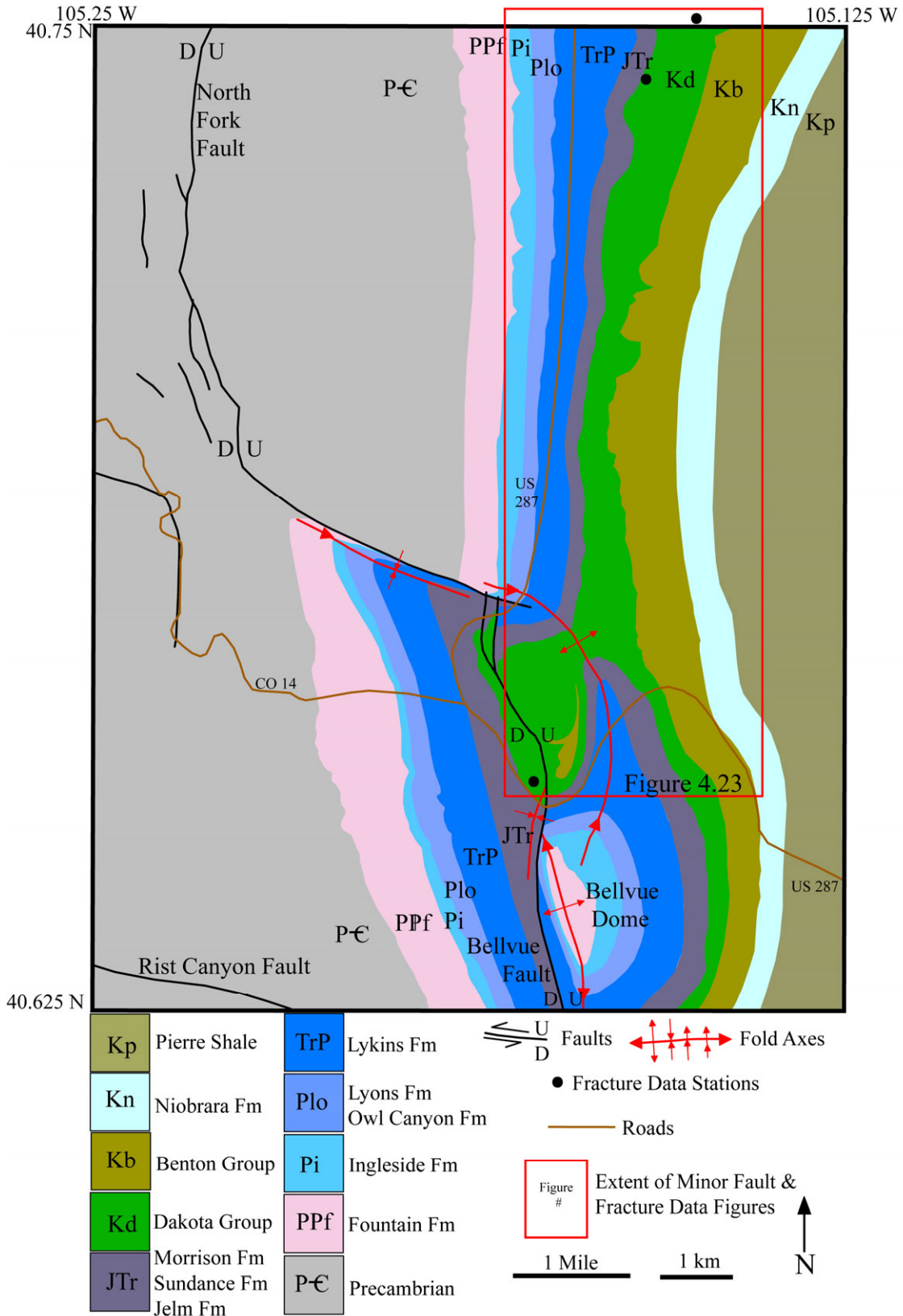


Fig. 4.8. Bedrock geologic map of the Laporte quadrangle.
Adapted from Braddock et al. (1988c).

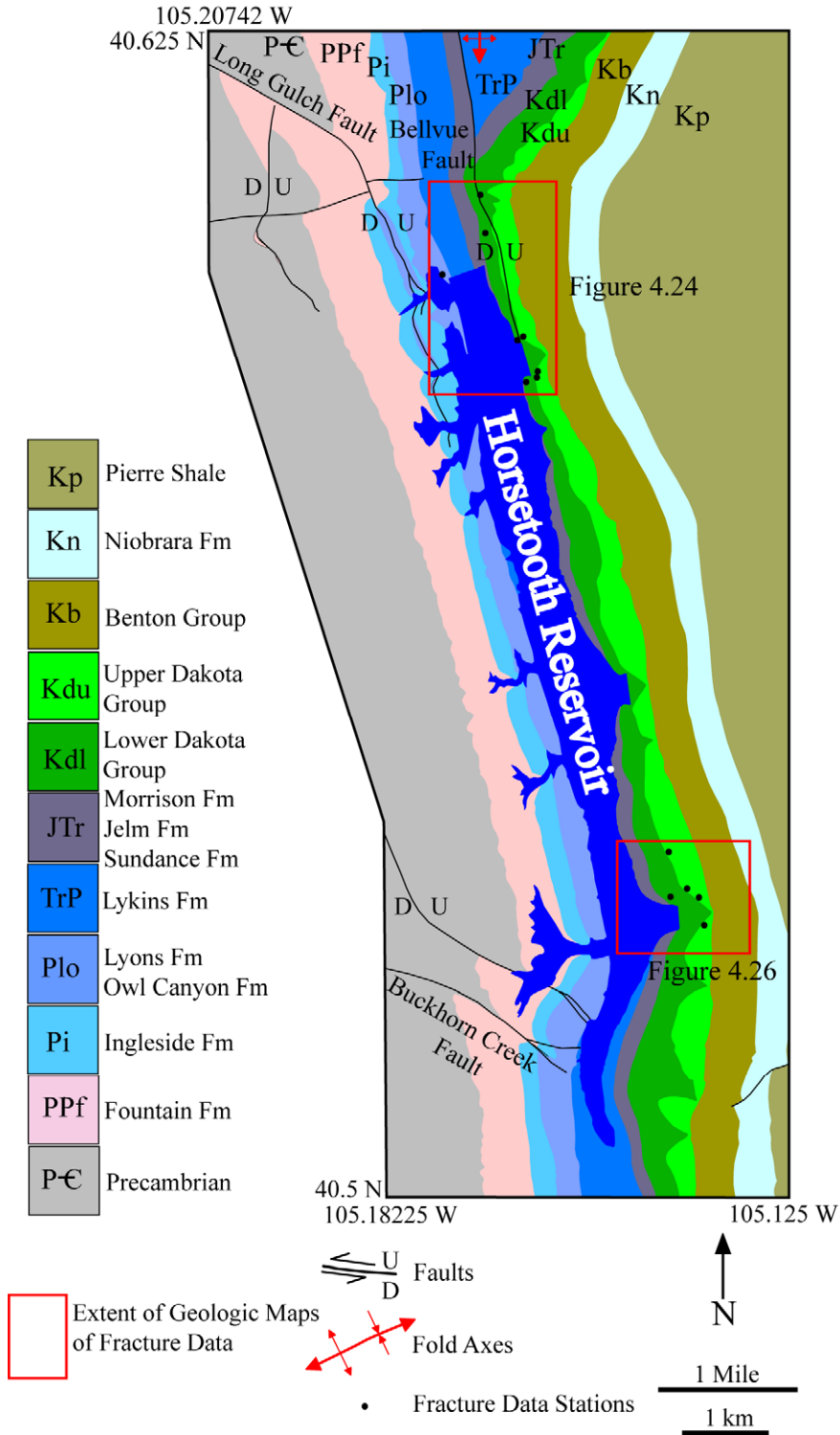


Fig. 4.9. Bedrock geologic map of the Horsetooth Reservoir quadrangle. Adapted from Braddock et al. (1989a).

Southeastern Granite Quadrangle

The northernmost extent of this investigation was in the foothills between I-80 and the Colorado-Wyoming border in the Granite quadrangle in southwestern Laramie County, Wyoming (Figs. 4.2 and 4.3). The Pennsylvanian nonconformity and overlying Pennsylvanian and Permian sedimentary strata dip between 10° - 50° SE. The area also includes a map-scale, NW-striking, E-dipping fault and a NE-plunging, asymmetric anticline that has an abrupt, concealed termination to the SW. Although the area contains relatively small-scale Laramide structures, 10 km to the north, the major thrust bounding the Laramie Range is exposed where Proterozoic basement has been thrust over upper Cretaceous strata (Fig. 4.2). Variable strike of the nonconformity and abruptly changing attitudes of Pennsylvanian strata suggests gentle basement folding in the north (Fig. 4.3). However, in the south, the consistent NNE strike and shallow dip of Pennsylvanian strata suggests virtually no folding of the basement (Figs. 4.3, 4.10).

Faulting on a S-dipping thrust coring an asymmetric anticline is dominated by synthetic thrusts with NW-SE trending slickenlines (station 1.1, Figs. 4.10 and 4.11). Less than 300 m to the E is a mapped NE-striking, SE-dipping, planar thrust fault with approximately 25m of throw. Faults in the NE- and N-trending hogbacks about 5-10 km to the southeast are E- and NE-dipping thrusts with ENE-trending slickenlines (stations 1.2, 1.3, Fig. 4.10). Dissolution cleavage planes strike subparallel to bedding and are cross-cut by minor thrusts (station GC, Fig. 4.10). Fault data to the south are dominated by thrusts but poor preservation of surface textures on NE- and NW-trending subvertical fractures made differentiating strike-slip faults, joints and cleavage planes impossible. Thrusts planes and slickenline trends measured in planar sections of shallowly-dipping

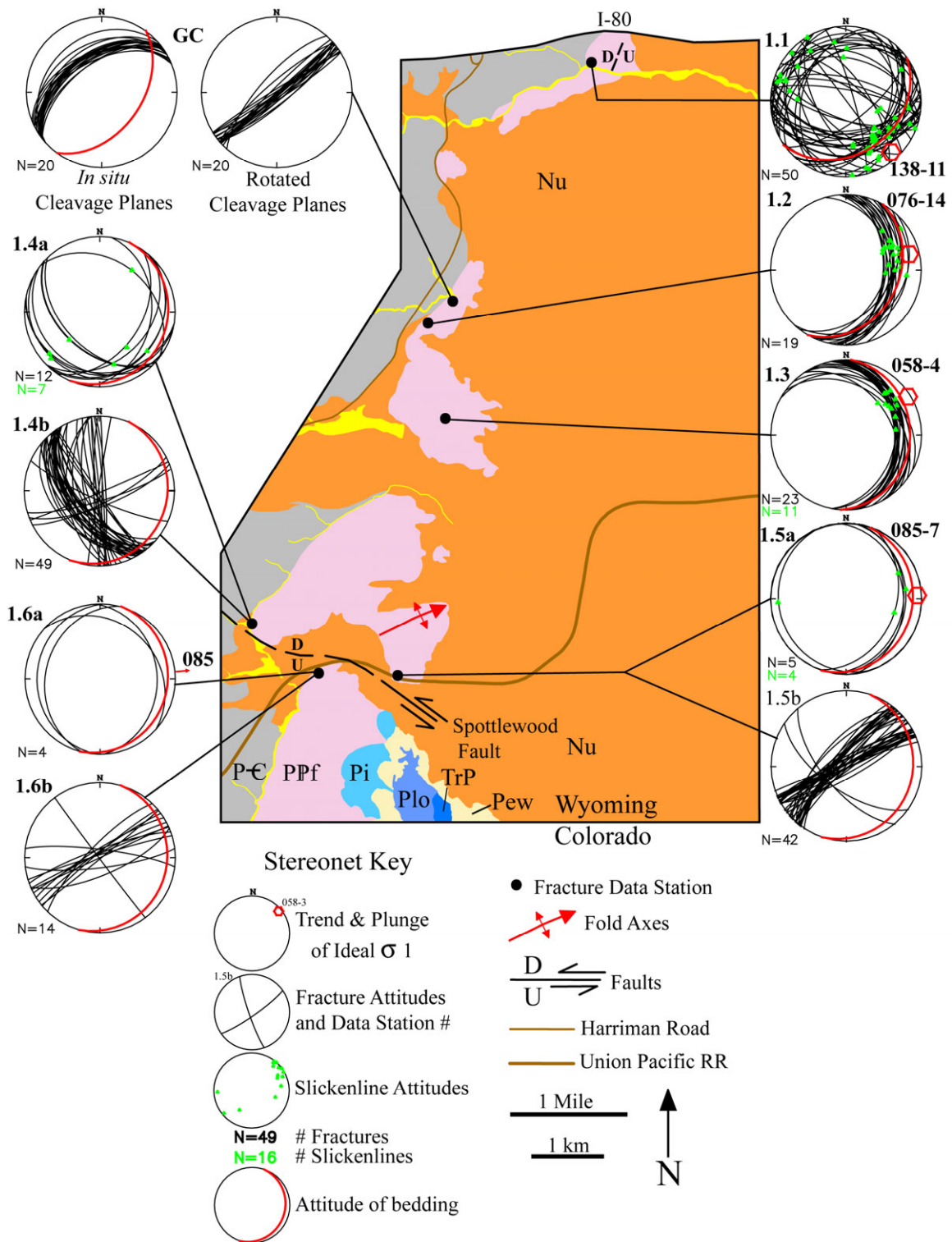


Fig. 4.10. Stereonets of fractures, minor faults, slickenlines and ideal σ_1 axes measured in the southeastern Granite quadrangle.

limestone are consistent in orientation (station 1.5a, 1.6a, Fig. 4.10). However, fractures were more complex with a low-angle conjugate pattern in limestone and an orthogonal pattern in sandstone (stations 1.5b, 1.6b, Fig. 4.10). Multidirectional slickenline trends and thrusting and extremely complex fracture patterns were measured where bedding strikes change from NNE to WNW (Fig. 4.3; stations 1.4a, 1.4b, Fig. 4.10). The map-view relative offset between the two NNE-trending hogbacks in the SW is due to the nonconformity being elevated to the S.

The parallelism of bedding dip directions and slickenlines trends, rapid changes in bedding attitudes and the dominance of SE- and E-dipping thrusts suggest basement folding is driving out-of-the-basin flexural slip. Cleavage planes were found to restore to subvertical attitudes if bedding were rotated to original horizontality (GC, Fig. 4.10). This suggests CaCO_3 dissolution was an early deformation mechanism in response to fold-related shortening prior to brittle faulting. The asymmetric, NE-plunging anticline is likely cored by a SE-dipping thrust formed by west-directed, out-of-the-basin flexural slip. The conjugate partings in the backlimb could be a product of two stages of cleavage formation as the fold hinge would reorient the fold-related shortening direction from NE to ENE. The orthogonal fractures in sandstone appear to be joints with a NE-striking primary set (station 1.5b, Fig. 4.10). The inability to separate faults, joints and cleavage planes limits the interpretation of station 1.4b (Fig. 4.10). It is likely all three are present. The abrupt termination of the anticline, changes in bedding attitudes, and the elevated nonconformity south of the UP railroad all suggest the concealed Spottlewood Fault continues SE as mapped by Houston and Marlatt (1997). Given an ENE trend of σ_1 and map-view offsets, the Spottlewood fault is likely a left-lateral fault dipping $80^\circ - 85^\circ$ SW.

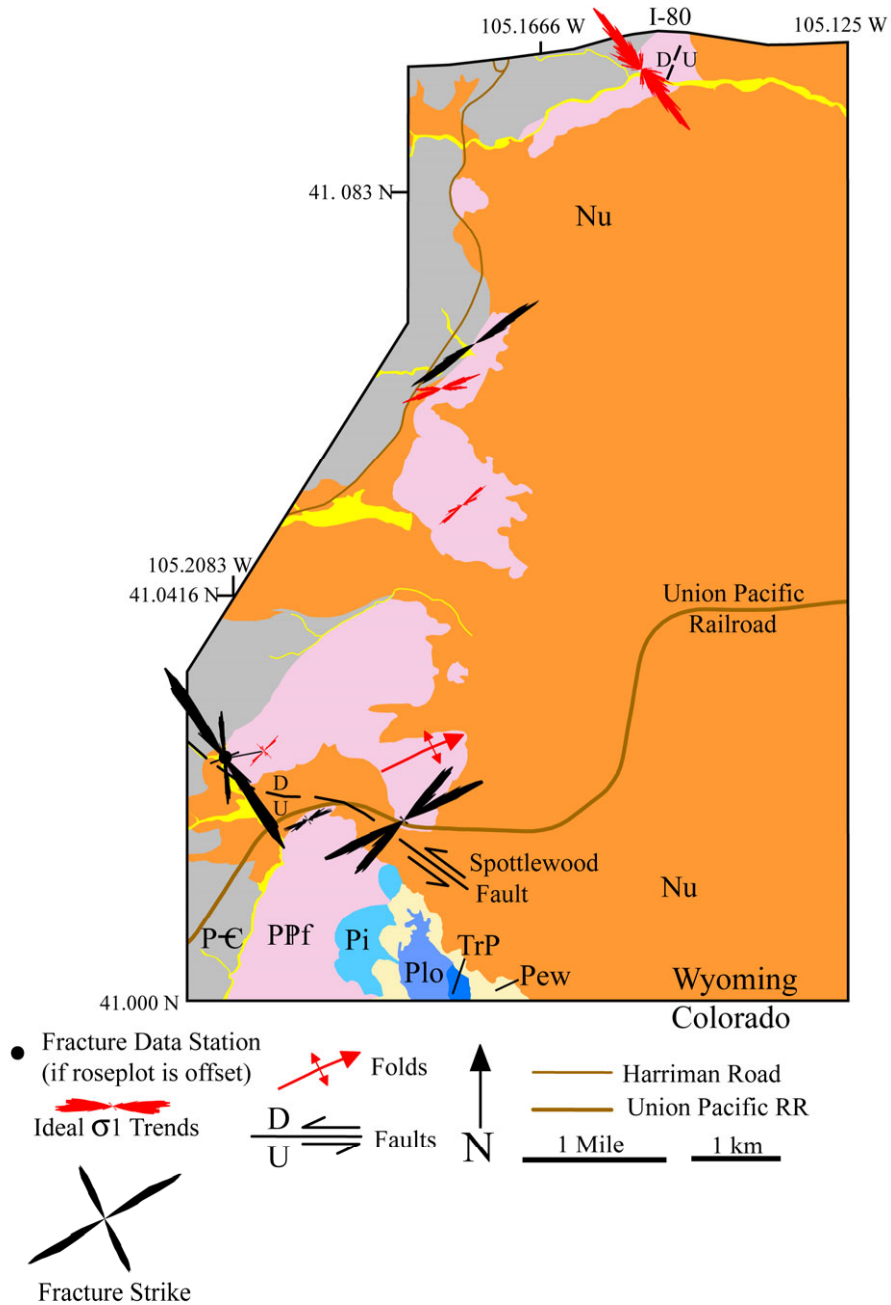


Fig. 4.11. Roseplots of ideal σ_1 trends and fracture strikes measured in the southeastern Granite quadrangle.

No observations were made supporting the concealed NE- or NNE- striking faults in the southern part of the Granite Quadrangle as mapped by Ver Ploeg et al. (2000).

Table Mountain Quadrangle

The Table Mountain quadrangle encompasses the northernmost foothills of the northeastern Front Range in northern Larimer County, Colorado (Fig. 4.2). Major structures include the Sand Creek and Ackerman Anticlines, the NW-striking Maxwell Fault, an unnamed NNW-trending anticline, and the Horseshoe Monocline (Fig. 4.4).

The Sand Creek Anticline (SCA) is asymmetric with gently curving hinges, a steep (40° - 60°) western forelimb and a shallow (12° - 16°) eastern backlimb. Backlimb attitudes are consistent; with local homoclinal dips of 12° - 16° E. Fold axes are sinuous in map-view with NE-, N- and NW-trending segments (Fig. 4.4). The SCA has two doubly-plunging structural culminations where fold axes trend N-S. The SCA plunges north where its terminus is concealed by post-Laramide Cenozoic strata. The SCA terminates to the south where fold axes abruptly bend and plunge SE near the northern end of the Ackerman Anticline (Fig. 4.4). Faults in the northern Sand Creek syncline are dominated by out-of-the-syncline thrusts with slickenlines trending perpendicular to fold axes (stations 2.1, 2.2, Fig. 4.12). Whereas W-dipping thrusts are dominant within the forelimb of the SCA, strike-slip faults become numerous where folds plunge (stations 2.4, 2.5, Fig. 4.12). Normal faults on the structural culminations of the SCA were found to strike parallel to the hinge (station SCA, Fig. 4.12). Faults in backlimb of the SCA are thrusts and the majority dip E (stations 2.3, 2.7, Fig. 4.12). Primary joint sets measured in Fountain Formation sandstone and Lykins Formation gypsum strike nearly perpendicular to each other (stations 1.7, GCF, Fig. 4.12).

The dominance of out-of-the-syncline thrusts and slickenlines perpendicular to fold axes suggests bedding-parallel flexural slip was driven by synclinal tightening. The

abundance of E-dipping thrusts in the backlimb of the SCA is suggestive of top-to-the-west flexural slip on bedding parallel detachments. Strike-slip faults in plunging segments of folds likely accommodate axis-parallel extension.

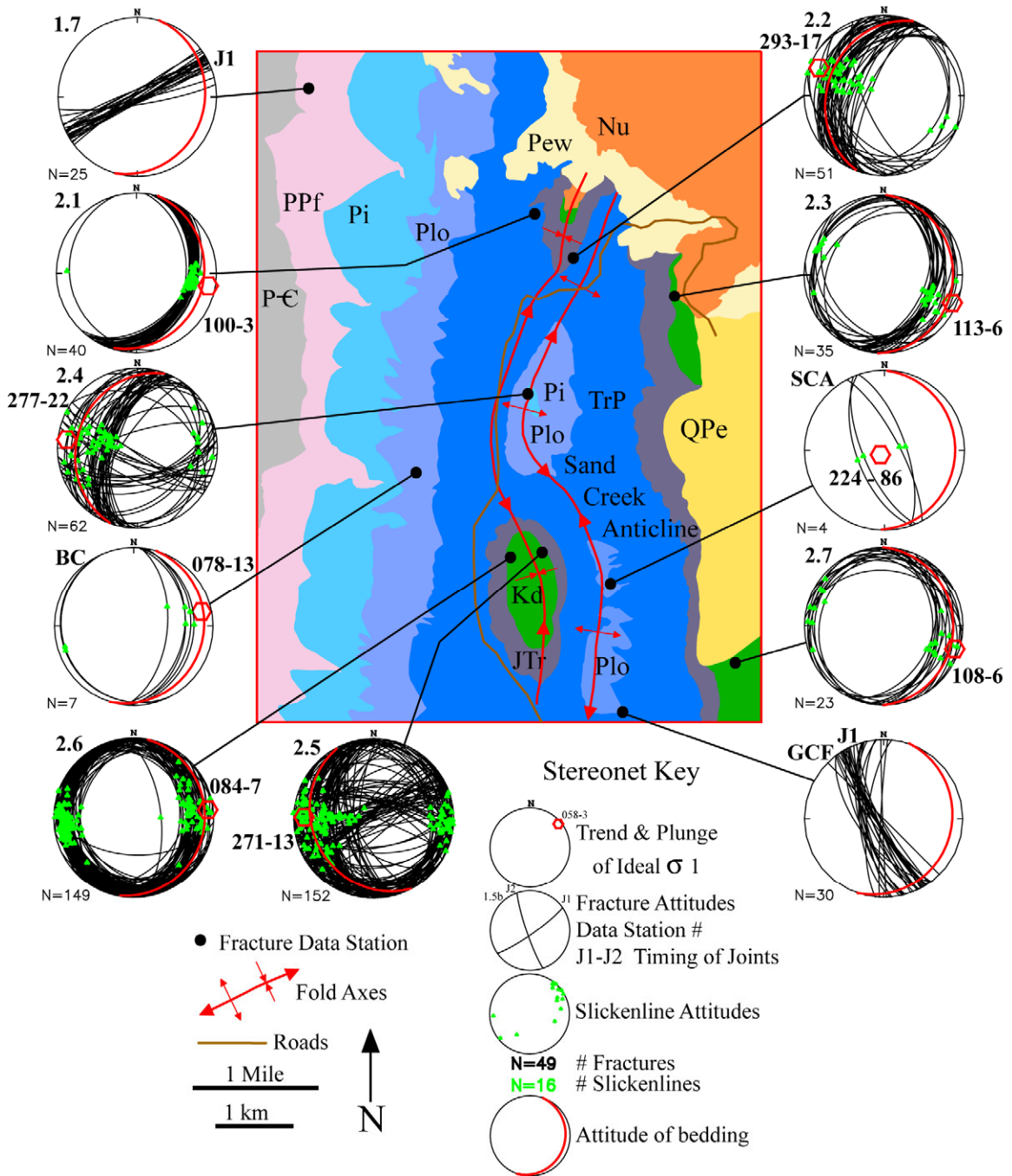


Fig. 4.12. Stereonets of fractures, minor faults, slickenlines and ideal σ_1 axes measured in the northern Table Mountain quadrangle.

The geometry, trend and asymmetry of the SCA and the E-trend of σ_1 predict the fold is cored by a planar, reverse fault dipping $50^\circ - 60^\circ$ E. The gently curving fold hinges, out-of-the-syncline thrusting and local extension on the anticlinal crest are suggestive of trishear fault-propagation folding (Erslev, 1991). An E-trend of σ_1 suggests structural culminations on the N-trending segments of the SCA may be elevated by more dip-slip and less strike-slip on the underlying fault (stations 2.4, 2.5, 2.6, Fig. 4.12). The contrasting orientations of joints in the Fountain and Lykins formations suggest different lithologies may have had different timing or mechanisms of fracturing (stations 1.7, GCF, Fig. 4.12). The SSE trend of fractures in the gypsum apparently guides groundwater flow, controlling gypsum dissolution and thus gypsum cave trends (station GCF, Fig. 4.12).

The Ackerman Anticline (AA) is an asymmetric anticline with a steep ($50^\circ - 80^\circ$) western forelimb and a shallow ($8^\circ - 12^\circ$) eastern backlimb (Fig. 4.4). The fold axes of the doubly-plunging AA vary in trend from N to NE, with the structural culmination on an N-trending segment of the anticlinal axis. The AA dies out to the north as fold axes curve and plunge to the NE near the southern terminus of the SCA. While the northern AA has backlimb dips consistent with local homoclinal dips of $12^\circ - 16^\circ$ E, the southern AA has fold axes plunging in opposite directions and bedding dip directions which change from ESE to SSE (Fig 4.4). Faults on the anticlinal crest are exclusively strike-slip while the forelimb has both thrust and strike-slip faults (stations 2.9, 2.10, 2.11, 2.13, Fig. 4.13). Faults in the eastern limb of the NNE-plunging syncline were exclusively thrusts and dominated by the W-dipping, out-of-the-syncline conjugate. The ENE-trend of σ_1 from the anticlinal hinge is 10° more oblique to the NNE-trending fold axes than the E-trend of σ_1 from the syncline and forelimb (stations 2.9, 2.10, 2.11, Fig. 4.13).

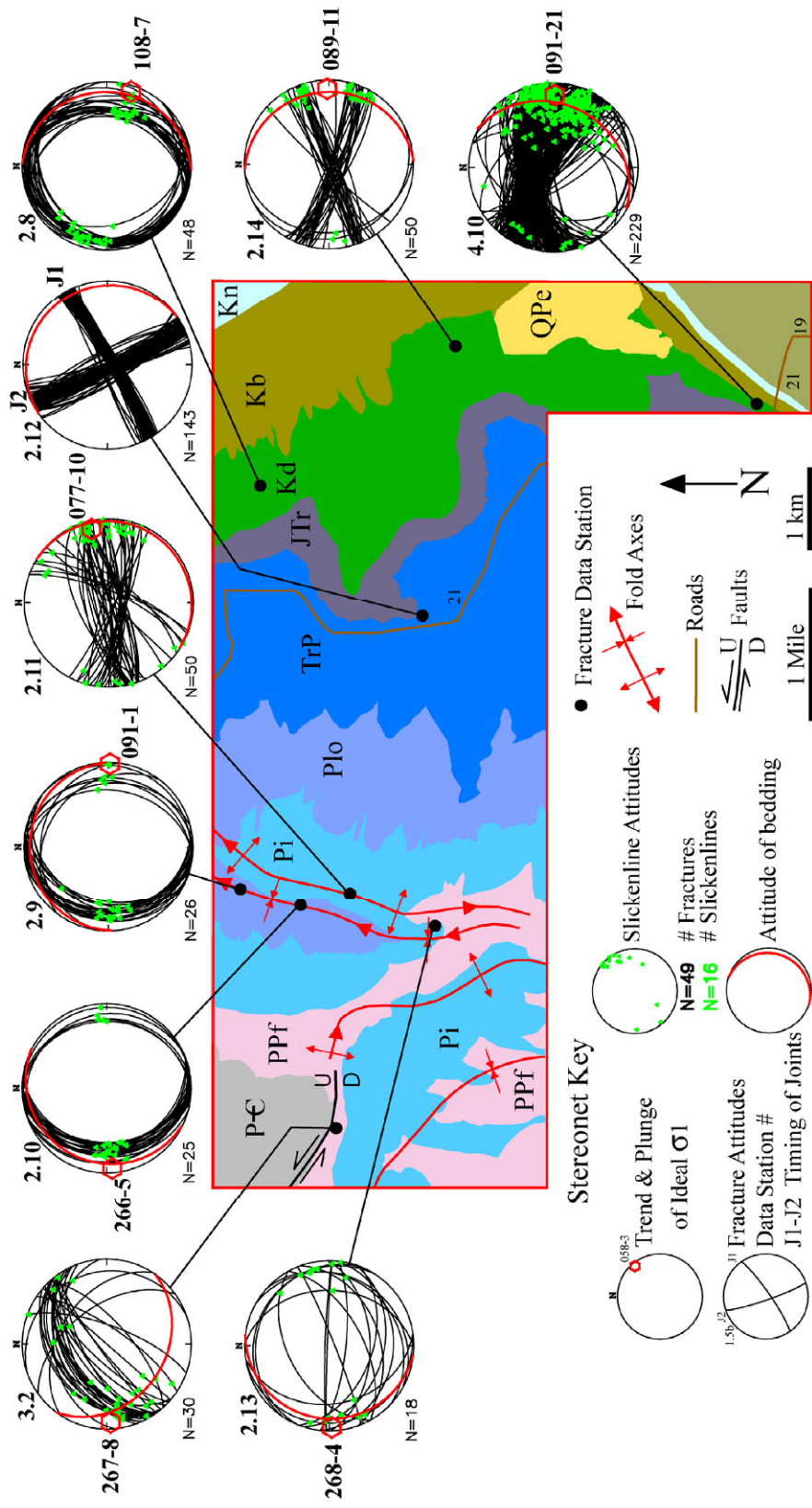


Fig. 4.13. Stereonets of fractures, minor faults, slickenlines and ideal σ_1 axes measured in the southern Table Mountain quadrangle.

Strike-slip faulting on the crest of the doubly-plunging AA likely accommodates axis parallel extension. The dominance of W-dipping, out-of-the-syncline conjugate thrusting suggests faulting was due to local flexural slip driven by synclinal tightening. The 10° deviation of σ_1 from the anticline and syncline suggests stress trajectories may have slightly bent to trend more perpendicular to synclinal axes. The geometry, trend and asymmetry of the AA and an E-trending σ_1 predict the fold is cored by a planar, reverse fault, dipping 50° - 60° E. The NNE-trend of the fold axes and the E-trend of σ_1 predict the fault had a minor component of right-lateral motion. The structural culmination on the N-trending segment of the anticline was likely due to more dip-slip and less strike-slip on the underlying fault. The tightly-curved fold hinges and out-of-the-syncline thrusting suggests of trishear fault-propagation folding and top-to-the-west flexural slip were important modes of deformation in the northern AA. The oppositely-plunging folds and changing elevations and attitudes of bedding in the southern AA suggest basement folding may have been a key mode of local deformation. Similar inferred attitudes of the faults which core the SCA and AA and the abrupt plunging and bending of folds towards one another suggest slip may have been transferred between these two faults.

The NW-striking Maxwell fault in the southwestern Table Mountain quadrangle strikes 324° and dips 80° NE. Map offsets show the NE side has moved up relative to the SW side. Faulting in the SSW-dipping footwall beds is dominated by right-lateral faults (station 3.2, Fig. 4.13). Fault attitude, relative offset, the right-lateral faults and an E-trending σ_1 predict oblique left-lateral / reverse slip on the Maxwell fault (Fig. 4.13).

An unnamed NNW-trending anticline plunges southward from a subtle arch of the nonconformity in the hanging wall of the Maxwell fault. The anticline's sinuous trend

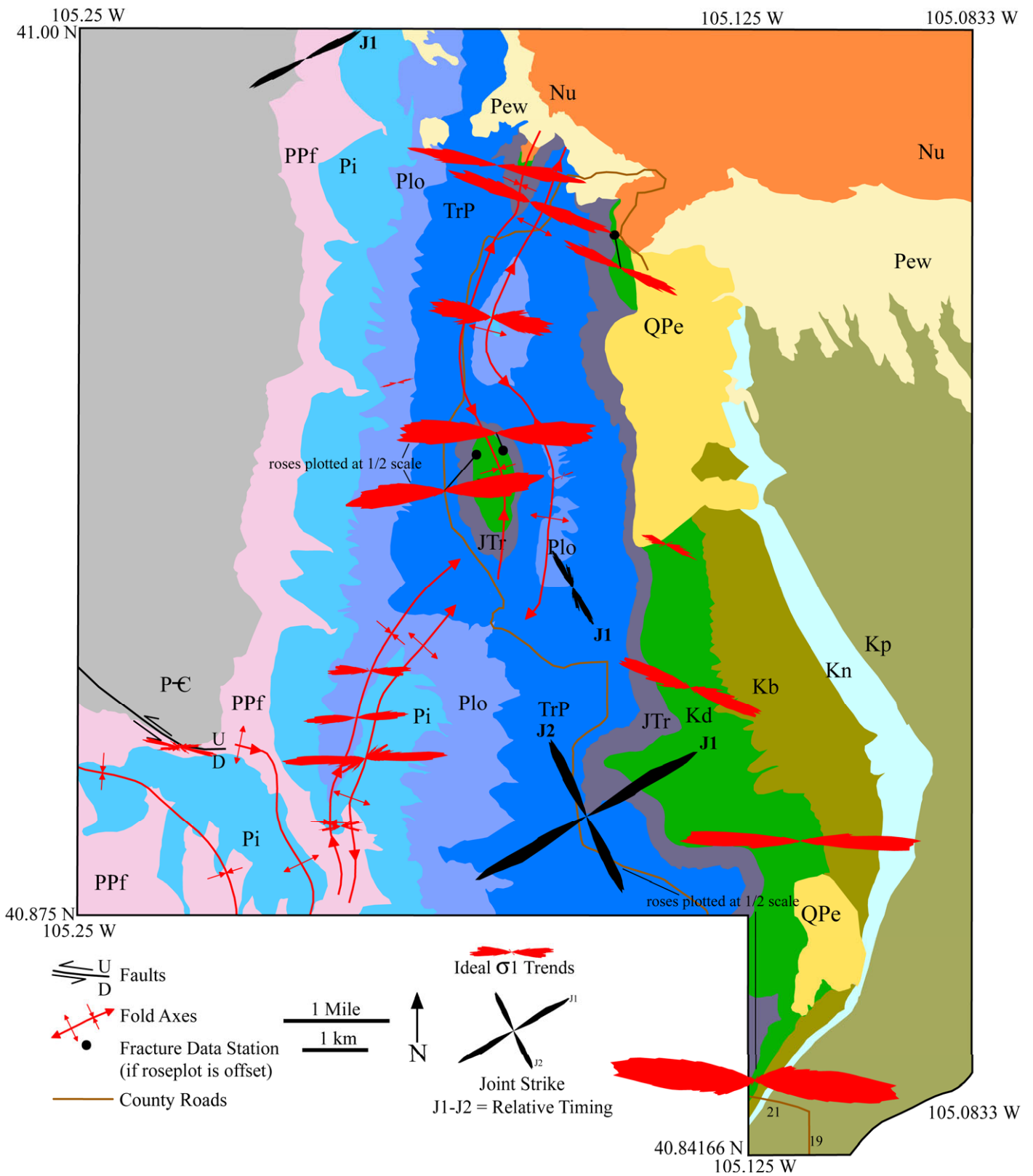


Fig. 4.14. Roseplots of ideal σ_1 trends and fracture strikes measured in the Table Mountain quadrangle.

and southern terminus are coincident with the AA. The fold straddles a transition where the basement is lower to the SW and dip directions of beds change from E to SW. The fold dies out to the south near two ENE-dipping thrusts in the Fountain Fm.

The subparallel trends and coincident termini near ENE-dipping thrusts and changes in basement attitude and elevation suggest the anticline is cored by an ENE-dipping thrust in the lower Fountain Formation. Thrusting is likely due to top-to-the-west flexural slip driven by synclinal tightening and localized on the crest of a basement fold.

Dakota Group faults change from ESE-slickenlined thrusts in NW-striking beds to strike-slip faults as the hogback bends into the NE-striking Horseshoe Monocline (HM) (stations 2.8, 2.14, 4.10, Fig. 4.13). The smoothly-curved forelimb of the HM separates subhorizontal strata to the west from strata dipping 7° E. The thicknesses of incompetent Mesozoic strata were highly attenuated in the forelimb, where bedding dips $40^\circ - 70^\circ$ SE. Although strike-slip faults were abundant in the forelimb, a larger fault wasn't exposed.

The change from thrust to strike-slip faulting likely accommodates the eastward bending of the hogback and/or extension parallel to the NE-trending monoclinical axis. The trend and geometry of the HM, abundant strike-slip faults, and an E-trending σ_1 predict the fold is cored by a concave-up, listric fault with oblique right-lateral / reverse slip that strikes NE and dips $45^\circ - 60^\circ$ NW. The smoothly curved forelimb, highly attenuated strata and lack of an exposed, macroscopic fault suggests the dominant mode of deformation was trishear fault-propagation folding.

NE-striking master joints predate the NW-striking cross joints (station 2.14, Fig. 4.13). RO fabrics in adjacent strata (Petit, 1987) and slickenlined calcite fibers on joint faces suggests NE-striking joints were subsequently reactivated as right-lateral faults.

Virginia Dale Quadrangle

The Virginia Dale quadrangle contains the NW-trending Red Mountain Embayment (RME) bounded by the NW-trending Red Mountain Monocline (RMM) and the Sixmile (SF) and Maxwell faults (MF), which strike NW and dip 70-80° NE (Fig 4.5). The area also contains the ESE-striking, subvertical Halligan Reservoir Fault, the SE-dipping Dale Creek Fault and remnants of the lower Fountain Fm. and the nonconformity. Map-view offsets of the SF and MF show the NE hanging wall has moved up relative to the SW footwall. The attitude of the nonconformity changes across the RME with shallow SE dips in the west and dips of 9° SW between the SF and MF. Faulting in the upper forelimb of the RMM are mostly thrusts and right-lateral faults (station 3.1a, b, Fig. 4.15). Dip arrows on the RMM are incorrect on the USGS geologic map of the Virginia Dale quadrangle (Braddock et al., 1989b), and should point SW.

The variable attitudes and isolated outcrops of the lower Fountain Formation and nonconformity indicate the basement has been gently folded but not substantially elevated. Map-view offsets, the ENE trend of σ_1 and the abundance of right-lateral faults suggest the RMM is cored by a NW-striking, NE-dipping fault with oblique left-lateral / reverse slip (Fig. 4.16). The RMM was likely formed by left-lateral transpression on the Sixmile Fault, which is exposed 1 km to the NW.

Livermore Quadrangle

The Livermore quadrangle is structurally complex, with NE-, E- and N-striking faults, N- and NE-trending monoclines, and N-, NE- and E-trending anticlines and synclines (Fig. 4.6). The structural complexity and the high density of minor fault data required the area to be divided into NW, W and E subareas (Figs. 4.17 - 4.19).

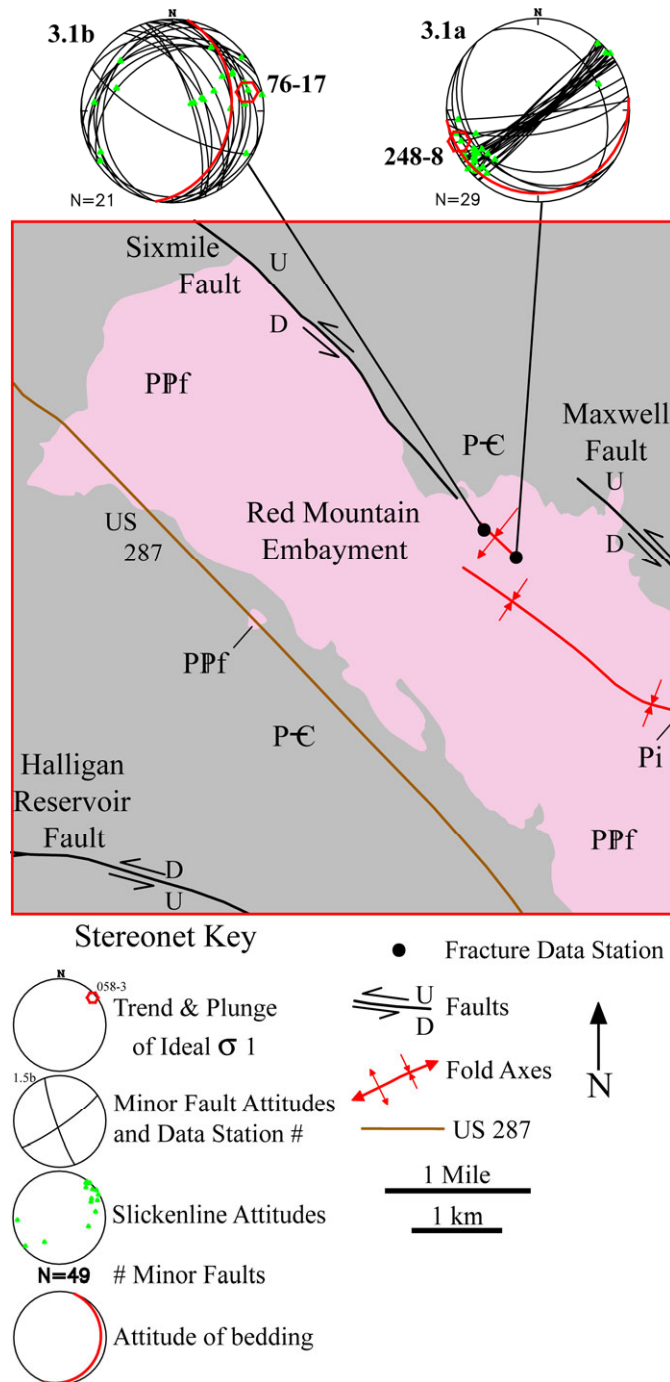


Fig. 4.15. Stereonets of minor faults, slickenlines and the best-fit ideal σ_1 axis measured in the Virginia Dale quadrangle.

The northwestern Livermore quadrangle contains ENE-dipping thrusts, the E-trending Halligan Syncline, the E-striking Halligan Reservoir Fault, the NE-striking North Livermore Fault, and the NE-trending Roberts Monocline (Fig. 4.6). Near the

thrusts bedding attitudes change from shallow dips ESE to moderate dips SSE. Fault data near the ENE-dipping thrusts are dominated by synthetic thrusts and strike-slip faults (stations 4.0 - 4.3, Fig. 4.17). Although the thrusts have been previously discussed, strike slip faulting is likely accommodating the local curving of the Ingleside hogback.

The Halligan Reservoir Fault (HRF) is a high-angle, E- and SE-striking fault, mapped to the west across the entire Front Range (Tweto, 1979). The North Livermore Fault and Roberts Monocline both terminate to the NE by abutting against the E-striking HRF. Map-view offsets on the HRF show the south side has moved up relative to the north. Minor faults on the HRF are dominantly left-lateral with W-plunging slickenlines

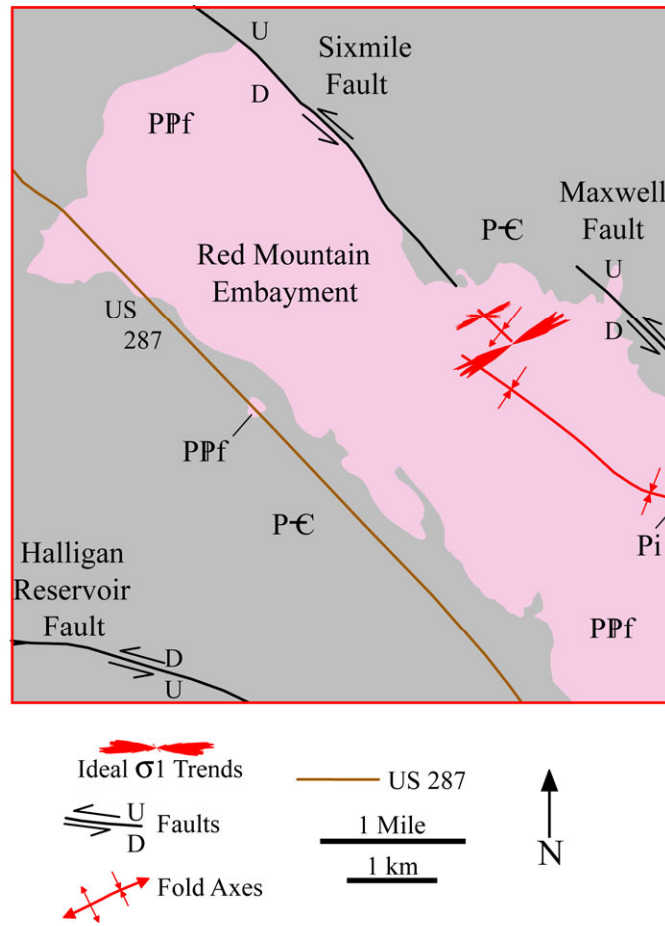


Fig. 4.16. Roseplots of ideal σ_1 trends measured in the Virginia Dale quadrangle.

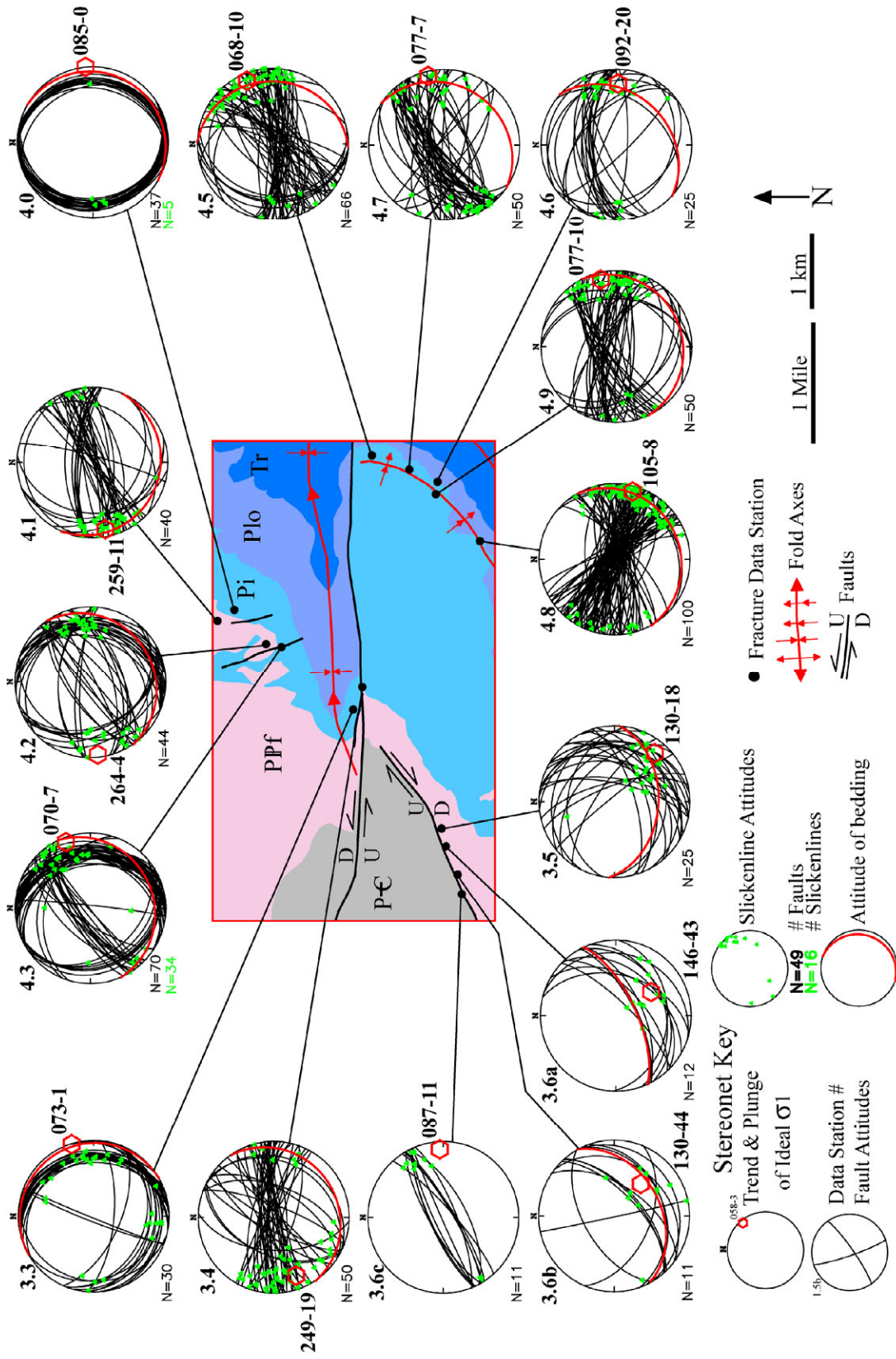


Fig. 4.17. Stereonets of minor fault planes, slickenlines and the best-fit ideal σ_1 axis measured in the NW Livermore quadrangle.

(station 3.4, Fig. 4.17). The Halligan Syncline (HS) is a variably plunging E-trending syncline with smoothly curved limbs is subparallel to the HRF. Thrusts in the south limb of the HS show bimodal slickenline trends both parallel and perpendicular to the fold axis (station 3.3, Fig. 4.17). Ideal σ_1 axes of faults near the HRF are some of the most NE-trending of all fault data in the Livermore quadrangle (stations 3.3, 3.4, 4.5, Fig. 4.20).

Map geometries of folds and faults, the abundance of left-lateral faults and slickenline attitudes suggest the HRF is an oblique left-lateral / reverse fault dipping $70^\circ - 80^\circ$ S. The ENE trend of σ_1 and the E trend of the HS show that oblique left-lateral / reverse slip on the HRF can cause the shortening of footwall strata in directions nearly perpendicular to regional σ_1 trends. The bimodal trends of thrust slickenlines in the HS are probably due to combination of regional slip with fold-related shortening trending perpendicular to regional σ_1 . The variable plunge of the HS is likely due to folding of the basement by a compressional bend within the HRF. The extreme NE trend of ideal σ_1 axes of data collected near the HRF suggests counterclockwise rotation by left-lateral slip likely occurs in the fault zone (Fig. 4.20). The parallelism of the HRF with Proterozoic contacts and foliations and abutment of major structures against the HRF strongly suggests this fault is an inherited Proterozoic structure.

The Roberts Monocline (RM) has a curved NE-trending fold axis in the north and a linear N-trending axis in the south (Fig. 4.6). The gently curved forelimb of the RM has maximum dips of $30^\circ - 35^\circ$ E and SE. The RM separates subhorizontal basement blocks and abruptly ends to the north where it abuts against the HRF (Fig. 4.6). Faults in the RM are almost all strike-slip and σ_1 trends from stations varied almost 40° from one another

(stations 4.5-4.9, Fig. 4.17 and 4.20). Roseplots of ideal σ_1 trends show both a clockwise deviation from north to south and bimodal distributions (Fig. 4.20).

Strike-slip faulting likely accommodated extension parallel to the curving fold axis of the RM. The geometry and trend of the RM and the E trend of σ_1 predict the fold is cored by a planar, right-lateral / reverse fault that strikes NE and dips $50^\circ - 60^\circ$ NW. The southeastward deviation and bimodal trends of ideal σ_1 roses suggest clockwise rotation by right-lateral shear occurs within the RM forelimb (Fig. 4.20). The abutment of the RM against the HRF suggests the HRF is an inherited structure and arrested the lateral propagation of the fault coring the RM.

The North Livermore Fault (NLF) strikes ENE, dips approximately 80° NNW and ends to the NW in a basement fold immediately south of the HRF. Published geologic maps show the NLF's strike parallels intrusive contacts and foliations within the Proterozoic basement (Braddock et al., 1989d). Fault and slickenline trends from the NLF differ substantially from the adjacent, steeply-dipping, footwall strata (stations 3.5, 3.6a-c, Fig. 4.17). NLF contains NE-striking, subvertical faults with slickenlines plunging at low angles to the NE (station 3.6c, Fig 4.17). Faulting within the steeply-dipping beds of the footwall are largely SE-dipping reverse and low-angle normal faults with slickenline trends nearly perpendicular to the NLF (stations 3.5, 3.6a-b, Fig. 4.17).

The geometry and trend of the NLF and an E-trend of σ_1 predicts oblique right-lateral / reverse slip on the NLF. The dominance of strike-slip on the basement fault and oblique dip-slip faulting in the footwall is suggestive of strain partitioning. The majority of SE-dipping faults in the footwall suggest folding caused top-to-the-NW flexural slip.

The abutment of the NLF against the HRF and its parallelism to Proterozoic structure suggest the NLF may be an inherited Proterozoic fault but apparently postdates the HRF.

The western Livermore quadrangle includes the NE-striking Grayback Monocline, a NE-trending asymmetric syncline and minor N-plunging folds (Figs. 4.6 and 4.18). The Grayback Monocline (GM) is a NE-striking fold with forelimb dips of 30°- 45° SE and separates two subhorizontal basement blocks. The northeastern terminus of the GM lies 2 km west from location where the RM fold axis abruptly bends to trend parallel to the GM. The GM ends to the SE where it obliquely abuts the Livermore fault. Faults in the upper forelimb are almost entirely strike-slip, with the majority left-lateral (3.9, 3.11, 3.12a-d, 3.14, Fig. 4.18). Map-scale and minor faults, slickenlines and ideal σ_1 axes in the upper forelimb have very diverse, multimodal trends (Figs 4.18 and 4.20). ESE-striking, left-lateral faults were observed to cross-cut SE-striking left-lateral faults. The map-scale faults striking nearly perpendicular to the fold axis were observed to be left-lateral faults which cross-cut ENE-striking conjugates. In the lower forelimb, data were collected from a map-scale, SE-dipping thrust (3.12e, Fig. 4.18). A SE-striking, subvertical fault within sandstone was observed to terminate at a lithologic boundary and not extend into the underlying limestone.

The geometry and trend of GM, an E-trending σ_1 , the abundance of left-lateral faults suggest the GM is cored by a planar, right-lateral / reverse fault that strikes parallel to the fold and dips approximately 80° NW. The observation of cross cutting left-lateral faults suggests clockwise rotation of the forelimb required the formation of new, more favorably-oriented faults given a static E-trending σ_1 . Given right-lateral transpressional folding and cross-cutting relations, the highly-oblique, map-scale left-lateral faults are

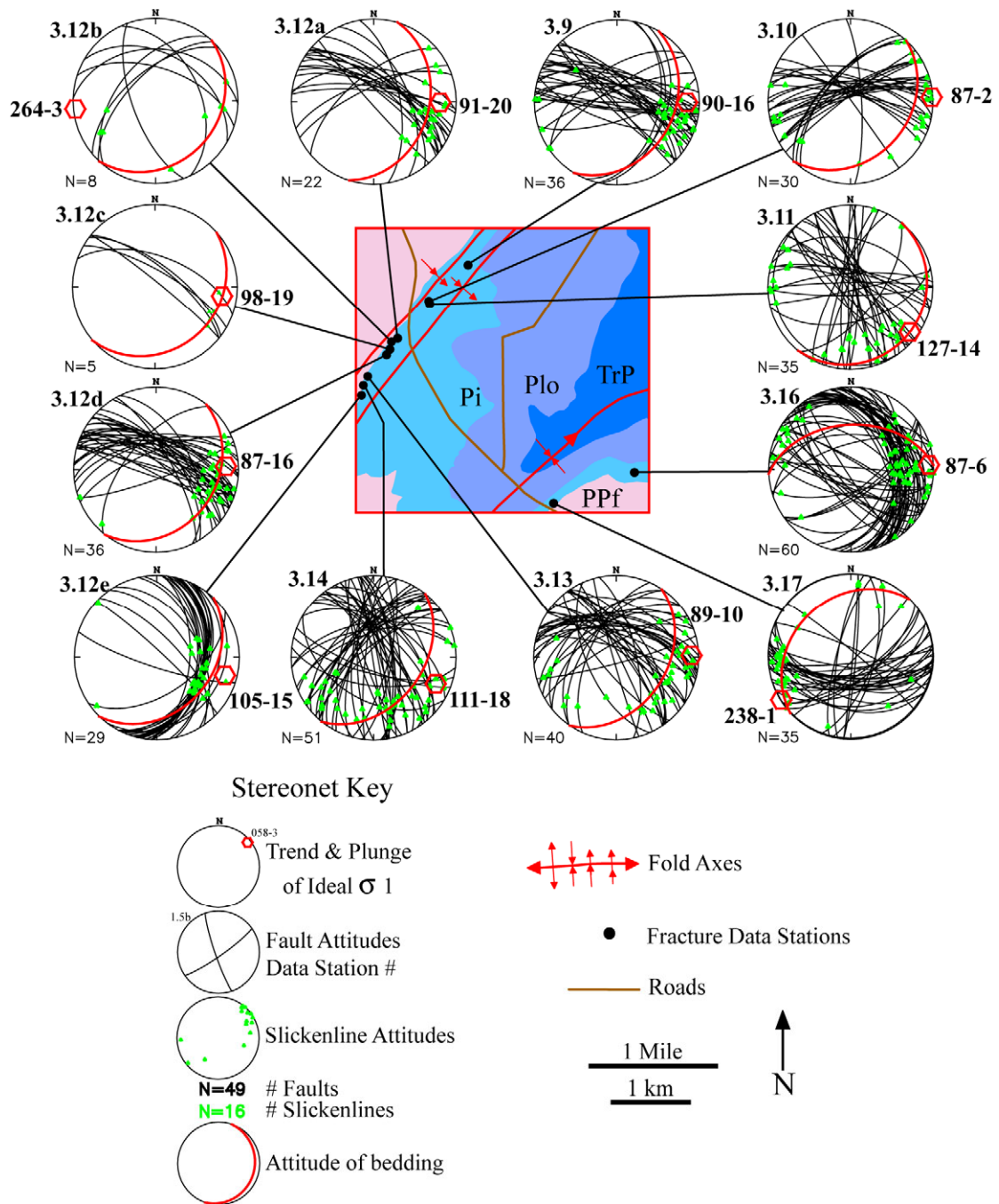


Fig. 4.18. Stereonets of minor fault planes, slickenlines and the best fit ideal σ_1 axis measured in the western Livermore quadrangle.

likely macroscopic antithetic R' shears which postdate E-W trending conjugate minor faults (A, Fig.4.1). Out-of-the-syncline thrusting and faults terminating at lithologic boundaries suggests right-lateral transpression and syncline tightening caused bedding

parallel detachment of the interbedded sandstone and limestone and top-to-the-WNW directed flexural slip. The abrupt NE termination of the GM where the RM is elevated and the fold axis bends to the NE suggest fault slip was transferred from GM to RM.

The NE-trending asymmetric syncline has a planar NW limb and a gently-curving SE limb dipping 25° - 45° NW. The SE limb lies immediately NE and along the strike of the Livermore Fault (LF) and has small, gentle folds plunging steeply N (Fig. 4.6). Faulting in the NW-dipping strata is dominated by left-lateral faults (station 3.17, Fig. 4.18). Faults in N-dipping beds lying on the E limb of an N-plunging anticline are dominated by E-dipping thrusts with lesser strike-slip faults.

The syncline's geometry, the ENE trend of σ_1 , and abundance of left-lateral faults require the fold to be cored by a right-lateral / reverse fault, striking NE and dipping 60° - 70° W. The along strike continuity of the fault-propagation fold with the LF suggests the LF continues as a blind fault for several kilometers to the NE.

The eastern Livermore quadrangle contains the NE-trending Horseshoe Monocline and the northern Campbell Valley Anticline (Fig. 4.6). Although the Horseshoe Monocline (HM) was previously discussed, this segment has macroscopic reverse and strike-slip faults and exposures where strata are either highly attenuated or missing altogether. In the upper forelimb, some E-striking fault planes had both dip-slip strike-slip slickenlines (station 4.13, Fig. 4.19). The consistency of σ_1 trends of fault data is remarkable given the variability of bedding attitudes within the HM (Fig. 4.19).

The consistency of σ_1 trends in the HM suggests strain may be more uniform and less partitioned at structurally higher levels or where detachment on bedding occurs.

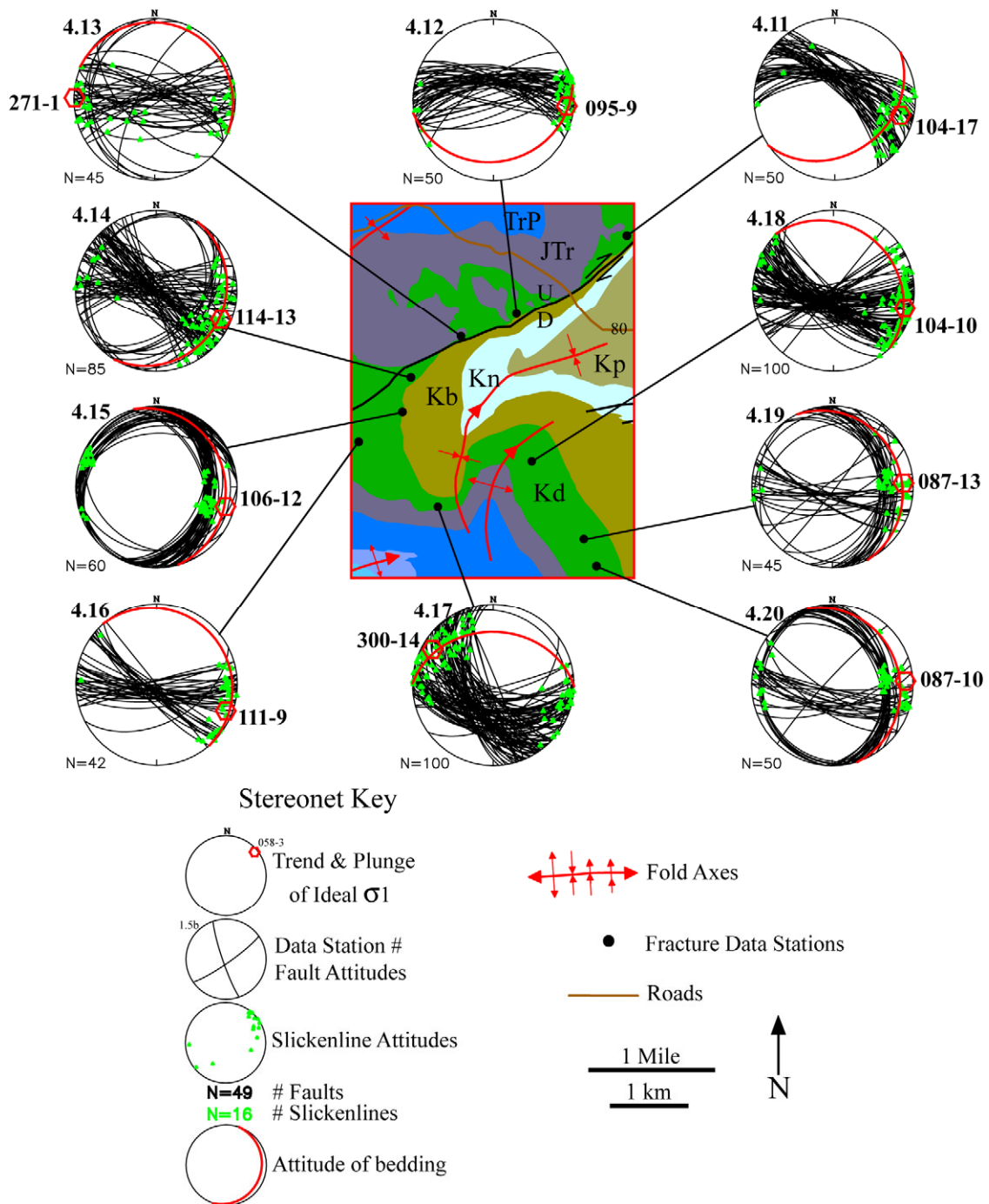


Fig. 4.19. Stereonets of minor fault planes, slickenlines and the best fit ideal σ_1 axis measured in the eastern Livermore quadrangle.

The Campbell Valley Anticline (CVA) is an asymmetric, N- to NE-trending anticline with a steeply-dipping western forelimb and a shallow eastern backlimb. The CVA plunges steeply with the bending of the fold axes to the NE. The anticline - syncline

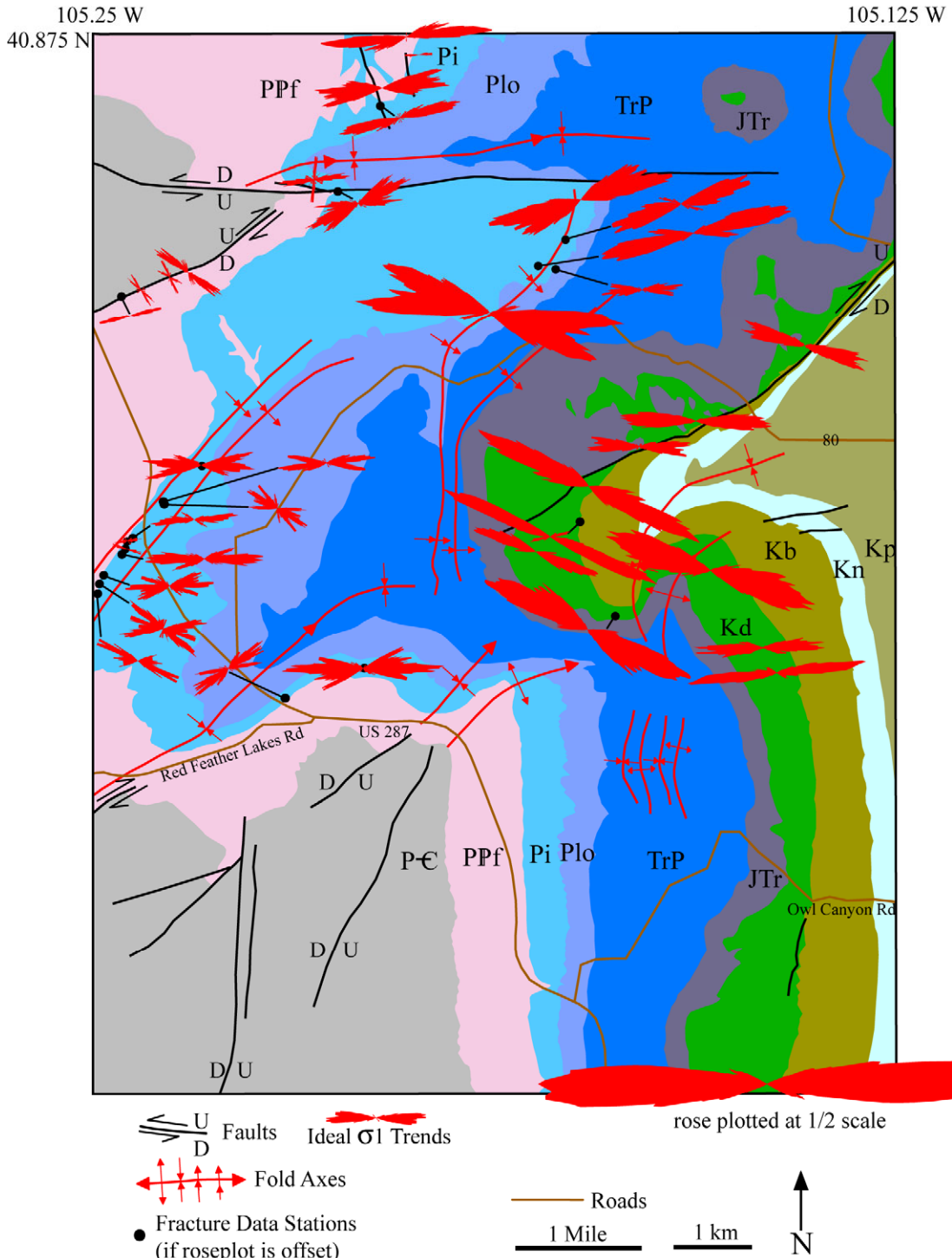


Fig. 4.20. Roseplots of ideal σ_1 trends measured in the Livermore quadrangle.

pair has abrupt changes in bedding attitudes and more angular hinges relative to adjacent folds (Fig. 4.6). Faulting in the N-plunging syncline is mostly strike-slip with slickenlines

and ideal σ_1 axes plunging NW. Faults near the crest of the N-plunging anticline are entirely strike slip with slickenline trends nearly perpendicular to fold axes. Faulting in the backlimb is almost entirely E-dipping thrusts and left-lateral faults with slickenlines and σ_1 axes trending ENE (stations 4.19, 4.20, Fig. 4.19).

The geometry of the fold, an E trend of σ_1 and the dominance of E-dipping thrusts and left-lateral faults requires the fold to be cored by a blind oblique reverse / right-lateral fault which strikes N and dips $50^\circ - 60^\circ$ E. The abundant E-dipping thrusts and angular hinges suggest the fold absorbed top-to-the-west flexural slip. Strike-slip faulting near the N-plunging hinges likely accommodated axis parallel extension during folding. Deviation of σ_1 trends in the hinges and backlimb suggest either oblique folding locally deflected σ_1 or the fold hinges were rotated clockwise by right-lateral shear.

Livermore Mountain Quadrangle

The Livermore Mountain quadrangle encompasses the Livermore Embayment (LE), a rhomb-shaped, fault-bound, subhorizontal embayment of the lower Fountain Formation (Fig. 4.7). The LE is bound to the N, W and S by the North Livermore Fault (NLF), the West Livermore Fault (WLF) and the Livermore Fault (LF), respectively. The Livermore Mountain Quadrangle also contains a segment of the Halligan Reservoir Fault, the N-striking Stonewall Fault (SF), the southwestern Grayback Monocline (GM) and the northern Hewlett / Dilky Ranch Fault (HDRF) (Braddock and Connor, 1988b) (Fig. 4.7).

The NLF strikes E where it joins the ENE-striking, subvertical North Rabbit Fault (NRF) and reverts to a NE-strike where it intersects the WLF. In the hanging wall of the NLF the base of the Fountain Fm rests at 1920 m but west of the SF the nonconformity has been elevated to over 2000 m. Basement faults are left-lateral with slickenlines

plunging WNW at 20 ° and σ_1 trends ENE while footwall faults are SE- and SE-dipping reverse faults and σ_1 trends SSE (stations 3.7, 3.8, Fig. 4.21).

The parallelism of the ENE-striking NRF and HRF suggests the NRF is a left-lateral conjugate of the NLF. The lower elevation of the NLF hanging wall to the NE suggests right-lateral slip is transferred to reverse slip on the W-dipping Stonewall fault. Minor faulting in the basement and footwall strata was nearly identical to faults along the strike of the NLF, suggesting strain partitioning was a regional phenomenon.

The WLF is a sinuous, NE-striking fault which dips 80° - 85° NW. The WLF abuts to the NE against the NLF and the southern terminus is mapped as abutting against the LF (Braddock and Connor, 1988b). Subhorizontal remnants of the nonconformity in the hanging wall at 1980 m constrain the maximum throw on the WLF to ~180 m, with at least 150 m where it abuts the LF. The hanging wall of the WLF at Lone Pine Creek contains mylonites and indurated breccias ~100 m from the fault and intense fracturing for >200m away from the fault. Faults in the basement are subvertical with slickenlines plunging 25°-40° SE and the σ_1 axis plunging 33° SE (station 3.19, Fig. 4.21). Faults in the subhorizontal footwall were strike-slip with slickenlines and ideal σ_1 axes plunging SW at low angles (station 3.18a, Fig. 4.21). Footwall joints abutted minor faulting and strike NW, nearly orthogonal to the WLF, and dip near vertical (station 3.18b, Fig. 4.21). The NE trend of slickenlines and ideal σ_1 axes and the attitude of the WLF suggests the fault is a planar, oblique right-lateral / reverse fault. The attitude of the WLF, 33° SE plunge of slickenlines and 180m of throw requires about 330m of slip.

The low-angle of slickenlines and the amount of offset on the WLF suggests

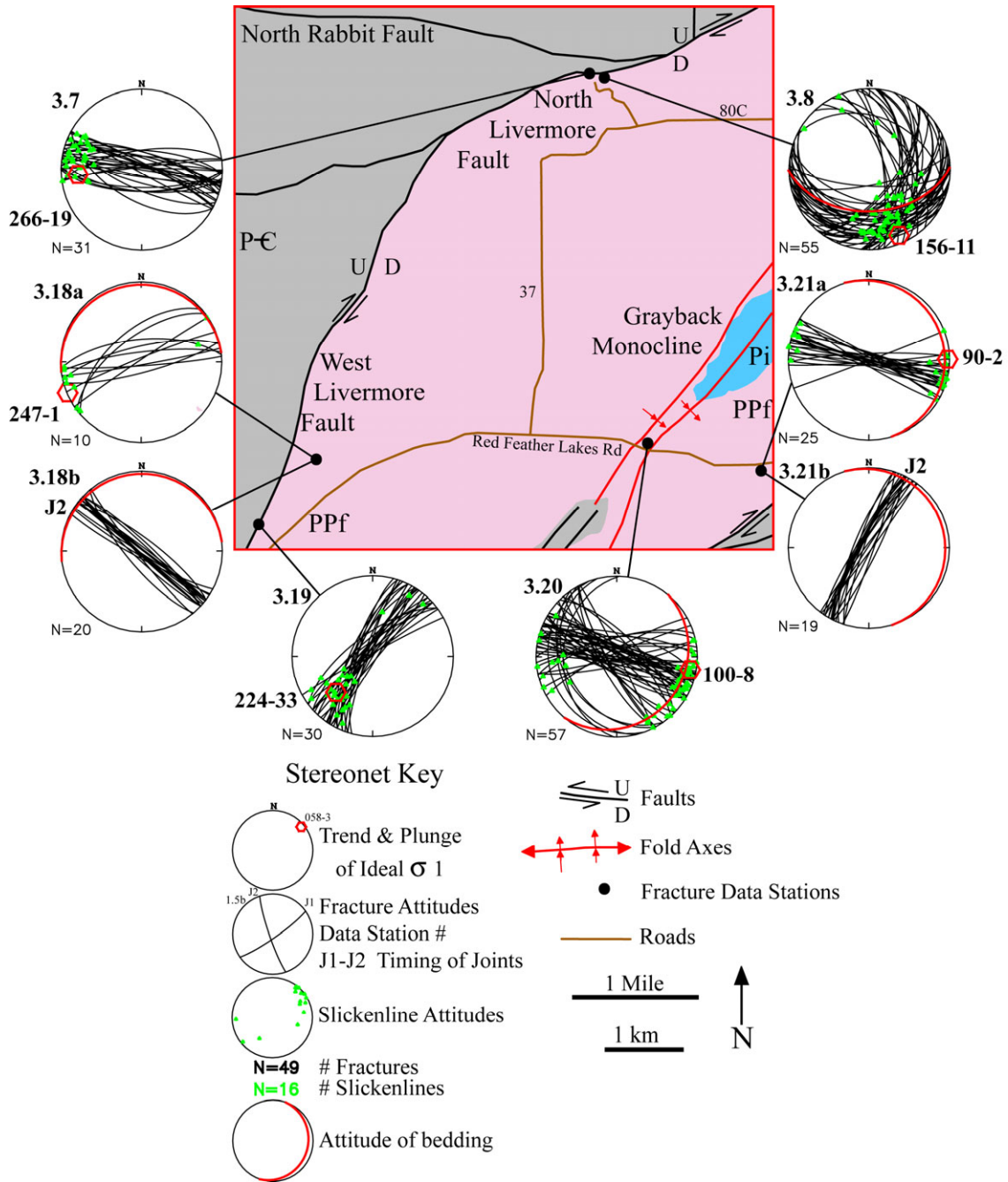


Fig. 4.21. Stereonets of fractures, minor fault planes, slickenlines and the best fit ideal σ_1 axis measured in the Livermore Mountain quadrangle.

it does not terminate by abutting against the LF and likely continues farther south as mapped by Tweto (1979). While the WLF is concealed in the southwestern Livermore Mountain Quadrangle by vegetation and alluvium, in the northwestern Poudre Park Quadrangle a NE-striking fault exists precisely along the trend of the WLF (Braddock

and Connor, 1988b; Braddock et al., 1988a). Anomalous NE-directed slip, intense fracturing, mylonites and indurated breccias all suggest the WLF is an inherited structure with previous deformations at higher P-T conditions. Local deviation of ideal σ_1 trend from NE in the WLF to ENE in the footwall strata suggests regional σ_1 may have been refracted into parallelism with the WLF. The near-perpendicular trends of the WLF and LF requires multiple stages of deformation for the southwestern LE. The lack of dip-slip faults with slickenlines perpendicular to fault strikes suggests strain partitioning in transpressional folds may only extend 100 - 200 m from faults in the lowest footwall strata. Laramide strike-slip faults likely influenced the orientation of subsequent extensional strain as joints trend nearly perpendicular to minor strike-slip faults.

The LF is a major E-striking fault which forms the southern boundary of the LE and extends for over 35 km to the W (Fig 4.2). The nonconformity and bedding shallowly dip away from the LF and remnants of the nonconformity in the hanging wall limit throw of the LF to ~ 120 m (Fig. 4.7). Fault data collected in shallowly-dipping footwall are dominated by left-lateral faults (station 3.21a, Fig. 4.21). Joints were observed to postdate and strike nearly perpendicular to minor faulting (station 3.21b, Fig. 4.21, Fig. 4.22).

The relatively low elevation of the nonconformity in hanging wall of the LF suggests a dominance of strike-slip on a nearly vertical fault. An elevated hanging wall and greater footwall folding to the E could be due to a shallowing of fault dip or the compressional bend in the right-lateral fault. The N dip of the nonconformity and bedding suggests gentle folding of the basement near the LF. The dominance of antithetic, left-

lateral faults suggests right-lateral shear extended hundreds of meters away from the compressional bend in the LF into the adjacent shallowly-dipping strata. ESE-striking left lateral faults likely influenced local tensile stress fields and forced joints to trend NNE.

The southwestern Grayback Monocline (GM) provides the structurally lowest exposures where it obliquely abuts against the LF (Fig. 4.7). The southwestern GM is mapped as an anticline/syncline pair cored by two NE-striking faults, with the eastern fault bisecting the fold axes (Braddock and Connor, 1988b). The eastern Grayback fault is mapped as crosscutting the LF and continuing S as the northernmost segment of the E-dipping Hewlett / Dilky Ranch Fault (HDRF) (Braddock and Connor, 1988b). Minor faults are almost entirely strike-slip with the majority being left-lateral and slickenlines and σ_1 axes trend ESE (3.20, Fig 4.21). The ENE trend of slickenlines from W-dipping thrusts were slightly deviated from the ESE trend of strike-slip slickenlines.

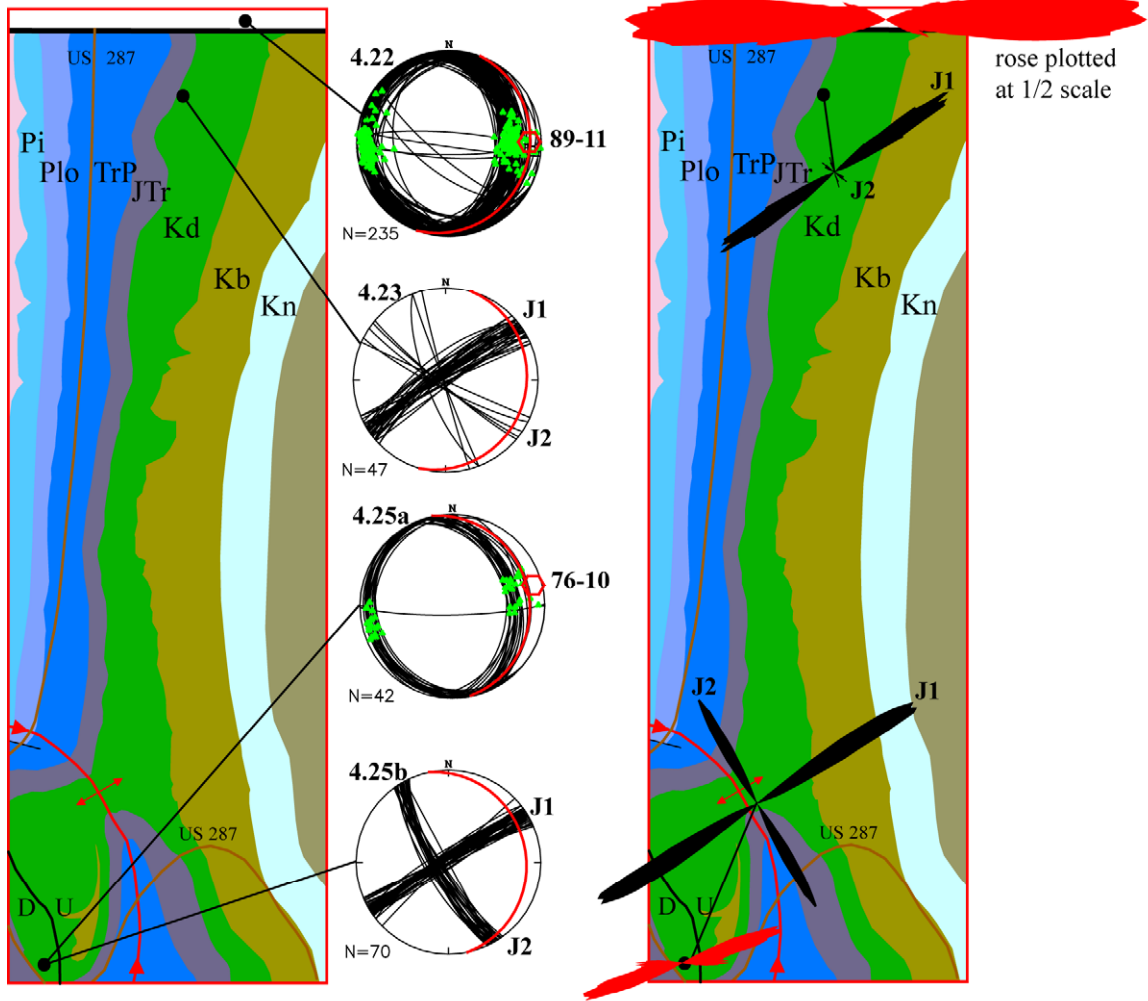
The opposite dip and vergence directions of the Grayback Fault and the HDRF question the mapping of the faults by Braddock and Connor (1988b). Although no Pennsylvanian strata remain to constrain slip on the Grayback Faults, the eastern fault is likely dominant as it bisects the fold axes and the western fault has no offset or folding. The 10° deviation between σ_1 trend from the forelimb and distal strata suggests strata were rotated clockwise in the GM forelimb (3.20, 3.21, Fig. 4.21). The deviation between thrust and strike-slip slickenline trends suggest strike-slip faults were rotated clockwise within a static E-trending σ_1 prior to fold-related thrust faulting (3.21, Fig. 4.21).

The elevation of the nonconformity in the footwall and on Livermore Mountain in the hanging wall requires >300 m of throw on the HDRF about 2 km south from its northern terminus. The abutment of the HDRF suggests it postdates the Livermore Fault.

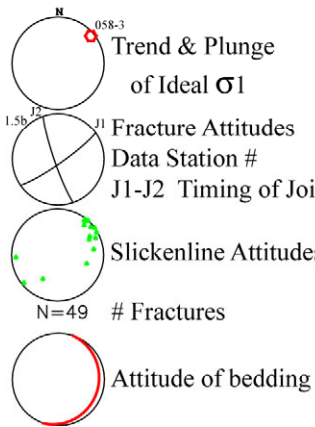
Laporte Quadrangle

The Laporte Quadrangle contains NNW-striking, E-dipping reverse faults and the transition of local homoclinal dip direction from E to ENE. The NNW-striking North Fork Fault (NFF) dies out to the S where it bends to the WNW to strike subparallel to basement foliation. The NFF was trenched by Erslev and Rogers (1993) along the WNW-striking segment and found to dip 45° NNE. An asymmetric anticline plunges ESE from the hanging wall of the NFF and continues S, increasing in amplitude as the axis bends to trend NW and N (Fig. 4.8). The anticline abruptly dies out to the south where the fold axes of the Bellvue Dome plunge N (Fig. 4.8). Faulting in the N-striking strata are dominantly thrusts with slickenlines and σ_1 axes trending nearly due E (station 4.22, Fig. 4.23). Master joints in the NNE-trending hogbacks strike ENE and cross joints strike both SE and SSE (station 4.23, Fig. 4.23). The ENE-dipping Bellvue Fault (BF) bounds the western Bellevue syncline and Bellvue Dome and dies out to the N by abutting against the NFF (Fig. 4.8). Synthetic minor thrusts in the footwall of the BF dip 30° - 35° ENE and their slickenlines and ideal σ_1 axes also trend ENE station (station 4.25a, Fig. 4.23). ENE-striking master joints were perpendicular to ESE-striking cross joints (station 4.25b, Fig. 4.23). Minor thrust faults were cross cut by ENE-striking master joints.

Given the uniform ENE trend of σ_1 , the abrupt ESE plunge of the southern Owl Canyon block where the NFF abruptly bends to strike WNW is likely due to more left-lateral strike-slip and less dip-slip on the NFF. The abutment of the BF against the NFF and greater throw on the NFF suggests slip on the NFF preceded the local lateral propagation of the BF. A 15° deviation of σ_1 trends corresponds to a 15° change in local dip direction, suggesting bedding-parallel flexural slip was a key mode of deformation.

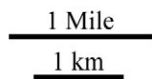


Stereonet Key



● Fracture Data Stations

— Roads



Ideal σ_1 Trends

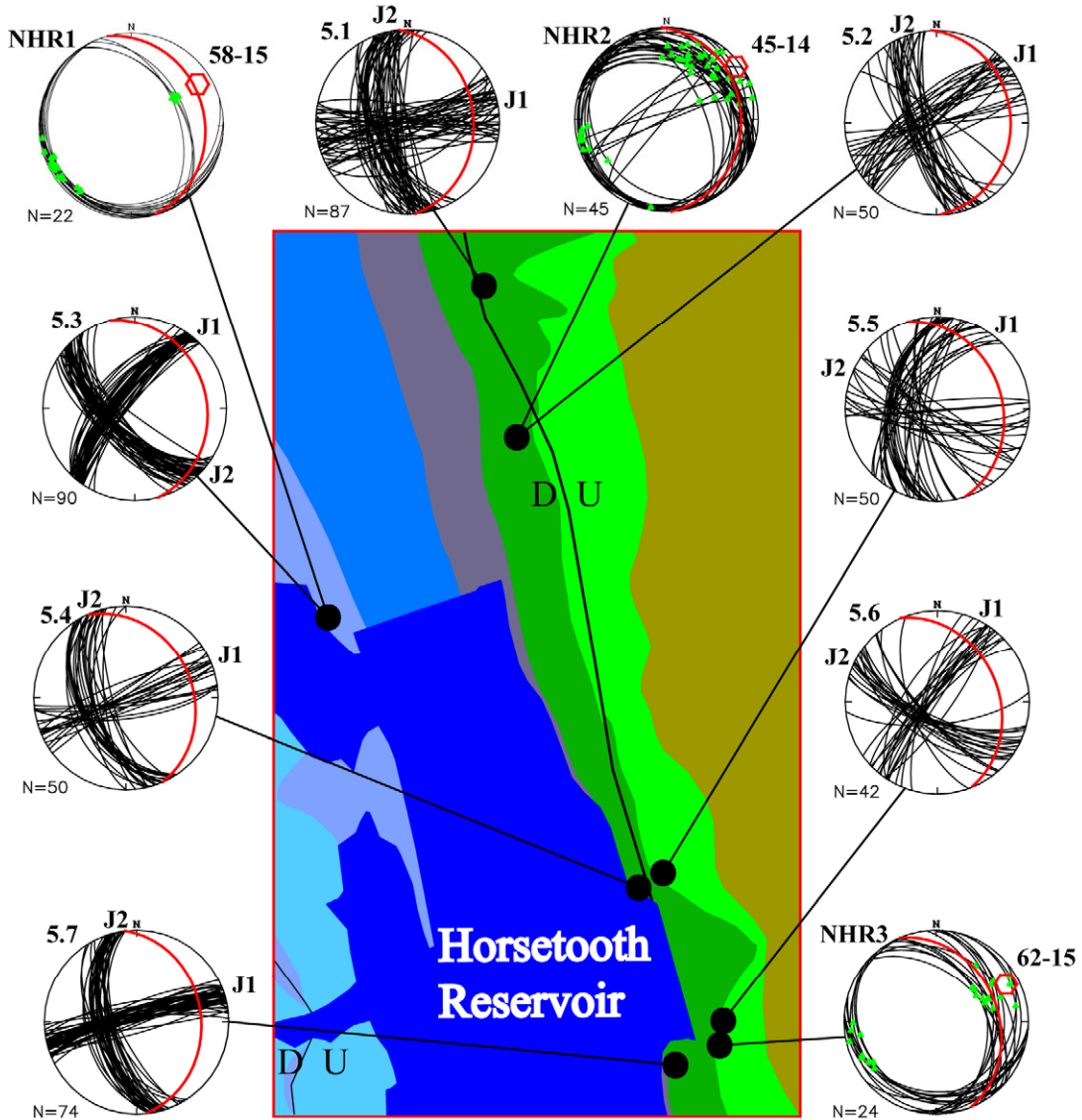


Fig. 4.23. Stereonets and roseplots of fractures, minor fault planes, slickenlines and the best-fit ideal σ_1 axis measured in the Laporte quadrangle.

Locally complex structure is likely due to the local transition of σ_1 trend causing the convergence of fault blocks to the E. The abrupt loss of slip on the BF between Bellvue dome and syncline, abrupt changes of the backlimb anticline with a consistent attitude and elevation of the distal backlimb is likely due to the interaction of multiple deformation modes. The near-vertical forelimb of the doubly-plunging Bellvue dome and the westward bend of the BF are likely a product of fault-bend folding on an upward shallowing fault (Holdaway, 1998) and top-to-the-WSW flexural slip on a detachment in the lower Fountain Fm. The abrupt loss of slip on the BF at Bellvue syncline is likely due to top-to-the-WSW flexural slip being absorbed by the backlimb anticline on a detachment in the lower Lykins Fm. Master joints consistently strike ENE in the E- and ENE-dipping strata suggesting minor thrusts and local deviations in Laramide σ_1 trends had little to no influence on the local stress field during joint formation and propagation. Cross joints strike NW, approximately perpendicular to master joints, but limited fracture data cannot explain the local variability observed.

Horsetooth Reservoir Quadrangle

The Horsetooth Reservoir quadrangle was the locus of an detailed investigation to test hypotheses of fracture mechanism(s) and the timing of extensional fracturing, or jointing, relative to the Laramide Orogeny. Attitudes of fractures and bedding, and any cross cutting or abutting relations of faults and joints were collected from the Owl Canyon and Dakota Group formations (Figs. 4.24 - 4.26). The Horsetooth Reservoir area has been the focus of substantial research into local Laramide kinematics and structural analyses (Erslev and Rogers, 1993; Erslev and Gregson, 1996; Erslev et al., 2004). The area was chosen because of the consistency of Laramide kinematics, bedding attitudes,



Stereonet Key

-  Trend & Plunge of Ideal σ_1
-  Fracture Attitudes J1 & J2 - Relative Ages of Joint Data
-  Slickenline Attitudes
- N=49** # Fractures
-  Attitude of bedding at fracture data station

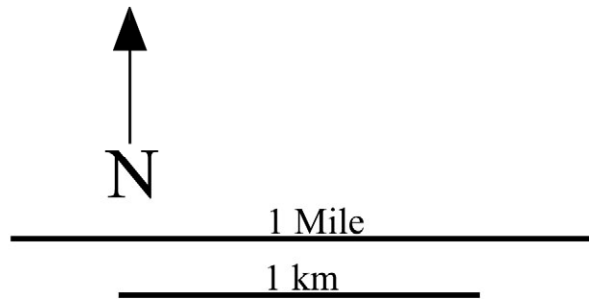


Fig. 4.24. Stereonets of fractures, minor fault planes, slickenlines and the best fit ideal σ_1 axis measured in the northern Horsetooth Reservoir quadrangle.

local variability of slope directions, and its proximity to Fort Collins, Colorado and Colorado State University.

Throughout the northern Horsetooth Reservoir area, master joints (J1) varied in strike from NNE to ENE (Figs. 4.24, 4.25). J1 strikes in the lower Dakota Group were generally ENE (stations 5.1, 5.2, 5.4, Fig. 4.24), while J1 in the upper Dakota Group strike NNE (stations 5.5, 5.6, Fig. 4.24) despite similar attitudes of bedding. Cross joints (J2) strike WNW and NW, perpendicular to, and abut against master joints (Figs. 4.24, 4.25). Minor faults are dominantly thrusts and strike subparallel to the BF with σ_1 trends varying from NE to ENE (stations NHR1-3, Fig. 4.24). Both master and cross joints cross cut minor thrusts and master joint strikes were consistently deviated 10° - 15° from ideal σ_1 trends (Figs. 4.24, 4.25). The orientations of joints were consistent despite variation in slope aspects, suggesting jointing was not influenced by topography (Figs. 4.24, 4.25).

The deviation of master joint strikes from Laramide σ_1 trends and the consistent relationship of joints cross-cutting minor thrusts suggest jointing post-dated Laramide minor faulting. Variation in master joint strikes between the upper and lower Dakota Group suggests the Skull Creek Fm. mechanically isolated the formations, allowing jointing at different times and/or stress regimes. The perpendicular strike of cross joints to master joints suggests master joints strongly influence any subsequent extensional fracturing. The consistency of fracture trends despite variations in slope aspect suggests jointing predated regional exhumation in the late Cenozoic (McMillan et al., 2002).

The southern Horsetooth Reservoir area differs from the northern area as oblique left-lateral / reverse slip on the Buckhorn Fault folded Dakota and Permian strata. The bending of the hogbacks was accommodated by NE- and ENE-trending, strike-slip

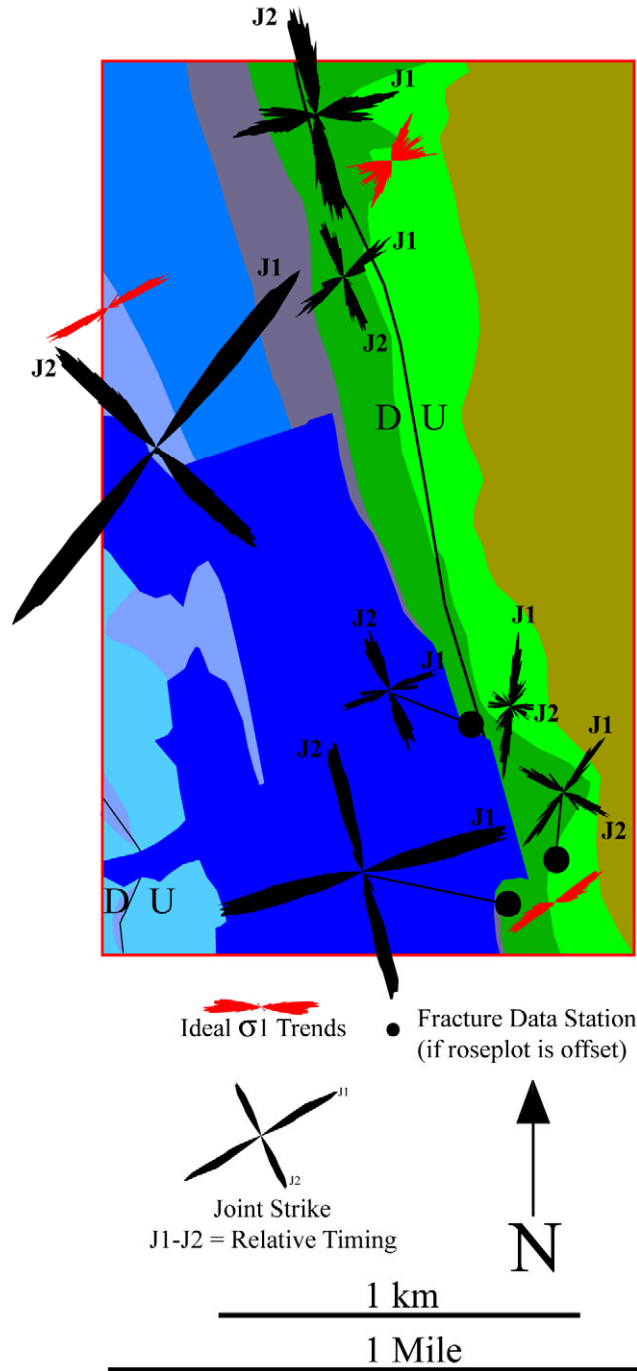


Fig. 4.25. Roseplots of ideal σ_1 trends and the strike of joints measured in the northern Horsetooth Reservoir quadrangle.

minor faults (Fig. 4.26). Where strike-slip faulting was intense, there are very few ENE- or NE-trending master joints, and NW- and N-striking joints form conjugate geometries as they abut NE- and ENE-striking fractures (stations 5.8-5.11, Fig. 4.26). Where NE-

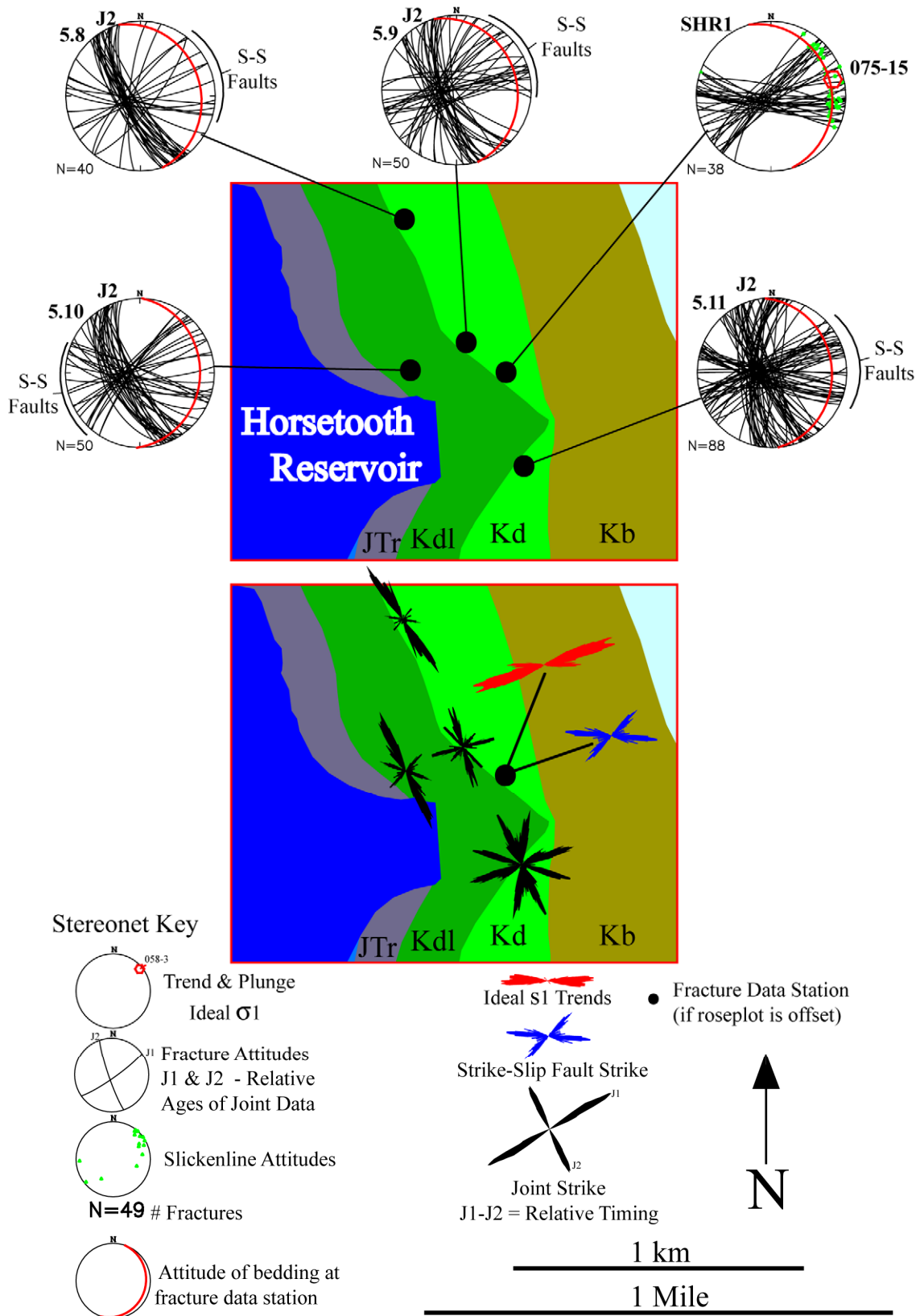


Fig. 4.26. Stereonets and roseplots of fractures, minor faults, slickenlines and the best-fit ideal σ_1 axis measured in the southern Horsetooth Reservoir quadrangle.

and ENE-striking conjugate fractures are less common in massively-bedded sandstone, NNW-striking fractures are more uniform in attitude (stations 5.8, 5.10, Fig. 4.26). Fault and joint attitudes are locally consistent regardless of proximity to Laramide structures or variation in slope aspect (Fig. 4.26).

The identical trend of strike-slip minor faults and the conjugate NE- and ENE-trending fractures in the southern Horsetooth Reservoir area suggests the NE- and ENE-trending fractures are strike-slip minor faults. Strike-slip minor faults are likely accommodating the basinward bending of the Dakota Hogback. A lack of an NE- or ENE-trending master joint set where strike-slip minor faults are dominant suggests strike-slip faults were reactivated and accommodated extensional strain relieved by jointing elsewhere. The relative timing relationships and conjugate geometry of NW- and NNW-striking cross joints suggests preexisting strike-slip faults influenced subsequent extensional stress fields and joints formed perpendicular to preexisting faults. Where strike-slip minor faults are less pervasive in massive sandstone beds, NW- and NNW-striking cross joints have a consistent trend, likely reflecting the orientation of regional extensional stresses.

Conclusions

The major E- and NE-striking, oblique-slip faults in the study area are likely structures inherited from Early and Middle Proterozoic episodes of deformation at higher P-T conditions. These subvertical, preexisting planes of weakness were oblique to E-trending, subhorizontal compression during the Laramide Orogeny, causing oblique reverse slip. The lateral propagation of faults reactivated by Laramide compression created highly-sinuuous faults with reactivated segments of oblique reverse slip and

neofomed dip-slip segments. The combination of wholly reactivated, partially reactivated faults with neofomed Laramide segments and strictly Laramide faults formed a complex network of strike-slip, and dip-slip thrust and reverse faults. The consistency of structural culminations on N-trending segments of fault-propagation anticlines and structurally low fault blocks bounded by strike-slip faults suggests elevation of the nonconformity is a proxy for estimating the relative amount of dip-slip or strike-slip across the study area. Kinematic data from folds formed by dextral transpression suggests strain was partitioned into zones of strike-slip and dip-slip deformation within structurally lower, late Paleozoic strata. Strain partitioning was less pronounced within the structurally higher Dakota Group.

Dominant modes of regional deformation include fault reactivation, trishear fault-propagation folding and basement folding, with lesser amounts of flexural-slip folding, detachment folding and fault-bend folding. Cleavage partings are cross-cut by minor faults, suggesting that brittle faulting and frictional sliding were dominant deformation mechanisms as strain rates during the height of the Laramide Orogeny were too high for pressure solution alone. The consistent NE- and ENE-trends of master joints in late Paleozoic and Mesozoic siliciclastic sediments across the region and the abutting and cross-cutting relationships to minor faults suggests jointing occurred after the height of local Laramide deformation within a slightly deviated stress field. The compatibility of master joint trends with early Eocene deformation in the Black Hills (Perry and Flores, 1997) and the reactivation of joints as strike-slip faults by an E-trending subhorizontal compressive stress suggest master joints likely formed during the Eocene as the Laramide Orogeny waned. A late Laramide timing for the formation of master joints may be due to

enhanced fluid pressures associated with the subsidence of the Denver Basin and the erosion of low-permeability late Cretaceous shales from the crest of the Front Range arch to the west. The consistency of NNW-trending cross joints in massive sandstone beds with few fractures suggests a later stage of jointing was caused by a regionally-consistent, post-Laramide stress field. A Miocene age for NNW-trending joints is attractive as it is mechanically compatible with NNW-striking normal faults which cut the Never Summer thrust and late Miocene igneous rocks on the western flank of the Front Range (O'Neill, 1981). A Miocene age is also temporally compatible with the onset of Rio Grande rifting (Kellogg, 1999) and regional uplift (McMillan et al., 2002). The difference of master joint trends in siltstone and gypsum beds of the Lykins Fm. suggests the different mechanical properties of siliciclastic sediments and gypsiferous evaporites influenced the relative timing of jointing.

Chapter 5

Detailed Analyses of Minor Fault and Joint Data

Minor Fault Slickenlines and Ideal σ_1 Axes

Slickenlines and ideal σ_1 axes were plotted on equal area stereonet and stereonet contoured at a 2% interval for 3082 minor faults measured in Pennsylvanian to Cretaceous strata between Owl Canyon, CO and the CO-WY border (Figs. 1.4, 5.1). The average orientation of Laramide fault slip directions, determined from slickenlines, is $094^\circ - 8^\circ$ with a first eigenvalue of 0.7056. Compton (1966) ideal σ_1 analysis of 3082 minor faults calculated an average regional Laramide σ_1 of $093^\circ - 7^\circ$ with a first eigenvalue of 0.8071 using an α angle of 22° (Fig. 5.1). The orientation of regional Laramide σ_1 and best-fit α angle were calculated using Orient (Vollmer, 1992) to determine the α angle ($\pm 1^\circ$) which provided the highest first eigenvalue (Fig. 5.1). The 2% contoured stereoplot of slickenline data shows two maxima, plunging at low angles to the east and west. The contoured stereoplot of ideal σ_1 axes has a single, asymmetric maxima plunging at 7° to the east (Fig. 5.1).

Poles to fault planes were plotted on equal area stereonet and contoured at a 2% interval for 3150 minor faults and shear planes (Fig. 5.2). Contoured stereoplots of poles to fault planes have three maxima, two plunging at high angles to the east and west corresponding to conjugate thrust faults, and one plunging at low angles to the north and south correlating to ENE- and ESE-striking conjugate strike-slip faults (Fig. 5.2).

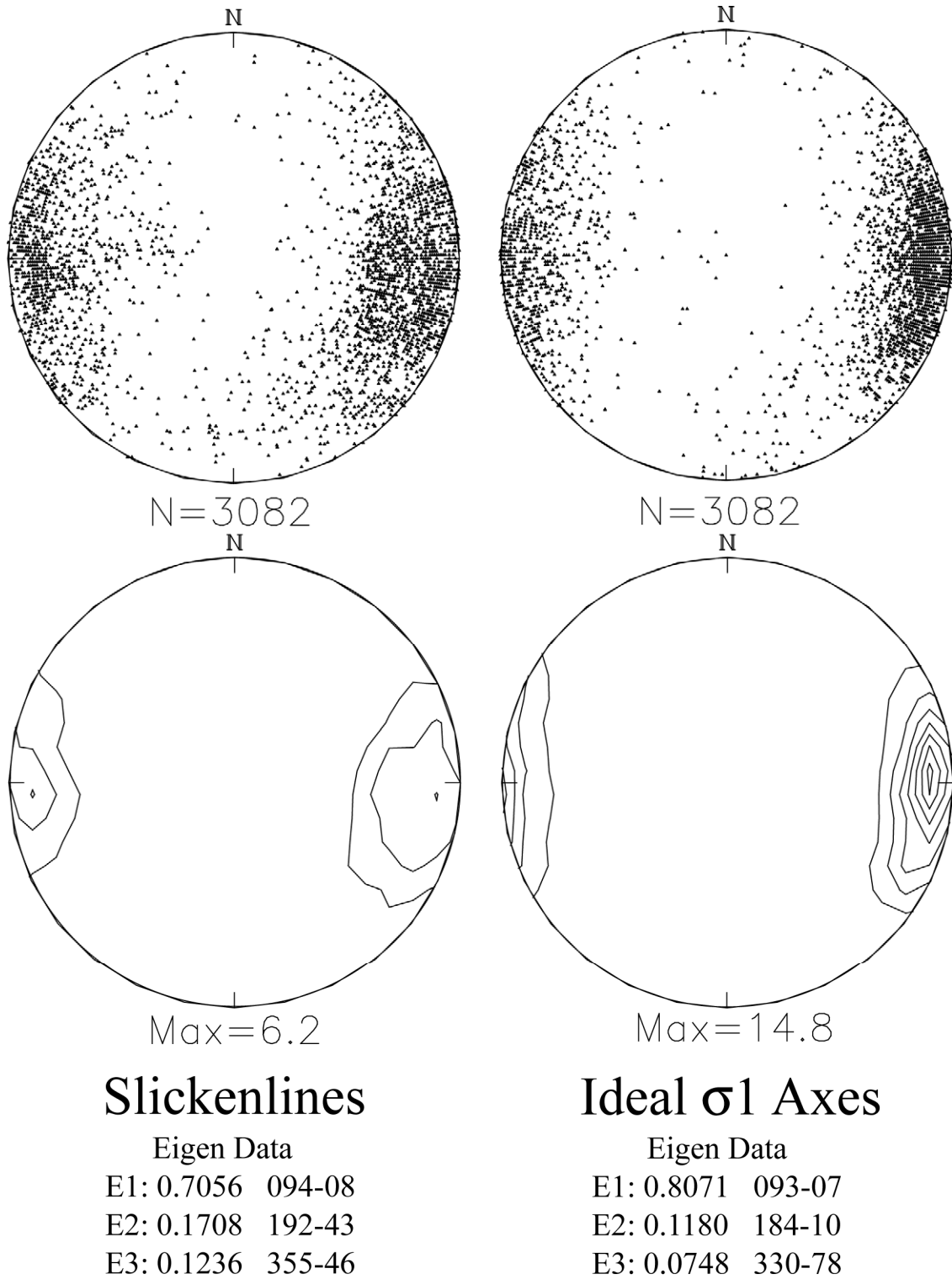


Fig. 5.1. Stereoplots and contoured stereoplots (2% CI) of slickenlines and ideal σ_1 axes ($\alpha=22^\circ$), eigenvalue and eigenvector data for regional σ_1 analysis.

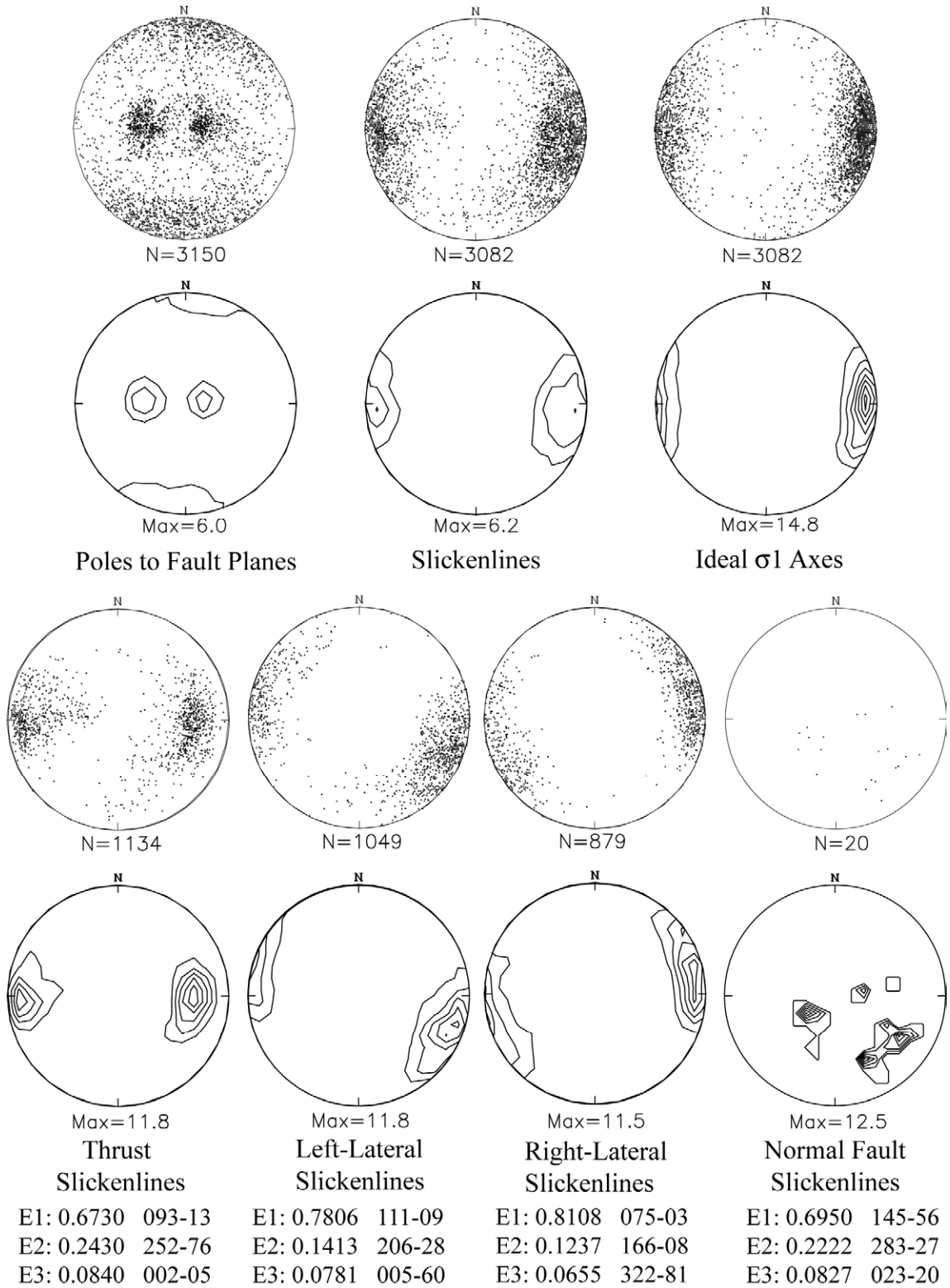


Fig. 5.2. Stereoplots and contoured stereoplots (2% CI) of poles to fault planes, slickenlines, and ideal σ_1 axes ($\alpha=22^\circ$) of all faults. Stereoplots of slickenlines, eigenvalue and eigenvector data broken down by fault slip sense.

All 3082 faults were separated by types and slickenlines were plotted on equal area stereonet contoured at a 2% interval (Fig. 5.2). Thrust slickenlines have an average orientation of $093^{\circ}-13^{\circ}$ and a bimodal distribution with maxima plunging at low angles to the east and west (Fig. 5.2). Slickenlines from left-lateral faults have an average orientation of $111^{\circ}-09^{\circ}$ and slickenlines from right-lateral faults have an average orientation of $075^{\circ}-03^{\circ}$ (Fig. 5.2). Normal fault slickenlines have an average orientation of $145^{\circ}-56^{\circ}$ and a highly-variable multimodal distribution (Fig. 5.2).

Strike-slip minor faults outnumbered dip-slip faults nearly two to one, with a 6:5 ratio of left-lateral to right-lateral faults. Thrust faults are nearly 37% of the data set with a majority of the east-dipping conjugate. Normal faults are less than 1% of the data set and the majority are rotated thrust faults and the remainder are from the crests of monoclinial and anticlinal folds. Smoothed roseplots of slickenline and ideal σ_1 trends (Fig. 5.3) are weakly bimodal with a lobate dominant trend and a minor secondary node. The shallow plunges of slickenlines and σ_1 axes allows stress and strain orientations to be approximated as rose plots (Fig 5.3).

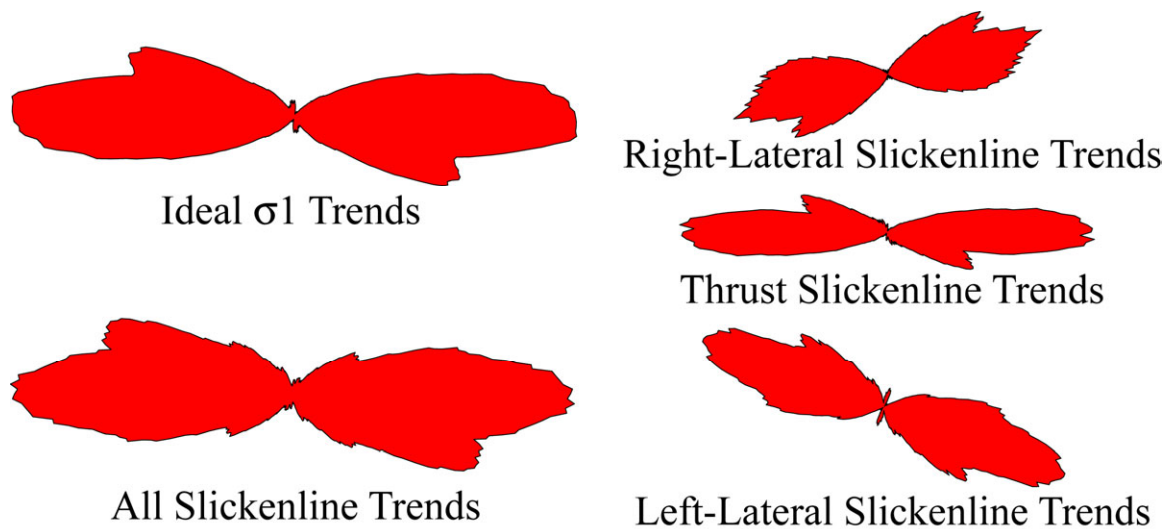


Fig. 5.3. Roseplots of ideal σ_1 trends and slickenline trends separated by fault type.

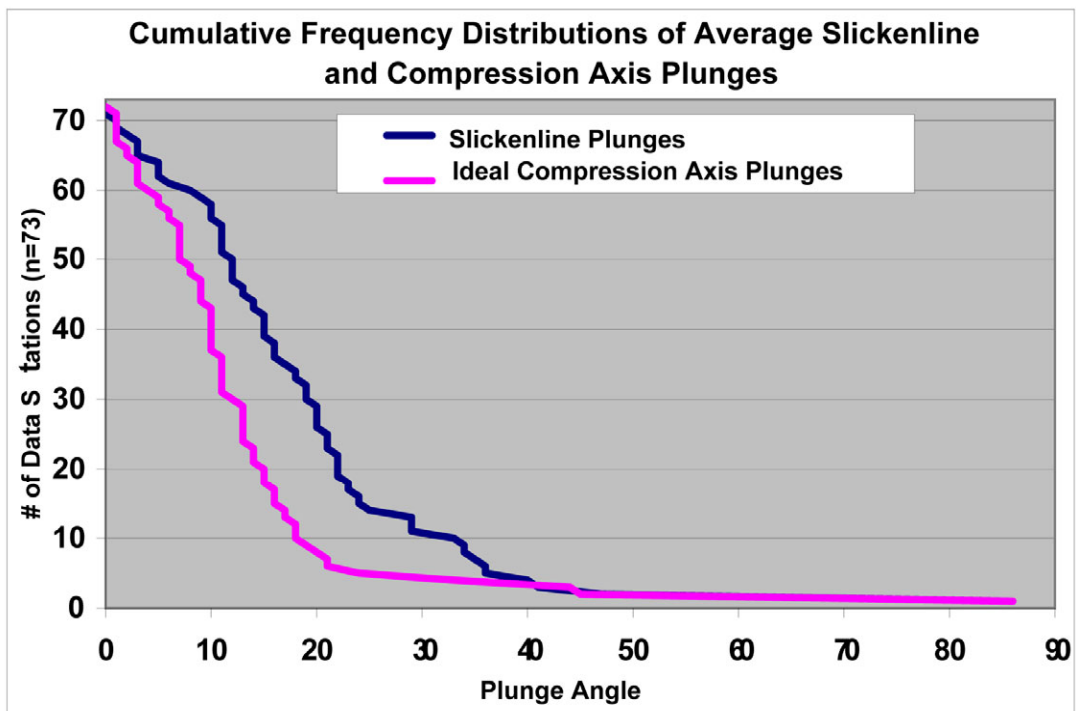


Fig. 5.4. Plunge angles of slickenlines and ideal σ_1 axes for 73 fault data stations.

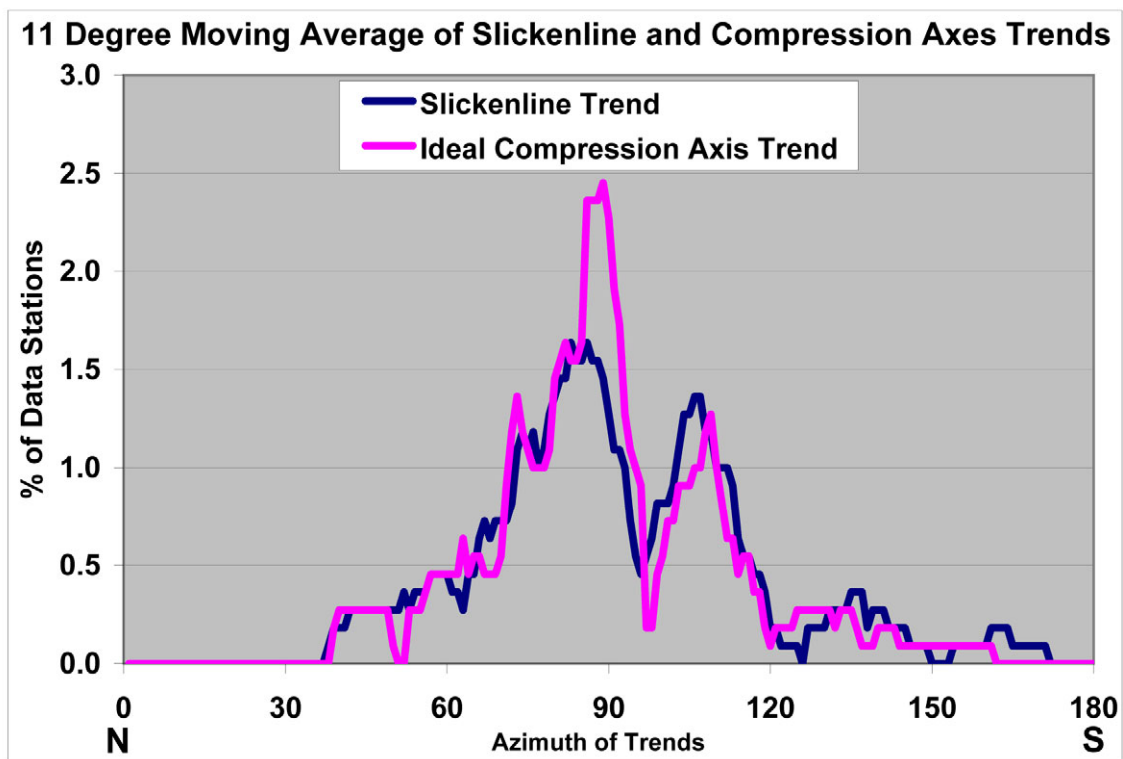
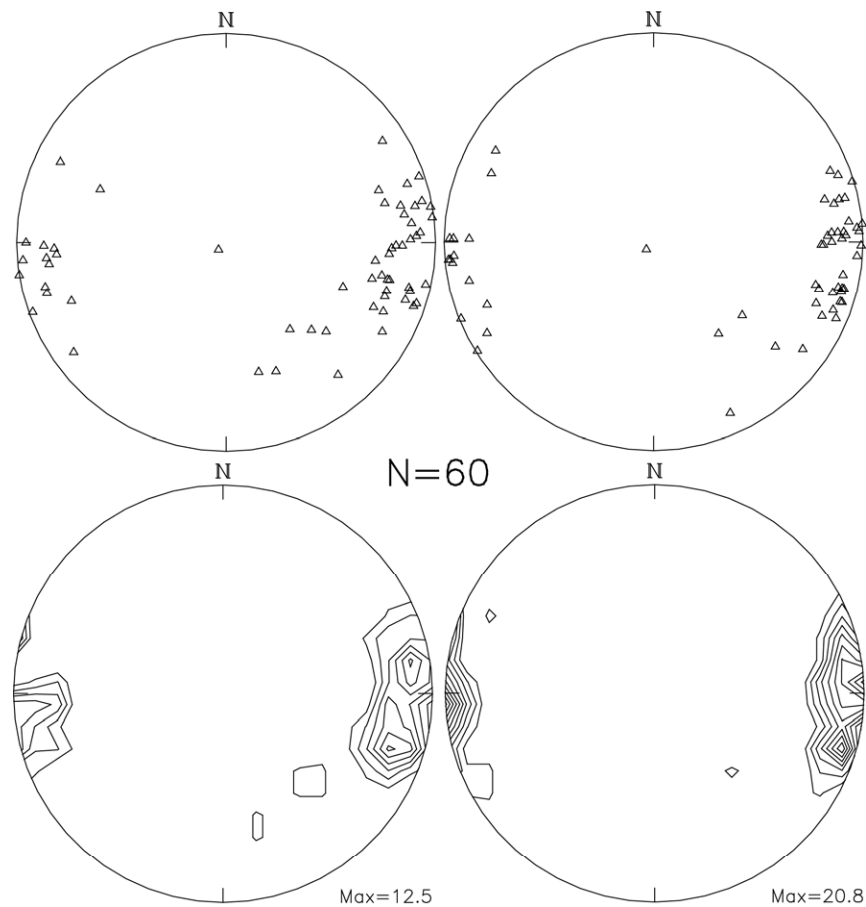


Fig. 5.5. 11° moving average of slickenline and ideal σ_1 trends for 73 fault data stations.

Calculations of regional strain and stress can be influenced by variable locations and sizes of fault data subsets. In an attempt to lessen this influence, the average attitude of slickenlines and ideal σ_1 axes for each data station were analyzed using an 11° moving average and eigenvector analysis (Figs. 5.5, 5.6). Eigenvector analysis calculated regional stress and strain as trending 094° and 092°, respectively, using the average slickenline and ideal σ_1 axis for 60 data stations (Figs. 5.1, 5.6).



Slickenlines

Eigen Data

E1: 0.7957 094-10

E2: 0.1518 194-46

E3: 0.0525 355-42

Ideal σ_1 Axes

Eigen Data

E1: 0.8580 092-07

E2: 0.0987 187-31

E3: 0.0433 351-58

Fig. 5.6. Stereoplots and contoured stereoplots (2% CI) and eigen data of average slickenlines and best-fit ideal σ_1 axes for each minor fault data station. Data stations outside the study area and in crystalline rocks were omitted.

Regardless the method used to determine the regional trends of stress and strain, the maximum values are consistently trend between 085° and 095° (Figs. 5.1, 5.5, 5.6). Regional compression directions between 092° to 094° are incompatible with footwall folding and left-lateral slip on the 090° striking Halligan Reservoir Fault (Fig. 4.17), and shallowly plunging slickenlines on the West Livermore Fault (Fig. 4.21). The recognition of clockwise rotation of paleomagnetic poles and faults in Grayback Monocline and similar multimodal σ_1 trends in other NE-trending monoclines suggest faults were rotated clockwise by right-lateral transpression and thus σ_1 must trend to the ENE (Fig. 2.10).

A second analysis of regional stress and strain directions was done with data from data stations over 1 km from fold axes and in shallowly dipping < 25° Permian through Cretaceous strata (Fig. 5.7). Stereoplots and contoured stereoplots (2% CI) of slickenlines and ideal σ_1 axes using an $\alpha=25^\circ$ (Byerlee, 1978), were plotted for the restricted fault data set (n=1317). Although the first eigenvector of ideal σ_1 axes was oriented at 089°-10°, the maximum has a trend of 085° (Fig. 5.7). A regional compression direction of 085° is compatible with deformation and chosen as the regional direction of slip for 2D and 3D structural interpretations and analyses.

The influence of bedding attitude upon regional trends of stress and strain were assessed by comparing slickenline and σ_1 trends to bedding dip directions (Fig. 5.8a, b). If strain and stress directions were parallel to bedding dip azimuths, best-fit lines using linear regression would have high R^2 values and slopes near 1. Slickenline and σ_1 trends vs. dip directions are scattered with lines sloping at 0.0657 and 0.0279, and R^2 values of 0.0123 and 0.0028, respectively (Fig. 5.8a, b). The influences of shortening both perpendicular and parallel to fold axes trends and fault strikes were evaluated by plotting

slickenline and σ_1 trends against fold axes trends and fault strikes plus 90 degrees (Fig. 5.8c, d), and the trends of strain and stress against the trends of fold axes and fault strikes (Fig. 5.9a, b). The correlations between trend of strain and stress and shortening

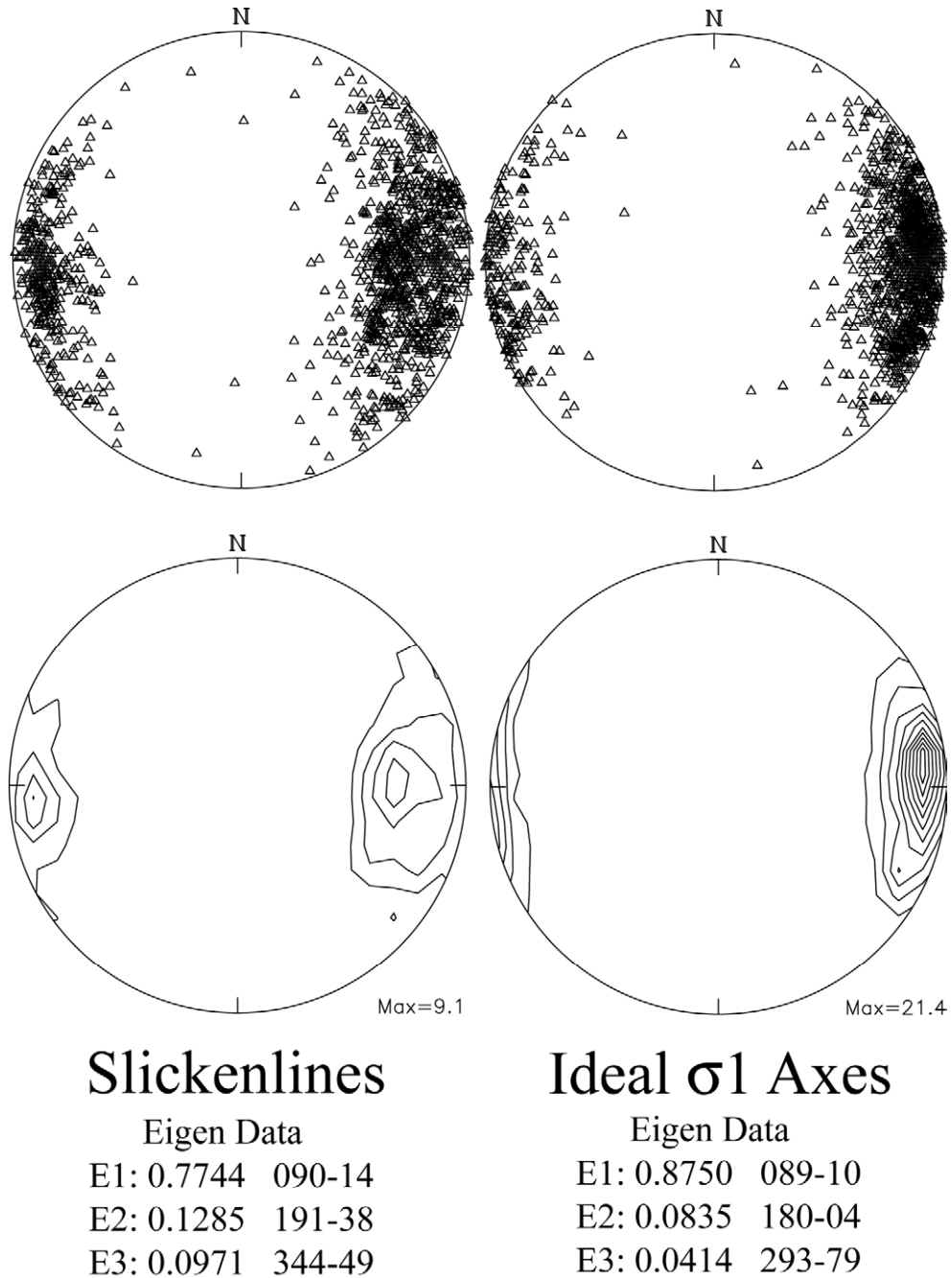


Fig. 5.7. Stereoplots and contoured stereoplots (2% CI) and eigen data of slickenlines and ideal σ_1 axes ($\alpha=25^\circ$) for the restricted fault data set (n=1317).

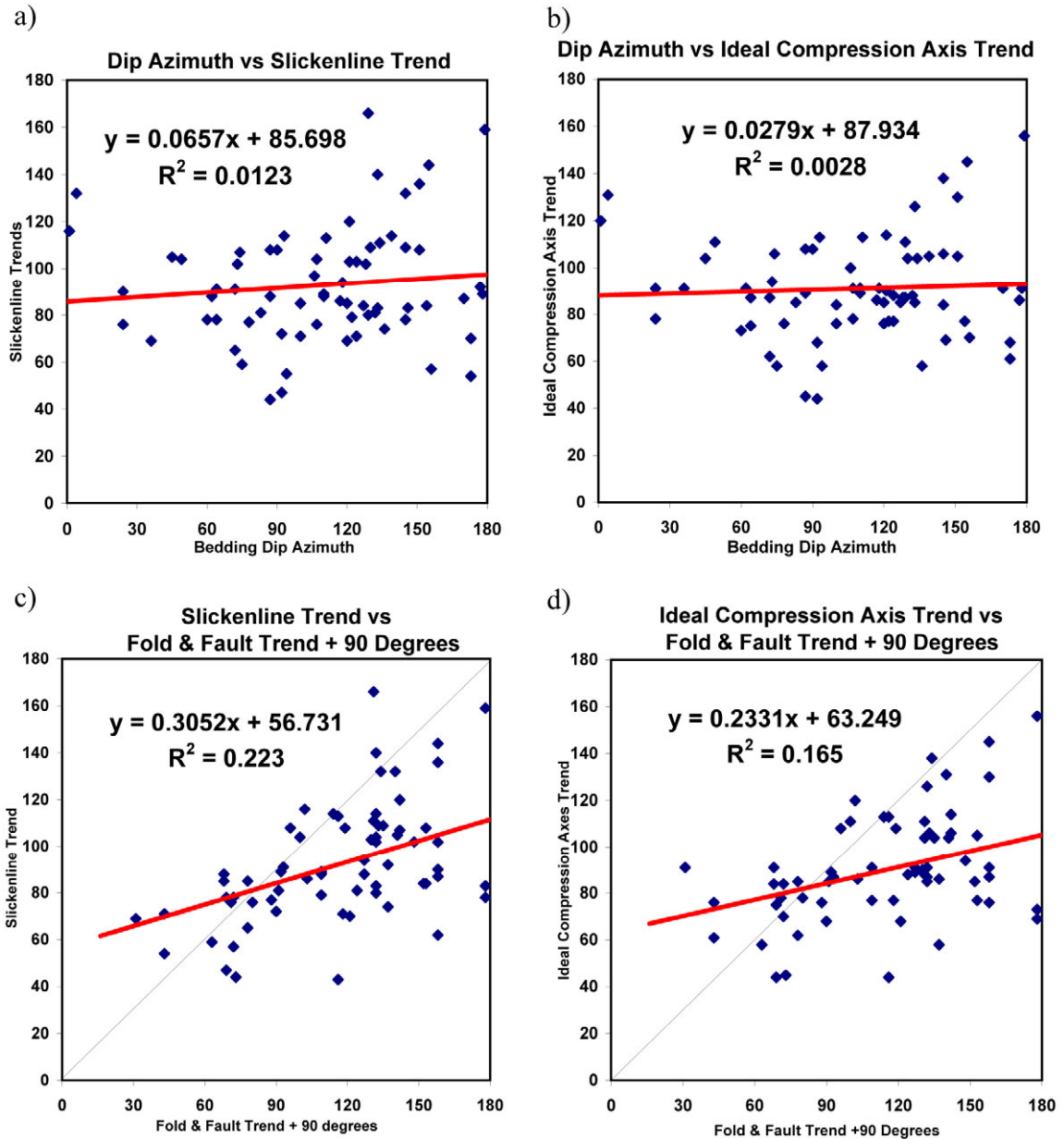


Fig. 5.8. Graphs comparing the influence of bedding dip direction on a) slickenline, and b) ideal σ_1 trends for each fault station (n=69). The influence of fold and fault perpendicular shortening were assessed by plotting fold and fault trends + 90° versus c) slickenline, and d) ideal σ_1 trends (n=70).

perpendicular to fold axes and fault strikes were slightly better as regression lines slope 0.3052 and 0.2331 and R^2 values were 0.223 and 0.165, respectively (Fig. 5.8c, d).

Correlations between trend of strain and stress and shortening parallel to fold axes and

fault strikes were weaker as regression lines slope -0.1262 and -0.0975 and R^2 values of 0.1031 and 0.0781 , respectively (Fig. 5.9a, b). Plotting slickenline trends versus ideal σ_1 trends compares of Laramide strain and stress directions (Fig 5.9c). The correlation was high with a regression line slope of 0.8111 and an R^2 value of 0.8406 (Fig 5.9c).

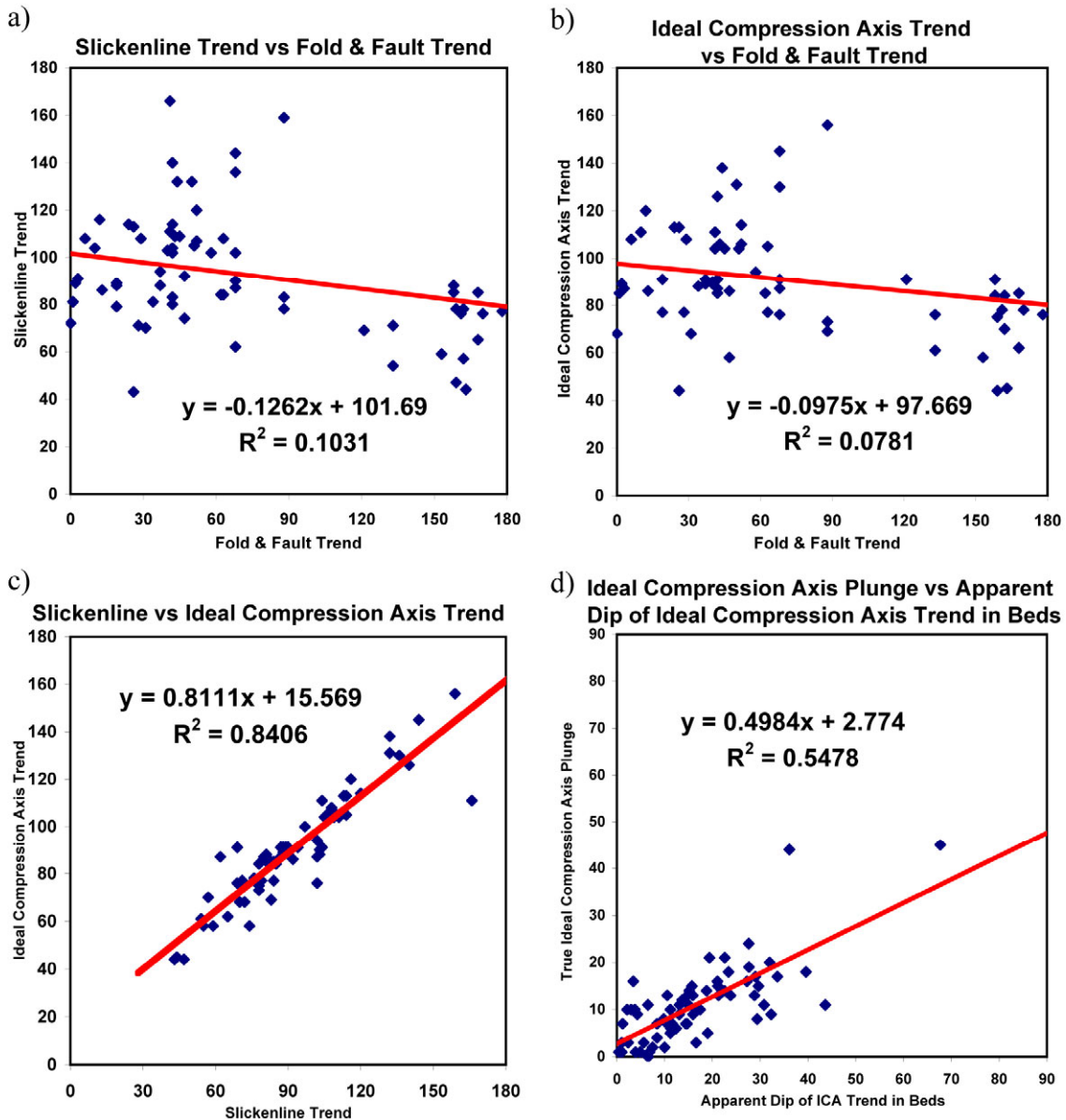


Fig. 5.9. Graphs comparing the influence of fold and fault parallel shortening to a) slickenline, and b) ideal σ_1 trends for each fault station ($n=70$). Strain and stress trends were compared by plotting c) slickenline trends against ideal σ_1 trends. The influence of bedding attitude on stress refraction were compared by plotting d) ideal σ_1 axes plunges versus apparent dip of ideal σ_1 trends in beds.

If Laramide stress were refracted into parallelism with bedding, a correlation between the plunge of ideal σ_1 axes and the apparent dip of bedding parallel to ideal σ_1 trends would exist (Fig. 5.9d). Plunge angles of ideal σ_1 axes were plotted against the apparent dips of ideal σ_1 trends in bedding, and using linear regression, a least-squares trend line slopes 0.4984 and has an R^2 value of 0.5478 (Fig 5.9d).

To assess the influence of stratigraphic position on strain partitioning and regional stress orientations, Laramide σ_1 trends of each fault data station were plotted based on the stratigraphic position of each formation, or elevation above the basement (Fig. 5.10). The σ_1 trends of 8 data stations in the Fountain Formation ranged over 90° , σ_1 trends of 27 fault stations in the Ingleside Formation varied by about 75° , and the 19 data stations in the Dakota group varied by about 45° in trends of σ_1 (Fig. 5.10). Fewer fault data stations in other rock units prohibit any meaningful discussion of observed patterns.

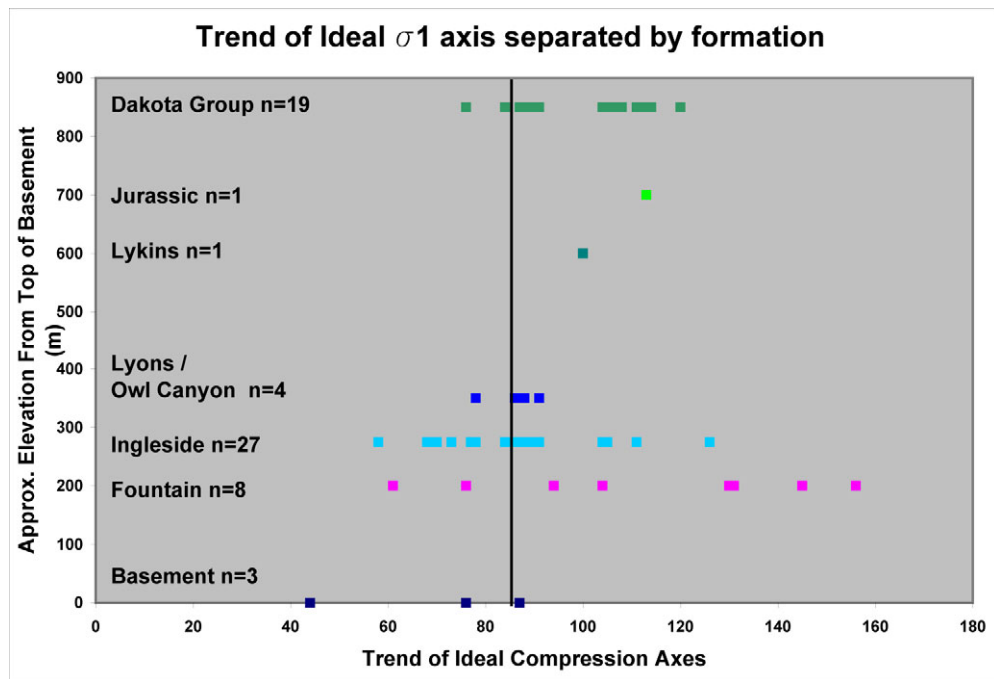


Fig. 5.10. σ_1 trends of fault stations and the elevation of formation tops above basement. Black line illustrates the trend of regional compression at 085° or N85E.

The best fit α angle ($\pm 1^\circ$) for each fault data station was calculated using Orient (Vollmer, 1992) to determine the α angle ($\pm 1^\circ$), between 11° and 33° , which provided the highest first eigenvalue. Means and standard deviations of alpha angles were calculated (Table 5.1) and alpha angle distributions were plotted in histograms (Fig. 5.11).

Formation or Member	# of Data Stations	Mean angle	Standard Deviation
Horsetooth Mbr	16	21.2°	3.1°
Plainview Fm.	3	19°	1.7°
Lytle Fm.	3	20°	4.6°
Jelm Fm.	1	21°	n/a
Lykins Fm.	1	22°	n/a
Lyons Fm.	1	22°	n/a
Owl Canyon Fm.	5	19.8°	2.8°
Ingleside Fm.	26	23.9°	5.9°
Fountain Fm.	13	19.3°	4.6°

Table 5.1. Mean and standard deviation of α angles for various formations.

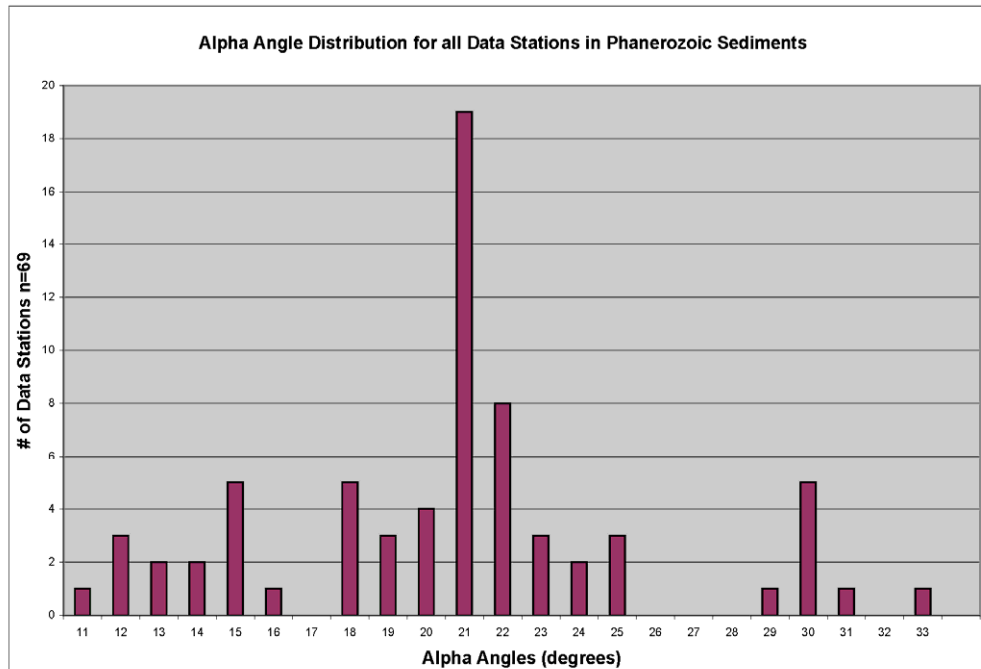


Fig. 5.11. Distribution of α angles producing the highest first eigenvalue for all stations.

Discussion and Interpretations of Minor Fault Data

Regional analyses of Laramide strain and stress using slickenlines and the ideal σ_1 method of kinematic analysis (Compton, 1966) of minor faults have documented that Laramide stress was unidirectional, subhorizontal and oriented 085° (Fig. 5.6). The recognition of strain incompatibilities with the results of a bulk kinematic analysis of all minor fault data suggests that clockwise material rotations were common in the forelimbs of NE-trending monoclinial folds. The relative abundance of left-lateral strike slip faults suggest right-lateral slip of faults coring NE-trending monoclines produced an abundance of antithetic faults in the overlying sedimentary cover (Fig. 5.2). The dominance of strike-slip minor faults over map-scale thrust faults is suggestive of a regional dominance of strike-slip deformation and mesoscopic faulting accommodating fold-axis-parallel extension (Fig. 5.2). The consistency of results for the analyses of Laramide strain and stress directions regardless of the method suggests the entire data set is indeed representative of regional deformation (Figs 5.1, 5.6, 5.7).

Plotting bedding dip azimuth against the average trends of slickenlines and ideal σ_1 axes generates low R^2 values and shallowly-sloping least-squares trendlines suggesting little to no correlation (Fig. 5.8a, b). Comparing the average trends of slickenlines and ideal σ_1 axes to a trend perpendicular to adjacent fold axes or faults tests if Laramide deformation was dominated by dip-slip motion (Fig. 5.8c, d). Comparing the average trends of slickenlines and ideal σ_1 axes to the trends of adjacent fold axes or faults tests if Laramide deformation was mostly strike-slip (Fig. 5.9a, b). The low R^2 values and shallowly sloping least-squares trendlines suggests Laramide deformation generated neither dip-slip nor strike-slip motions on regional faults. The direct correlation

of slickenlines and ideal σ_1 axes suggests Laramide stress resulted in regional coaxial deformation (Fig. 5.9c). Abundant thrusts in an area dominated by strike-slip suggests sediments experienced axially symmetric shortening, or pure shear “pancake” strain.

The consistency of ideal σ_1 axes from Dakota Group strata suggests strain partitioning was more pronounced in late Paleozoic strata directly above the basement (Fig. 5.10). The detachment and flowage of incompetent Mesozoic shales may have limited strain partitioning at structurally higher levels in transpressional folds (Fig. 5.10).

The distribution of best-fit alpha angles (11° to 33°) (Fig. 5.11), was greater than range of best-fit alpha angles (15° to 27°) of Holdaway (1998). There are several lines of reasoning to explain this discrepancy between adjacent areas of identical strata. The collection of kinematic data in strata rotated about a vertical axis or steeply-dipping can record the orientations of several generations of minor faults. Transpressional folds can have highly partitioned strain creating subdomains of strike-slip and dip-slip motions. Transpressional folds are dominated by the subvertical antithetic conjugate fault which strike at a high angle to the fold axes and create unbalanced data sets. The reactivation of faults or linear zones of weakness can create anomalously low alpha angles.

Joint Data and Analysis Methods

1087 joint attitudes were collected in Pennsylvanian to Cretaceous strata between the Colorado-Wyoming border and Fort Collins, Colorado (Fig. 5.12). Master joints, or J1, generally strike NE to ENE and are found only in areas of minor thrust faulting. This fact and observations of minor thrusts cross cut by master joints suggest that Laramide minor faulting largely preceded the formation of master joints. Uncertainty of the relative

timing stems from an observation of slickenlines on primary joints and parallel, low-angle shear fractures immediately below it in the Lykins Formation (Fig. 5.13a). This suggests that in at least one locality, NNE-trending master joints were reactivated as right-lateral, strike-slip faults (Fig. 5.13a). Cross joints, or J2, trend NW to NNW, approximately orthogonal to master joints. Cross joints consistently abut against conjugate strike-slip faults at high angles, creating a conjugate pattern (Fig. 5.13b).

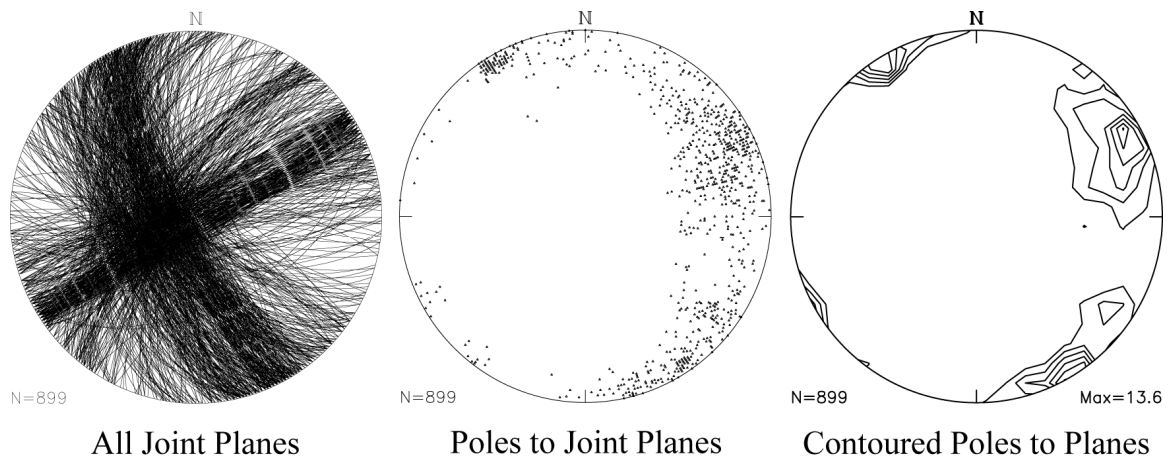


Fig. 5.12. Stereoplots and contoured stereoplots (2% CI) of joint planes and poles to joint planes. Primary joints trend ENE and secondary joints trend NNW.

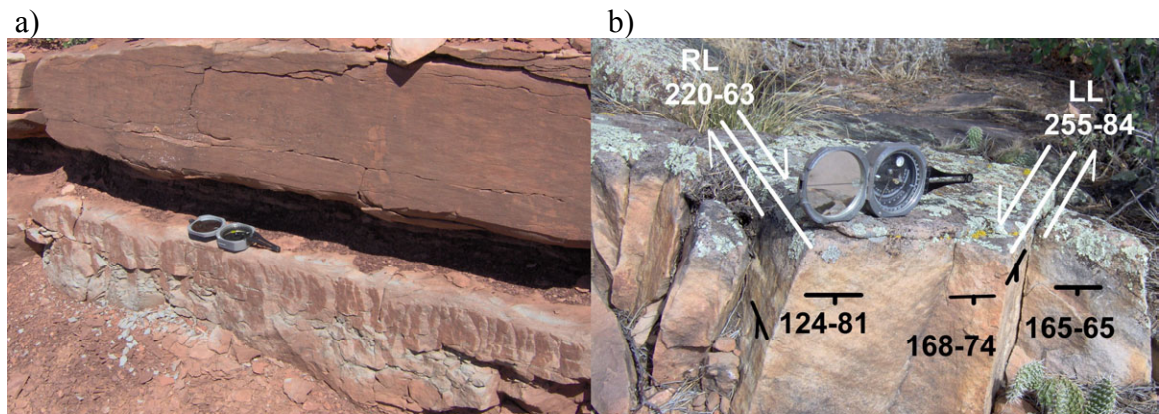


Fig. 5.13. Field observations of jointing; a) NE-trending primary joint in the Lykins Fm. reactivated as a right-lateral, strike-slip fault; b) Conjugate patterns of jointing abutting conjugate strike-slip faults in the Horsetooth Sandstone.

Cross joints dip 60° - 80° WSW, approximately perpendicular to master joints and the 15° – 25° ENE regional dip of strata in the northeastern Front Range (Fig. 5.12).

The influence of strike-slip faults on conjugate cross joints resulted in the formation of the following hypotheses: if J2 planes are consistently perpendicular to strike-slip faults and bedding, then J2 planes should lie along poles to bedding and strike slip faults (Fig.5.14a); or if J2 planes are consistently perpendicular to master joints and bedding, then J2 planes should lie along poles to master joints and bedding (Fig.5.14b).

Hypotheses of J2 planes formed by the release of elastic strain energy (Price, 1966; Harper, 1966; Ruf and Erslev, 2005) can be tested with minor fault data as J2 planes should be perpendicular Laramide σ_1 axes and bedding (Fig.5.14c). Hypotheses of pre-Laramide jointing (Hennings et al., 2000, Bergbauer and Pollard, 2004), were tested by rotating joint and bedding attitudes about a horizontal axis parallel to strike, restoring bedding to original horizontality. If jointing preceded folding, the first eigenvalue and contour maxima should increase substantially (Bergbauer and Pollard, 2004).

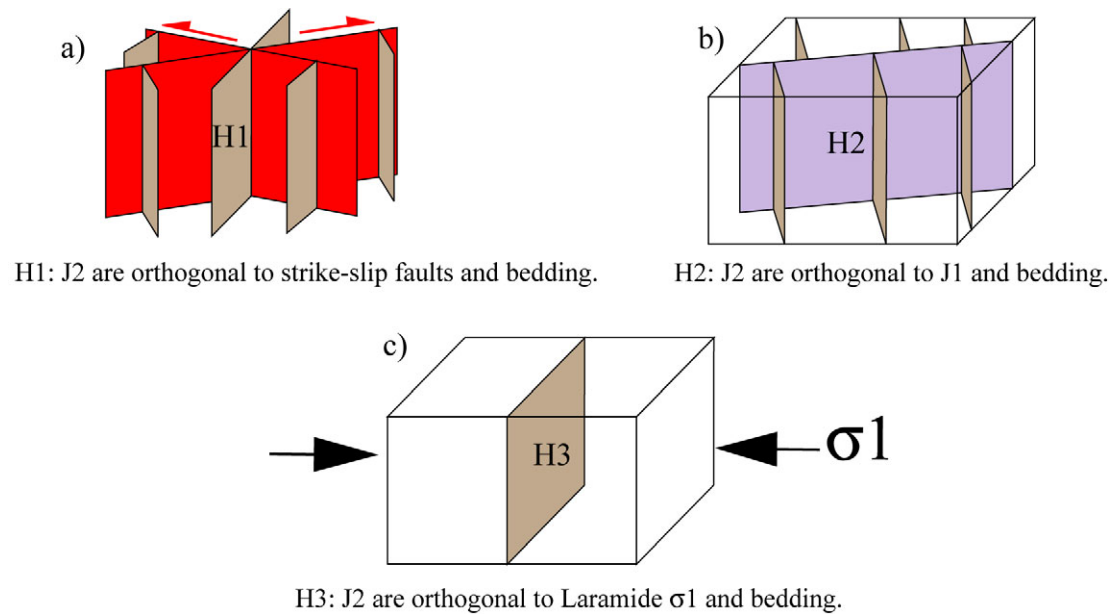


Fig. 5.13. Hypotheses of mechanisms controlling cross joint (J2) formation.

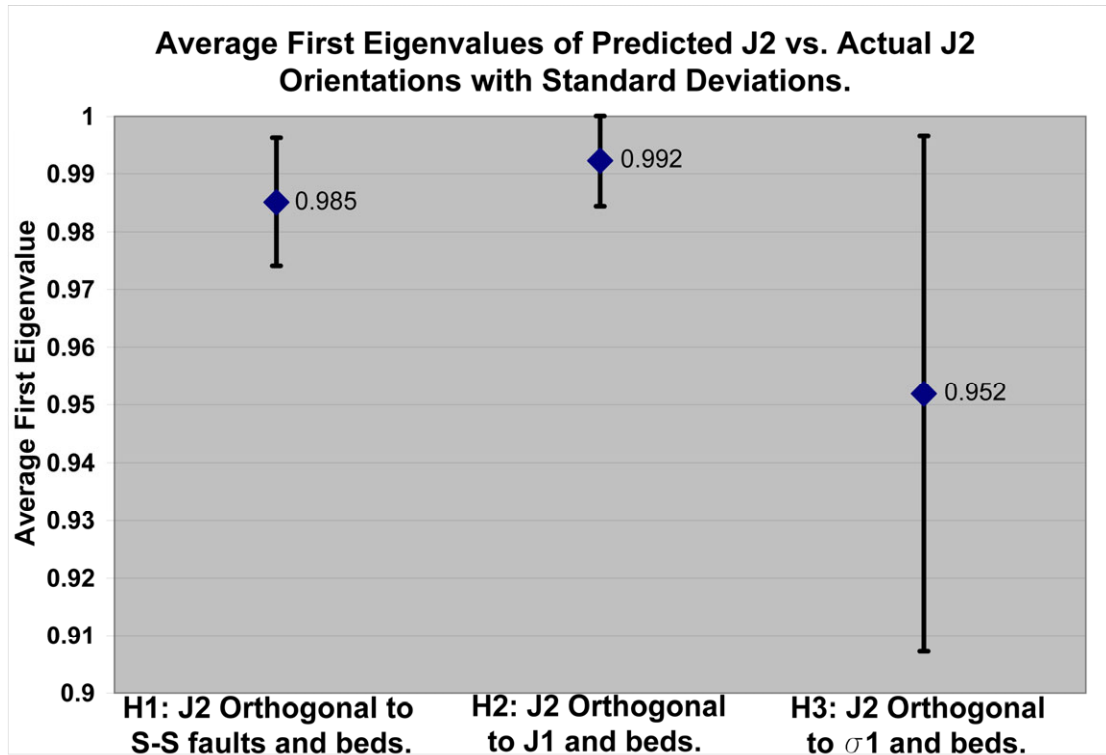


Fig. 5.15. Average first eigenvalue and standard deviation of eigenvalues of actual J2 planes vs. J2 planes predicted by hypotheses 1 through 3.

The average first eigenvalues of poles to J2 and poles of planes predicted by H1 and H2 were 0.985 and 0.992, with standard deviations of 0.011 and 0.008, respectively (Fig. 5.15). The average first eigenvalue of poles to J2 and poles of planes predicted by H3 was 0.952 with a standard deviation of 0.045 (Fig. 5.15).

The average attitude of *in situ* J1 planes was 238°-84° for 15 data stations and poles to J1 planes provided a first eigenvalue of 0.8864 and contour maxima of 30% (Fig. 5.16a). The average attitude of *in situ* J2 planes was 149°-73° for 20 data stations and poles to J2 planes provided a first eigenvalue of 0.8829 and contour maxima of 27.5% (Fig. 5.16b). The average attitude of rotated J1 planes was 057°-86° and poles to J1 planes provided a first eigenvalue of 0.9095 and contour maxima of 43.3% (Fig. 5.16c).

The average attitude of rotated J2 was 150° - 90° and poles to J2 planes provided a first eigenvalue of 0.8912 and contour maxima of 37.5% (Fig. 5.15d).

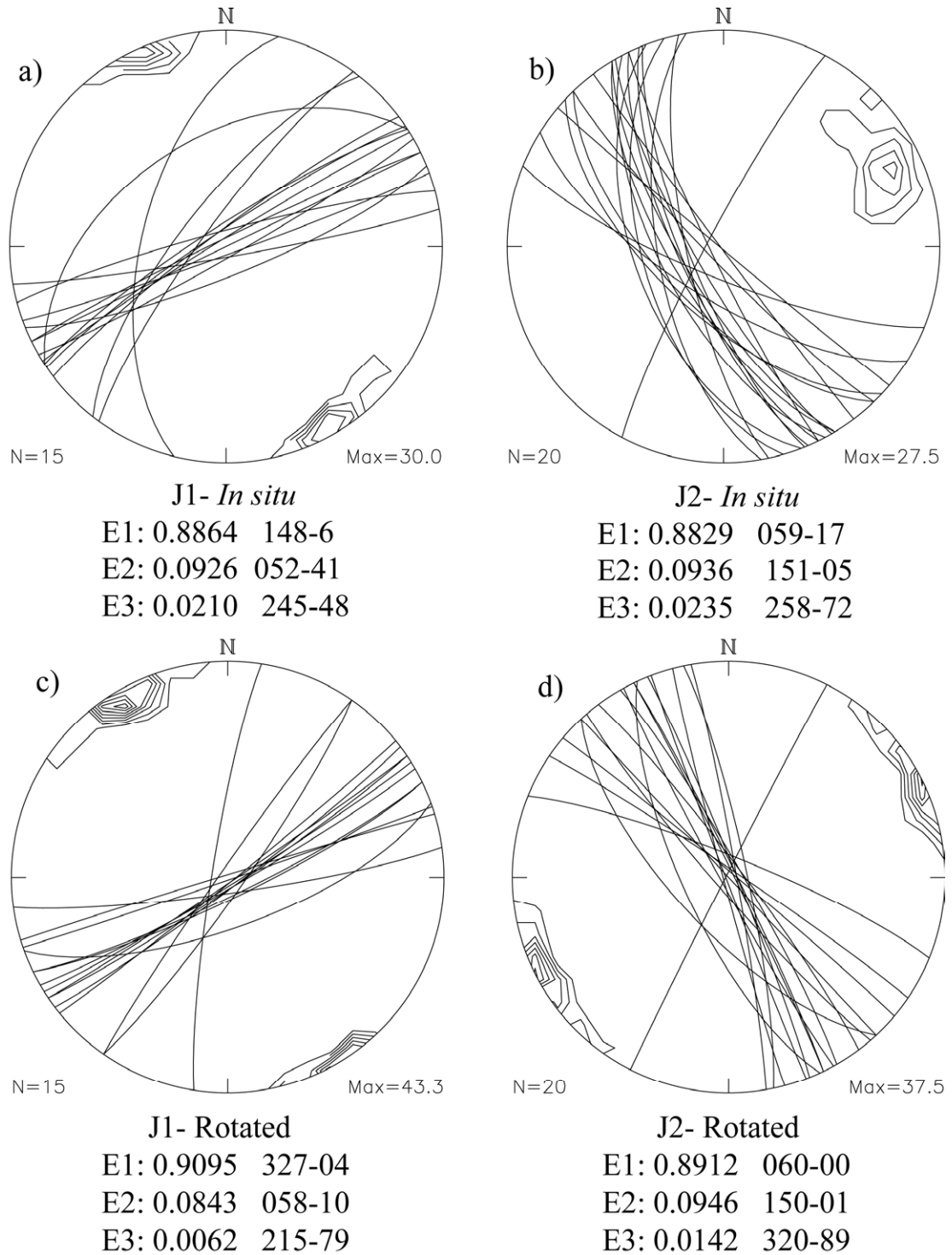


Fig. 5.16. Stereonets of average joint attitudes for each station, contoured poles to planes (5% CI), and eigen data for *in situ* and rotated J1 and J2 planes.

Discussion and Interpretations of Joint Data

Observed cross cutting relationships and the lack of NE- or ENE-trending joints in strike-slip faulted strata provides strong evidence for minor faulting preceding jointing. The lack of a J1 set in strike-slip faulted strata suggests that subvertical strike-slip faults were reactivated as opening-mode fractures during subsequent extensional stress fields. Variability in J1 trends of almost 60° occur over distances of less than 1 km (stations 5.5, 5.7, Fig. 4.24). This suggests jointing occurred at low differential stresses relative to the Laramide Orogeny, as principle stress orientations could be easily perturbed, or joints formed as principle stress orientations changed. Local variations in bedding attitudes and topography had no direct influence on jointing. However, Laramide fold geometry influenced jointing as strike-slip faults are dominant in eastward-bowed hogbacks. Minor thrusts likely had little to no influence on jointing as master joint trends vary widely despite uniform attitudes of thrusts (stations NHR1, 3, Fig. 4.24).

The 21° deviation between the regional trend of Laramide σ_1 at 079° and average J1 strike at 058° (Fig. 5.16) suggests jointing occurred within a subsequent stress field that was deviated from the stress direction during Laramide deformation and faulting. This discrepancy between Laramide σ_1 and J1 attitudes questions the occurrence of syn-Laramide extensional fracturing. Comparing J2 poles and poles of planes perpendicular to both strike-slip faults and J1 planes produced very high first eigenvalues and low standard deviations. This suggests J2 attitudes are largely controlled by two mechanical boundaries, bedding and preexisting fractures. The relatively low first eigenvalue and high standard deviation generated by comparing J2 poles to poles predicted for joints formed by the relaxation of stored elastic strain question ideas of strain rebound joints.

Hypotheses of pre-Laramide jointing can be tested by a fold test, or restoring jointed beds to their original horizontality. If regionally consistent joints formed prior to the Laramide Orogeny then joints in horizontal beds would have a consistent attitude. The consistency of these attitudes can be quantified by eigenvector analysis of poles to joints with rotated joints having a higher first eigenvalue relative to *in situ* joints. The slight increase of first eigenvalue and contour maxima of rotated joints is far too scant to be interpreted as providing evidence for pre-Laramide timing of jointing (Fig. 5.16). The localized reactivation of J1 in the Lykins Fm as right-lateral strike-slip faults could be indicative of post-orogenic gravitational spreading of the basement arch or local deformation during the rehydration of massive gypsum beds. Parallel trends of the J2 set and normal faulting associated with the late Miocene onset of Rio Grande rifting suggests J2 formed during the Miocene, associated with regional uplift and extension (Kellogg, 1999; McMillan et al., 2002).

Chapter 6

Two-Dimensional Structural Interpretations and Analyses

Motivation for 2D Structural Interpretations and Analyses

The balancing and restoration of geologic cross sections are powerful tools for testing and rejecting models of Laramide deformation (Brown, 1984; 1988; Erslev, 1986; 2005; Stone, 2005). The constraints imposed by mass and line-length balancing of two-dimensional interpretations posed by several workers (e.g. Brown, 1984; 1988; Erslev, 1986; Spang and Evans, 1988; Erslev et al., 2004, Stone 2005) have questioned the validity of previous interpretations invoking subvertical faulting across the Colorado Front Range and Laramide Foreland (e.g. Prucha et al., 1965; LeMasurier, 1970; Stearns, 1971; 1975; 1978; Matthews and Sherman, 1976; Matthews and Work, 1978; Jacob, 1983). The creation of a series of balanced cross sections is the fundamental first step in any detailed three dimensional structural analyses without a 3D seismic data volume. The software package 2DMove (MVE, 2006a) permits the generation and the testing of 2D interpretations of fault and fold geometries for balance and restorability.

Methods of Cross Section Construction

Geologic maps of the nine 7.5 ' quadrangles encompassing study area were scanned and georeferenced in ArcMap using georeferenced topographic base maps. Formation contacts, structure contours, faults, fold axes and bedding data were digitized

in ArcMap and draped upon a 30 m DEM in ArcScene to collect elevations for 3D polyline and point data. 3D Shapefiles were exported to .dxf files by ArcCatalog and imported into 2DMove (MVE, 2006a, b). Well data (n=115) was collected from the Colorado Oil and Gas Conservation Commission and the Wyoming Oil and Gas Conservation Commission (COOGCC, 2006; WYOGCC, 2006). Well elevations and depths to formation tops were converted to elevations in meters. Bedding and well data coordinates were converted from NAD83 Lat/Long to UTM NAD27.

Structural cross sections were oriented at 085°, parallel with the direction of regional slip inferred from the detailed kinematic analysis of the study area (Figs. 5.7, 6.1). Elevations to formation tops above and below formation contacts were determined using apparent dips and formation thicknesses from geologic maps (Braddock et al., 1988c, 1988d, 1989a; Courtwright and Braddock, 1989). Restorable geometries of blind thrust and reverse faults were estimated using the methods of Erslev (1986; Fig. 6.2). Cross sections were located to optimize structural data and section spacing was based on along-strike variations in structural geometries (Figs 6.3- 6.8). 2DMove collected the X, Y, and Z coordinates of formation contacts where they intersect sections and projected apparent dips of bedding parallel to strike and into the planes of sections and made down-plunge projections of formation tops from wells.

Motivation for Multiple Structural Restoration Methods

Cross sections were restored with the fault-parallel flow and flexural-slip unfolding algorithms and line-length balancing in 2DMove (Figs. 6.9-6.14). The fault-parallel flow algorithm restores the basement nonconformity across faults but preserves

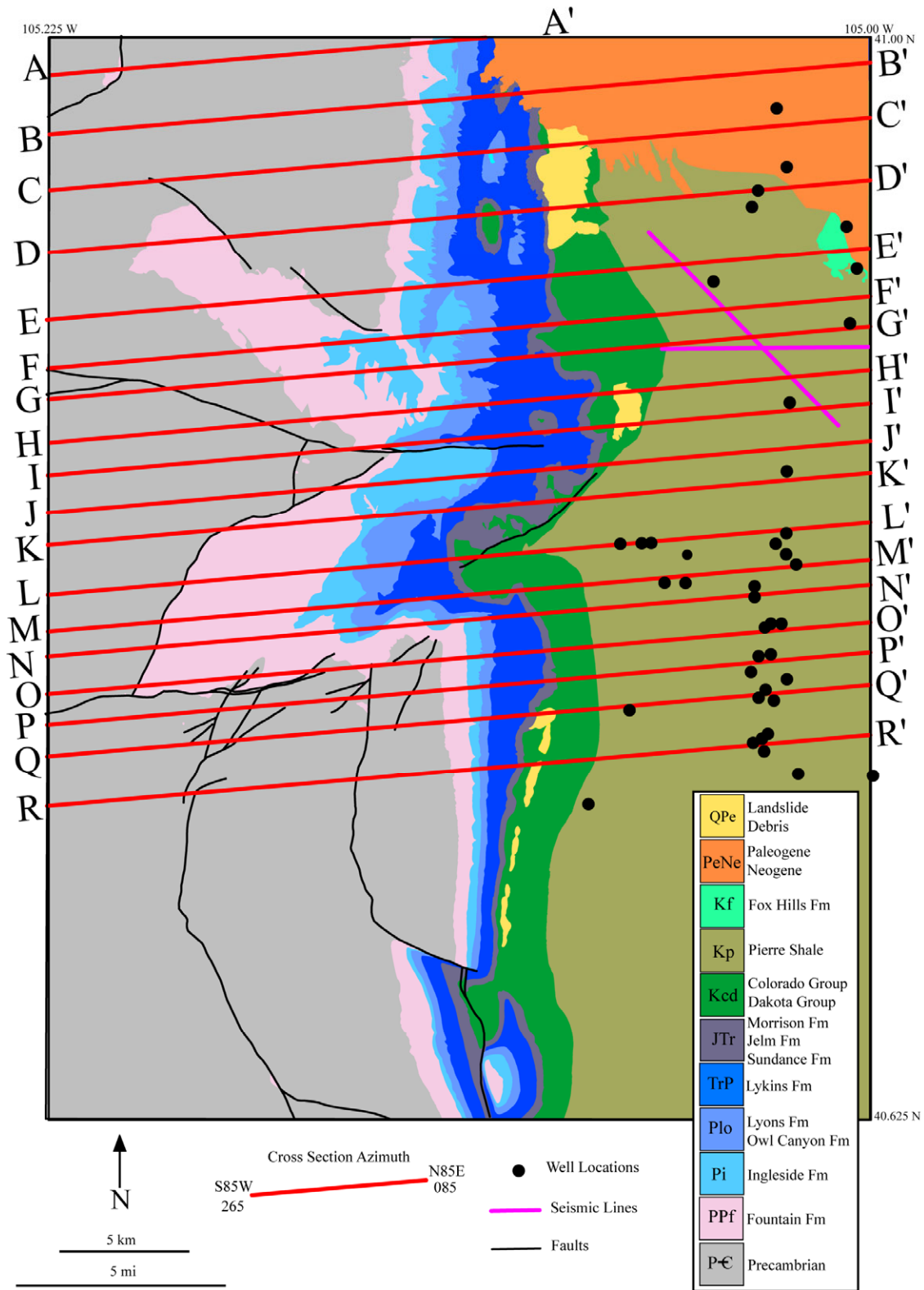
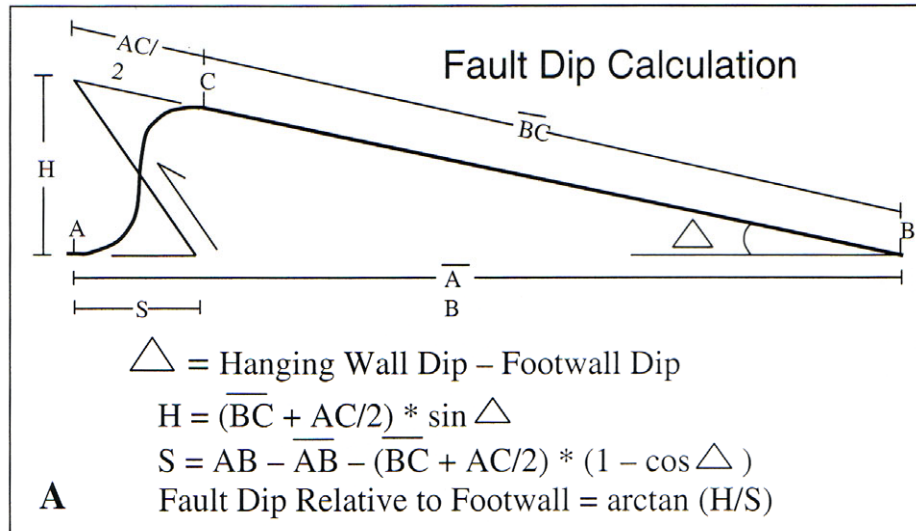
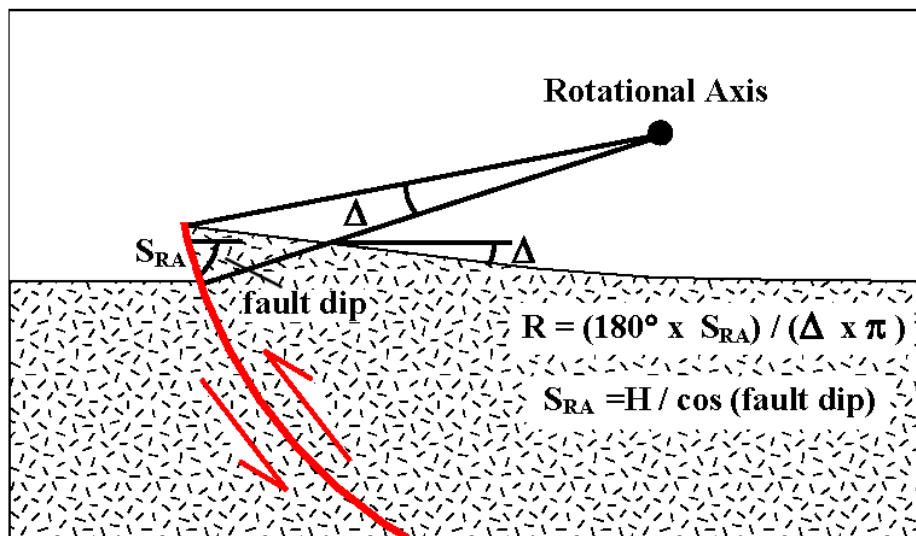


Figure 6.1. Map showing locations of cross sections constructed in this study.



a)



b)

Figure 6.2. Geometric formulas for determining a) fault dip angle and b) fault curvature for listric fault-propagation folds (Erslev, 1986).

nonconformity to any regional folding of the basement. Flexural-slip unfolding allows the basement be restored to a regionally planar surface while preserving area and line lengths in the overlying sediments. Line-length restorations were done to test for basic restorability, flexural slip and thickening or attenuation of strata during folding. Pins were placed perpendicular to local dips and the intersections of loose pins and formation top lines were marked and the lines unfolded. Restored sections were pinned on the eastern side

and new loose pin lines were drawn linking pin intersection markers to illustrate the sense of flexural shear and bed-parallel slip and fold-related variation in line lengths.

Two-Dimensional Structural Interpretations

Eighteen two-dimensional structural interpretations were made spanning the western Denver Basin near the Colorado-Wyoming border and the central Owl Canyon Block midway between Livermore and Ted's Place, Colorado (Fig. 6.1) Observations and subsequent discussions of cross sections occur in a north-to-south progression.

Section A-A' spans the eastern Virginia Dale Ring Structure, an isolated outcrop of the lower Fountain Formation and an N-striking segment of the Dale Creek Fault. A-A' ends at the CO-WY border where Permian sediments have planar homoclinal dips of 10-14° ESE (Figs. 6.1; 6.3a) (Braddock et al., 1989a; Courtwright and Braddock, 1989). The Dale Creek Fault has >220 m of throw if the planar, subhorizontal 2410 m summit of Table Mountain (NW Virginia Dale Quad) is the Pennsylvanian nonconformity and given a 2190 m elevation of the nonconformity in the footwall, which dips <5° SE. Map-view sinuosity of the Dale Creek Fault and its apparent right-lateral offsets of subvertical Proterozoic contacts on the northeast-trending segment of the fault is anomalous given local kinematic constraints (Braddock et al., 1989a). Remnants of the lower Fountain Fm. and local variations in the attitude of the nonconformity and Permian strata suggests the basement was gently folded and not substantially elevated.

Sections B-B' and C-C' contain subplanar, homoclinal dip domains, the northern Sand Creek Anticline (SCA), and the northern Sixmile Fault (SF) (Figs. 6.1; 6.3b, c). The asymmetric SCA has a rounded hinge, offsets strata dipping 10-14° ESE and homoclinal

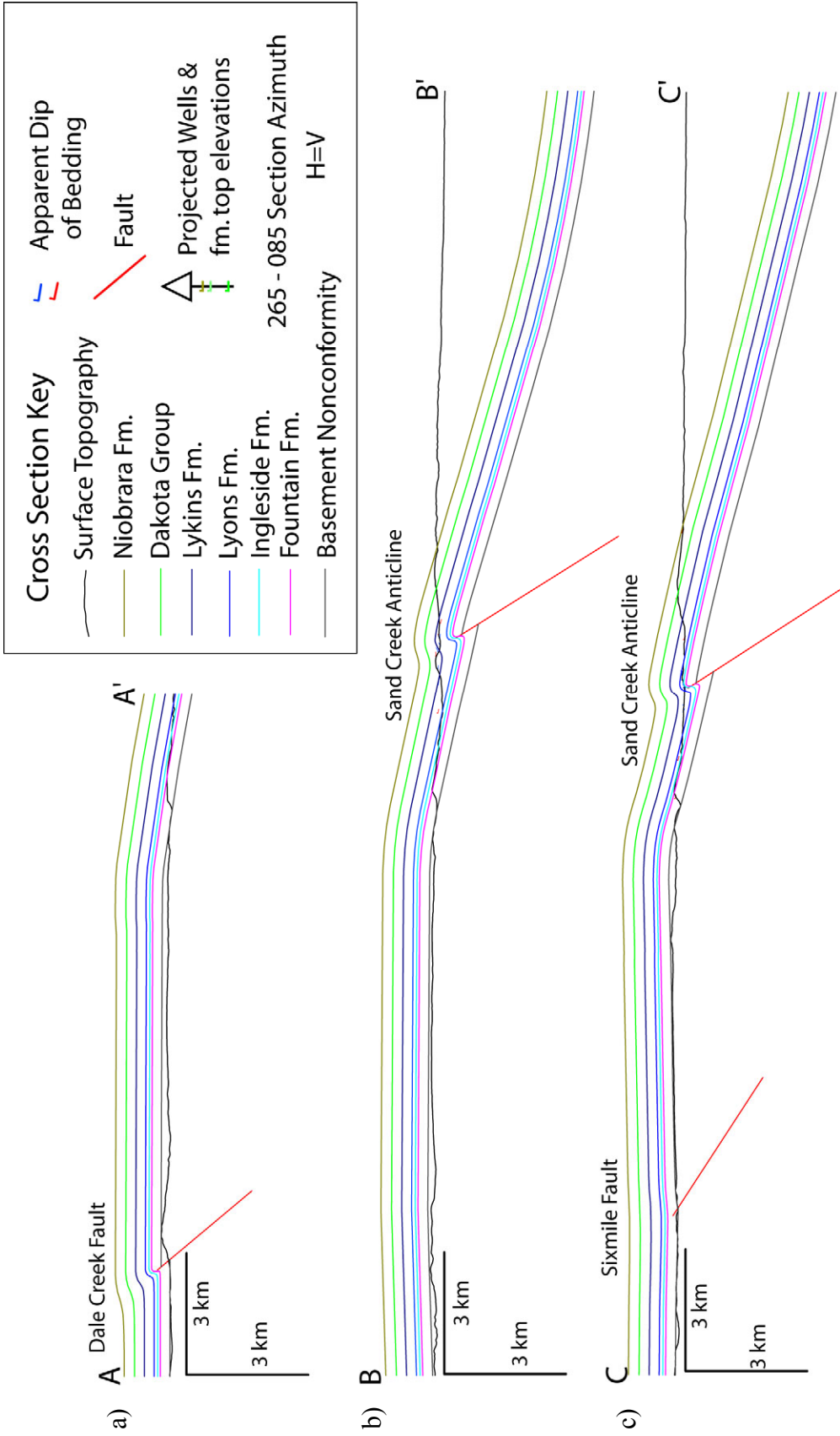


Fig. 6.3. Cross Sections A-A', B-B', and C-C' (a-c) showing interpreted 2D geometries based on surface and well data.

dips in the distal forelimb and backlimb. The SF gently folds basement, offsetting the nonconformity, and its shallow dip in C-C' is an apparent dip due to the acute angle between cross section trend and fault strike (Fig. 6.3c).

The asymmetry of the SCA and consistent regional dips are suggestive of trishear folding above an E-dipping, planar reverse fault. The northward plunge of the SCA is likely the product of the obliquity of fault strike to regional compression, enhancing strike-slip. Basement folding near the northwestern terminus of the SF is likely due to fault-propagation folding in front of an oblique, left-lateral / reverse fault. Fault-parallel flow restorations of A-A', B-B' and C-C' illustrate gentle basement folding and the inability to restore the nonconformity to a planar, subhorizontal surface (Fig. 6.9).

Section D-D' spans the Sixmile Fault (SF), the Sand Creek Anticline (SCA), the Round Butte Thrust (RBT), and the Meadow Springs Anticline (MSA) and two dip domains (Fig. 6.4a). Attitudes of the lower Fountain Fm. in the northern Red Mountain Embayment (RME) and the lack of faults suggests that basement folding accommodated slight changes in regional dip yet wasn't substantially elevated (Fig. 6.1). D-D' intersects the SF where it has a maximum throw of 180 m and gently folded the basement. D-D' intersects the SCA at a structural culmination on a north-trending segment of the fold where the blind reverse fault which cores the fold has a local maximum of throw. The Round Butte Thrust (RBT) is a major, into-the-basin, blind thrust with maximum throws of approximately 1300 m (Fig. 6.4a). The Texaco Warren Livestock #1 well penetrated repeated Permian stratigraphy, suggesting the RBT forms a splay of reverse faults.

A structure contour map of the Dakota Group from the depth conversion of a proprietary and confidential 3D seismic data volume of the Meadow Springs Anticline

(MSA) provided tight constraints on fold and basin geometries in sections D-D' through I-I' (Mollerstuen, pers. comm., 2006). Elevations of the Dakota Group in wells west of the RBT document both basement folding and rotation of the hangingwall, suggestive of a concave-up, listric geometry of the RBT (Fig. 6.4a). An E- trending confidential seismic profile across the MSA reveals a slightly-asymmetric, gently folded anticline cored by an E-dipping, planar reverse fault. The crest of the MSA contains east-dipping thrusts within the Dakota Group, Niobrara Fm. and Pierre Shale.

The presence of a reverse fault splay, low elevations of the upper Dakota Group to the east and the observation of only gentle folding of the nonconformity in 2D seismic suggests the Permian strata near TD in the Texaco well were elevated by an additional reverse fault (Fig. 6.4a). Basement folding of the hanging wall could be a due to hangingwall backthrusting, fault-bend folding on a shallowing fault, or a compressional bend in the oblique right-lateral / reverse fault as fault dip increases to the NE (Fig. 6.4a). East-dipping, out-of-the-basin thrusts on the crests of anticlines and east-tilting shear pins of sections restored with line-length balancing suggests that top-to-the-west, out-of-the-basin flexural slip was a common mode of deformation (Figs. 6.4a, 6.10).

Sections E-E' contains the Red Mountain Embayment, the Maxwell Fault (MF), the oppositely-plunging axes of the Sand Creek (SCA) and Ackerman Anticlines (AA) and the Round Butte Thrust (RBT) (Fig. 6.4b). To the west, the subhorizontal nonconformity dips 2° NE and is gently folded where it is offset by the MF. Abrupt changes in the attitude of the nonconformity requires a gentle, SE-plunging basement arch in the hanging wall of the MF. Section E-E' illustrates the similar geometries of the SCA and AA and the abrupt loss of slip on the blind faults where the fold axes overlap.

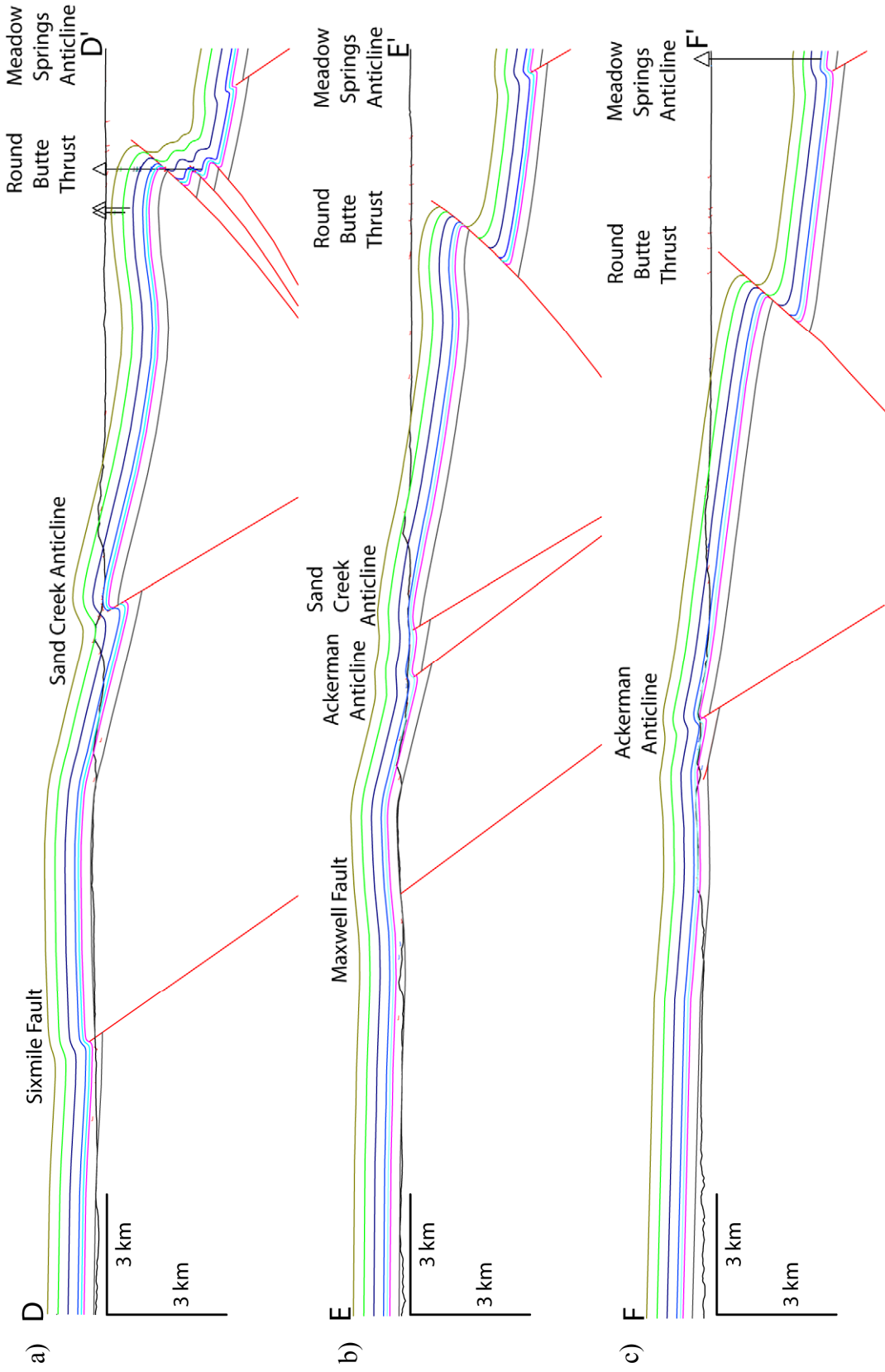


Fig. 6.4. Cross Sections D-D', E-E', and F-F' (a-c) showing interpreted 2D geometries based on surface and well data.

This suggests is strain is relayed between the faults which core the SCA and AA. The southwest plunge of the arch in the hangingwall of the RBT is evident in E-E' (Fig 6.4b). Fault-parallel flow restorations of D-D' and E-E' demonstrates both short and long wavelength basement folding during regional shortening (Figs. 6.4b, c, 6.10).

Structural geometries in F-F' are similar to D-D' and E-E', however there is little folding of the nonconformity in the hanging wall of the RBT (Fig 6.4c). The symmetric low-amplitude anticline on the crest of the SE-plunging basement arch is interpreted as cored by an E-dipping thrust which soles into the nonconformity as a detachment surface (Fig 6.4c). This interpretation is supported by eastward-leaning loose pins created during line-length restoration which suggests top-to-the-west, out-of-the-basin flexural slip occurred during deformation (Fig. 6.10). Gently-curved fold hinges, diffuse deformation and abrupt changes in strata thicknesses within folds with few macroscopic faults suggest of trishear fault-propagation folding was the mode of deformation in D-D', E-E' and F-F'.

Section G-G' spans the Halligan Reservoir Fault (HRF), the Ackerman Anticline (AA), and the Round Butte Thrust (RBT), the Rawhide Anticline (RA) and the Meadow Springs Anticline (MSA) and is constrained by NW- and W-trending 2D seismic profiles (Fig. 6.1) (Mollerstuen, pers. comm., 2006). The HRF has little throw where it separates two subhorizontal fault blocks, suggesting nearly pure left-lateral strike-slip (Figs. 6.5a). Although G-G' crosses the doubly-plunging crest of the AA, slip on the underlying fault remains consistent with areas to the north as footwall elevations increase to the south. The geometry of RBT is best constrained in G-G' as a single blind thrust fault as a proprietary 2D seismic profile is subparallel with section azimuth (Fig. 6.5a) (Mollerstuen, 2006). Displacement on the RBT decreases to zero as slip is transferred to

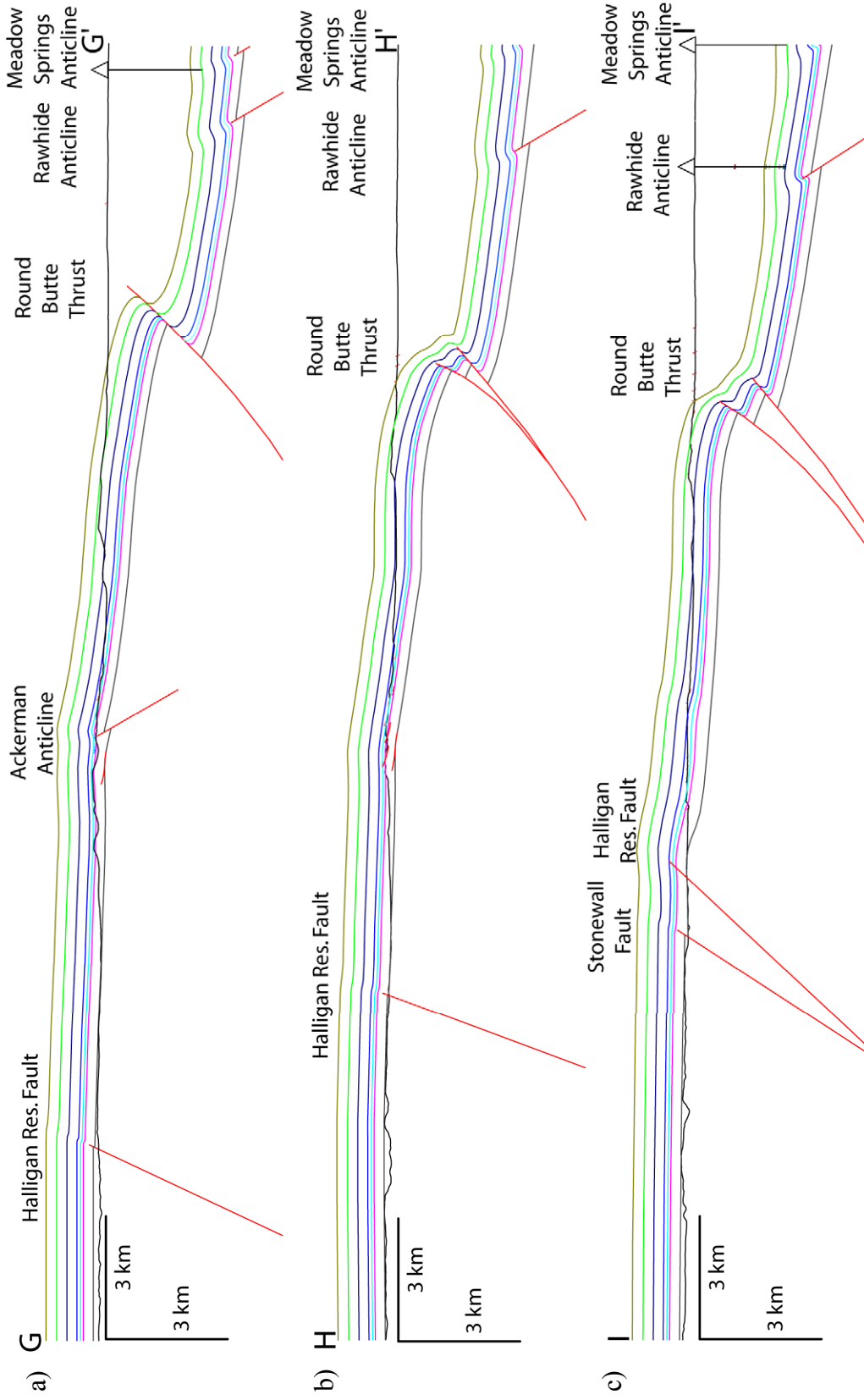


Fig. 6.5. Cross Sections G-G', H-H', and I-I' (a-c) showing interpreted 2D geometries based on surface and well data.

diffuse folding of incompetent upper Cretaceous shales. 2D seismic data through RA and MSA suggest they are structurally identical as both folds are slightly asymmetric and cored by east-dipping, reverse faults (Mollerstuen, 2006). A proprietary time-structure map of the top of the Dakota Group shows the fold amplitude of the RA increasing as the MSA plunges to the south, suggesting fault slip may have been transferred across the structures (Mollerstuen, 2006). Fault-parallel flow restorations exhibit an arcuate basement surface across the area (Fig. 6.11). East-leaning loose pins created during line-length restoration suggest top-to-the-west, out-of-the-basin flexural slip dominated despite local top-to-the-east flexural slip during movement on the RBT (Fig. 6.11).

Section H-H' spans the Halligan Reservoir Fault (HRF), several east-dipping, unnamed thrusts, the Round Butte Thrust (RBT), and the Rawhide (RA) and Meadow Springs Anticlines (MSA) (Figs. 6.1, 6.5b). The nonconformity is subplanar near the HRF yet a slight offset of the top of basement suggests there is a reverse slip component. Eastward-dipping thrusts on the crest of a basement fold are interpreted as driven by top-to-the-west flexural slip and soling into detachments near the nonconformity and the upper Fountain Fm. H-H' crosses multiple dip domains in the hanging wall of the RBT where shallowly-dipping strata change dip directions while in some areas remaining subhorizontal. An abrupt, along-strike increase in the dip of the Cretaceous strata and the great width of the zone of folding were interpreted as the products of the RBT changing to a splay of two reverse faults (Fig. 6.5b).

Section I-I' crosses the same structures as H-H', but also crosses the Stonewall Fault and the E-W trending Halligan Reservoir Syncline (Fig. 6.1). Isolated remnants of the nonconformity in both the hangingwall and footwall constrains the throw on the

Stonewall Fault to about 100 m. The abrupt folding of the nonconformity near a compressional bend in the left-lateral HRF suggests a small-scale flower structure was formed within the basement along the fault. Diffuse deformation of strata in the footwall of the HRF suggests trishear folding occurs at nearly 90° to the azimuth of regional slip in structures formed by transpression (Fig. 6.5c).

J-J' spans the Stonewall Fault, the North Livermore Fault (NLF), the Roberts Monocline (RM), and the Round Butte Thrust (RBT), and the northern Wellington Anticline (WA) (Figs. 6.1, 6.6a). The NLF is a planar, right-lateral fault with about 400 m of net slip and 200 m of throw (Fig. 6.6a). The RM is cored by a planar, right-lateral / reverse fault which offsets two subhorizontal basement blocks with about 400 m of throw. Acute angles between section azimuth and the strikes of the NLF and the fault which cores RM creates low apparent dips and longer fold wavelengths. Surface mapping of a high-angle, oblique right-lateral fault to the southwest suggests slip was transferred to a steeper splay of the RBT (Fig. 6.1). A contour map from 2D seismic data suggests J-J' crosses the northeast-plunging axis of the WA (Mollerstuen, 2006). Regional kinematics suggests the northeast-plunging terminus of the fold is likely due to strike-slip rather than reverse-slip on the underlying fault. Fault parallel flow restorations are unable to explain abrupt changes in dip domains by rotations on curved faults (Fig. 6.12). This could be due to the interpretations being invalid, basement folding by crustal buckling, or by variable isostatic subsidence of the basin tilting the nonconformity to the east.

K-K' and L-L' spans the North (NLF) and West Livermore Faults (WLF), the Grayback (GM) and Roberts Monoclines (RM), the Round Butte Thrust (RBT), the Wellington Anticline (WA) and a transition of regional dips (Figs. 6.1, 6.6b, c).

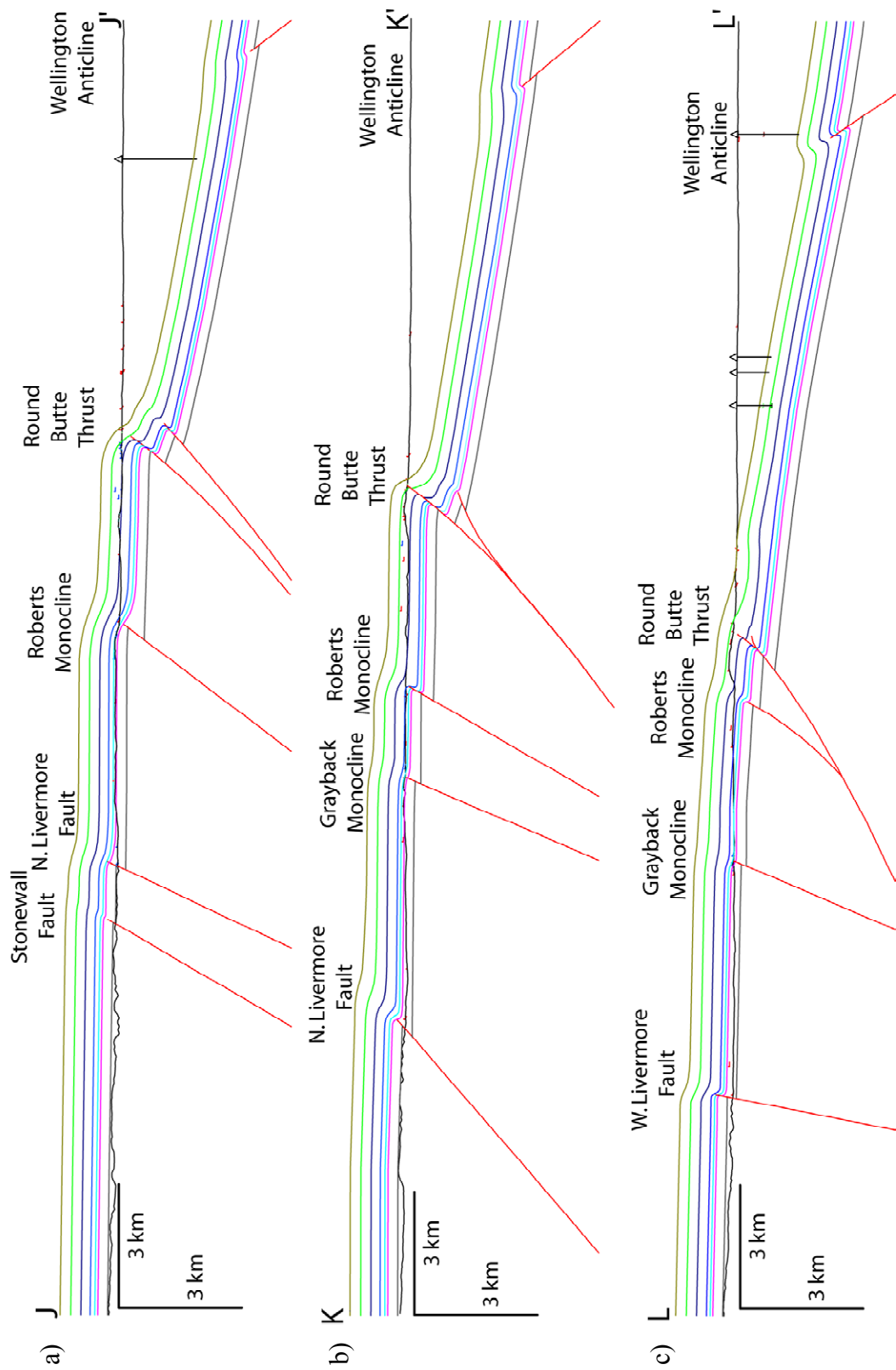


Fig. 6.6. Cross Sections J-J', K-K', and L-L' (a-c) showing interpreted 2D geometries based on surface and well data.

The WLF and NLF are both high-angle, oblique right-lateral / reverse faults with slickenlines plunging at 20-30° to the southwest. The faults are likely planar as they separate subhorizontal fault blocks and have net slip amounts of about 450 - 500 m, approximately twice the throw amounts of 225 - 250 m.

The northern GM is an NE-trending fold, cored by a planar high-angle, oblique right-lateral / reverse fault, which separates two horizontal basement blocks and has about 120 m of throw in K-K' and L-L'. Throw on the fault coring the RM drops to about 300 m in K-K' and 160 m in L-L' despite the dominance of reverse slip on the N-striking segment (Figs. 6.1, 6.6b, c). The significant drop in the throw of the RM is likely due to fault slip being transferred to the fault which coring the GM. The geometry of the RBT in K-K' is similar to section J-J' however the merging of the fault splays at a shallow depth caused the basement wedge to be tilted eastward on the shallowing fault. L-L' is the southernmost section which contains the RBT as the fault and related monoclinial fold abruptly terminate to the southeast (Figs. 6.1 and 6.6c). The abrupt increase in the fold amplitude of the WA to the south suggests slip rapidly increases on the east-dipping reverse fault coring the fold. The increase in amplitude of the WA correlates with the abrupt southward plunge of the Rawhide Anticline (RA) observed within a proprietary time-structure map from a high density grid of 2D seismic data (Mollerstuen, 2006). These observations are suggestive of slip being transferred from the southern RA to the northern WA. Thickening of Permian through Cretaceous strata east of the RBT is due to out-of-the-basin flexural slip driven by the WA and basin development being captured by the hinge of the north-plunging Campbell Valley Anticline. Fault-parallel flow restorations of the L-L' show the very gradual bending of the nonconformity (Fig. 6.12).

Sections M-M', N-N' and O-O' cover the southern Livermore Embayment and include the West Livermore Fault (WLF), the Grayback Monocline (GM), the Livermore Fault (LF), the North Fork Fault (NFF), the Campbell Valley Anticline (CVA), and the Wellington Anticline (WA) (Figs. 6.1; 6.7a, b). Structural geometries and kinematics of the WLF and the oblique right-lateral / reverse fault coring the GM are similar aside from the WLF having greater overall slip and being exposed at a deeper structural level. The abrupt increase in the amplitude of the CVA suggests slip on the underlying fault increased to the south near the termini of the RM and RBT and reverse slip increases on the NFF and several small reverse faults (Figs. 6.1; 6.7b, c). This suggests fault slip was transferred between structures cored by faults of both synthetic and antithetic dips.

Sections N-N' and O-O' illustrate basement folding adjacent to the Livermore Fault (Figs. 6.7b, c). Throw of the Livermore Fault reaches a maximum where it's strike bends to the northeast, suggestive of oblique right-lateral / reverse slip. The terminations of the GM, NFF, CVA, RM and HM against the LF and increased folding of the basement adjacent to the structure suggests it was a preexisting zone of weakness during Laramide deformation. The geometry of the WA, constrained by wells and structure contour maps of the Hygiene Sandstone (Scott and Cobban, 1978), varies slightly along the sinuous trend of the fold axes. Eastward leaning loose pins created during the line-length balancing of M-M', N-N' and O-O' and the angular hinge of the WA suggests top-to-the-west, out-of-the-basin flexural slip has been captured by, and amplified the anticlinal crest (Fig. 6.13).

Sections P-P', Q-Q' and R-R' span the Helwett Fault (HF), the North Fork Fault (NFF), the Campbell Valley Anticline (CVA), and the Wellington Anticline (WA) and lie

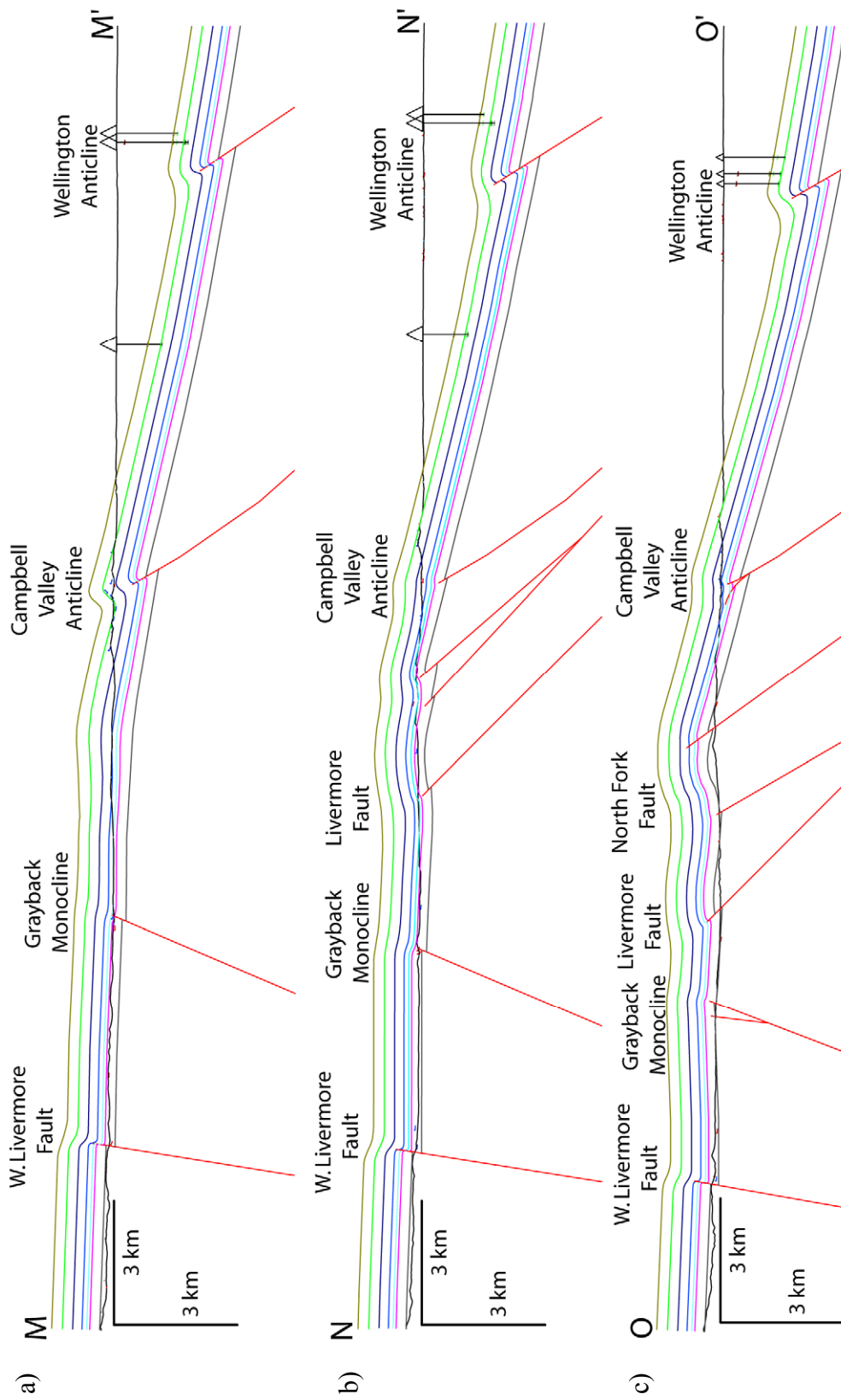


Fig. 6.7. Cross Sections M-M', N-N', and O-O' (a-c) showing interpreted 2D geometries based on surface and well data.

within the relatively homogeneous structural domain to the south of the Livermore Fault (Figs. 6.1, 6.8a-c). Hangingwall geometries of the NFF in P-P', Q-Q' and R-R' illustrate the abrupt increase of regional ENE dips and the decrease of basement folding to the south (Fig. 6.8a-c). The abrupt southward increase in structural elevation is due to increased dip-slip on faults as fault strikes change from NE- and N- to NNW-striking, perpendicular to ENE-directed regional shortening (Figs. 6.1, 6.8a-c). The slight increase dips of the backlimbs of the NFF and fault coring the CVA relative to the forelimb suggests concave-up listric fault geometries. The sinuosity of fold axes and the abrupt plunges of asymmetric anticlines and losses of slip occur where the N-trending, *en echelon* array of folds overlap each other along the regional strike (Figs. 6.1, 6.8a-c).

Fault-parallel flow and line-length restorations of sections P-P', Q-Q' and R-R' illustrate total shortening and out-of-the-basin shear increasing to the south (Fig. 6.14). The abrupt changes in fault attitudes to an NNW-strike and lesser basement folding to the south are likely due to the greater coherency of the crust away from the Skin Gulch Shear Zone. The sinuous traces and abrupt plunging of asymmetric fault-propagation anticlines suggests slip and lateral propagation of these faults were contemporaneous and the faults transferred slip to one another, creating a compressional relay array. The dominance of ENE-dipping, moderate-angle reverse faults such as the HF, NFF, WA, and the Bellvue and Douglass Lake Faults suggests Laramide compression generated neofomed faults by top-to-the-west, out-of-the-basin flexural shear within the upper crust.

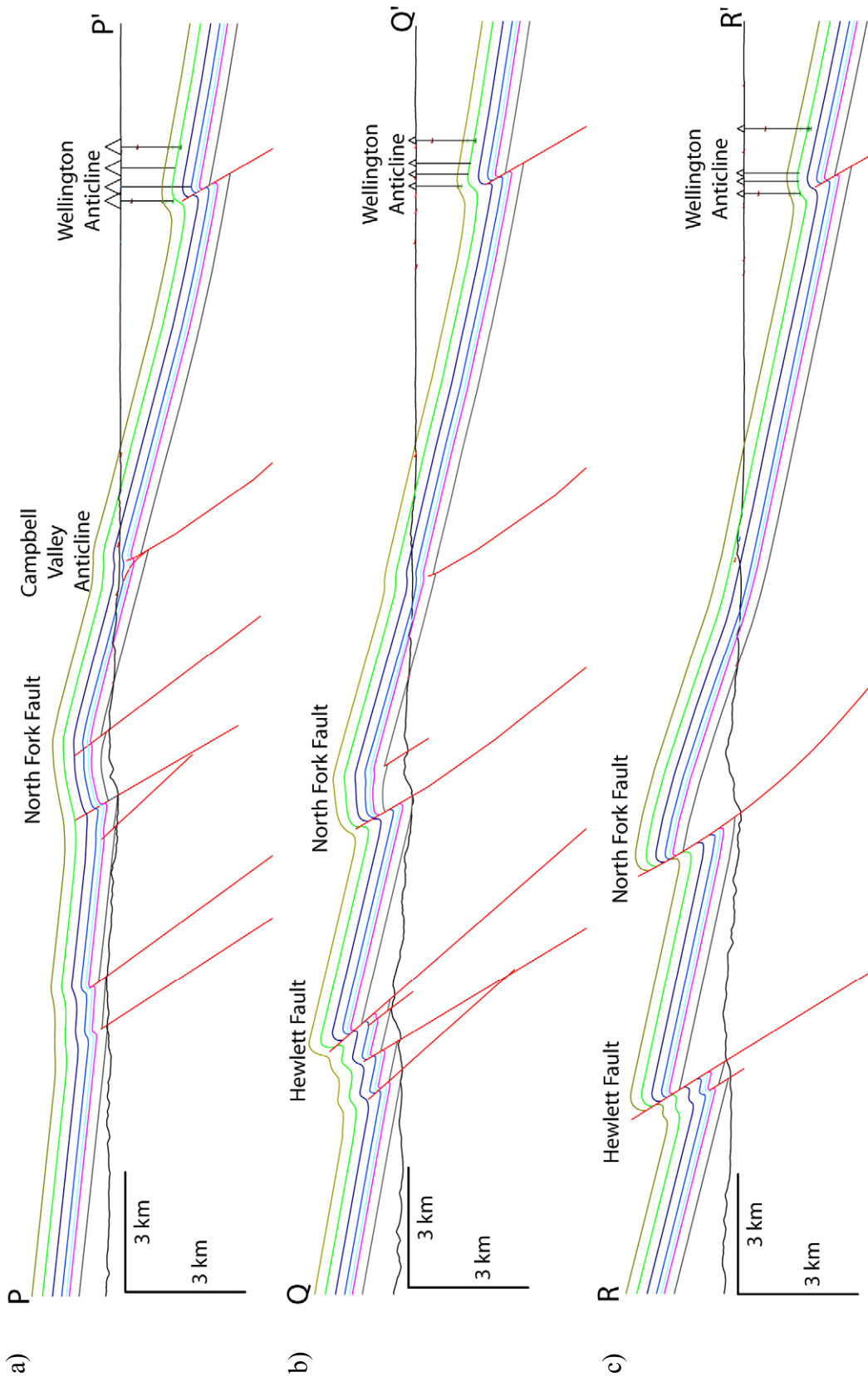


Fig. 6.8. Cross Sections P-P', Q-Q', and S-S' (a-c) showing interpreted 2D geometries based on surface and well data.

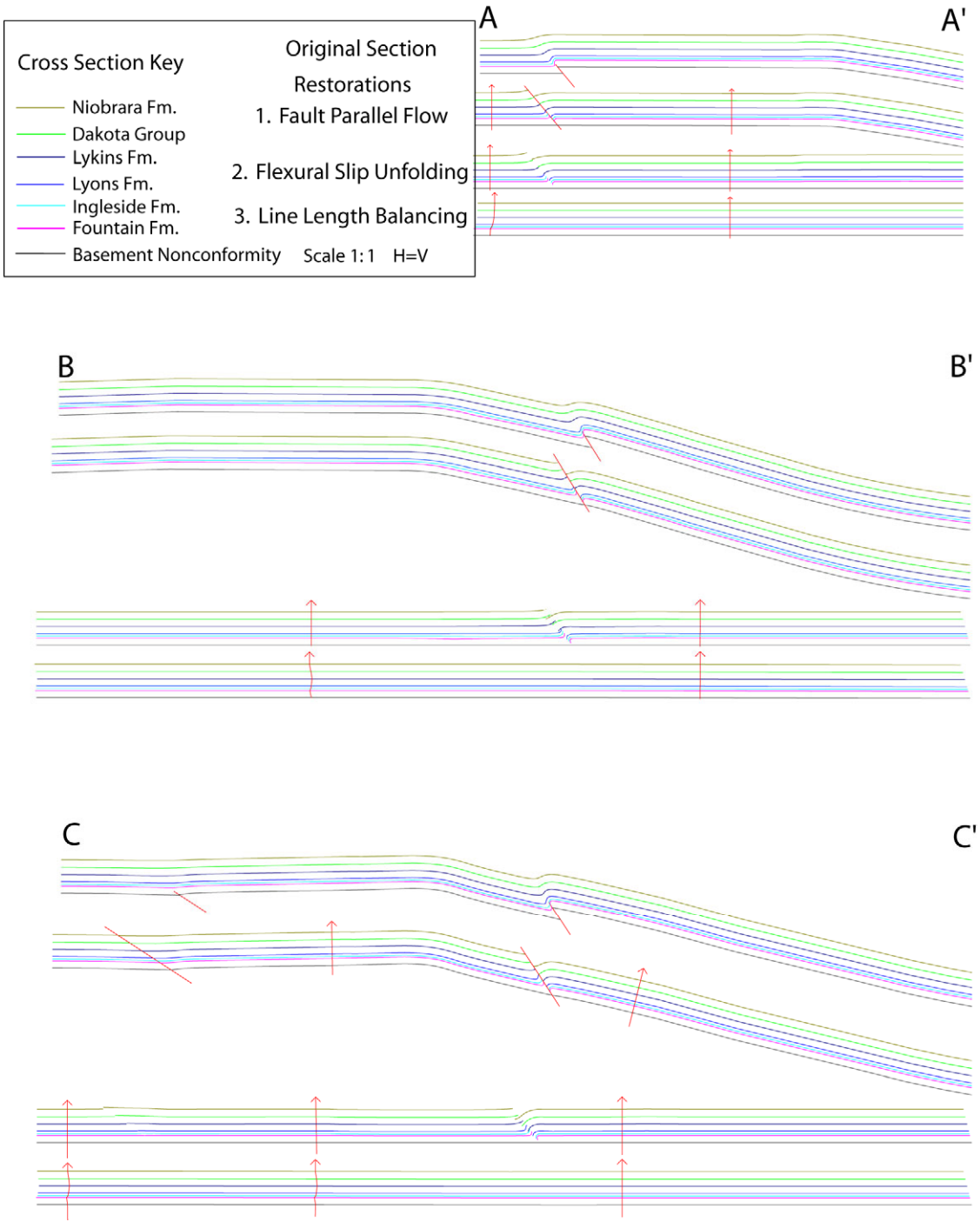


Fig. 6.9. Restorations of cross sections A-C using fault parallel flow, flexural slip unfolding, and line length balancing. Red arrows are pin lines and faults are projected up dip to split fault blocks.

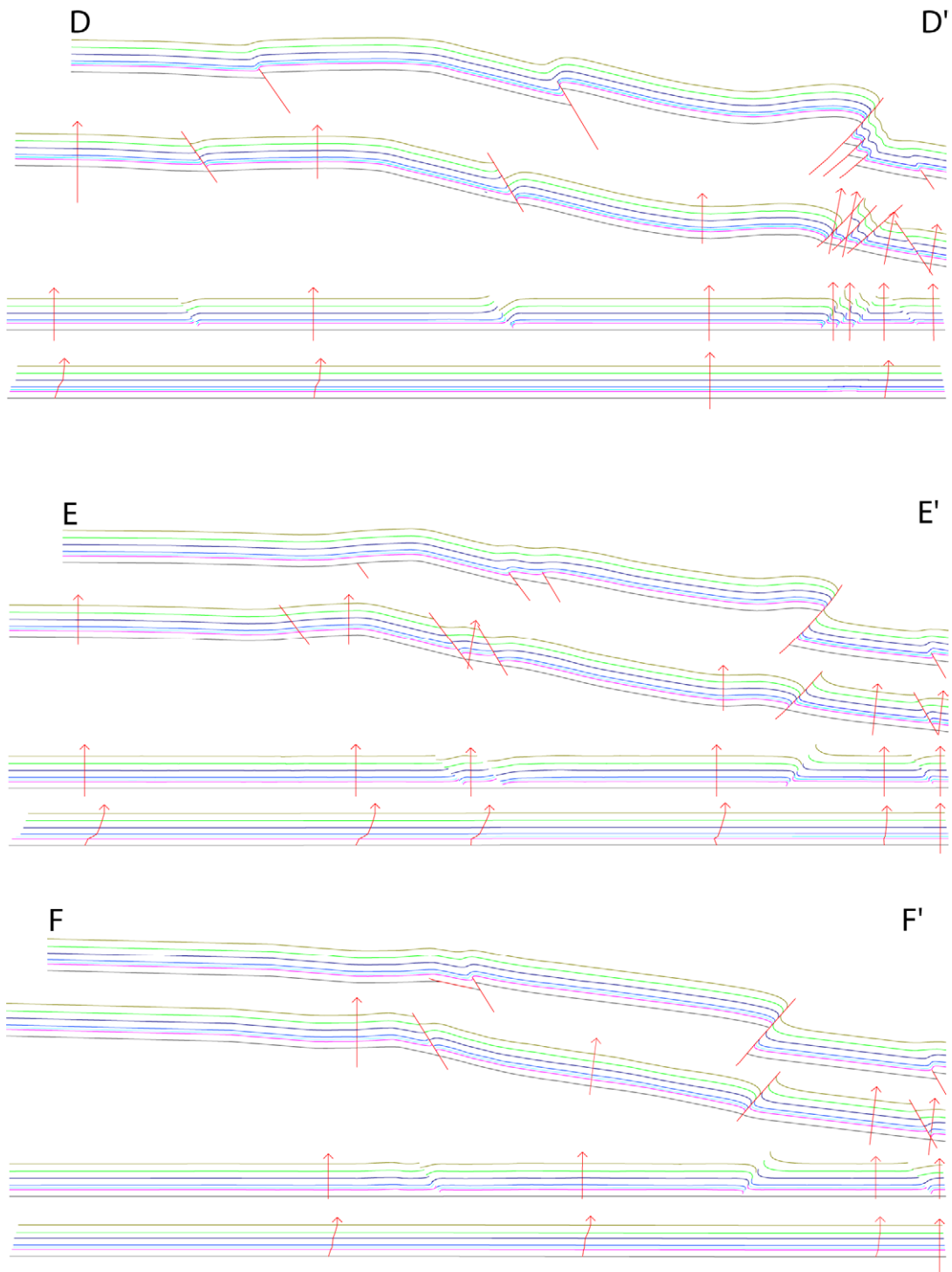


Fig. 6.10. Restorations of cross sections D-F using fault parallel flow, flexural slip unfolding, and line length balancing. Red arrows are pin lines and faults are projected up dip to split fault blocks.

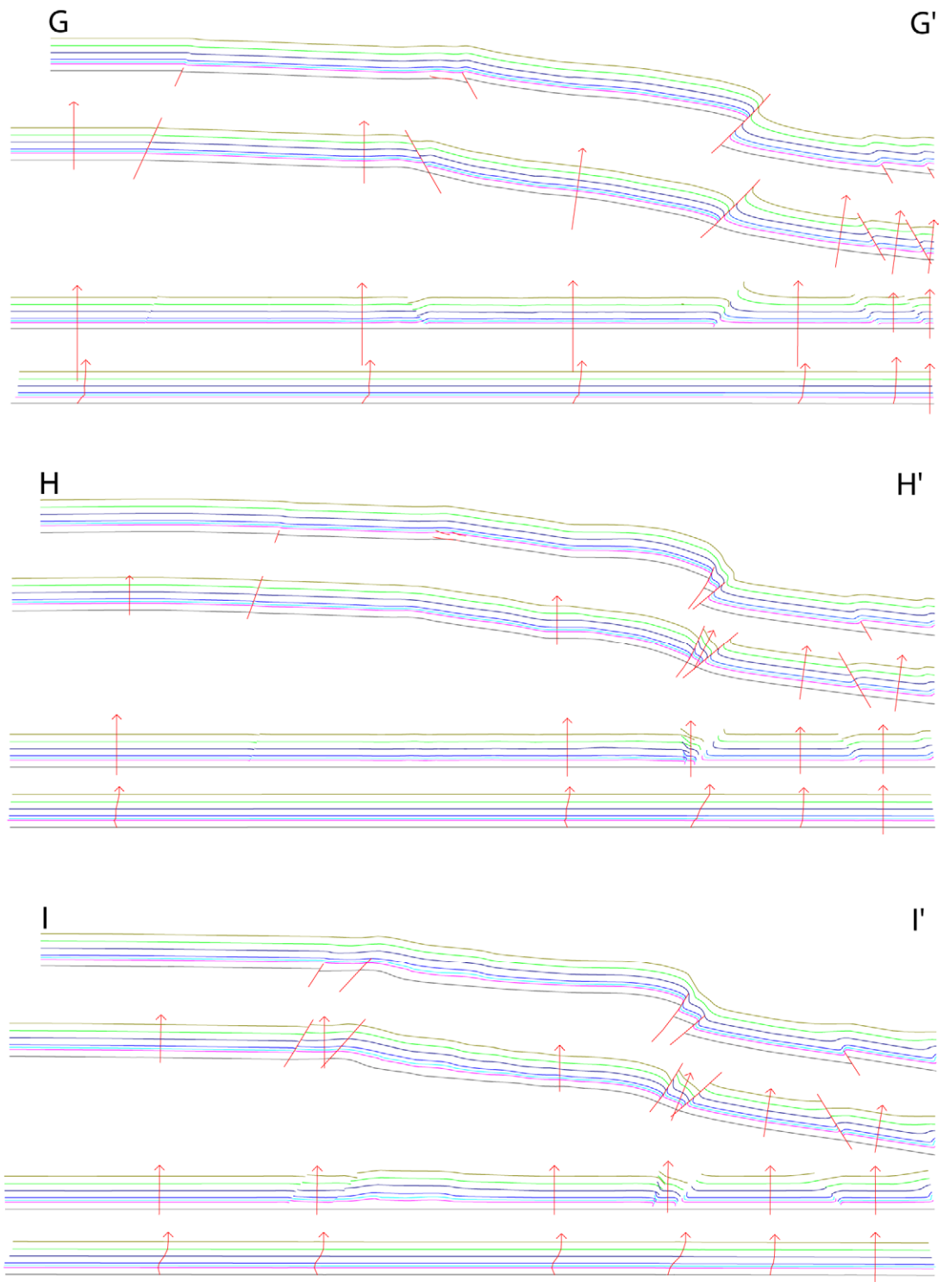


Fig. 6.11. Restorations of cross sections G-I using fault parallel flow, flexural slip unfolding, and line length balancing. Red arrows are pin lines and faults are projected up dip to split fault blocks.

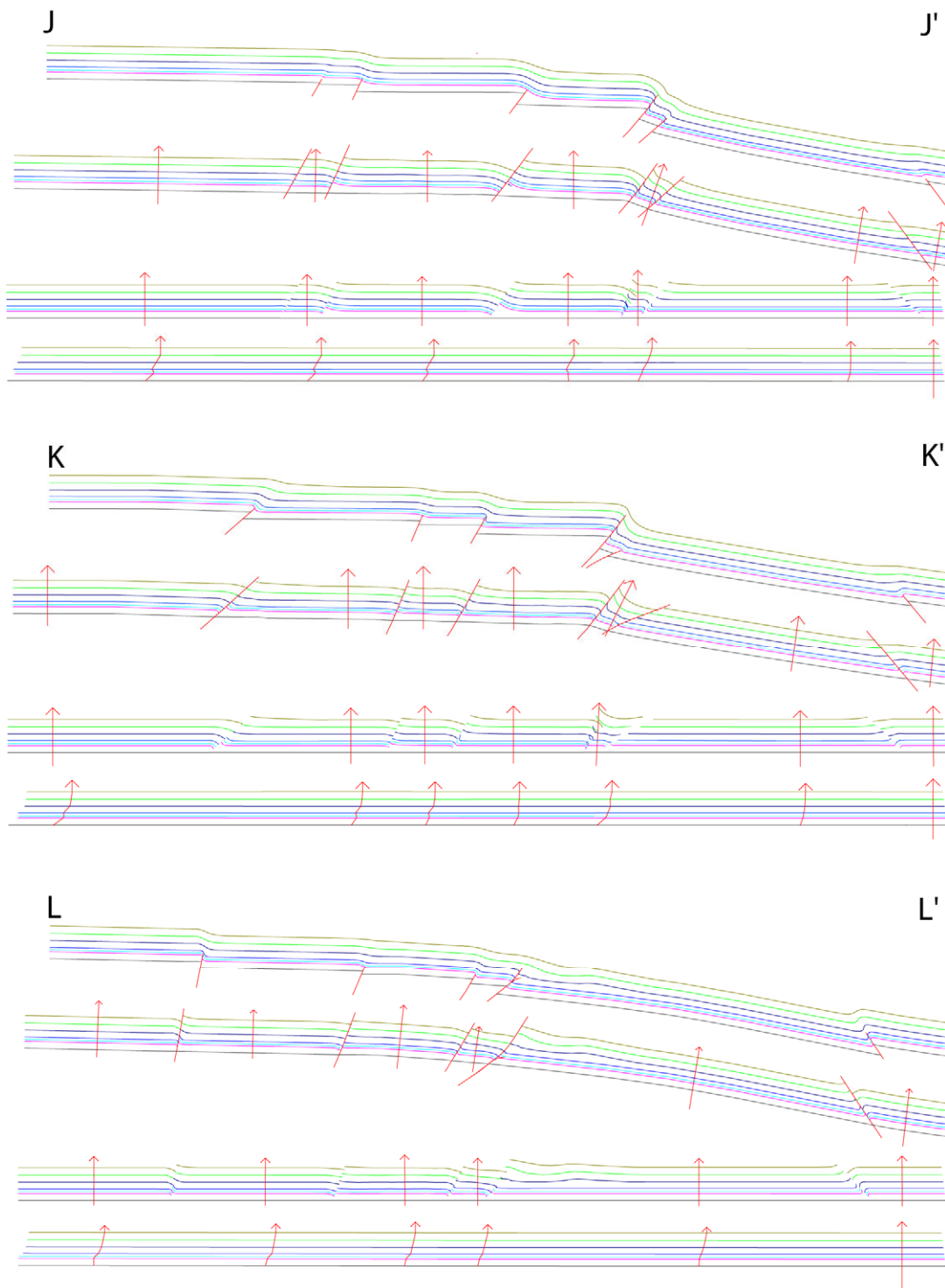


Fig. 6.12. Restorations of cross sections J-L using fault parallel flow, flexural slip unfolding, and line length balancing. Red arrows are pin lines and faults are projected up dip to split fault blocks.

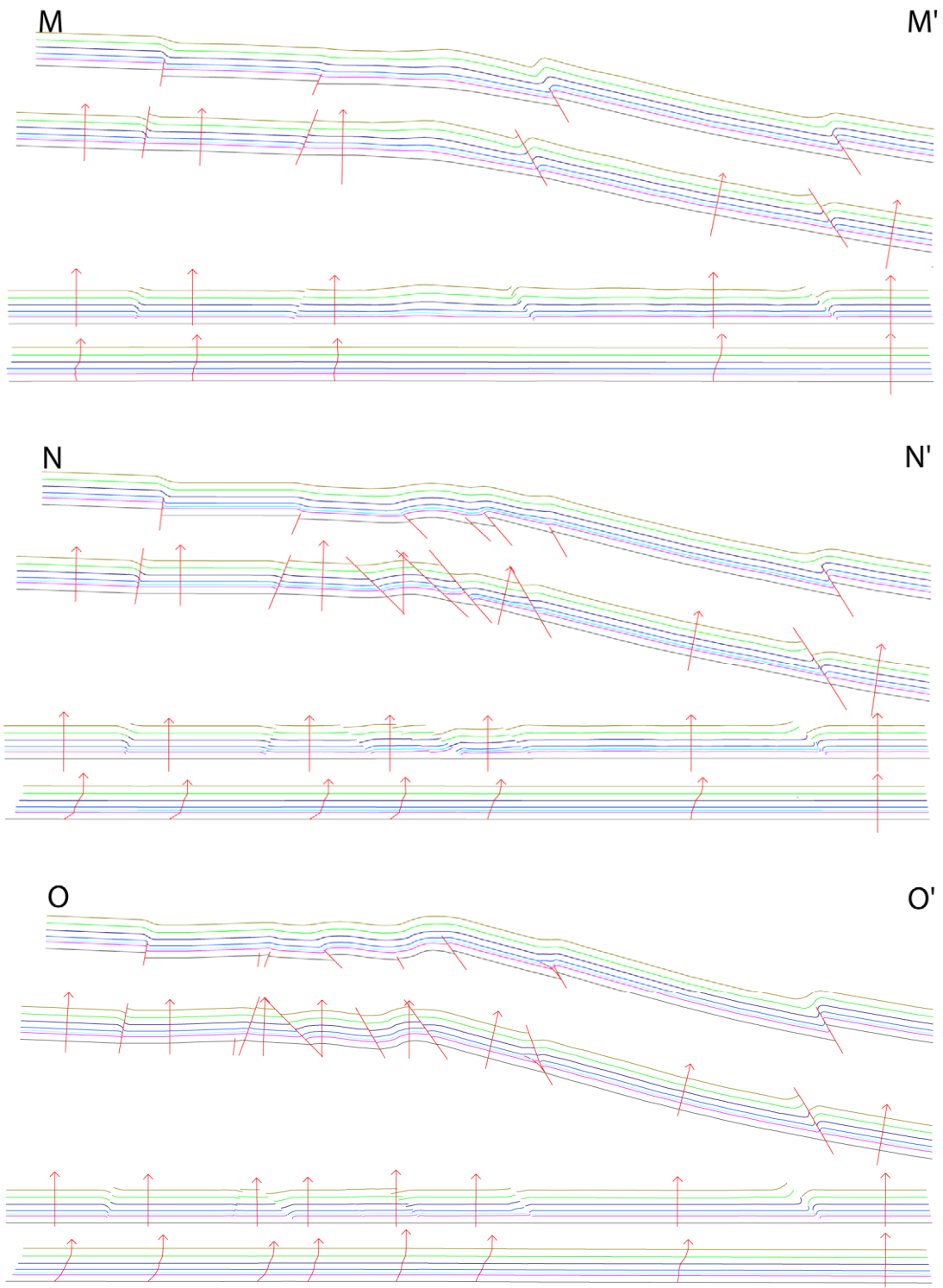


Fig. 6.13. Restorations of cross sections M-O using fault parallel flow, flexural slip unfolding, and line length balancing. Red arrows are pin lines and faults are projected up dip to split fault blocks.

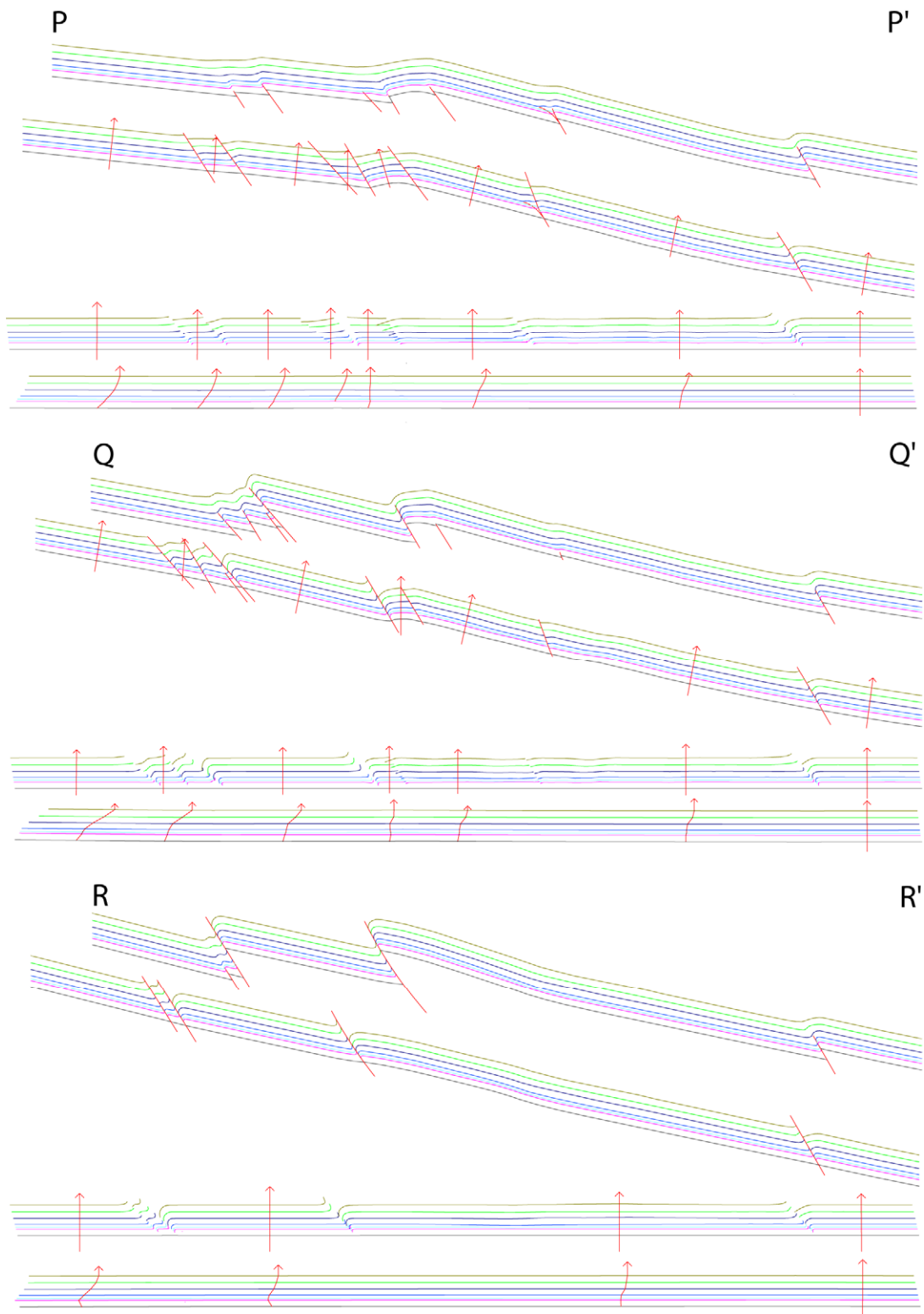


Fig. 6.14. Restorations of cross sections P-R using fault parallel flow, flexural slip unfolding, and line length balancing. Red arrows are pin lines and faults are projected up dip to split fault blocks.

Conclusions

- 1) Laramide compression resulted in the east-northeastward translation of basement blocks by oblique right-lateral / reverse slip on pre-existing NE- and E-striking, high-angle faults. The Livermore Embayment is a structural trough due to the local dominance of strike-slip limiting crustal thickening by reverse faulting.
- 2) Oblique reverse slip on steeply-dipping, planar faults abruptly die out into overlying strata forming asymmetric, cylindrical folds with smoothly rounded fold hinges and abrupt changes in formation thicknesses. This suggests trishear fault-propagation-folding occurs in transpressional monoclines where material is flowing in and out of the plane parallel to the regional direction of slip.
- 3) Fault-parallel-flow restorations are unable to restore the Pennsylvanian nonconformity to a planar, subhorizontal attitude. Regionally consistent eastward dips of the nonconformity have been hypothesized to be due to the insertion of a lower crustal wedge at depth (Erslev et al., 2004a). However short wavelength folding of the nonconformity suggests the basement is accommodating some shortening. This could be due to compressional bends in sinuous oblique- and strike-slip faults, basement buckling of hangingwall blocks and trishear folding of the basement during fault propagation.
- 4) The consistency of shear pins reclined to the east during line-length restorations suggests top-to-the-west, out-of-the-basin flexural shear. Irregularly-shaped shear

pins created by line-length restorations may be due to invalid structural interpretations or trishear fault-propagation-folding which elongates line lengths of lower strata while shortening the line lengths of higher beds. The latter hypothesis is favored as 2D interpretations required abrupt thickening and thinning of shale-rich units to honor formation contacts, thicknesses and bedding attitudes. This suggests 2D area balancing of cross sections using trishear restoration should supersede any constraints imposed by line-length balancing of sections through basement-involved structures.

- 5) The abrupt plunging of N-trending folds where *en echelon* and relay arrays overlap each other suggest the faults coring these folds were formed contemporaneously and transferred slip from one another. The plunging of oppositely-vergent folds towards one another suggests slip can be transferred across both synthetic and antithetic reverse faults.

Chapter 7

Three-Dimensional Structural Interpretations and Analyses

Motivations for 3D Structural Interpretations and Analyses

The kinematic analysis of minor faults suggests the Livermore Embayment was formed by horizontally-driven basement blocks during a single-stage of unidirectional Laramide compression. The three-dimensionality of 2nd order structures motivated the creation of a 3D model to constrain structural interpretations between 2D cross sections (Figs. 7.1-7.5). 3DMove provides a suite of tools for the visualization and analysis of structural restorations of 3D models, the quantification of regional shortening and the interaction and compatibility of faults and basement blocks.

Methods of 3D Model Construction

A three dimensional model was constructed in 3DMove (MVE, 2006b) using the linear algorithm to create surfaces by linking formation lines from 2D cross sections. 3DMove has numerous tools for creating and editing surfaces to honor structural features which may exist between section planes. Surfaces were created in a patchwork fashion to accommodate along-strike structural terminations within the 3D model. Supplemental cross sections were drawn to create realistic surfaces for the model near the complex intersections of multiple faults. Fault and formation top surfaces were also projected in 3D Move for short distances (<200 m) beyond 2D cross sections to eliminate unrealistic gaps at surface boundaries.

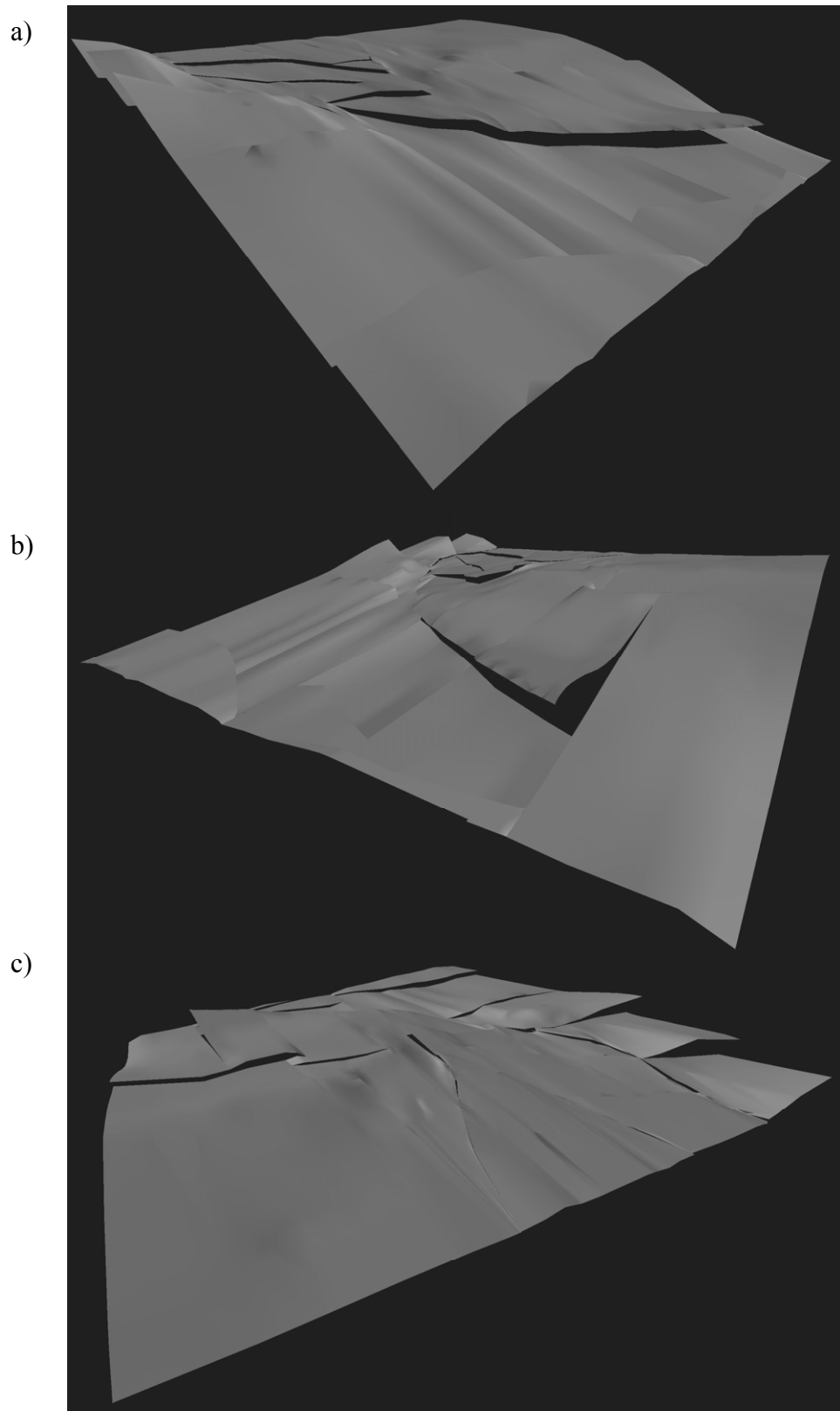


Fig. 7.1. Perspective point views of the modeled surfaces of the Pennsylvanian nonconformity looking to the: a) NW, b) SW, and c) SE. Modeled area is approximately 32 km N to S and 32 km W to E.

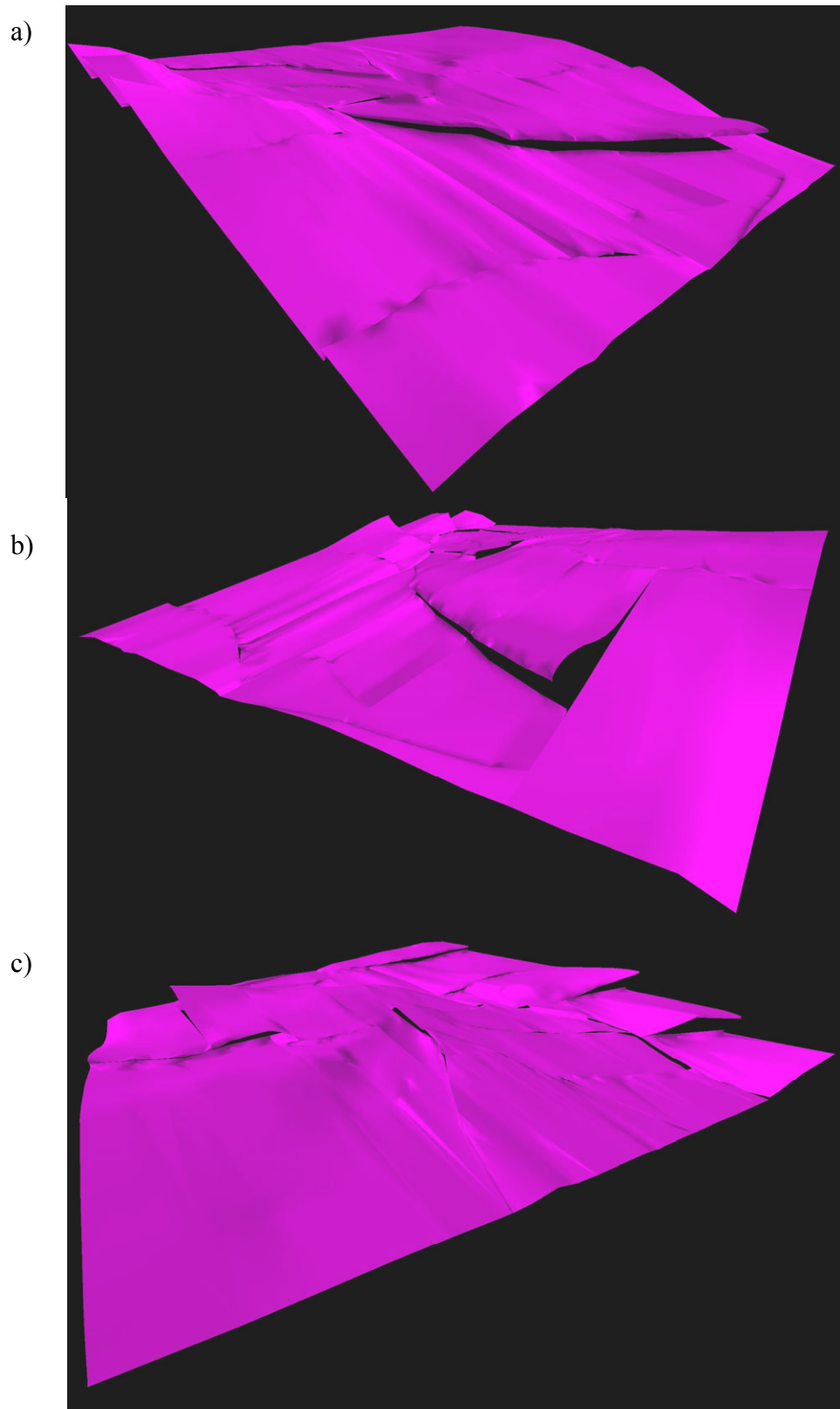


Fig. 7.2. Perspective point views of the modeled surfaces of the Pennsylvania Fountain Formation looking to the: a) NW, b) SW, and c) SE. Modeled area is approximately 32 km N to S and 32 km W to E.

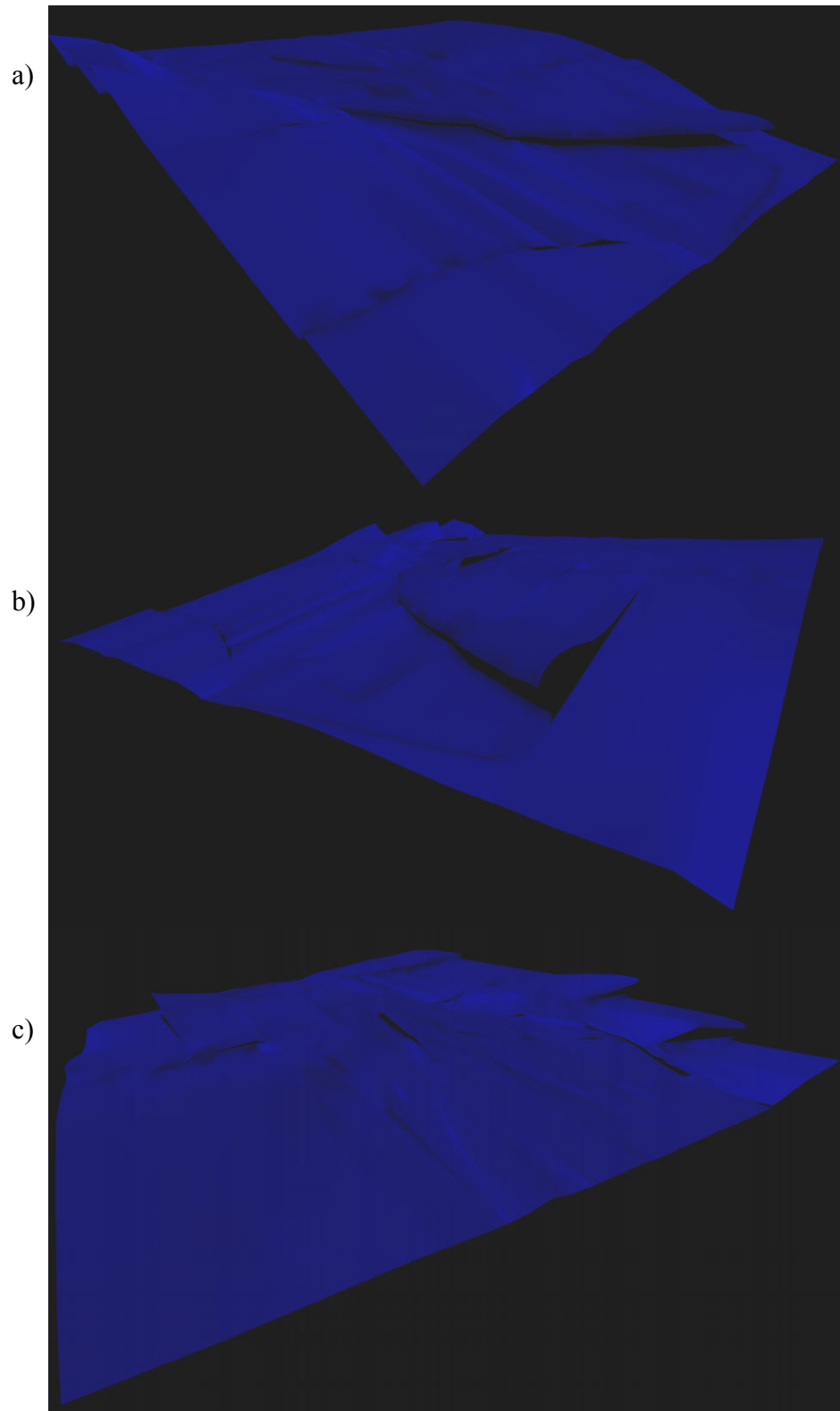


Fig. 7.3. Perspective point views of the modeled surfaces of the Permian-Triassic Lykins Formation looking to the: a) NW, b) SW, and c) SE. Modeled area is approximately 32 km N to S and 32 km W to E.

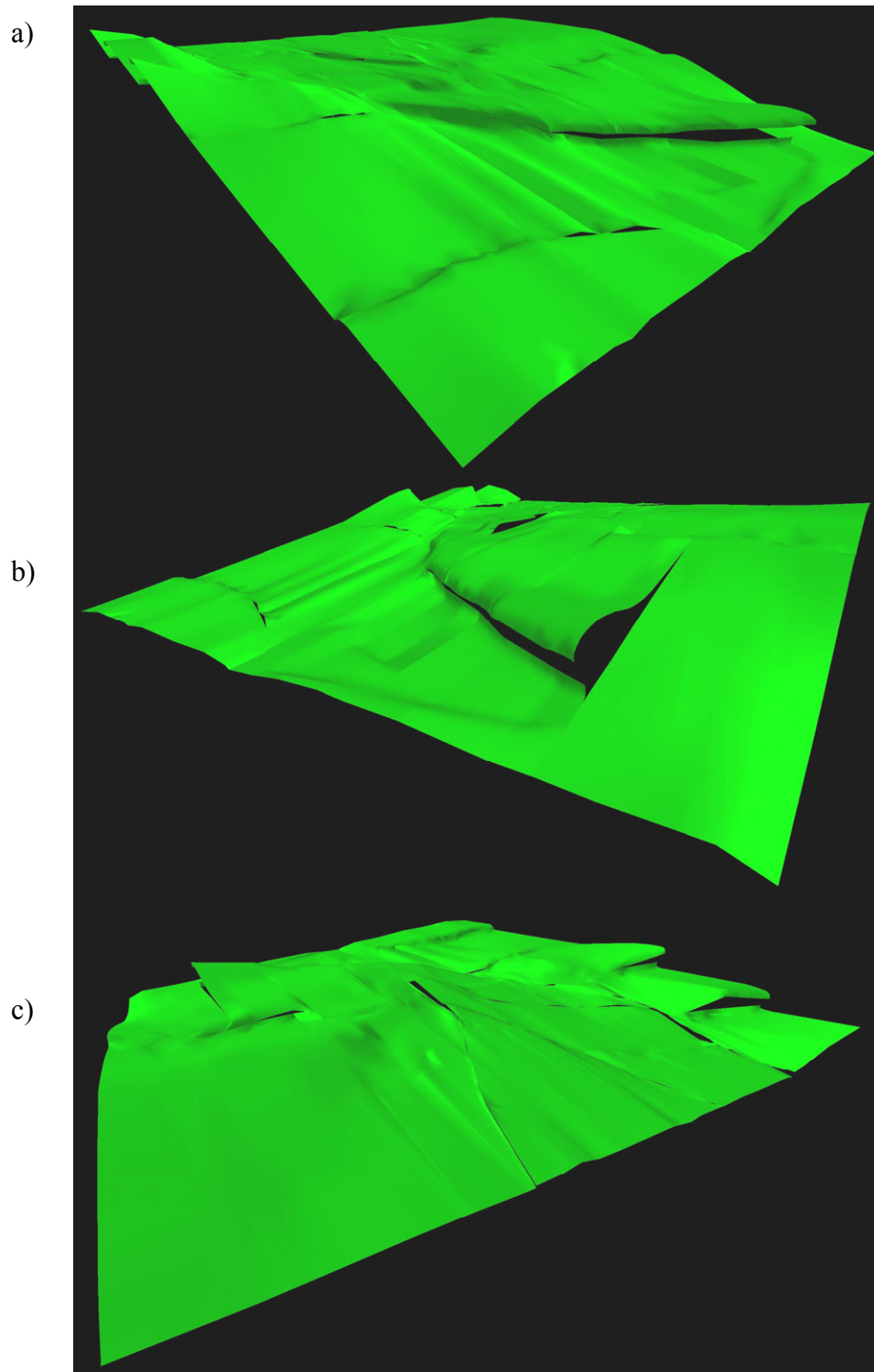


Fig. 7.4. Perspective point views of the modeled surfaces of the Cretaceous Dakota Group looking to the: a) NW, b) SW, and c) SE. Modeled area is approximately 32 km N to S and 32 km W to E.

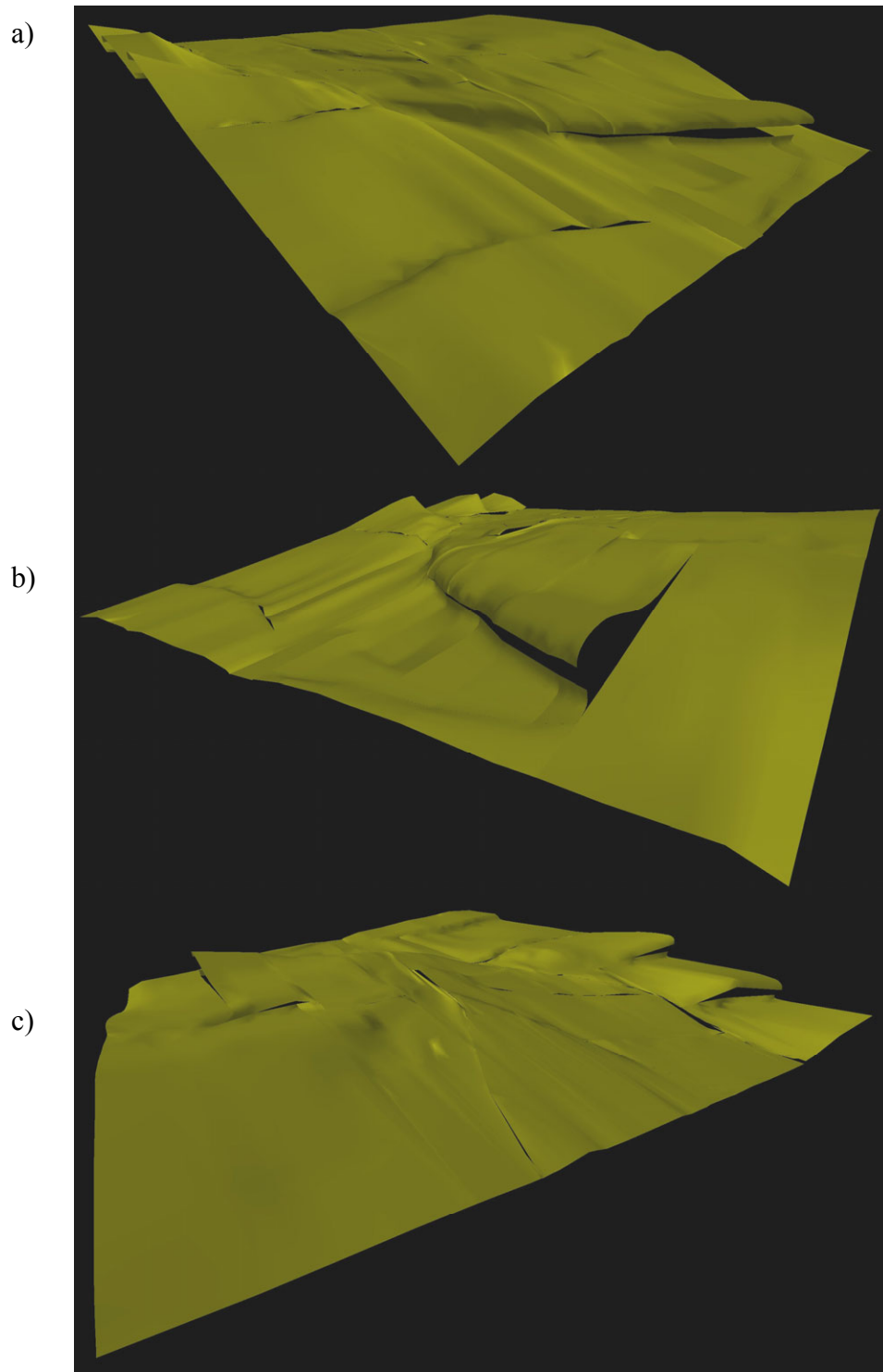


Fig. 7.5. Perspective point views of the modeled surfaces of the Cretaceous Niobrara Formation looking to the: a) NW, b) SW, and c) SE. Modeled area is approximately 32 km N to S and 32 km W to E.

Observations

Structure contour maps for the top of the Muddy (J) Fm. suggest the Pennsylvanian nonconformity in the western Denver Basin and the southeastern Laramie Arch is subplanar with homoclinal dips of 14° E (Barlow and Haun, 1992). Northward into Wyoming, the nonconformity's dip increases as the exposure of the Laramie thrust along the Middle Fork of Crow Creek is approached (Barlow and Haun, 1992, Love and Christiansen, 1985). In the northeastern portion of the modeled area, the nonconformity is tilted, dipping at 11° to 14° E. However in the northwestern portion the nonconformity is subplanar where preserved in the footwall of the Dale Creek Fault. The southward plunge of the Laramie Range Arch is evident by the presence of the lower Fountain Fm. in the Red Mountain Embayment. The 3D geometries of deeply-eroded structures in the western portion of the northern domain were constrained by geologic map and bedding data (Braddock et al., 1989b, Courtwright and Braddock, 1989).

The doubly-plunging, W-vergent Sand Creek (SCA) and Ackerman anticlines (AA) are exposed at multiple levels and have structural culminations on the N-trending segments of the folds (Courtwright and Braddock, 1989). The 3D geometries of the SCA and AA are constrained by geologic map and bedding data and 2D modeling (Courtwright and Braddock, 1989). The Rawhide Anticline (RA) and Meadow Springs Anticline (MSA), two NNE-trending, doubly-plunging W-vergent anticlines are further to the east. Although the structures are not evident from geologic maps, the geometries of the RA and MSA are constrained by well and 2D seismic data, as well as a structure contour map created from a depth conversion of a 3D seismic data volume of the MSA

(Mollerstuen, 2006). A structure contour map made from 2D seismic data suggests the RA terminates to the south against the Halligan Reservoir Fault (Mollerstuen, 2006).

The hangingwall and footwall geometries of the Round Butte Thrust (RBT) are constrained by proprietary W-, and NW- trending seismic lines courtesy of Stan Mollerstuen (2006), and abundant public well data (COGCC, 2006). The abrupt termination of the NE-trending, doubly-plunging Round Butte Anticline is constrained by the Warren Livestock #1 and Spottlewood Creek # 1-30 wells as the top of the Muddy Fm. drops 1342 m (4406 ft) in elevation over a distance of 2400 m (7900 ft). The Round Butte Anticline plunges along strike to the SW and the structure's geometry changes to the ESE-vergent Horseshoe Monocline. Well and seismic data suggest the nonconformity in the footwall dips 15° E near the RBT but shallows to 7° E immediately to the east.

The 3D geometries of central portion of the modeled area, encompassing the Livermore Embayment, are constrained by published USGS geologic maps (Braddock et al., 1988b, d; 1989b), bedding data and 2D balancing, with the exception of the poorly-exposed Wellington Anticline (WA). The 3D geometry of the WA is constrained by well data, structure contour maps of the Hygiene sandstone, and bedding data (Scott and Cobban, 1978). Structure contour mapping of 2D seismic data suggest the WA terminates to the north against the Halligan Reservoir Fault in the western Denver Basin.

To the west, isolated subplanar surfaces capped by outcrops of the lower Fountain Fm. are present upon the basement blocks bound by the Halligan Reservoir, Stonewall, North Rabbit, the North and West Livermore and Livermore faults (Braddock et al., 1988a-d). These subplanar, shallowly E-dipping surfaces were used to provide a minimum elevation of the nonconformity prior to post-Laramide erosion. The 3D

geometries of these deeply-eroded, NE- and E-trending monoclines and the reverse faults which core them were constrained by published USGS geologic maps (Scott and Cobban, 1978, Braddock et al., 1988a-d), bedding and fault attitude data, and 2D modeling using geometric formulas for restorable fault-bend folds (Erslev, 1986).

The 3D geometries of the asymmetric W-vergent anticlines and ENE-dipping reverse faults in the southern study area are constrained by USGS mapping (Scott and Cobban, 1978, Braddock et al., 1988a-d), fault attitude data (Erslev and Rogers, 1993), public well data and bedding data (COGCC, 2006) and 2D modeling (Holdaway, 1998).

Structural Interpretations

Southern Laramie Range and Western Denver Basin

The increasing dip of the Pennsylvanian nonconformity to the north and along the strike of the Laramie Range Arch is likely due to basement folding above a W-dipping listric thrust. The southward plunge of the Laramie Range Arch and the termination of this arch-bounding thrust appear to be due to the transfer of slip to the E-dipping Never Summer Thrust on the W flank of the Front Range / Laramie Range Arch (O'Neill, 1981). Although these N-striking thrusts do not overlap one another at the surface, the continuity of fault-related folding and the Laramie Range Arch suggests the thrusts share a lower-crustal detachment and overlap at mid-crustal depths.

Northern Domain

The homoclinal dips of 14 to 16° E of the Pennsylvanian nonconformity and overlying strata and the formation of the E-dipping reverse faults which core W-vergent, asymmetric Sand Creek and Ackerman anticlines, are likely backlimb tightening structures (BLTs) (Holdaway, 1998; Stanton and Erslev, 2004; Erslev et al., 2004a). The

BLT hypothesis suggests the consistent regional dip in the backlimb of the Front Range Arch is due to rotational fault-bend folding of the Pennsylvanian nonconformity above an eastwardly translated lower crustal wedge, bound by a subhorizontal detachment and an E-dipping listric thrust (Holdaway, 1998; Stanton and Erslev, 2004; Erslev et al., 2004a) (Fig. 7.6a, b). Fault-parallel flow restorations of the top of the Precambrian in cross sections through BLT structures cannot restore the basement to its original horizontality, requiring external deformation and rejecting hypotheses of these 2nd order structures as cored by backthrusts above a W-dipping, mid-crustal detachment (Holdaway, 1998;

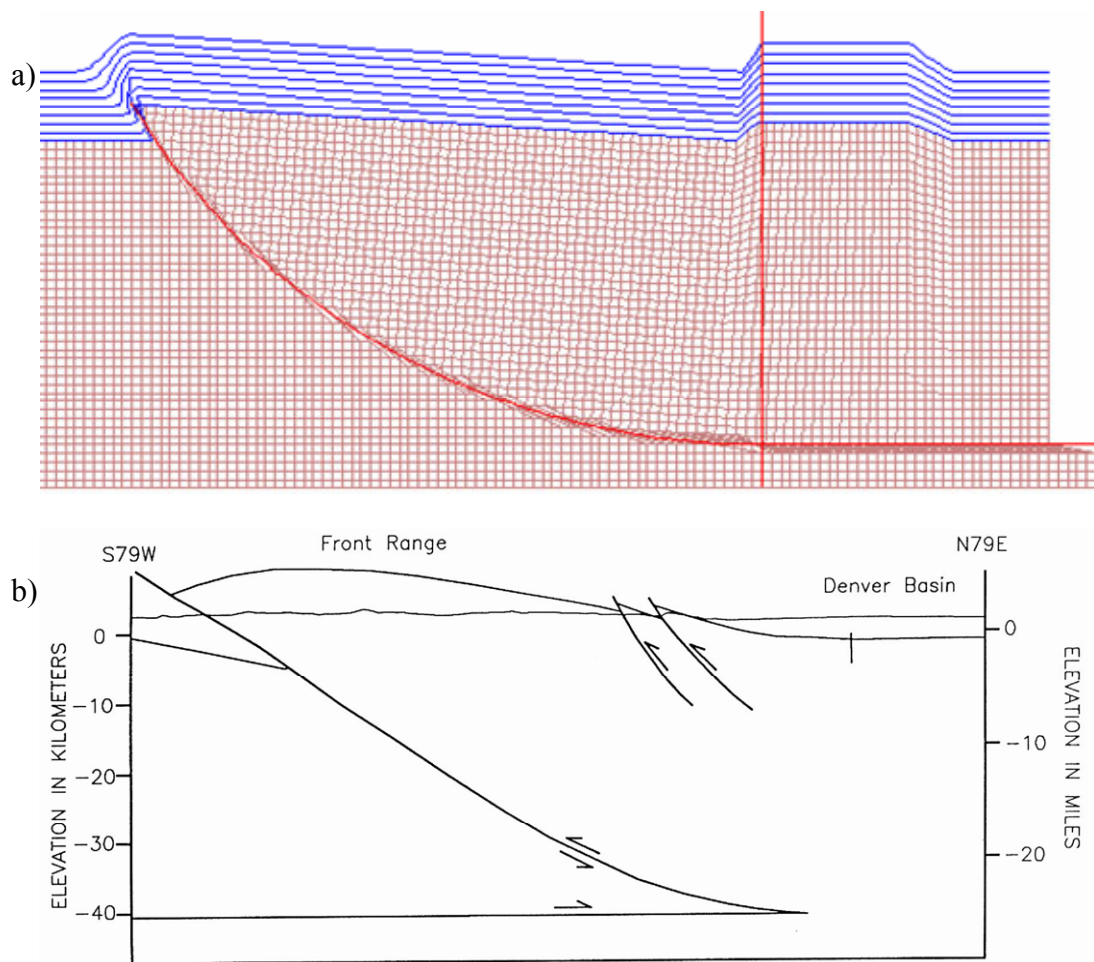


Fig. 7.6. 2D models modified from a) Stanton and Erslev (2004) and b) Holdaway (1998) of backlimb tightening (BLT) structures above listric thrusts.

Erslev et al., 2004a). Line-length restoration of cross sections through BLT structures suggests top-to-the-west, out-of-the-basin flexural shear within the Phanerozoic stratigraphy and the Precambrian basement explains why these 2nd-order, reverse faults are generally synthetic to the 1st-order, arch-bounding thrust (Holdaway, 1998). 2D modeling predicts a W to E progression of the formation the growth of BLT structures in the northeastern Front Range (Stanton and Erslev, 2004). The mechanisms driving the formation of BLT structures and their relative timing has important implications for the modeled area as the opposing dip directions of the faults coring the Sand Creek and Ackerman anticlines and the Round Butte Thrust prohibits simultaneous slip on both E- and W-dipping structures and requires a two stage model of deformation (Fig 6.4).

Two stage models of deformation within BLT zones have been proposed by Erslev and Selvig (1997) and Stanton and Erslev (2004) (Fig. 7.7a, b). These models propose that early-stage, synthetic, out-of-the-basin reverse faults are truncated by late-stage, antithetic, into-the-basin thrusts as out-of-the-basin faults shallow the taper angle of the arch-cored orogenic wedge and hanging wall rotation decreases the shear stress on out-of-the-basin reverse faults (Erslev and Selvig, 1997; Stanton and Erslev, 2004).

The E-dipping reverse faults coring the Sand Creek and Ackerman anticlines are interpreted as early-stage out-of-the-basin reverse faults which were subsequently truncated by the Round Butte Thrust, a late stage, into-the-basin thrust (Fig. 7.7c). This two-stage interpretation is supported by Anderson (1957) fracture mechanics as an early-formed, lower angle fault like the RBT would slip prior to the formation of a reverse fault. The two-stage interpretation is supported by the low amplitudes of the Meadow Springs and Rawhide anticlines which lie immediately east in the footwall of the RBT

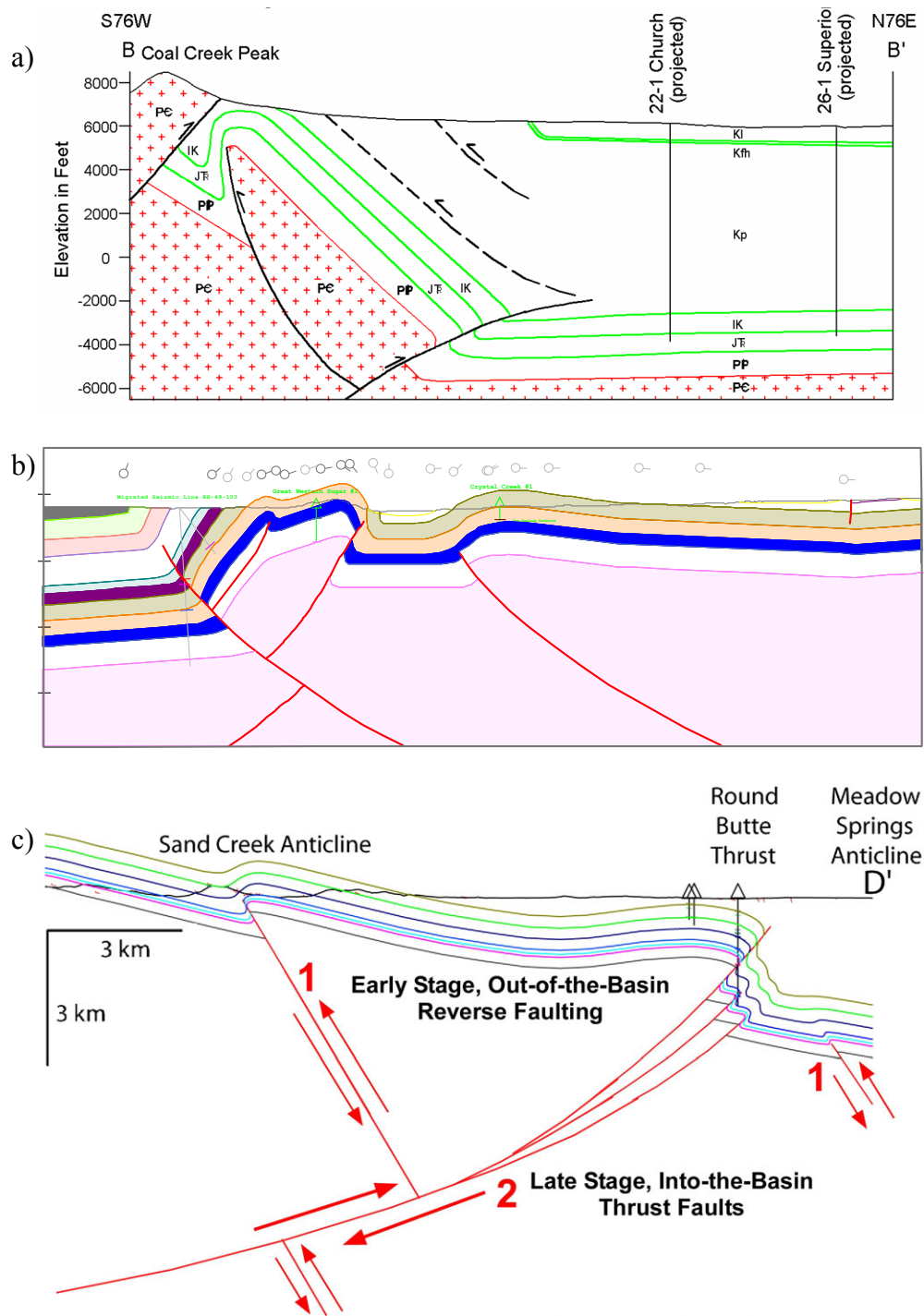


Fig. 7.7. Cross sections through second-order, basement-involved, fault-propagation folds on the flanks of first-order Laramide arches: a) the Golden Fault near Boulder, Colorado (Erslev and Selvig, 1997), b) the Sheep Mountain Anticline near Greybull, Wyoming, (Stanton and Erslev, 2004), and c) the Sand Creek Anticline and Round Butte Thrust near Livermore, Colorado.

near the locus of maximum slip on the RBT. However as slip decreases along the strike of the RBT to the southwest there is a substantial increase in the amount of slip on the Hewlett / Dilky Ranch and North Fork faults and the amplitudes of the Campbell Valley and Wellington anticlines (Figs. 6.4 – 6.8). Despite the evidence for the RBT being a late-stage, into-the-basin thrust, the NE-strike of the structure parallels the regional tectonic fabric, suggesting inheritance exerted some control over the structure.

Data from wells penetrating the Dakota Group provides irrefutable evidence for an anomalously abrupt northern termination of the RBT near the locus of maximum slip (Fig. 7.8). The abrupt termination of the RBT suggests it abutted against an E-striking, left-lateral tear fault, forming a trapdoor structure (Stone, 1969) (Fig. 7.9a, b). The lack of visible left-lateral offsets of strata within the Dakota hogback to the west suggests the hypothesized E-striking, left-lateral tear fault did not propagate that far west at the level of Cretaceous strata. This requires a large loss of slip on the hypothesized left-lateral tear fault, requiring it to extend eastward and/or absorb strain via distributing slip on fault splays, facilitating ductile deformation and detachment of overlying sediments. Although these indirect observations of the Round Butte Trapdoor Structure were inferred, they are also supported by observations from the northern terminus of the Roberts Monocline against the left-lateral Halligan Reservoir Fault (Fig. 4.6). The recognition of this eastward extension of the E-striking, left-lateral tear fault into the Denver Basin illustrates the importance of detailed structural modeling to identify zones of strike-slip faulting. Strike-slip faults can act as conduits for secondary, fracture porosity, or act as lateral permeability barriers, i.e. Jonah Field in the Green River Basin of Wyoming.

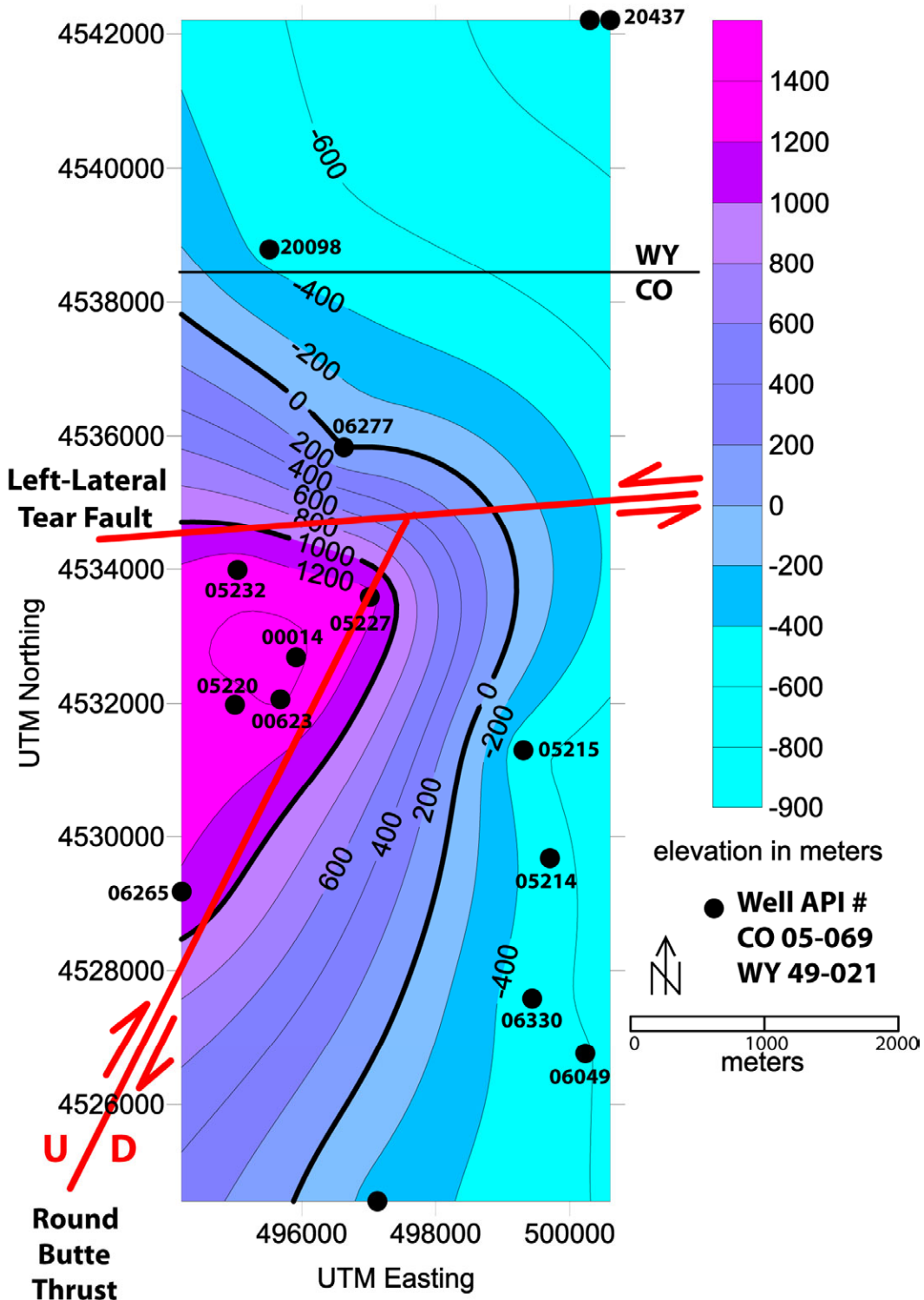


Fig. 7.8. Structure contour map of the top of the Dakota Group made from available well data (COGCC, 2006; WYOGCC, 2006). Location of Round Butte Thrust constrained by well 05227 with repeated sections of upper Paleozoic strata.

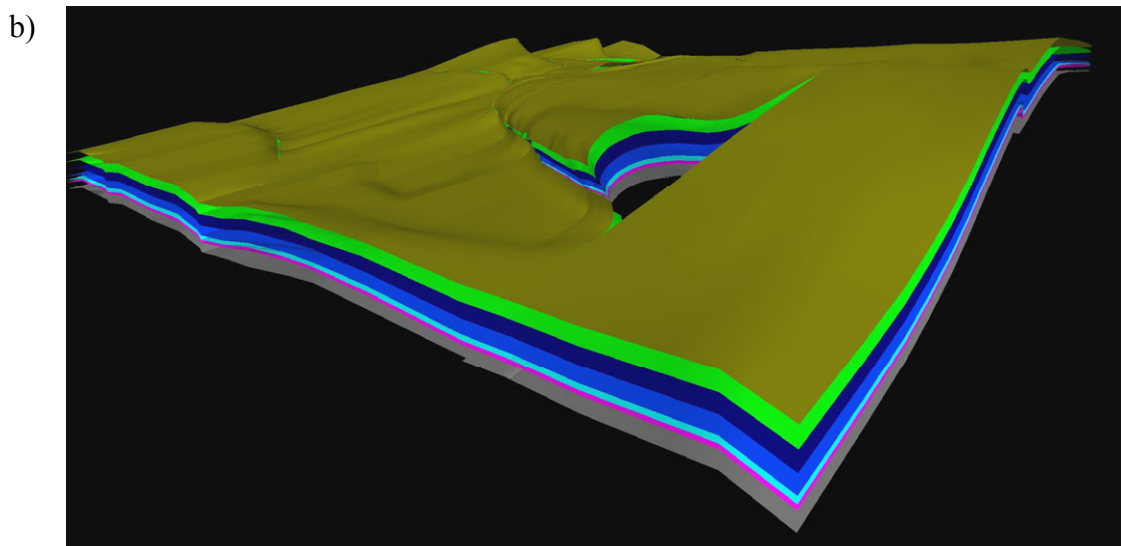
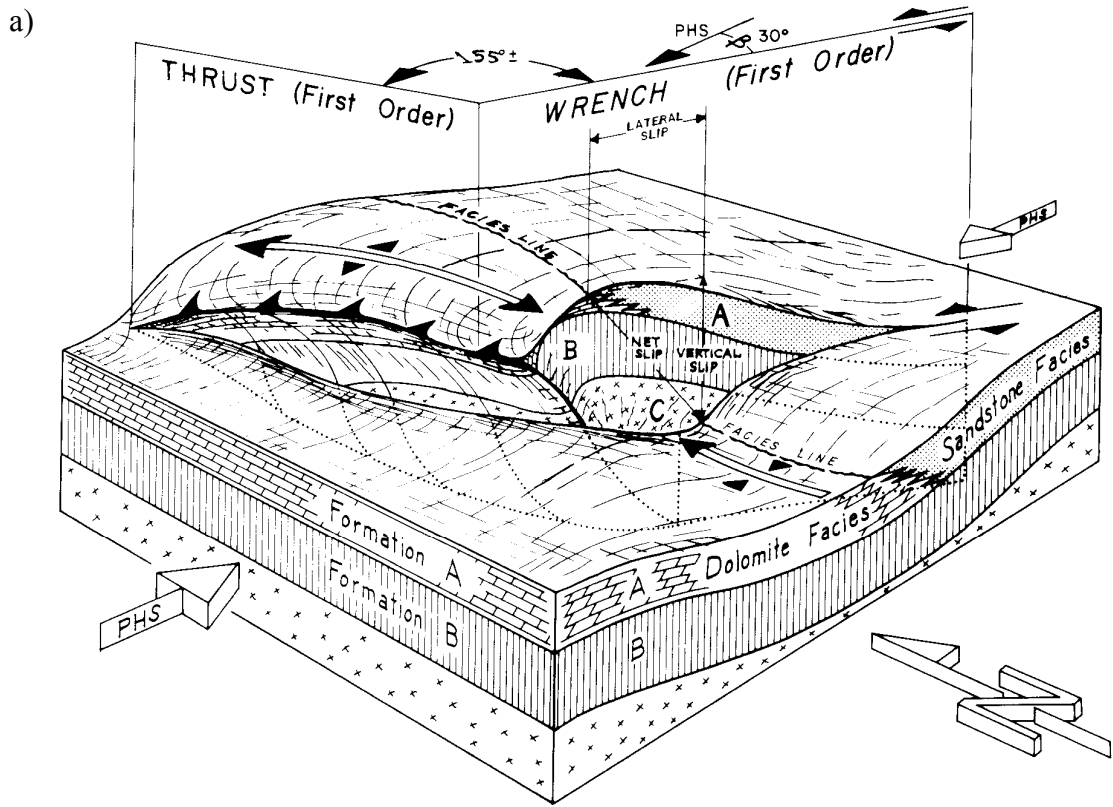


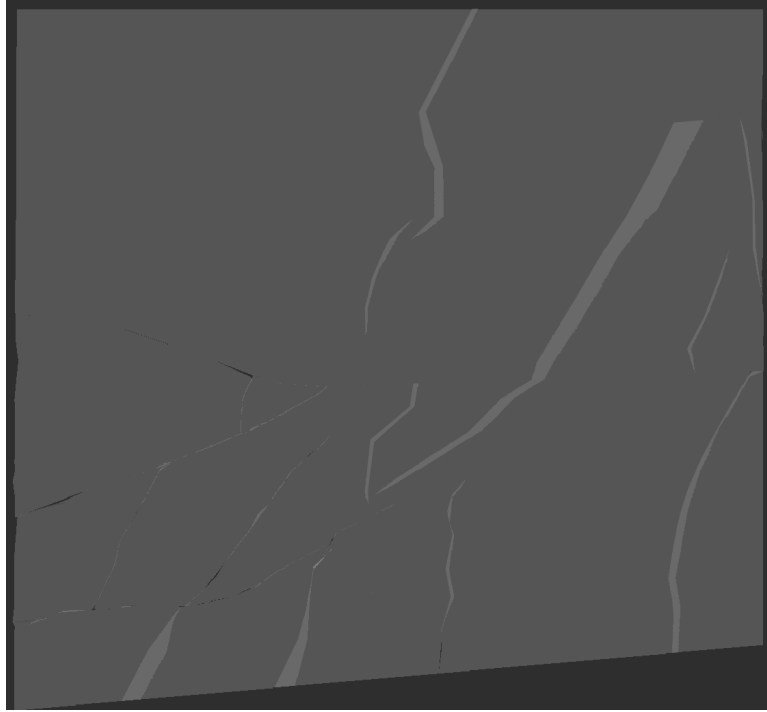
Fig. 7.9. a) A 3D drawing of a trapdoor structure by Stone (1969), and b) the trapdoor structure interpreted for the northern termination of the Round Butte Thrust.

The complex northern terminus of the Round Butte Trapdoor Structure and other complex intersections of multiple structures motivated the “jigsaw” restoration of the basement nonconformity surface within the modeled area. The jigsaw restoration of the basement nonconformity surface was done by flattening the folded surfaces to a uniform elevation using vertical inclined shear and translating the surfaces, parallel to the regional slip direction, to minimize gaps and overlaps in 3D Move (MVE, 2006b) (Fig. 7.10). Despite the ability of software to quantify translation to the meter, the accuracy of jigsaw restorations are limited as they average slip amounts for individual fault blocks and do not capture the small amount of regional shortening accommodated by short-wavelength basement folding. A “translation map” was made by quantifying the net slip of each basement surface with arrow lengths scaled by the amount of translation of each surface, with the southeastern-most basement surface held stationary (Fig. 7.11). The translation map illustrates the regional consistency of translation in the western portion of the modeled area despite the along-strike change in fault trend and geometry (Fig. 7.11).

Central Domain

The northeast-trending monoclines of the Livermore Embayment form a complex transpressional relay system between the Livermore and Halligan Reservoir faults (Fig. 7.12a-d). The oblique orientation of the monoclines relative to Laramide compression is due to the reactivation of pre-existing, Precambrian weaknesses associated with the Skin Gulch Shear Zone within the Livermore Embayment (Abbott, 1976). The presence of weak, high-angle faults and fractured basement resulted in a local dominance of strike-slip faulting and limited crustal thickening on thrust, thus creating a northeast-trending structural embayment. The inability of Laramide compression to

a)



b)

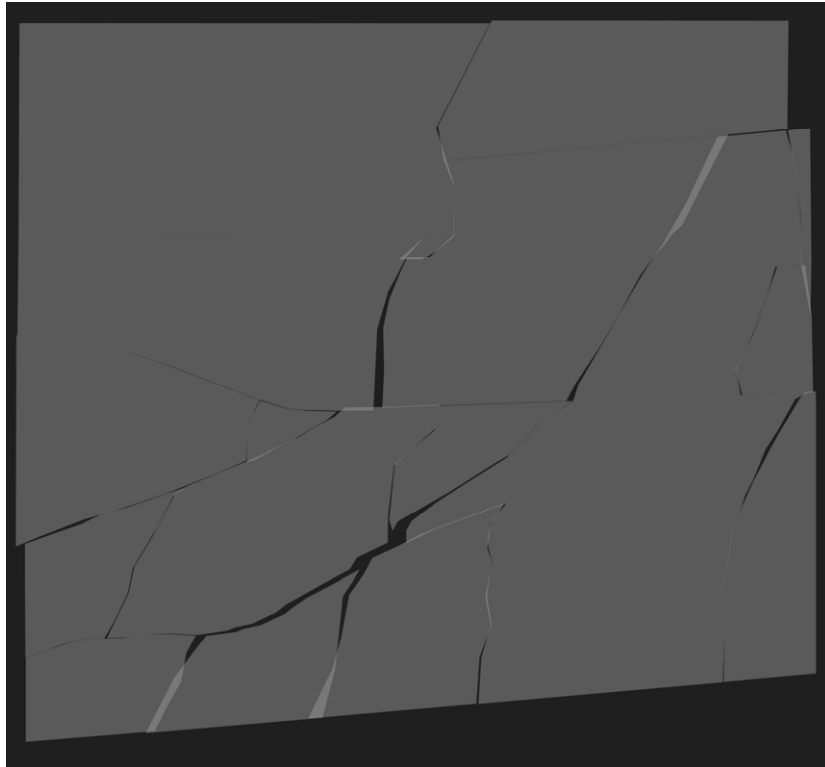


Fig. 7.10. Flattened surfaces of the basement nonconformity with fault heaves a) unrestored and b) restored. Light areas indicate surface overlaps and dark areas between surfaces are gaps.

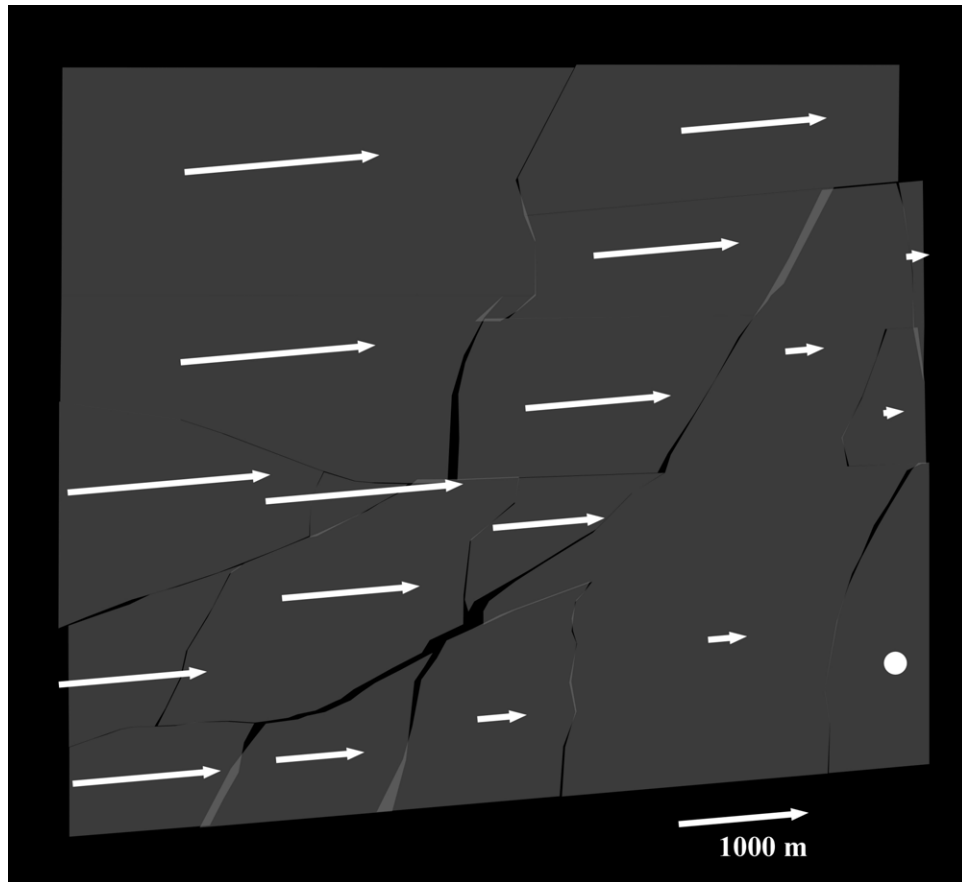


Fig. 7.11. Flattened surfaces of the basement nonconformity with fault heaves restored. Arrow lengths are scaled to amount of ENE translation. Surface with white circle remained stationary.

structurally elevate the fault blocks bound by inherited, subvertical faults resulted in their northeastward translation of distances between 1500 and 2000 m (Fig. 7.11).

The abrupt increase in the slip on the fault coring the Roberts Monocline coincides with the northeastern termination of the Grayback Monocline, suggests that slip was transferred across several transpressional structures. The highly sinuous N-, and NE-trending segments of the fault coring the Roberts Monocline suggests Laramide stress forced the lateral propagation of pre-existing faults (foreground, Fig. 7.12a-d). Local faults may have both inherited Proterozoic and neofomed Laramide segments.

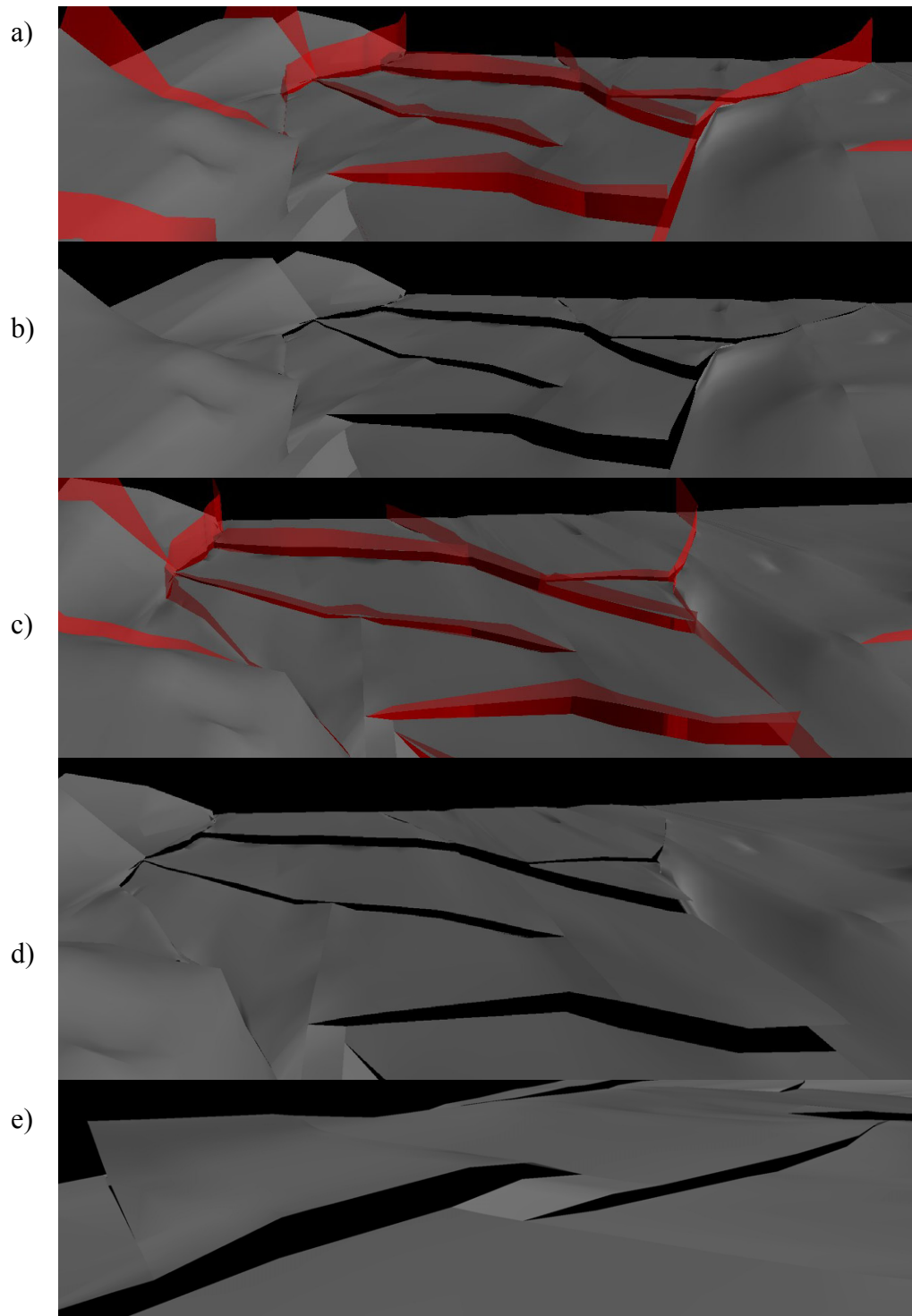


Fig. 7.12. Views of the top of the basement surface with and without faults, looking to the WSW (a, b), and W (c, d) at the right-lateral transpressional structures of the Livermore Embayment. View of the top of the basement surface looking to the SE at (e) the compressional relay ramp between the reverse faults coring the Sand Creek and Ackerman anticlines.

Strain relay was also observed across the reverse faults coring the Ackerman and Sand Creek anticlines (Fig. 7.12e). The subhorizontal to shallow dips of the basement nonconformity in the vicinity of the Livermore Embayment suggests Early Proterozoic structures influenced and/or limited the amount of rotational fault-bend-folding by deep crustal wedging relative to the area immediately south (Holdaway, 1998). The abutting relations of faults within the central domain, as well as field observations, can be used to deduce the relative ages of the faults. The abutment of all major structures against the Livermore Fault and its parallelism to the Skin Gulch Shear Zone suggests the LF dates to the Early Proterozoic (Abbott, 1976). The abutment of all major structures against the Halligan Reservoir Fault, its parallelism to the structural grain of the Proterozoic basement, and the ability to map the HRF as a lineament across the northern Front Range (Tweto, 1979), all imply an Early Proterozoic age of the fault. Observations of extensive fracturing, mylonites and indurated breccias in the hangingwalls of the West and North Livermore faults suggest all NE-trending structures in the area experienced multiple episodes of deformation at different P-T conditions. The highly oblique trend of the West Livermore Fault (WLF) to the Livermore Fault (LF), the presence of a NE-striking fault to the SW and the substantial elevation of the hanging wall of the WLF in such close proximity to the LF requires the interpretation of the WLF crosscutting the LF in the SW corner of the Livermore Embayment.

Southern Domain

The right-stepping, *en echelon* array of ENE-dipping reverse faults and SSE-plunging asymmetric anticlines of the southern domain are interpreted as BLT structures formed during Laramide compression (Holdaway, 1998). The enhanced elevation of the

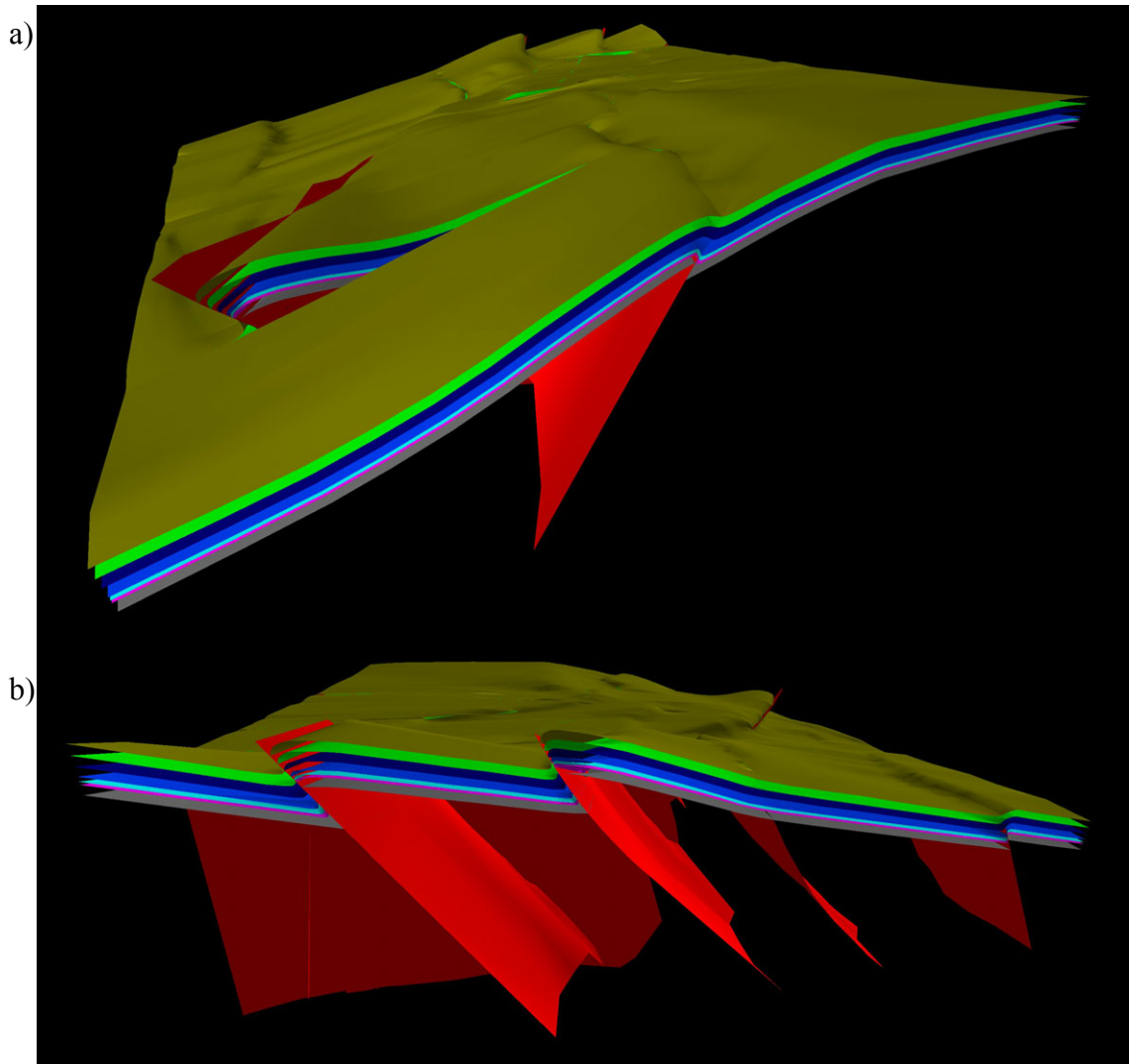


Fig. 7.13. Views of all modeled formation top and fault surfaces looking to a) the SSW and b) the N.

nonconformity to the south coincides with an increasing amount of dip slip on reverse faults as the faults are oriented nearly perpendicular to regional shortening (Holdaway, 1998) (Fig. 7.13). Isolated patches of the Fountain Fm. immediately south of the Livermore Fault and the abutment of the Hewlett / Dilky Ranch and North Fork faults and the fault coring the Campbell Valley Anticline against the Livermore Fault suggest the extensive fracturing adjacent to major pre-existing structures arrested the lateral

propagation and slip of reverse faults. The southward plunge of the Campbell Valley Anticline as slip on the North Fork Fault increases to the south and the structural low within the Wellington Anticline immediately to the east of the Douglass Lake Anticline suggests strain relay occurs across multiple BLT structures in the southern domain.

Interpretations of Orogen Scale Processes

First-order Laramide thrusts likely initiated as ideal conjugate thrusts within relatively coherent crust near the structural culminations of the Medicine Bow, Laramie Range and Front Range arches. As these Laramide thrusts propagated laterally towards the NE-trending Early Proterozoic Skin Gulch Shear Zone, the lateral propagation of thrusts was likely slowed, and ultimately arrested by the transfer of thrust motions to oblique strike-slip on weak, high-angle faults. This may explain why the Skin Gulch Shear Zone is the locus for the intersection and bifurcation of the oppositely-vergent, conjugate thrusts which core the Front Range, Medicine Bow and Laramie Range arches.

The anastomosing and bifurcating nature of basement arches and the transfer of slip across arches suggest they share a subhorizontal, lower crustal detachment. Observations of unidirectional shortening subperpendicular to the northeastern and eastern margins of the Laramide Orogen require radially-divergent translation of the upper and middle crust during Laramide deformation (Erslev, 2005). This regional change in Laramide kinematics requires conjugate strike-slip faulting to accommodate extension parallel to the axis of the northeastward-bowing orogenic arc. This suggests localized zones of oblique strike-slip like the Livermore Embayment / Skin Gulch Shear Zone may not be entirely a product of tectonic inheritance but also required for strain compatibility at the orogen scale.

Chapter 8

Conclusions

The northeastern Front Range contains a complex transition zone between the oppositely-vergent first-order thrusts, the Never Summer and Laramie Range thrusts. The kinematic analysis of minor faults suggests regional Laramide compression was subhorizontal, unidirectional and oriented 085°. Previously published 2D and 3D models invoking variably-directed, dip-slip motions on high-angle reverse or normal faults (Matthews and Sherman, 1976; Matthews and Work, 1978) are untenable given the overwhelming dominance of horizontal compression.

The abrupt change in the trends and geometries of 2nd-order structures from the NNW-trending structures to the south to NE-trending structures of the study area appears to be facilitated by the tectonic inheritance of the NE-trending, Early Proterozoic Skin Gulch Shear Zone. The structural low of the Livermore Embayment was due to the local dominance of oblique, right-lateral slip on reactivated, NE-trending faults. The presence of these weak, subvertical faults facilitated the ENE translation of fault blocks and limited crustal thickening by reverse faulting. The remarkable consistency in lateral translation of fault blocks and the results of kinematic and paleomagnetic data analyses suggest the Livermore Embayment is a broad, right-lateral, transpressional shear zone. Fault reactivation of this NE-trending shear zone by Laramide compression was a

regionally dominant mode of deformation and resulted in right-lateral strike slip and the lateral propagation of pre-existing faults. Minor fault and paleomagnetic data suggests clockwise vertical axis rotations and strain partitioning occurred in the forelimbs of NE-trending monoclines formed by right-lateral transpression. Trishear fault-propagation-folding appears to have been the locally dominant mode of deformation near oblique-slip and dip-slip reverse faults, evident by the smoothly-rounded hinges of asymmetric anticlines and monoclines. Basement folding was common in heavily-fractured basement near reactivated faults and compressional bends in oblique-slip faults and listric thrusts. Tilting and folding of the basement nonconformity resulted in top-to-the-west, out-of-the-basin flexural shear within the basement and sedimentary cover evident by the dominance of ENE-dipping reverse faults coring asymmetric, west-vergent anticlines and E-dipping minor thrusts on their crests and backlimbs. The *en echelon* and relay arrays of ENE-dipping reverse faults and their abrupt loss of slip where they overlap suggests the faults formed simultaneously and strain was transferred across multiple faults during the Laramide Orogeny. The irregular distribution of ENE-dipping reverse faults suggests strain was locally transferred across oppositely-dipping, oblique-slip faults. Backlimb tightening structures formed in two stages as early-stage, out-of-the-basin reverse faults were subsequently truncated by late-stage, in-to-the-basin thrusts, consistent with the models of Stanton and Erslev (2004) and Erslev and Selvig (1997).

The relative timing of deformation mechanisms during the Laramide Orogeny were constrained by cross-cutting relationships observed in the field. The Pennsylvanian-Permian carbonates of southern Wyoming contain dissolution cleavage planes which appear to be approximately perpendicular to bedding and parallel to early-formed fold

axes. Cleavage planes were subsequently cut by minor faults as Laramide strain rates exceeded those accommodated by dissolution. The abundance of Laramide minor faults suggests shear fracturing and frictional sliding were dominant deformation mechanisms resulting in strain hardening by generating quartz-rich cataclasite on fault surfaces in Phanerozoic quartzarenites.

Observations of ENE-striking master joints being absent in areas of pervasive NE-, and ENE-striking conjugate strike-slip faults and cross joint strike varying to form perpendicular abutments to strike-slip faults are suggestive of regional jointing post-dating minor faulting. The average trend of master joints is 058° and the trend of cross joints averaged 149° . However observations of local reactivation of master joints by right-lateral shear suggest a late-Laramide timing of jointing as σ_1 remained subhorizontal but likely varied in trend between NE-SW and E-W. The consistent NNW-strikes of cross joints in areas of few master joints are suggestive of a second stage of jointing that is kinematically-compatible with the mid-, to late-Miocene normal faulting in the northwestern Front Range.

Questions for Future Research

Unanswered questions remain and problems requiring further work have arisen from this investigation.

Regarding hypotheses of lower crustal wedging and backlimb tightening:

1) Can numerical or analog models reproduce the sequence of deformation within backlimb tightening zones of synthetic, out-of-the-basin reverse faults crosscut by subsequent into-the-basin thrusts as proposed by Erslev and Selvig (1997), Erslev and Stanton (2004), and this study?

Regarding hypotheses of complex transition zones between oppositely-vergent thrusts:

1) Can 4D photogrammetric analyses of scaled dynamic models test hypotheses of stress refraction, strain relay, and vertical axis rotations within complex transition zones between oppositely-vergent conjugate thrusts?

2) Could dynamic models reproduce the slowing of the lateral propagation rates of thrust faults by subvertical zones of weakness as proposed by this study?

Regarding the complex structures of the Livermore Embayment:

1) Could the collection of seismic, gravity and magnetic data further constrain the poorly-understood, complex areas where variably-oriented, oppositely-dipping faults terminate and modes of deformation change abruptly?

2) How many episodes of deformation have reactivated the Halligan Reservoir, North Livermore, West Livermore, and Livermore faults? And what was the absolute timing and P-T condition of these deformations?

Regarding the absolute timing and mechanisms of regional jointing:

1) Can the hydrodynamic modeling of intra-formational fluid pressure during the formation of the Front Range Arch and Denver Basin test hypotheses of hydraulically-influenced jointing?

2) Can the mapping of faults and joints at multiple structural positions within the asymmetric anticlines of the northeastern Front Range be used to create an empirical 3D fold-fracture model for fault-propagation anticlines across the Laramide Foreland?

REFERENCES CITED

- Abbott, J.T., 1976, Geologic map of the Big Narrows quadrangle, Larimer County, Colorado: U.S. Geological Survey Geologic Quadrangle Map GQ-1323, scale 1:24,000.
- Allmendinger, R. W., Brewer, J. A., Brown, L. D., Kaufman, S., Oliver, J. E., and Houston, R. S., 1982, COCORP profiling across the Rocky Mountain Front in southern Wyoming, Part 2: Precambrian basement structure and its influence on Laramide deformation, *Geological Society of America Bulletin*, v. 93, p. 1253-1263.
- Anderson, E.M., 1951, *The dynamics of faulting and dyke formation with applications to Britain*, Edinburgh, Oliver and Boyd Publishing, London, England, 191 p.
- Angelier, J., 1984, Tectonic analysis of fault slip data sets, *Journal of Geophysical Research*, v. 89, p. 5835-5848.
- Angelier, J., 1990, Inversion of field data in fault tectonics to obtain the regional stress-III, a new rapid direct inversion method by analytical means, *Geophysical Journal International*, v. 103, p. 363-376.
- Barlow and Haun, Inc., 2000, Structure contour map of the central 1/3 of the Denver Basin, Colorado and Wyoming, Barlow and Haun, Inc., Casper, Wyoming.
- Bergbauer, S.B., and Pollard, D.D., A new conceptual fold-fracture model including prefolding joints, based on the Emigrant Gap anticline, Wyoming, *Geological Society of America Bulletin*, v. 116, p. 294-307.
- Bird, P., 1988, Formation of the Rocky Mountains, Western United States; a continuum computer model, *Science*, v. 239, p. 1501-1507.
- Bird, P., 1998, Kinematic history of the Laramide Orogeny in latitudes 35 degrees - 49 degrees N, western United States, *Tectonics*, v. 17, p. 780-801.
- Bolay-Koenig, N. V., and Erslev, E. A., 2003, Internal and external controls on Phanerozoic Rocky Mountain structures, U.S.A.: Insights from GIS-enhanced tectonic maps, *in* Reynolds, R. G., and Flores, R. M., eds., *Cenozoic systems of the Rocky Mountain region: Denver, Colorado*, Rocky Mountain Section, Society of Economic Paleontologists and Mineralogists, p. 33-63.
- Boos, C.M., and Boos, M.F., 1957, Tectonics of eastern flank and foothills of Front Range, Colorado, *American Association of Petroleum Geologists Bulletin*, v. 41, p. 2603-2676.

- Braddock, W.A., and Eicher, D.L., 1962, Block-Glide Landslides in the Dakota Group of the Front Range Foothills, Colorado, Geological Society of America Bulletin, v. 73, p. 317-324.
- Braddock, W.A., Abbott, J.T., Connor, J.J., and Swann, G.A., 1988a, Geologic map of the Poudre Park quadrangle, Larimer County, Colorado: U.S. Geological Survey Geologic Quadrangle Map GQ-1620, scale 1:24,000.
- Braddock, W.A., and Connor, J.J., 1988b, Geologic map of the Livermore Mountain quadrangle, Larimer County, Colorado: U.S. Geological Survey Geologic Quadrangle Map GQ-1617, scale 1:24,000.
- Braddock, W.A., Connor, J.J., Swann, G.A., and Wohlford, D.D., 1988c, Geologic map of the Laporte quadrangle, Larimer County, Colorado: U.S. Geological Survey Geologic Quadrangle Map GQ-1621, scale 1:24,000.
- Braddock, W. A., Wohlford, D. D., and Connor, J. J., 1988d, Geologic map of the Livermore quadrangle, Larimer County, Colorado: U.S. Geological Survey Geologic Quadrangle Map GQ-1618, scale 1:24,000.
- Braddock, W.A., Calvert, R.H., O'Connor, J.T., and Swann, G.A., 1989a, Geologic map of the Horsetooth Reservoir quadrangle, Larimer County, Colorado: U.S. Geological Survey Geologic Quadrangle Map GQ-1625, scale 1:24,000.
- Braddock, W.A., Eggler, D.H., and Courtwright, T.R., 1989b, Geologic map of the Virginia Dale quadrangle, Larimer County, Colorado and Albany and Laramie Counties, Wyoming: U.S. Geological Survey Geologic Quadrangle Map GQ-1616, scale 1:24,000.
- Braddock, W.A., Cole, J. C., and Eggler, D.H., 1989c, Geologic map of the Diamond Peak quadrangle, Larimer County, Colorado and Albany County, Wyoming: U.S. Geological Survey Geologic Quadrangle Map GQ-1614, scale 1:24,000.
- Breitsprecher, K., Thorkelson, D.J., Groome, W.G., and J. Dostal, 2003, Geochemical confirmation of the Kula-Farallon slab window beneath the Pacific Northwest in Eocene time, *Geology*, v. 31, p. 351-354.
- Brewer, J.A., Allmendinger, R.W., Brown, L.D., Oliver, J.E., and Kaufman, S., 1982, COCORP profiling across the Rocky Mountain front in southern Wyoming, Part 1, Laramide structure, Geological Society of America Bulletin, v. 93, p. 1242-1252.
- Brown, W.G., 1984, A reverse fault interpretation of Rattlesnake Mountain anticline, Big Horn basin, Wyoming, *The Mountain Geologist*, v. 21, p. 31-35.

- Brown, W.G., 1988, Deformation style of Laramide uplifts in the Wyoming foreland, *in* C.J. Schmidt and W.J. Perry, Jr., eds., Interaction of the Rocky Mountain foreland and the Cordilleran thrust belt, Geological Society of America Memoir 171, p. 1-26.
- Bump, A.P., 2003, Reactivation, trishear modeling, and folded basement in Laramide uplifts: Implications for the origins of intracontinental faults, *GSA Today*, v. 13, p. 4-10.
- Byerlee, J., 1978, Friction of rocks, *Pure and Applied Geophysics*, v. 116, p. 615-626.
- Cather, S.M., 1999, Implications of Jurassic and Cretaceous piercing lines for Laramide oblique slip faulting in New Mexico and the rotation of the Colorado Plateau, *Geological Society of America Bulletin*, v. 111, p. 849-868.
- Cather, S.M., Karlstrom, K. E., Timmons, J.M. and Heizler, M.T., 2006, Palinspastic reconstruction of Proterozoic basement-related aeromagnetic features in north-central New Mexico: Implications for Mesoproterozoic to late Cenozoic tectonism, *Geosphere*, v. 2, p. 299-323
- Cahill, T., and Isacks, B., 1992, Seismicity and shape of the subducted Nazca Plate, *Journal of Geophysical Research*, v. 97, p. 503-539.
- Chamberlain, K.R., 1998, Medicine Bow orogeny: Timing and deformation and model of crustal structure produced during continent arc collision, ca. 1.78 Ga, southeastern Wyoming, *Rocky Mountain Geology*, v. 33, no. 2, p. 259-277.
- Chapin, C.E., and Cather, S.M., 1981, Eocene tectonism and sedimentation in the Colorado Plateau-Rocky Mountain area, *Arizona Geological Digest*, v. 14, p. 175-198.
- Cloos, M., 1993, Lithospheric Buoyancy and collisional orogenesis: subduction of oceanic plateaus, continental margins, island arcs, spreading ridges, and seamounts, *Geological Society of America Bulletin*, v. 105, p.715-737.
- COGCC, 2006, Colorado Oil and Gas Conservation Commission website, <http://oil-gas.state.co.us/>.
- Compton, R.R, 1966, Analyses of Pliocene-Pleistocene deformation and stresses in northern Santa Lucia range, California, *Geological Society of America Bulletin*, v. 77, n.12, p.1361-1380.
- Coney, P. J., and Reynolds, S. J., 1977, Cordilleran Benioff zones, *Nature*, v. 270, p. 403-406.

- Courtwright, T.R., and Braddock, W.A., 1989, Geologic map of the Table Mountain quadrangle and adjacent parts of the Round Butte and Buckeye Quadrangles, Larimer County, Colorado and Laramie County, Wyoming: U.S. Geological Survey Miscellaneous Investigations Series Map I-1805, scale 1:24,000.
- Cross, T.A., and Pilger, R.H., 1982, Controls of subduction geometry, location of magmatic arcs, and tectonics of arcs and back-arc regions, *Geological Society of America Bulletin*, v. 93, p. 545-562.
- DePaolo, D.J., 1981, Neodymium isotopes in the Colorado Front Range and crust-mantle evolution in the Proterozoic, *Nature*, v.291, p.136-196.
- Dickinson, W.R., and Snyder, W.S., 1978, Plate tectonics of the Laramide Orogeny, *Geological Society of America Memoir* 151, p. 355-366.
- Dolson, J., Muller, D., Evetts, M.J., and Stein, J.A., 1991, Regional paleotopographic trends and production, Muddy Sandstone (Lower Cretaceous), Central and Northern Rocky Mountains, *American Association of Petroleum Geologists Bulletin*, v. 75, p. 409-435.
- Dueker, K., Yuan, H., and Zurek, B., 2001, Thick Proterozoic lithosphere of the Rocky Mountain region, *GSA Today*, v.11, p. 4-9.
- Egan, S.S., and Urquhart, J.M., 1993, Numerical modeling of lithosphere shortening: application to the Laramide orogenic province, western USA, *Tectonophysics*, v. 221, p. 385-411.
- Eggler, D.H., and Braddock, W.A., 1988, Geologic map of the Cherokee Park quadrangle, Larimer County, Colorado: U.S. Geological Survey Geologic Quadrangle Map GQ-1615, scale 1:24,000.
- Erslev, E.A., 1986, Basement balancing of Rocky Mountain foreland uplifts, *Geology*, v. 14, p. 259-262.
- Erslev, E.A., 1991, Trishear fault-propagation folding, *Geology*, v.19, p. 617-620.
- Erslev, E.A., 1993, Thrusts, backthrusts and detachment of Laramide foreland arches, *in* C.J. Schmidt, R. Chase, and E.A. Erslev, eds., *Laramide basement deformation in the Rocky Mountain foreland of the western United States*, *Geological Society of America Special Paper* 280, p. 125-146.
- Erslev, E.A., and Rogers, J.L., 1993, Basement-cover kinematics of Laramide fault-propagation folds: *in* C.J. Schmidt, R. Chase, and E.A. Erslev, eds., *Laramide basement deformation in the Rocky Mountain foreland of the western United States: Geological Society of America Special Paper* 280, p. 339-358.

- Erslev, E.A., and Gregson, J.D., 1996, Oblique Laramide convergence in the northeastern Front Range; regional implications from the analysis of minor faults, *in* Thompson, R. A., Hudson, M. R., and Pillmore, C. L., eds., *Geologic excursions to the Rocky Mountains and beyond*, Special Publication - Colorado Geological Survey, Open-File Report 96-4, 11 p.
- Erslev, E.A., and Selvig, B.W, 1997, Thrusts, backthrusts, and triangle zones, *in* Bolyard, D.W., and Sonnenberg, S.A., eds., *Geologic History of the Colorado Front Range*, Denver, Colorado, Rocky Mountain Associations of Geologists, p. 65-76
- Erslev, E.A., 2001, Multi-stage, multi-directional Tertiary shortening and compression in north-central New Mexico, *Geological Society of America Bulletin*, v.113, p. 63–74.
- Erslev, E.A., Holdaway, S.M., O’Meara, S.A., Jurista, B., and Selvig, B.W, 2004a, Laramide minor faulting in the Colorado Front Range, *in* Cather, S.M., McIntosh, W.C., and Kelley, S.A., eds., *Tectonics, geochronology, and volcanism in the southern Rocky Mountains and Rio Grande Rift*, New Mexico Bureau of Geology and Mineral Resources Bulletin 160, p. 181-204.
- Erslev, E.A., Fankhauser, S.D., Heizler, M., Sanders, R., and Cather, S.M., 2004b, Strike-slip tectonics and thermochronology of northern New Mexico: A field guide to critical exposures in the southern Sangre de Cristo Mountains, *in* Nelson, E.P. and Erslev, E.A., *Field trips in the southern Rocky Mountains, USA: Geological Society of America Field Guide 5*, p. 15-40.
- Erslev, E.A., 2005, 2D Laramide geometries and kinematics of the Rocky Mountains, Western U.S.A., *in* K.E. Karlstrom and G.R. Keller, eds., 2005, *The Rocky Mountain Region — An Evolving Lithosphere: Tectonics, Geochemistry, and Geophysics: American Geophysical Union Geophysical Monograph 154*, p. 7-20.
- Erslev, E.A., and Larson, S.M., 2006, Testing Laramide Hypotheses for the Colorado Front Range Arch Using Minor Faults, *The Mountain Geologist*, v. 43, p 45-64.
- Fankhauser, S.D., and Erslev, E.A., 2004, Unconformable and cross-cutting relationships indicate major Precambrian faulting on the Picuris-Pecos fault system, southern Sangre de Cristo Mountains, New Mexico: Socorro, New Mexico Geological Society, 55th Annual Field Conference Guidebook, p. 121–133.
- Graham, J., and Ethridge, F.G., 1995, Sequence stratigraphic implications of gutter casts in the Skull Creek Shale, Lower Cretaceous, northern Colorado, *The Mountain Geologist*, v. 32, p. 95–106.

- Gregson, J.D., and Erslev, E.A., 1997, Heterogeneous Laramide Deformation in the Uinta Mountains, Colorado and Utah, *in* Fractured Reservoirs: Characterization and Modeling, Hoak, T.E., Klawitter, A.L., Blomquist, P.K., eds., Rocky Mountain Association of Geologist Guidebook, Denver, Colorado, p. 137-154.
- Gries, R.R., 1983a, Oil and gas prospecting beneath the Precambrian of foreland thrust plates in Rocky Mountains, American Association of Petroleum Geologists Bulletin, v. 67, p. 1-28.
- Gries, R.R., 1983b, North-south compression of the Rocky Mountain foreland structures, *in* Rocky Mountain foreland basins and uplifts Lowell, J.D., and Gries, R.R., eds., Rocky Mountain Association of Geologists, Denver, Colorado, p. 9-32.
- Gutscher, M.-A., Spakman, W., Bijwaard, H., Engdahl, E.R., 2000, Geodynamics of flat subduction: Seismicity and tomographic constraints from the Andean margin, Tectonics, v. 19, p. 814-833.
- Gutscher, M.-A., 2002, Andean subduction styles and their effect on thermal structure and interplate coupling, Journal of South American Earth Sciences, v. 15, p. 3-10.
- Hall, M.K., and Chase, C.G., 1989, Uplift, unbuckling, and collapse: Flexural history and isostasy of the Wind River Range and Granite Mountains, Wyoming, Journal of Geophysical Research, v. 94, p. 17,581–17,593.
- Harper, M.L., 1966, Joints and microfractures in Glenwood Canyon, CO, The Mountain Geologist, v.3, p.185-192
- Hayden, F.V., 1874, Annual Report of the United States Geological and Geographical Survey of The Territories Embracing Colorado: 7th Annual Report (1873).
- Hayden, F.V., 1877, Annual Report of the United States Geological and Geographical Survey of the Territories, Embracing Colorado and Parts of Adjacent Territories: 9th Annual Report (1875).
- Hennings, P.H., Olson, J.E., and Thompson, L.B., 2000, Combining outcrop data and three-dimensional models to characterize fractured reservoirs: An example from Wyoming, American Association of Petroleum Geologists Bulletin, v. 84, no. 6, p. 830-849
- Henry, S.G., and Pollack, H.N., 1988, Terrestrial heat flow above the Andean subduction zone in Bolivia and Peru, Journal of Geophysical Research, v. 93, p. 153-162.
- Holdaway, S.M., 1998, Laramide deformation for the Northeastern Front Range, Colorado: Evidence for deep crustal wedging during horizontal compression: Master's Thesis, Colorado State University, Fort Collins, CO, 146p.

- Houston, R.S., 1993, Late Archean and early Proterozoic geology of southeastern Wyoming, *in* *Memoir - Geological Survey of Wyoming*, v. 5, p. 78-116.
- Houston, R.S. and Marlatt, G., 1997, Proterozoic geology of the Granite Village area, Albany and Laramie Counties, Wyoming, compared with that of the Sierra Madre and Medicine Bow Mountains of southeastern Wyoming, U.S. Geological Survey Bulletin 2159, scale 1:24,000.
- van Hunen, J., van den Berg, A.P., and Vlaar, N.J., 2001. Latent heat effects of the major mantle phase transitions on low-angle subduction, *Earth Planetary Science Letters*, v. 190, p. 125–135.
- Hurich, C.A., and Smithson, S.B., 1982, Gravity interpretation of the southern Wind River Mountains, Wyoming, *Geophysics*, v. 47, p. 1550–1561.
- Jacob, A.F., 1983, Mountain front thrust, southeastern Front Range and northeastern Wet Mountains, Colorado *in* J. D. Lowell (ed.), *Rocky Mountain foreland basins and uplifts*, Rocky Mountain Association of Geologists, p. 229-244.
- Johnson, R.A., and Smithson, S.B., 1985, Thrust faulting in the Laramie Mountains, Wyoming, from reanalysis of COCORP data, *Geology*, v. 13, p. 534-537.
- Jordan, T.E., Isacks B.L., Allmendinger, R.W., Brewer J.A., Ramos, V.A., and Ando C.J., 1983, Andean tectonics related to geometry of subducted Nazca plate, *Geological Society of America Bulletin*, v. 94, p. 341-61.
- Jordan, T.E., and Allmendinger, R.W., 1986, The Sierras Pampeanas of Argentina: A modern analogue of Rocky Mountain foreland deformation, *American Journal of Science*, v. 286, p.737-764.
- Karlstrom, K.E., Bowring, S.A., Chamberlain, K.R., Dueker, K.G., Eshete, T., Erslev, E.A., Farmer, G.L., Heizler, M., Humphreys, E.D., Johnson, R.A., Keller, G.R., Kelley, S.A., Levander, A., Magnani, M.B., Matzel, J.P., McCoy, A.M., Miller, K.C., Morozova, E.A., Pazzaglia, F.J., Prodehl, C., Rumpel, H.-M., Shaw, C.A., Sheehan, A.F., Shoshitaishvili, E., Smithson, S.B., Snelson, C.M., Stevens, L.M., Tyson, A.R., and Williams, M.L., 2002, Structure and evolution of the lithosphere beneath the Rocky Mountains: Initial results from the CD-ROM experiment, *GSA Today*, v. 12, no. 3, p 4-10.
- Karlstrom, K.E., and Daniel, C.G., 1993, Restoration of Laramide right-lateral strike slip in northern New Mexico by using Proterozoic piercing points: Tectonic implications from the Proterozoic to the Cenozoic, *Geology*, v. 21, p. 1139-1142.
- Keefer, W. R. and Love, J. D., 1963, Laramide vertical movements in central Wyoming, *Contributions to Geology*, v. 2, p. 47-54.

- Keller, G.R., Snelson, C.M., Sheehan, A.F., and Dueker, K.G, 1998, Geophysical studies of crustal structure in the Rocky Mountain region: A review, *Rocky Mountain Geology*, v. 33, no. 2, p. 217-228.
- Kellogg, K.S., 1999, Neogene basins of the northern Rio Grande rift: partitioning and asymmetry inherited from Laramide and older uplifts, *Tectonophysics*, v. 305, p. 141-152.
- Kelley, S.A., and Chapin, C.E., 2004, Denudation history and internal structure of the Front Range and Wet Mountains, Colorado, based on apatite-fission-track thermochronology, *in* Cather, S.M., McIntosh, W.C., and Kelley, S.A., eds., *Tectonics, geochronology, and volcanism in the southern Rocky Mountains and Rio Grande Rift*, New Mexico Bureau of Geology and Mineral Resources Bulletin 160, p. 41-77.
- Kluth, C.F., and Coney, P.J., 1981, Plate Tectonics of the Ancestral Rocky Mountains: *Geology*, v. 9, p. 10-15.
- Kluth, C.F., 1986, Plate Tectonics of the Ancestral Rocky Mountains, *in* Peterson, J.A., ed., *Paleotectonics and sedimentation in the Rocky Mountain region, United States*, American Association of Petroleum Geologists Memoir, v. 41, p. 353-369.
- Kluth, C.F., 1997, Comparison of the location and structure of the Late Paleozoic and Late Cretaceous-Early Tertiary Front Range Uplift, *in* Bolyard, D.W., and Sonnenberg, S.A., eds., *Geologic History of the Colorado Front Range: Denver, Colorado*, Rocky Mountain Association of Geologists, p. 31-42.
- LeMasurier, W.E., 1970, Structural study of a Laramide fold involving shallow seated basement rock, Front Range, Colorado: *Geological Society of America Bulletin*, v. 81, p. 421-434.
- Li, A., Forsyth, D.W., and Fisher, K.M., 2002, Evidence for shallow isostatic compensation of the southern Rocky Mountains from Rayleigh wave tomography, *Geology*, v. 30, p. 683–686.
- Love, J.D. and Christiansen, A.C., 1985, *Geologic Map of Wyoming, United States Geological Survey Map*, scale 1:500,000.
- Lowell, J. D., 1983, Foreland Deformation, *in* Lowell, J. D., ed., *Rocky Mountain foreland basins and uplifts: Rocky Mountain Association of Geologists*, p. 1-8.
- Matthews, V., III and Sherman, G.D., 1976, Origin of monoclinial folding near Livermore, CO, *Mountain Geologist*, v.13, p.61-66.

- Matthews, V., III and Work, D.F., 1978, Laramide folding associated with basement block faulting along the northeastern Front Range, Colorado, *in* Matthews, V., III, ed., Laramide folding associated with basement block faulting in the western United States, Geological Society of America Memoir 151, p. 101-124.
- McCallum, M.E., and Mabarak, C.D, 1976, Diamond in state-line kimberlite diatremes, Albany County, Wyoming; Larimer County, Colorado, Report of Investigations Issue 12; Geological Survey of Wyoming: Laramie, WY.
- McMillan, M.E., Angevine, C.L., and Heller, P.L., 2002, Postdepositional tilt of the Miocene Pliocene Ogallala Group on the western Great Plains: Evidence of late Cenozoic uplift of the Rocky Mountains, *Geology*, v. 30, no. 1, p. 63-66.
- McQuarrie, N., and Chase, C.G., 2000, Raising the Colorado Plateau, *Geology*, v. 28, p. 91-94.
- McQueen, H.W.S., and Beaumont, C., 1989, Mechanical models of tilted block basins: *in* Price, R.A., ed., Origin and evolution of sedimentary basins and their energy and mineral resources, *Geophysical Monograph*, v. 48, p. 65-71.
- MVE, 2006a, 2DMOVE v. 5.0, Midland Valley Exploration Ltd., Glasgow, Scotland, United Kingdom.
- MVE, 2006b, 3DMOVE v. 5.0, Midland Valley Exploration Ltd., Glasgow, Scotland, United Kingdom.
- Mollerstuen, S.A., 2006, proprietary 2D seismic data, Northern Denver Basin.
- Molzer, P. and Erslev, E.A., 1995, Oblique convergence on east-west Laramide arches, Wind River Basin, Wyoming, *American Association of Petroleum Geologists Bulletin*, v. 19, p. 1377-1394.
- Narr, W., and Suppe, J., 1999, Kinematics of basement-involved compressive structures: *American Journal of Science*, v. 294, p. 802-860.
- Neely, T.G., and Erslev, E.A., in review, The interplay of fold mechanisms and basement weaknesses at the transition between Laramide basement-involved arches, north-central Wyoming, U.S.A., submitted to *Journal of Structural Geology*.
- Nesse, W.D., and Braddock, W.A., 1989, Geologic map of the Pingree Park quadrangle, Larimer County, Colorado: U.S. Geological Survey Geologic Quadrangle Map GQ-1622, scale 1:24,000.
- Nesse, W.D., 2006, Geometry and Tectonics of the Laramide Front Range, Colorado, *The Mountain Geologist*, Vol. 43, No. 1, p. 25-44.

- Nibbelink, K.A., 1983, Depositional environments of the Fox Hills Sandstone (Upper Cretaceous), Cheyenne Basin, Colorado: Master's Thesis, Colorado State University, Fort Collins, CO, 245p.
- Nicholson, P.G., and Groshong, Richard H. Jr., 2006, A structural model for typical hydrocarbon traps in Saudi Arabia, Geological Society of America Abstracts with Programs, Vol. 38, No. 7, p. 543.
- Nikinshin, A.M., Cloetingh, S., Lobkovsky, L.I., Burov, E.B., and Lankreijer, A.C., 1993 Continental lithospheric folding in central Asia (Part 1): constraints from geological observations, Tectonophysics, v. 226, p. 59–72.
- O'Neill, J.M., 1981, Geologic map of the Mount Richthofen quadrangle and the western part of the Fall River Pass quadrangle, Grand and Jackson Counties, Colorado: U.S. Geological Survey Miscellaneous Investigations Series Map I-1291, scale 1:24,000.
- Oldow, J.S., A.W. Bally, H.G. Ave Lallemand, and Leeman, W.P., 1989, Phanerozoic evolution of the North American Cordillera: United States and Canada, *in* A.W. Bally and A.R. Palmer, eds., The geology of North America, an overview: The Geological Society of America, The Geology of North America, v. 1A, p. 139-232.
- Peterman, Z.E., Hedge, C.E., and Braddock, W.A, 1968, Age of Precambrian events in the northeastern Front Range, Colorado, Journal of Geophysical Research, v. 73, no. 6, p. 2277-2296.
- Perry, W.J., Jr., Nichols, D.J., Dyman, T.S., and Haley, C.J., 1992, Sequential Laramide deformation in Montana and Wyoming, *in* Thorman, C.H., ed., Application of structural geology to mineral and energy resources of the central and western United States: U.S. Geological Survey Bulletin 2012, p. C1–C14.
- Perry, W.J., Jr., and Flores, R.M., 1997, Sequential Laramide Deformation and Paleocene Depositional Patterns in Deep Gas-Prone Basins of the Rocky Mountain Region, *in* Dyman, TS, Rice, DD, and Westcott, PA, eds., Geologic controls of deep natural gas resources in the United States: U.S. Geological Survey Bulletin 2146-E, p. 49–59.
- Petit, J.P., 1987, Criteria for the sense of movement on fault surfaces in brittle rocks: Journal of Structural Geology, v. 9, p. 597-608.
- Price, N.J., 1966, Fault and joint development in brittle and semi-brittle rock, Pergamon Publishing, London, United Kingdom, 176p.
- Prucha, J.J., J.A. Graham, and R.P. Nickelson, 1965, Basement-controlled deformation in Wyoming Province of Rocky Mountain foreland: American Association of Petroleum Geologist Bulletin, v. 49, p. 966-992.

- Punongbayan, R., Cole, J.C., Braddock, W.A., and Colton, R.B., 1989, Geologic map of the Pinewood Lake quadrangle, Boulder and Larimer Counties, Colorado: U.S. Geological Survey Geologic Quadrangle Map GQ-1627, scale 1:24,000.
- Ramos, V.A, Cristallinni, E.O., and Pérez, D.J., 2002, The Pampean flat-slab of the Central Andes, *Journal of South American Earth Sciences*, v. 15, p. 59-78.
- Raynolds, R.G., 1997, Synorogenic and post-orogenic strata in the central Front Range, Colorado, *in* Bolyard, D.W., and Sonnenberg, S.A., eds., *Geologic History of the Colorado Front Range: Denver, Colorado*, Rocky Mountain Association of Geologists, p. 43-47.
- Rhoads, H., 1987, Facies relationships of the Ingleside Formation in northern Colorado and southeastern Wyoming: Master's Thesis, Colorado School of Mines, Golden, CO, 98p.
- Ruf, J.C., and Erslev, E.A., 2005, Origin of Cretaceous to Holocene fractures in the northern San Juan Basin, Colorado and New Mexico, *Rocky Mountain Geology*, v. 40, no. 1, p. 91-114.
- Sahagian, D.L., Proussevitch, A., and Carlson, W., 2002, Timing of Colorado Plateau uplift: Initial constraints from vesicular basalt-derived paleoelevations, *Geology*, v. 30, p. 807-810.
- Saleeby, J., 2003, Segmentation of the Laramide slab-evidence from the southern Sierra Nevada region, *Geological Society of America Bulletin*, v.115, p. 655-668.
- Scott, G.R., and Cobban, W.A., 1986, Geologic, biostratigraphic, and structure map of the Pierre Shale between Loveland and Round Butte, Colorado: U.S. Geological Survey Miscellaneous Investigations Series Map I-1700, scale 1:50,000.
- Silverstone, J., Hodgins, M., Alehikoffz, J.N, and Fanning, C.M., 2000, Mesoproterozoic reactivation of a Paleoproterozoic transcurrent boundary in the northern Colorado Front Range: Implications for ~ 1.7- and 1.4-Ga tectonism, *Rocky Mountain Geology*, v. 35, no. 2, p.139-162.
- Shaver, K.C., Nesse, W.D., Braddock, W.A., 1988, Geologic map of the Rustic quadrangle, Larimer County, Colorado: U.S. Geological Survey Geologic Quadrangle Map GQ-1619, scale 1:24,000.
- Smalley, R.F., Jr. and Isacks, B. L., 1987, A high resolution local network study of the Nazca Plate Wadati-Benioff zone under western Argentina, *Journal of Geophysical Research*, v. 92, p. 13,903-13,912.
- Smith, C.B., 1977, Kimberlite and mantle derived xenoliths at Iron Mountain, Wyoming: Master's Thesis, Colorado State University, Fort Collins, CO, 218p.

- Smithson, S. B., J.A. Brewer, S. Kaufman, J.E. Oliver, and Hurich, C.A., 1979, Structure of the Laramide Wind River uplift, Wyoming, from COCORP deep reflection data and from gravity data, *Journal of Geophysical Research*, v. 84, p. 5955-5972.
- Snelson, C.M., Henstock, T.J., Keller, G.R., Miller, K.C., and Levander, A., 1998, Crustal and uppermost mantle structure along the Deep Probe seismic profile, *Rocky Mountain Geology*, v. 33, p. 181–198.
- Spang, J.H., and Evans, J.P., 1988, Geometrical and mechanical constraints on basement-involved thrusts in the Rocky Mountain foreland province, *in* C.J. Schmidt and W.J. Perry, Jr., eds., *Interaction of the Rocky Mountain foreland and the Cordilleran thrust belt: Geological Society of America Memoir 171*, p. 41-52.
- Stanton, H. I., and Erslev, E. A., 2004, Sheep Mountain: backlimb tightening and sequential deformation in the Bighorn Basin, Wyoming, *Wyoming Geological Association Guidebook 54*, p. 75-87.
- Stearns, D. W., 1971, Mechanisms of drape folding in the Wyoming Province, *in* Renfro, A. R., ed., *Symposium on Wyoming Tectonics and their Economic Significance. Wyoming Geological Association, Annual Field Conference, 23rd Guidebook*, p. 125-143.
- Stearns, D. W., 1975, Laramide basement deformation in the Bighorn Basin – the controlling factor for structure in the layered rocks, *Wyoming Geological Association 27th annual field conference guidebook*, p. 149-158.
- Stearns, D. W., 1978, Faulting and forced folding in the Rocky Mountain foreland, *in* Mathews, V., III, ed., *Laramide folding associated with block faulting in the western United States*, *Geological Society of America Memoir 151*, p. 1-37.
- Stone, D.S., 1969, Wrench faulting and Rocky Mountain tectonics: *The Mountain Geologist*, v. 6, no. 2, p. 67-79.
- Stone, D.S., 2005, On illogical interpretation of geological structures in the Rocky Mountain foreland province, *The Mountain Geologist*, v. 42, no. 4, p. 159-185.
- Tetreault, J., Jones, C.H., Erslev, E.A., Larson, S.M., Hudson, M., and Holdaway, S.M., 2008, Paleomagnetic and structural evidence for oblique slip in a fault-related fold, Grayback Monocline, Colorado, *Geological Society of America Bulletin*, v.120, p. 877-892.
- Tikoff, B., and Maxson, J., 2001, Lithospheric buckling of the Laramide foreland during Late Cretaceous to Paleogene, western United States, *Rocky Mountain Geology*, v. 36, p. 13-35.

- Trudgill, B.D. and Cartwright, J.A., 1994, Relay-ramp forms and normal-fault linkages, Canyonlands National Park, Geological Society of America Bulletin, v. 106, p. 1143-1157.
- Tweto, O, 1979, Geologic Map of Colorado, United States Geological Survey Map, scale 1:500,000.
- Wawrzyniec, T.F. Ault, A.K., Geissman, J. W., Erslev, E.A., and Fankhauser, S.D., 2007, Paleomagnetic dating of fault slip in the Southern Rocky Mountains, USA, and its importance to an integrated Laramide foreland strain field, *Geosphere*, v. 3, p. 16-25.
- WYOGCC, 2006, Wyoming Oil and Gas Conservation Commission website, <http://woogcc.state.wy.us/>.
- Varga, R.J., 1993, Rocky Mountain foreland uplifts: Products of a rotating stress field or strain partitioning?, *Geology*, v. 21, p. 1115-1118.
- Ver Ploeg, A.J., Boyd, C.S., and Kirkaldie, A.L., 2000, Preliminary digital geologic map of the Laramie 30 minute x 60 minute Quadrangle, Albany and Laramie Counties, Wyoming, Wyoming State Geological Survey, Geologic Hazards Section Digital Map HSDM 00-1, scale 1:100,000.
- Vollmer, F.W., 1992, ORIENT v. 1.62 orientation data analysis program user's manual: State University of New York-New Paltz, New Paltz, New York, 26p.
- Ye, H., Royden, L., Burchfiel, C., and Schuepbach, M., 1996, Late Paleozoic Deformation of Interior North America: The Greater Ancestral Rocky Mountains, *American Association of Petroleum Geologists Bulletin*, v. 80, p. 1397-1432.
- Ziegler, V., 1917, Foothills structure in northern Colorado, *Journal of Geology*, v. 25, p. 715-743
- Zielinski, R.A., Peterman, Z.E., Stuckless, J.S., Rosholt, J.N., and Nkomo, I.T., 1981, The chemical and isotopic record of rock-water interaction of the Sherman Granite, Wyoming and Colorado, *Contributions to Mineralogy and Petrology*, v. 78, p. 209-219.

APPENDICES

Appendix 1: Complete Shear Fracture Data Tables

Station #	N	Lat. °N	Long. °W	Fm	Attitude of Beds	Ideal σ_1 Stress Analysis (Compton, 1966) Best Fit Alpha				Strain Analysis Average Slickenline				
1.1*	50	41.09549	105.1524	PPf	055/31	E1: 0.8040 E2: 0.1337 E3: 0.0624 $\alpha=$ 23	138 46 277	11 9 75	E1: 0.8035 E2: 0.1359 E3: 0.0606 $\alpha=$ 25	138 46 273	10 10 75	E1: 0.7101 E2: 0.1540 E3: 0.1359	132 275 36	22 64 14
1.2b*	19	41.06	105.18424	PPf	030/30	E1: 0.9340 E2: 0.0458 E3: 0.0202 $\alpha=$ 20	76 168 288	14 8 74	E1: 0.9335 E2: 0.0461 E3: 0.0204 $\alpha=$ 25	77 169 298	9 8 78	E1: 0.9359 E2: 0.0445 E3: 0.0195	69 166 271	33 10 55
1.3*	11	41.04932	105.1759	PPf	004/16	E1: 0.9445 E2: 0.0442 E3: 0.0113 $\alpha=$ 20	58 150 293	9 15 73	E1: 0.9411 E2: 0.0475 E3: 0.0114 $\alpha=$ 25	58 149 314	4 13 76	E1: 0.9557 E2: 0.0338 E3: 0.0105	55 156 275	29 19 54
1.4*	7	41.02293	105.20745	PPf	315/21	E1: 0.5820 E2: 0.3761 E3: 0.0419 $\alpha=$ 24	208 118 301	0 8 82	E1: 0.5813 E2: 0.3775 E3: 0.0412 $\alpha=$ 25	28 119 295	0 7 83	E1: 0.7101 E2: 0.1540 E3: 0.1359	132 275 36	22 64 14
1.5*	4	41.01817	105.18629	PPf	037/14	E1: 0.9357 E2: 0.0617 E3: 0.0026 $\alpha=$ 19	85 178 332	7 17 72	E1: 0.9294 E2: 0.0617 E3: 0.0026 $\alpha=$ 25	85 178 332	7 17 72	E1: 0.8656 E2: 0.0859 E3: 0.0486	84 234 350	18 69 10
1.6*	4	41.01673	105.1985	PPf	012/12	E1: Shear E2: Planes E3:	265 355 173	0 7 83	E1: Shear E2: Planes E3:	265 355 173	0 7 83	E1: No Slickenlines E2: E3:	No Slickenlines	

*Data not included in analysis of regional compressive stress but presented in the Granite quadrangle map.

Appendix 1: Complete Shear Fracture Data Tables (continued).

Station #	N	Lat. °N	Long. °W	Fm	Attitude of Beds	Ideal σ_1 Stress Analysis (Compton, 1966) (Erslev and Larson, 2006)	Strain Analysis Average Slickenside	
2.1	40	40.98123	105.17259	TrPI	016/16	E1: 0.9833 100 9 E2: 0.0142 194 21 E3: 0.0025 347 67 $\alpha=$ 22	E1: 0.9824 101 7 E2: 0.0149 193 18 E3: 0.0027 351 70 $\alpha=$ 25	E1: 0.9714 97 29 E2: 0.0197 223 47 E3: 0.0089 349 29
2.2	51	40.97138	105.15086	JTrsj	201/29	E1: 0.9031 293 17 E2: 0.0700 90 72 E3: 0.0268 201 7 $\alpha=$ 21	E1: 0.9022 293 14 E2: 0.069 79 73 E3: 0.0288 200 9 $\alpha=$ 25	E1: 0.8572 293 35 E2: 0.1230 114 55 E3: 0.0198 23 0
2.3	35	40.97138	105.15086	KI	003/12	E1: 0.9460 113 6 E2: 0.0334 18 37 E3: 0.0206 211 52 $\alpha=$ 24	E1: 0.9452 113 6 E2: 0.0346 18 38 E3: 0.0202 211 51 $\alpha=$ 25	E1: 0.8351 114 19 E2: 0.1387 277 71 E3: 0.0262 22 5
2.4	62	40.95899	105.17387	Poc	200/25	E1: 0.8646 277 22 E2: 0.0902 63 64 E3: 0.0452 182 13 $\alpha=$ 25	E1: 0.8646 277 22 E2: 0.0902 63 64 E3: 0.0452 182 13 $\alpha=$ 25	E1: 0.7579 274 38 E2: 0.1856 73 50 E3: 0.0565 175 11
2.5	152	40.93908	105.17126	Ksf	152/24	E1: 0.8992 271 13 E2: 0.0736 94 77 E3: 0.0272 1 1 $\alpha=$ 21	E1: 0.8954 272 12 E2: 0.0754 77 77 E3: 0.0301 181 3 $\alpha=$ 25	E1: 0.7983 268 19 E2: 0.1484 120 68 E3: 0.0533 2 10
BC	7	40.9504	105.19108	Poc	017/12	E1: 0.9668 78 13 E2: 0.0224 332 51 E3: 0.0108 178 36 $\alpha=$ 20	E1: 0.9648 79 11 E2: 0.0292 334 52 E3: 0.006 177 36 $\alpha=$ 25	E1: 0.9288 76 23 E2: 0.0674 250 67 E3: 0.0038 345 2
2.6	149	40.94013	105.17896	Ksf	010/12	E1: 0.9369 84 7 E2: 0.0435 175 8 E3: 0.0196 316 79 $\alpha=$ 21	E1: 0.9327 84 8 E2: 0.0438 176 11 E3: 0.0236 319 76 $\alpha=$ 25	E1: 0.8423 265 3 E2: 0.1168 25 84 E3: 0.0410 175 5

Appendix 1: Complete Shear Fracture Data Tables (continued).

Station #	N	Lat. °N	Long. °W	Fm	Attitude of Beds	Ideal σ_1 Stress Analysis (Compton, 1966) (Erslev and Larson, 2006)	Strain Analysis Average Slickenside
SCA	4	40.93703	105.1609	Plo	002/12	Best Fit Alpha E1: 0.9943 224 86 E2: 0.0044 34 4 E3: 0.0013 124 1 $\alpha=$ 22	E1: 0.8551 227 86 E2: 0.1446 75 3 E3: 0.0003 345 2
2.7	23	40.92717	105.14188	Ksf	000/13	E1: 0.9070 108 6 E2: 0.0654 200 23 E3: 0.0275 4 66 $\alpha=$ 18	E1: 0.8492 108 11 E2: 0.1001 256 77 E3: 0.0508 17 7
2.8	48	40.9058	105.13644	Ksf	002/13	E1: 0.9445 108 7 E2: 0.0374 17 9 E3: 0.0181 236 78 $\alpha=$ 21	E1: 0.8283 108 5 E2: 0.1444 276 88 E3: 0.0273 18 1
2.9	26	40.90846	105.19641	Poc	268/8	E1: 0.9261 91 1 E2: 0.0405 0 35 E3: 0.0334 181 55 $\alpha=$ 21	E1: 0.8603 269 14 E2: 0.1099 53 73 E3: 0.0298 177 10
2.10	25	40.90231	105.19856	Poc	207/13	E1: 0.9753 266 5 E2: 0.0133 356 6 E3: 0.0114 137 82 $\alpha=$ 22	E1: 0.8960 266 20 E2: 0.0904 86 70 E3: 0.0137 356 0
2.11	50	40.89672	105.19703	Pi	032/3	E1: 0.8990 77 10 E2: 0.0728 169 7 E3: 0.0282 294 78 $\alpha=$ 15	E1: 0.8469 79 9 E2: 0.1283 348 3 E3: 0.0248 240 80
2.13	18	40.88697	105.2013	Pi	187/15	E1: 0.8902 265 2 E2: 0.0720 355 24 E3: 0.0378 170 66 $\alpha=$ 11	E1: 0.8616 261 0 E2: 0.0735 170 88 E3: 0.0649 351 2

Appendix 1: Complete Shear Fracture Data Tables (continued).

Station #	N	Lat. °N	Long. °W	Fm	Attitude of Beds	Ideal σ_1 Stress Analysis (Best Fit Alpha)	Compton, 1966 (Erslev and Larson, 2006)	Strain Analysis Average Slickenside						
2.1	50	40.88405	105.11552	Ksf	357/15	E1: 0.9725	89	11	E1: 0.9682	89	11	E1: 0.8448	88	10
						E2: 0.0143	197	58	E2: 0.019	353	31	E2: 0.1360	179	3
3.1a	29	40.91169	105.27241	PPf	083/10	E3: 0.0132	353	30	E3: 0.0128	197	57	E3: 0.0193	283	79
						$\alpha=$ 21			$\alpha=$ 25					
3.1b	21	40.91409	105.276	PPf	010/36	E1: 0.9619	241	10	E1: 0.9277	248	8	E1: 0.9351	234	11
						E2: 0.0259	65	80	E2: 0.0541	342	26	E2: 0.0379	65	79
3.2	30	40.89853	105.23183	Pi	126/31	E3: 0.0122	331	1	E3: 0.0183	142	63	E3: 0.0270	324	2
						$\alpha=$ 12			$\alpha=$ 25					
3.3	30	40.85773	105.21664	Pi	330/4	E1: 0.7933	76	17	E1: 0.7928	76	17	E1: 0.6842	71	24
						E2: 0.1262	326	48	E2: 0.1251	325	50	E2: 0.2195	300	55
3.4	50	40.85661	105.21295	Pi	056/15	E3: 0.0805	180	37	E3: 0.0821	179	35	E3: 0.0963	172	24
						$\alpha=$ 24			$\alpha=$ 25					
3.5	25	40.84666	105.23608	PPf	094/41	E1: 0.7700	271	5	E1: 0.7673	267	8	E1: 0.7263	249	22
						E2: 0.1657	2	10	E2: 0.1728	360	18	E2: 0.2198	358	40
3.5	25	40.84666	105.23608	PPf	094/41	E3: 0.0643	156	79	E3: 0.0599	156	11	E3: 0.0540	138	42
						$\alpha=$ 30			$\alpha=$ 25					
3.5	25	40.84666	105.23608	PPf	094/41	E1: 0.6320	73	1	E1: 0.6302	253	1	E1: 0.5871	78	16
						E2: 0.3493	343	7	E2: 0.3525	343	10	E2: 0.3295	171	13
3.5	25	40.84666	105.23608	PPf	094/41	E3: 0.0187	172	83	E3: 0.0173	160	80	E3: 0.0834	298	69
						$\alpha=$ 21			$\alpha=$ 25					
3.5	25	40.84666	105.23608	PPf	094/41	E1: 0.8430	249	16	E1: 0.8424	248	15	E1: 0.7542	263	16
						E2: 0.1037	155	16	E2: 0.1043	155	13	E2: 0.1800	167	21
3.5	25	40.84666	105.23608	PPf	094/41	E3: 0.0533	21	67	E3: 0.0532	25	69	E3: 0.0658	26	63
						$\alpha=$ 23			$\alpha=$ 25					
3.5	25	40.84666	105.23608	PPf	094/41	E1: 0.8681	131	24	E1: 0.8498	130	18	E1: 0.8440	132	36
						E2: 0.0690	271	60	E2: 0.0842	223	8	E2: 0.1117	289	52
3.5	25	40.84666	105.23608	PPf	094/41	E3: 0.0629	33	17	E3: 0.066	335	70	E3: 0.0443	34	12
						$\alpha=$ 16			$\alpha=$ 25					

Appendix 1: Complete Shear Fracture Data Tables (continued).

Station #	N	Lat. °N	Long. °W	Fm	Attitude of Beds	Ideal σ_1 Stress Analysis (Compton, 1966) (Erslev and Larson, 2006)			Strain Analysis					
						Best Fit Alpha	E1	E2	E3	Average Slickenline	E1	E2	E3	
3.6A	12	40.8461	105.23898	PPF	065/68	E1: 0.8794 E2: 0.0770 E3: 0.0437 $\alpha=$ 14	145 235 326	45 0 45	E1: 0.8466 E2: 0.1032 E3: 0.0502 $\alpha=$ 25	146 23 271	43 31 32	E1: 0.8338 E2: 0.1271 E3: 0.0390	144 277 24	47 32 25
3.6B	11	40.84462	105.24362	PPF	061/38	E1: 0.8116 E2: 0.1094 E3: 0.0790 $\alpha=$ 20	130 13 263	44 25 36	E1: 0.8051 E2: 0.1188 E3: 0.0761 $\alpha=$ 25	128 345 238	45 39 19	E1: 0.7382 E2: 0.1639 E3: 0.0979	136 34 290	41 13 47
3.6C*	11	40.84409	105.2468	XY	n/a	E1: 0.9436 E2: 0.0453 E3: 0.0111 $\alpha=$ 25	87 229 356	11 75 9	E1: 0.9436 E2: 0.0453 E3: 0.0111 $\alpha=$ 25	87 229 356	11 75 9	E1: 0.9451 E2: 0.0448 E3: 0.0100	62 193 328	14 69 15
3.7*	31	40.83419	105.28027	XY	n/a	E1: 0.9218 E2: 0.0437 E3: 0.0345 $\alpha=$ 25	256 61 164	18 71 4	E1: 0.9218 E2: 0.0437 E3: 0.0345 $\alpha=$ 25	256 61 164	18 71 4	E1: 0.9315 E2: 0.0358 E3: 0.0327	282 190 83	20 6 69
3.8	55	40.83392	105.27791	PPF	089/46	E1: 0.7851 E2: 0.1577 E3: 0.0572 $\alpha=$ 25	156 61 268	11 25 63	E1: 0.7851 E2: 0.1577 E3: 0.0572 $\alpha=$ 25	156 61 268	11 25 63	E1: 0.8106 E2: 0.1290 E3: 0.0604	159 35 273	34 40 32
3.9	36	40.82388	105.23412	Pi	031/31	E1: 0.8837 E2: 0.0746 E3: 0.0417 $\alpha=$ 21	90 229 356	16 69 13	E1: 0.8798 E2: 0.0743 E3: 0.0459 $\alpha=$ 25	87 221 354	15 69 14	E1: 0.8264 E2: 0.1009 E3: 0.0727	103 206 342	22 29 53
3.10	30	40.81966	105.2401	Pi	039/10	E1: 0.8898 E2: 0.0819 E3: 0.0283 $\alpha=$ 22	87 178 349	2 16 74	E1: 0.8868 E2: 0.0847 E3: 0.0285 $\alpha=$ 25	88 179 349	3 16 74	E1: 0.7871 E2: 0.1811 E3: 0.0318	80 170 345	1 15 75

*Data not included in analysis of regional compressive stress but presented in the NW Livermore and Livermore Mtn fault data figures.

Appendix 1: Complete Shear Fracture Data Tables (continued).

Station #	N	Lat. °N	Long. °W	Fm	Attitude of Beds	Ideal σ_1 Stress Analysis (Best Fit Alpha)	Stress Analysis (Erslev and Larson, 2006)	Strain Analysis (Compton, 1966)	Average Slickenside					
3.11	35	40.81937	105.23997	Pi	043/29	E1: 0.7652	126	13	E1: 0.757	127	14	E1: 0.6070	140	18
						E2: 0.1572	217	5	E2: 0.168	220	11	E2: 0.3373	236	16
						E3: 0.0776	328	76	E3: 0.075	348	72	E3: 0.0557	6	66
						$\alpha=$ 30			$\alpha=$ 25					
3.12a	22	40.8153	105.24485	Pi	017/33	E1: 0.9123	91	20	E1: 0.9088	90	20	E1: 0.8366	104	29
						E2: 0.0594	184	7	E2: 0.0613	183	10	E2: 0.1340	200	10
						E3: 0.0283	290	68	E3: 0.0299	297	67	E3: 0.0294	306	59
						$\alpha=$ 22			$\alpha=$ 25					
3.12b	8	40.81448	105.24571	Pi	043/24	E1: 0.8469	265	3	E1: 0.8364	264	3	E1: 0.6413	83	1
						E2: 0.1306	173	28	E2: 0.1331	173	28	E2: 0.2935	173	46
						E3: 0.0225	1	62	E3: 0.0305	360	61	E3: 0.0651	352	44
						$\alpha=$ 31			$\alpha=$ 25					
3.12c	5	40.81402	105.24603	Pi	049/23	E1: 0.9851	105	21	E1: 0.9475	98	19	E1: 0.9692	114	24
						E2: 0.0103	217	44	E2: 0.0499	204	38	E2: 0.0295	23	4
						E3: 0.0046	357	38	E3: 0.0025	348	46	E3: 0.0013	284	66
						$\alpha=$ 15			$\alpha=$ 25					
3.12d	36	40.81337	105.24653	Pi	038/27	E1: 0.9034	87	16	E1: 0.8999	85	15	E1: 0.8470	102	25
						E2: 0.0627	355	6	E2: 0.0647	353	6	E2: 0.1203	199	14
						E3: 0.0339	245	73	E3: 0.0355	242	74	E3: 0.0327	316	61
						$\alpha=$ 22			$\alpha=$ 25					
3.12e	34	40.8096	105.24982	Pi	044/33	E1: 0.8836	104	8	E1: 0.8806	105	15	E1: 0.8545	111	40
						E2: 0.0880	13	6	E2: 0.0875	15	2	E2: 0.0989	16	6
						E3: 0.0284	246	81	E3: 0.032	279	75	E3: 0.0466	279	50
						$\alpha=$ 33			$\alpha=$ 25					
3.13	40	40.81063	105.24918	Pi	034/38	E1: 0.8058	88	9	E1: 0.7994	89	10	E1: 0.6693	103	21
						E2: 0.1309	183	31	E2: 0.1356	186	32	E2: 0.2744	206	30
						E3: 0.0633	343	58	E3: 0.065	344	56	E3: 0.0563	343	52
						$\alpha=$ 30			$\alpha=$ 25					

Appendix 1: Complete Shear Fracture Data Tables (continued).

Station #	N	Lat. °N	Long. °W	Fm	Attitude of Beds	Ideal σ_1 Stress Analysis (Compton, 1966) (Erslev and Larson, 2006)	Strain Analysis Average Slickenline
3.14	51	40.8101	105.24964	Pi	039/41	Best Fit Alpha E1: 0.7289 111 18 E2: 0.2237 213 32 E3: 0.0475 356 52 $\alpha=$ 30	E1: 0.5616 166 36 E2: 0.3867 259 4 E3: 0.0517 354 54
3.16	60	40.80103	105.21051	Pi	267/45	E1: 0.8615 86 3 E2: 0.0973 355 15 E3: 0.0412 186 74 $\alpha=$ 30	E1: 0.7417 92 22 E2: 0.1828 343 38 E3: 0.0755 205 43
3.17	35	40.79624	105.22095	Pi	226-30	E1: 0.8387 238 1 E2: 0.1024 329 17 E3: 0.0588 147 73 $\alpha=$ 29	E1: 0.7207 254 12 E2: 0.2321 347 13 E3: 0.0472 124 72
3.18a	10	40.79086	105.32285	PPf	263/4	E1: 0.9647 248 1 E2: 0.0295 340 61 E3: 0.0057 157 29 $\alpha=$ 13	E1: 0.9270 250 2 E2: 0.0436 341 18 E3: 0.0294 154 72
3.19*	30	40.78433	105.32791	XY	n/a	E1: 0.8604 224 33 E2: 0.1278 34 57 E3: 0.1118 131 4 $\alpha=$ 7	E1: 0.8471 223 34 E2: 0.0126 18 54 E3: 0.0265 125 12
3.20	57	40.78967	105.27051	PPf	040/16	E1: 0.8724 104 7 E2: 0.1062 196 18 E3: 0.0214 353 71 $\alpha=$ 14	E1: 0.8265 109 6 E2: 0.1411 201 21 E3: 0.0323 4 68
3.21	25	40.7857	105.25236	PPf	343/6	E1: 0.9636 94 3 E2: 0.0227 2 31 E3: 0.0137 188 59 $\alpha=$ 12	E1: 0.9441 102 3 E2: 0.0388 12 6 E3: 0.0171 215 83

*Data not included in analysis of regional compressive stress but presented in the Livermore Mtn fault data figure.

Appendix 1: Complete Shear Fracture Data Tables (continued).

Station #	N	Lat. °N	Long. °W	Fm	Attitude of Beds	Ideal σ_1 Stress Analysis (Compton, 1966) (Erslev and Larson, 2006)	Strain Analysis Average Slickenside
4.0	5	40.87262	105.20021	Pi	030/8	Best Fit Alpha E1: 0.9905 85 0 E2: 0.0065 355 8 E3: 0.0030 172 82 $\alpha=$ 21	E1: 0.9032 265 15 E2: 0.0906 94 75 E3: 0.0062 355 2
4.1	40	40.87472	105.20202	PPf	114/11	E1: 0.9172 258 11 E2: 0.0530 166 7 E3: 0.0298 46 77 $\alpha=$ 13	E1: 0.8770 256 12 E2: 0.0843 166 1 E3: 0.0387 73 78
4.2	44	40.86865	105.20583	PPf	055/17	E1: 0.9351 264 4 E2: 0.0457 172 29 E3: 0.0191 1 61 $\alpha=$ 25	E1: 0.7951 78 5 E2: 0.1371 202 80 E3: 0.0679 347 8
4.3	34	40.86673	105.20632	Pi	066/17	E1: 0.8811 70 7 E2: 0.0819 340 3 E3: 0.0370 231 82 $\alpha=$ 22	E1: 0.8193 57 12 E2: 0.1093 162 50 E3: 0.0714 318 38
4.5	66	40.85555	105.17442	Pi	002/18	E1: 0.9238 68 10 E2: 0.0495 334 19 E3: 0.0267 185 68 $\alpha=$ 21	E1: 0.8052 72 10 E2: 0.1480 340 7 E3: 0.0469 216 77
4.6	25	40.84727	105.1791	Poc	042/31	E1: 0.8912 88 18 E2: 0.0619 247 71 E3: 0.0469 356 6 $\alpha=$ 15	E1: 0.8397 81 15 E2: 0.0983 340 36 E3: 0.0620 190 51
4.7	50	40.85079	105.1771	Pi	034/21	E1: 0.8643 77 7 E2: 0.0941 176 53 E3: 0.0416 342 36 $\alpha=$ 21	E1: 0.7704 71 3 E2: 0.1518 162 26 E3: 0.0779 335 63

Appendix 1: Complete Shear Fracture Data Tables (continued).

Station #	N	Lat. °N	Long. °W	Fm	Attitude of Beds	Ideal σ_1 Stress Analysis (Best Fit Alpha)	Stress Analysis (Compton, 1966) (Erslev and Larson, 2006)	Strain Analysis (Average Slickenside)
4.8	100	40.84196	105.1888	Pi	061/14	E1: 0.9114 105 8 E2: 0.0615 198 21 E3: 0.0271 354 68 $\alpha=$ 18	E1: 0.8996 104 8 E2: 0.0697 195 11 E3: 0.0308 341 76 $\alpha=$ 25	E1: 0.8312 108 11 E2: 0.1406 200 9 E3: 0.0281 330 76
4.9	50	40.8747	105.18114	Pi	064/13	E1: 0.9430 77 10 E2: 0.0338 174 33 E3: 0.0232 333 55 $\alpha=$ 21	E1: 0.9375 76 9 E2: 0.0396 171 28 E3: 0.0229 330 60 $\alpha=$ 25	E1: 0.8431 84 12 E2: 0.1033 176 12 E3: 0.0537 311 73
4.10	229	40.85729	105.12229	Ksf	028/25	E1: 0.8860 91 21 E2: 0.0605 341 41 E3: 0.0535 201 41 $\alpha=$ 19	E1: 0.8753 90 21 E2: 0.067 182 6 E3: 0.0577 287 68 $\alpha=$ 25	E1: 0.8048 94 23 E2: 0.1324 192 17 E3: 0.0629 315 61
4.11	50	40.83727	105.14018	Ksf	055/34	E1: 0.9092 106 19 E2: 0.0621 343 58 E3: 0.0287 205 25 $\alpha=$ 15	E1: 0.8838 104 17 E2: 0.0636 233 64 E3: 0.0526 7 19 $\alpha=$ 25	E1: 0.8559 109 21 E2: 0.0868 19 0 E3: 0.0573 288 69
4.12	50	40.82912	105.1699	Ksf	080/24	E1: 0.9596 91 1 E2: 0.0250 183 13 E3: 0.0154 330 74 $\alpha=$ 12	E1: 0.9091 95 9 E2: 0.0735 189 21 E3: 0.0174 343 67 $\alpha=$ 25	E1: 0.9307 87 8 E2: 0.0546 178 8 E3: 0.0147 315 79
4.13	45	40.82733	105.1675	Kl	294/6	E1: 0.8079 271 3 E2: 0.1470 170 78 E3: 0.0451 2 12 $\alpha=$ 15	E1: 0.7898 271 1 E2: 0.1466 32 87 E3: 0.0636 181 2 $\alpha=$ 25	E1: 0.7516 270 5 E2: 0.1836 175 50 E3: 0.0648 4 40
4.14	85	40.81905	105.17506	Ksf	031/16	E1: 0.9176 114 13 E2: 0.0496 3 57 E3: 0.0328 211 29 $\alpha=$ 21	E1: 0.9142 113 12 E2: 0.0531 9 48 E3: 0.0327 213 39 $\alpha=$ 25	E1: 0.8087 120 15 E2: 0.1261 211 4 E3: 0.0652 314 74

Appendix 1: Complete Shear Fracture Data Tables (continued).

Station #	N	Lat. °N	Long. °W	Fm	Attitude of Beds	Ideal σ_1 Stress Analysis (Compton, 1966) (Erslev and Larson, 2006)	Strain Analysis Average Slickenside
4.15	60	40.81739	105.1749	Ksf	344/16	E1: 0.9241 106 12 E2: 0.0651 15 6 E3: 0.0108 260 76 $\alpha=$ 21	E1: 0.8430 107 21 E2: 0.1107 283 69 E3: 0.0463 16 1
4.16	42	40.81384	105.18173	Ksf	319/9	E1: 0.9624 111 9 E2: 0.0264 21 1 E3: 0.0112 286 81 $\alpha=$ 18	E1: 0.8801 104 11 E2: 0.1085 12 6 E3: 0.0114 255 78
4.17	100	40.8059	105.17125	Kl	271/35	E1: 0.9043 300 14 E2: 0.0538 42 42 E3: 0.0420 195 45 $\alpha=$ 21	E1: 0.7990 296 13 E2: 0.1492 35 33 E3: 0.0518 187 54
4.18	100	40.81387	105.17125	Ksf	315/21	E1: 0.9198 104 10 E2: 0.0503 14 1 E3: 0.0299 281 80 $\alpha=$ 19	E1: 0.8307 105 10 E2: 0.1360 13 11 E3: 0.0334 237 75
4.19	45	40.7992	105.14457	Ksf	334/16	E1: 0.9512 87 13 E2: 0.0370 356 6 E3: 0.0117 242 75 $\alpha=$ 18	E1: 0.8790 91 20 E2: 0.0739 348 30 E3: 0.0471 209 52
4.20	50	40.80033	105.14566	Ksf	342-18	E1: 0.9378 87 10 E2: 0.0516 354 13 E3: 0.0106 213 74 $\alpha=$ 21	E1: 0.8524 91 17 E2: 0.1056 328 60 E3: 0.0420 188 23
4.22	235	40.76829	105.1469	Kpl	020/14	E1: 0.9547 89 11 E2: 0.0308 181 7 E3: 0.0145 303 77 $\alpha=$ 22	E1: 0.8264 89 13 E2: 0.1475 261 77 E3: 0.0261 359 2

Appendix 1: Complete Shear Fracture Data Tables (continued).

Station #	N	Lat. °N	Long. °W	Fm	Attitude of Beds	Ideal σ_1 Stress Analysis (Compton, 1966) Best Fit Alpha	Strain Analysis Average Slickenside	
4.25b*	42	40.65514	105.17943	Kpl	348/17	E1: 0.9651 76 10	E1: 0.9609 76 10	E1: 0.8456 77 11
						E2: 0.0243 167 5	E2: 0.0251 167 7	E2: 0.1307 260 79
						E3: 0.0106 281 79	E3: 0.0139 292 78	E3: 0.0237 167 1
						$\alpha=$ 21	$\alpha=$ 25	
NHR1*	22	40.59947	105.17458	Poc	345/22	E1: 0.9436 58 15	E1: 0.9412 58 17	E1: 0.8703 239 0
						E2: 0.0355 325 13	E2: 0.0373 321 21	E2: 0.0991 146 87
						E3: 0.0209 195 70	E3: 0.0215 184 63	E3: 0.0306 329 3
						$\alpha=$ 21	$\alpha=$ 25	
NHR2*	45	40.6038	105.16852	Kpl	357/20	E1: 0.817 45 14	E1: 0.8039 45 11	E1: 0.7552 44 20
						E2: 0.1599 136 3	E2: 0.1689 138 14	E2: 0.1974 303 28
						E3: 0.0232 237 76	E3: 0.0272 278 72	E3: 0.0475 165 54
						$\alpha=$ 18	$\alpha=$ 25	
NHR3*	24	40.58752	105.16115	Ksf	342/30	E1: 0.9363 62 15	E1: 0.9363 62 15	E1: 0.8023 65 16
						E2: 0.0375 155 9	E2: 0.0375 155 9	E2: 0.1652 278 71
						E3: 0.0262 274 73	E3: 0.0262 274 73	E3: 0.0325 157 10
						$\alpha=$ 25	$\alpha=$ 25	
SHR1*	38	40.53259	105.13883	Ksf	334/16	E1: 0.9508 75 15	E1: 0.9503 75 15	E1: 0.8087 78 15
						E2: 0.0372 314 13	E2: 0.0379 341 15	E2: 0.1802 347 1
						E3: 0.0120 212 70	E3: 0.0118 208 69	E3: 0.0111 255 75
						$\alpha=$ 23	$\alpha=$ 25	

*Data not included in analysis of regional compressive stress but presented in the Laporte and Horsetooth fault data figures.

Appendix 2: Complete Joint Data Tables.

Station #	N	Lat. °N	Long. °W	Fm	S/D Beds	Poles to Planes		Joint poles w/ beds rotated to horiz	
						J1 Joints	J2 Joints	J1 Joints	J2 Joints
1.2a*	20	41.06	105.18424	PPf	036/46	E1 0.9796 147 42 E2 0.0162 331 48 E3 0.0042 239 2 20 J1 S/D 237 48	E1 0.87 62 24 E2 0.1006 310 29 E3 0.0293 175 41 45 J2 S/D 152 66	E1 0.9796 321 2 E2 0.0162 56 72 E3 0.0042 231 17 J1 S/D 51 88	E1 0.87 65 17 E2 0.1006 314 50 E3 0.0293 168 35 J2 S/D 155 73
1.4	49	41.02293	105.20745	PPf	315/21	E1 0.9867 338 11 E2 0.0096 157 79 E3 0.0038 248 0 4 J1 S/D 68 79	E1 0.986 43 26 E2 0.014 311 4 E3 0 213 64 2 J2 S/D 133 64	E1 0.9867 340 19 E2 0.0096 136 70 E3 0.0038 247 8 J1 S/D 70 71	E1 0.986 47 20 E2 0.014 312 16 E3 0 186 64 J1 S/D 137 70
1.5*	42	41.01817	105.18629	PPf	037/14	E1 0.9478 143 6 E2 0.0418 49 31 E3 0.0104 244 59 40 J1 S/D 233 84	E1 0.986 43 26 E2 0.014 311 4 E3 0 213 64 2 J2 S/D 133 64	E1 0.9478 323 4 E2 0.0418 55 23 E3 0.0104 223 66 J1 S/D 53 86	E1 0.986 47 20 E2 0.014 312 16 E3 0 186 64 J1 S/D 137 70
1.6	14	41.01673	105.1985	PPf	012/12	E1 0.9256 154 3 E2 0.0549 64 12 E3 0.0196 256 77 13 J1 S/D 244 87	E1 1 53 1 E2 0 289 88 E3 0 143 1 1 J2 S/D 143 89	E1 0.9256 334 7 E2 0.0549 65 5 E3 0.0196 190 82 J1 S/D 64 83	E1 1 233 5 E2 0 119 78 E3 0 324 11 J1 S/D 323 85
1.7	25	40.99642	105.20812	PPf	016/12	E1 0.9837 334 0 E2 0.0116 64 19 E3 0.0047 242 71 25 J1 S/D 64 90		E1 0.9837 334 8 E2 0.0116 66 10 E3 0.0047 205 77 J1 S/D 64 82	
GCF	30	40.92049	105.15883	TrP1	019/15		E1 0.937 68 13 E2 0.0475 162 20 E3 0.0155 308 66 30 J2 S/D 158 77		E1 0.937 69 1 E2 0.0475 159 11 E3 0.0155 332 79 J2 S/D 159 89
2.12	143	40.88877	105.15578	TrP1	325/7	E1 0.9923 330 4 E2 0.0052 235 44 E3 0.0026 64 45 76 J1 S/D 60 86	E1 0.9801 64 5 E2 0.0116 322 68 E3 0.0082 156 21 67 J2 S/D 154 85	E1 0.9923 330 4 E2 0.0052 235 51 E3 0.0026 63 38 J1 S/D 60 86	E1 0.9801 244 2 E2 0.0116 339 68 E3 0.0082 153 22 J2 S/D 334 88
3.18b	19	40.79086	105.32285	PPf	263/4		E1 0.9804 40 1 E2 0.0121 132 60 E3 0.0075 309 30 19 J2 S/D 130 89		E1 0.9804 220 2 E2 0.0121 127 63 E3 0.0075 311 27 J2 S/D 310 88

*Uncertainty regarding origin of fractures, may be dissolution cleavage planes.

Appendix 2: Complete Joint Data Tables (continued).

Station #	N	Lat. °N	Long. °W	Fm	S/D Beds	Poles to Planes		Joint poles w/ beds rotated to horiz					
						J1 Joints	J2 Joints	J1 Joints	J2 Joints				
3.21b	19	40.7857	105.25236	PPf	343/6	E1 0.9787	118	6	E1 0.9787	117	1		
						E2 0.0125	8	73	E2 0.0125	24	70		
						E3 0.0088	209	16	E3 0.0088	208	20		
						19	J2 S/D	208	84				
4.23	47	40.73992	105.16237	K1	016/13	E1 0.9819	146	6	E1 0.9819	326	4		
						E2 0.0122	47	56	E2 0.0122	60	48		
						E3 0.0059	240	33	E3 0.0059	232	41		
						39	J1 S/D	236	84	8	J2 S/D	136	84
						E1 0.9915	148	3	E1 0.9915	328	3		
						E2 0.0053	56	29	E2 0.0053	58	14		
E3 0.0032	243	60	E3 0.0032	226	76								
44	J1 S/D	238	87	26	J2 S/D	150	79						
4.25b	70	40.65514	105.17943	Kpl	348/17	E1 0.9163	350	4	E1 0.9163	352	6		
						E2 0.0504	257	29	E2 0.0504	252	58		
						E3 0.0333	87	60	E3 0.0333	86	31		
						43	J1 S/D	80	86	44	J2 S/D	170	65
						E1 0.9282	147	8	E1 0.9282	326	2		
						E2 0.0469	52	31	E2 0.0469	56	14		
E3 0.0248	249	58	E3 0.0248	226	73								
25	J1 S/D	237	82	25	J2 S/D	157	74						
5.1	87	40.60776	105.16908	Ksf	355/29	E1 0.9784	128	17	E1 0.9784	125	3		
						E2 0.0182	280	71	E2 0.0182	17	81		
						E3 0.0033	35	8	E3 0.0033	215	9		
						45	J1 S/D	218	73	45	J2 S/D	136	66
						E1 0.956	340	3	E1 0.956	341	1		
						E2 0.0356	72	37	E2 0.0356	71	4		
E3 0.0084	246	53	E3 0.0084	237	86								
19	J1 S/D	70	87	25	J2 S/D	159	56						
5.2	50	40.60366	105.16888	Kpl	357/20	E1 0.9112	104	32	E1 0.9112	99	6		
						E2 0.0549	208	20	E2 0.0549	194	39		
						E3 0.0339	324	51	E3 0.0339	2	50		
						30	J2 S/D	194	58	19	J1 S/D	112	78
						E1 0.9282	147	8	E1 0.9282	326	2		
						E2 0.0469	52	31	E2 0.0469	56	14		
E3 0.0248	249	58	E3 0.0248	226	73								
25	J1 S/D	237	82	25	J2 S/D	157	74						
5.3	90	40.59859	105.17458	Poc	345/22	E1 0.9784	128	17	E1 0.9784	125	3		
						E2 0.0182	280	71	E2 0.0182	17	81		
						E3 0.0033	35	8	E3 0.0033	215	9		
						45	J1 S/D	218	73	45	J2 S/D	136	66
						E1 0.956	340	3	E1 0.956	341	1		
						E2 0.0356	72	37	E2 0.0356	71	4		
E3 0.0084	246	53	E3 0.0084	237	86								
19	J1 S/D	70	87	25	J2 S/D	159	56						
5.4	50	40.59183	105.16408	Kpl/K1	337/33	E1 0.9112	104	32	E1 0.9112	99	6		
						E2 0.0549	208	20	E2 0.0549	194	39		
						E3 0.0339	324	51	E3 0.0339	2	50		
						30	J2 S/D	194	58	19	J1 S/D	112	78
						E1 0.9282	147	8	E1 0.9282	326	2		
						E2 0.0469	52	31	E2 0.0469	56	14		
E3 0.0248	249	58	E3 0.0248	226	73								
25	J1 S/D	237	82	25	J2 S/D	157	74						
5.5	50	40.59138	105.16279	Ksf	342/30	E1 0.9784	128	17	E1 0.9784	125	3		
						E2 0.0182	280	71	E2 0.0182	17	81		
						E3 0.0033	35	8	E3 0.0033	215	9		
						45	J1 S/D	218	73	45	J2 S/D	136	66
						E1 0.956	340	3	E1 0.956	341	1		
						E2 0.0356	72	37	E2 0.0356	71	4		
E3 0.0084	246	53	E3 0.0084	237	86								
19	J1 S/D	70	87	25	J2 S/D	159	56						
						39	J1 S/D	236	84				
						E1 0.9819	146	6	E1 0.9819	326	4		
						E2 0.0122	47	56	E2 0.0122	60	48		
						E3 0.0059	240	33	E3 0.0059	232	41		
						39	J1 S/D	236	84	J1 S/D	56	86	
						E1 0.9915	148	3	E1 0.9915	328	3		
						E2 0.0053	56	29	E2 0.0053	58	14		
						E3 0.0032	243	60	E3 0.0032	226	76		
						44	J1 S/D	238	87	J1 S/D	58	87	
						E1 0.9163	350	4	E1 0.9163	352	6		
						E2 0.0504	257	29	E2 0.0504	252	58		
						E3 0.0333	87	60	E3 0.0333	86	31		
						43	J1 S/D	80	86	J1 S/D	82	84	
						E1 0.9282	147	8	E1 0.9282	326	2		
						E2 0.0469	52	31	E2 0.0469	56	14		
						E3 0.0248	249	58	E3 0.0248	226	73		
						25	J1 S/D	237	82	J1 S/D	56	88	
						E1 0.9784	128	17	E1 0.9784	125	3		
						E2 0.0182	280	71	E2 0.0182	17	81		
						E3 0.0033	35	8	E3 0.0033	215	9		
						45	J1 S/D	218	73	J1 S/D	215	87	
						E1 0.956	340	3	E1 0.956	341	1		
						E2 0.0356	72	37	E2 0.0356	71	4		
						E3 0.0084	246	53	E3 0.0084	237	86		
						19	J1 S/D	70	87	J1 S/D	71	89	
						E1 0.9112	104	32	E1 0.9112	99	6		
						E2 0.0549	208	20	E2 0.0549	194	39		
						E3 0.0339	324	51	E3 0.0339	2	50		
						30	J2 S/D	194	58	J2 S/D	189	84	
						E1 0.863	22	12	E1 0.863	202	8		
						E2 0.1134	114	9	E2 0.1134	294	13		
						E3 0.0236	241	75	E3 0.0236	83	73		
						19	J1 S/D	112	78	J1 S/D	292	82	

Appendix 2: Complete Joint Data Tables (continued).

Station #	N	Lat. °N	Long. °W	Fm	S/D Beds	Poles to Planes		Joint poles w/ beds rotated to horiz					
						J1 Joints	J2 Joints	J1 Joints	J2 Joints				
5.6	42	40.58891	105.161	Ksf	336/28	E1 0.9607	126 9	E1 0.9359	32 20	E1 0.9607	305 6	E1 0.9359	214 3
						E2 0.0207	35 7	E2 0.0563	123 5	E2 0.0207	214 17	E2 0.0563	304 10
						E3 0.0186	266 79	E3 0.0077	226 69	E3 0.0186	53 72	E3 0.0077	106 79
5.7	74	40.5878	105.1627	Kpl/Kl	353/30	J1 S/D	216 81	J2 S/D	122 70	J1 S/D	35 84	J2 S/D	304 87
						E1 0.9823	165 6	E1 0.9745	74 31	E1 0.9823	163 1	E1 0.9745	75 2
						E2 0.0093	68 49	E2 0.0174	229 56	E2 0.0093	73 20	E2 0.0174	170 75
5.8	40	40.53583	105.14217	ksf	343/21	E3 0.0084	260 40	E3 0.0081	337 11	E3 0.0084	255 70	E3 0.0081	345 18
						J1 S/D	255 84	J2 S/D	164 59	J1 S/D	253 89	J2 S/D	165 88
						E1 0.7023	341 2	E1 0.972	59 16	E1 0.7023	342 3	E1 0.972	240 5
5.9	50	40.53302	105.14002	Ksf	343/20	E2 0.2847	72 13	E2 0.0176	159 31	E2 0.2847	252 8	E2 0.0176	147 28
						E3 0.0131	241 77	E3 0.0104	307 54	E3 0.0131	91 81	E3 0.0104	339 62
						J1 S/D	71 88	J2 S/D	149 74	J1 S/D	72 87	J2 S/D	330 85
5.10	50	40.53128	105.14158	Kl	002/20	E1 0.8126	149 8	E1 0.9287	64 17	E1 0.8126	148 2	E1 0.9287	244 3
						E2 0.1643	58 13	E2 0.0547	334 1	E2 0.1643	238 7	E2 0.0547	334 4
						E3 0.0231	269 75	E3 0.0166	241 73	E3 0.0231	37 83	E3 0.0166	122 85
5.11	88	40.52987	105.13739	Ksf	355/21	J1 S/D	239 82	J2 S/D	154 73	J1 S/D	238 88	J2 S/D	334 87
						E1 0.7585	162 3	E1 0.9414	59 20	E1 0.7585	164 9	E1 0.9414	61 3
						E2 0.2307	72 15	E2 0.0307	166 39	E2 0.2307	68 33	E2 0.0307	153 31
5.11	88	40.52987	105.13739	Ksf	355/21	E3 0.0108	262 75	E3 0.0279	308 44	E3 0.0108	267 55	E3 0.0279	326 59
						J1 S/D	252 87	J2 S/D	149 70	J1 S/D	254 81	J2 S/D	151 87
						E1 0.8521	171 1	E1 0.8836	78 14	E1 0.8521	351 0	E1 0.8836	258 7
5.11	88	40.52987	105.13739	Ksf	355/21	E2 0.1325	81 16	E2 0.0906	171 14	E2 0.1325	261 5	E2 0.0906	167 11
						E3 0.0154	265 74	E3 0.0258	303 70	E3 0.0154	84 85	E3 0.0258	17 77
						J1 S/D	261 89	J2 S/D	168 76	J1 S/D	81 90	J2 S/D	348 83

Appendix 3: Complete Bedding Attitude Data Tables (Continued)

#	Lat. °N (WGS 84)	Long. °W	m E (13N NAD 27)	m N	Strike	Dip	Dip Az
1	41.0973	105.15256	472504	4514695	40	23	130
2	41.09549	105.1524	473153	4515505	55	31	145
3	41.09221	105.1596	476244	4520128	74	30	164
4	41.09124	105.16138	476614	4520148	73	35	163
5	41.09077	105.16564	476732	4528938	56	52	146
6	41.09075	105.16697	476773	4520136	58	46	148
7	41.06709	105.17644	476803	4529047	39	49	129
8	41.06648	105.17477	476946	4529005	40	40	130
9	41.06644	105.17559	477104	4528780	34	43	124
10	41.06626	105.17576	477186	4528841	40	37	130
11	41.06563	105.17393	477222	4515234	27	30	117
12	41.06431	105.17999	477263	4515219	41	20	131
13	41.03078	105.20076	477286	4528896	28	14	118
14	41.03075	105.19872	478753	4514997	35	11	125
15	41.02784	105.19478	478869	4515013	38	13	128
16	41.02587	105.20745	478951	4515024	23	8	113
17	41.02547	105.18448	478972	4517517	293	12	23
18	41.0253	105.18816	478980	4517610	253	38	343
19	41.02528	105.18709	478984	4517456	254	23	344
20	41.02521	105.18981	479001	4517499	265	27	355
21	41.02518	105.19036	479001	4517504	254	24	344
22	41.02437	105.18848	479003	4517485	260	16	350
23	41.02425	105.20806	479014	4517511	342	10	72
24	41.02415	105.20803	479029	4517556	346	11	76
25	41.02408	105.18751	479107	4517652	138	4	228
26	41.02357	105.18735	479114	4517503	15	5	105
27	41.02347	105.2078	479177	4517723	317	20	47
28	41.02301	105.18829	479259	4517833	28	7	118
29	41.02293	105.20745	479264	4517870	315	21	45
30	41.02279	105.18722	479268	4517884	9	18	99
31	41.02213	105.18713	479295	4517931	50	6	140
32	41.0198	105.1972	479327	4518134	174	6	264
33	41.01817	105.18629	479395	4518073	37	14	127
34	41.01812	105.19743	479399	4518307	24	12	114
35	41.01773	105.18435	479447	4521335	6	10	96
36	41.01753	105.18179	479451	4518171	19	13	109
37	41.01673	105.1985	479474	4518105	24	12	114
38	41.01489	105.19976	479481	4518205	24	12	114
39	40.99642	105.20812	479497	4518184	16	12	106
40	40.98314	105.16151	479506	4518224	207	11	297
41	40.98197	105.15996	479508	4521327	336	5	66
42	40.98173	105.17378	479509	4518200	21	10	111
43	40.98169	105.16427	479533	4521368	196	27	286
44	40.98149	105.16443	479535	4521381	201	29	291
45	40.98123	105.17259	479537	4518220	16	16	106
46	40.98119	105.16364	479648	4518453	198	32	288
47	40.98085	105.1638	479658	4518415	195	30	285
48	40.9808	105.17242	479663	4518371	34	16	124
49	40.98055	105.17186	479676	4518520	44	13	134
50	40.98022	105.1701	479720	4518588	38	7	128
51	40.97918	105.16068	479737	4518480	350	4	80

Appendix 3: Complete Bedding Attitude Data Tables (Continued)

#	Lat. °N (WGS 84)	Long. °W	m E (13N NAD 27)	m N	Strike	Dip	Dip Az
52	40.97915	105.16544	479794	4518543	198	34	288
53	40.97871	105.16426	479797	4518556	197	32	287
54	40.97838	105.16128	479801	4518567	36	1.5	126
55	40.97812	105.16588	479805	4518540	193	34	283
56	40.97782	105.16093	479815	4518698	307	6	37
57	40.97739	105.16707	479847	4518631	82	12	172
58	40.97726	105.16641	479850	4518758	196	39	286
59	40.9772	105.16759	479869	4518598	15	24	105
60	40.97678	105.15843	479892	4518551	1	14	91
61	40.97575	105.16742	479899	4521491	203	40	293
62	40.9756	105.15395	479923	4518842	17	16	107
63	40.9754	105.16713	479923	4518566	208	40	298
64	40.97523	105.15377	479929	4518665	16	15	106
65	40.97501	105.15477	479935	4518779	53	36	143
66	40.97485	105.15852	479936	4518665	24	12	114
67	40.97416	105.1559	479938	4518670	10	15	100
68	40.97367	105.1676	479993	4521488	220	37	310
69	40.97294	105.16871	480004	4518863	247	37	337
70	40.97293	105.15383	480144	4518954	7	14	97
71	40.97272	105.1694	480144	4521552	235	35	325
72	40.9715	105.16545	480164	4518929	266	17	356
73	40.97138	105.15086	480202	4518961	3	12	93
74	40.97115	105.15221	480205	4519122	14	14	104
75	40.9702	105.16641	480246	4519099	358	13	88
76	40.96976	105.16832	480272	4519082	215	36	305
77	40.96967	105.17342	480288	4519063	221	10	311
78	40.96931	105.17754	480303	4519023	1	18	91
79	40.96922	105.16938	480309	4519059	214	51	304
80	40.96915	105.16961	480330	4519045	227	41	317
81	40.9691	105.17001	480335	4521562	215	42	305
82	40.96875	105.16698	480456	4521504	1	6	91
83	40.96865	105.17042	480518	4527309	218	41	308
84	40.96804	105.16999	480662	4521848	210	31	300
85	40.9679	105.16961	480668	4521822	210	22	300
86	40.96773	105.16932	480676	4521806	258	7	348
87	40.96751	105.16878	480803	4521278	354	10	84
88	40.96738	105.17718	480840	4527276	311	7	41
89	40.96644	105.17235	480907	4527335	204	54	294
90	40.96639	105.17226	481405	4515952	204	53	294
91	40.9659	105.17156	481540	4523131	202	37	292
92	40.96582	105.17137	481552	4523003	201	35	291
93	40.96566	105.1711	481568	4527310	200	33	290
94	40.96532	105.1706	481568	4527310	254	6	344
95	40.96524	105.17047	481755	4522117	1	8	91
96	40.96518	105.17038	481783	4522496	2	6	92
97	40.96469	105.17073	481786	4522777	19	13	109
98	40.96446	105.17754	481868	4523341	1	7	91
99	40.96392	105.17075	481876	4530565	313	3	43
100	40.96384	105.17256	481909	4522219	203	46	293
101	40.96378	105.17175	481939	4523215	224	18	314
102	40.96378	105.17306	481988	4522955	204	46	294

Appendix 3: Complete Bedding Attitude Data Tables (Continued)

#	Lat. °N (WGS 84)	Long. °W	m E (13N NAD 27)	m N	Strike	Dip	Dip Az
103	40.96376	105.17144	482016	4522283	266	6	356
104	40.96375	105.17111	482041	4522517	194	8	284
105	40.96367	105.1721	482058	4522790	204	39	294
106	40.96324	105.16984	482061	4522411	9	8	99
107	40.96304	105.16957	482089	4523401	8	13	98
108	40.96301	105.1735	482090	4522726	209	49	299
109	40.96287	105.1692	482094	4522552	360	13	90
110	40.96257	105.16906	482097	4522652	2	14	92
111	40.96188	105.17365	482097	4522652	223	52	313
112	40.96132	105.17383	482207	4522776	201	50	291
113	40.96119	105.17236	482287	4516482	270	7	0
114	40.96115	105.17363	482421	4523229	205	38	295
115	40.96087	105.17468	482510	4523974	202	41	292
116	40.96082	105.17353	482513	4524275	208	36	298
117	40.96066	105.17325	482533	4523827	211	31	301
118	40.96041	105.17164	482540	4538170	358	2.5	88
119	40.9604	105.17505	482553	4541260	207	48	297
120	40.96032	105.17284	482555	4541248	185	5	275
121	40.96002	105.17169	482574	4541173	359	6	89
122	40.95996	105.17258	482604	4541113	356	1.5	86
123	40.95987	105.17379	482604	4541439	205	29	295
124	40.9598	105.17367	482635	4526672	209	14	299
125	40.95971	105.17318	482657	4526489	24	6	114
126	40.95953	105.1748	482658	4523774	198	44	288
127	40.95942	105.1743	482700	4523987	208	37	298
128	40.95932	105.1741	482704	4526344	200	25	290
129	40.95915	105.17419	482770	4526199	198	32	288
130	40.95904	105.17409	482790	4523521	216	19	306
131	40.95899	105.17387	482856	4526159	210	13	300
132	40.95895	105.17288	482890	4526111	7	6	97
133	40.95895	105.17398	482994	4523603	196	17	286
134	40.95892	105.17357	483022	4524660	214	7	304
135	40.95885	105.17371	483078	4526226	245	4	335
136	40.95878	105.17339	483081	4526136	323	2	53
137	40.95826	105.17126	483086	4526019	48	7	138
138	40.95739	105.17171	483163	4529838	38	17	128
139	40.95448	105.17479	483168	4541983	41	4	131
140	40.95446	105.17445	483174	4524426	54	3	144
141	40.95443	105.17493	483191	4527787	43	4	133
142	40.95436	105.17547	483248	4540219	164	16	254
143	40.95435	105.17583	483289	4527759	181	33	271
144	40.9543	105.16818	483311	4526716	356	13	86
145	40.95428	105.17524	483315	4527751	148	15	238
146	40.95424	105.17627	483318	4527594	177	35	267
147	40.95423	105.17339	483321	4527722	45	9	135
148	40.95417	105.17679	483340	4541979	176	39	266
149	40.95412	105.17648	483345	4526852	177	34	267
150	40.95385	105.17777	483348	4526779	176	39	266
151	40.95374	105.17241	483348	4527575	47	11	137
152	40.9537	105.16595	483355	4540423	182	14	272
153	40.95346	105.16716	483365	4527505	360	12	90

Appendix 3: Complete Bedding Attitude Data Tables (Continued)

#	Lat. °N (WGS 84)	Long. °W	m E (13N NAD 27)	m N	Strike	Dip	Dip Az
154	40.9528	105.17479	483365	4527585	73	5	163
155	40.95249	105.17706	483382	4526751	179	34	269
156	40.95234	105.17392	483385	4528007	49	11	139
157	40.95227	105.17482	483396	4527461	136	8	226
158	40.95176	105.17203	483414	4527453	66	20	156
159	40.95164	105.17422	483424	4528169	38	11	128
160	40.95137	105.18501	483434	4528426	76	24	166
161	40.95134	105.1769	483445	4526680	168	26	258
162	40.95123	105.17361	483445	4540577	35	12	125
163	40.9512	105.17223	483447	4527435	50	10	140
164	40.95118	105.175	483448	4527101	115	15	205
165	40.95104	105.17564	483465	4540763	140	15	230
166	40.951	105.17619	483467	4527376	135	23	225
167	40.95063	105.17014	483488	4528416	20	12	110
168	40.9502	105.1722	483493	4528189	60	11	150
169	40.94868	105.17604	483500	4528181	112	34	202
170	40.94798	105.1678	483516	4527428	4	11	94
171	40.94797	105.1686	483519	4527062	212	14	302
172	40.94675	105.16628	483541	4527767	236	10	326
173	40.94672	105.16651	483563	4526796	281	15	11
174	40.94391	105.16451	483565	4528424	336	12	66
175	40.94352	105.16706	483591	4526825	168	21	258
176	40.94269	105.16164	483592	4528406	322	14	52
177	40.94185	105.16365	483595	4528484	290	8	20
178	40.94168	105.16239	483598	4528407	327	9	57
179	40.94111	105.17521	483652	4528444	28	12	118
180	40.94104	105.16028	483670	4541656	325	14	55
181	40.94074	105.1755	483705	4528512	38	18	128
182	40.94013	105.17896	483723	4528531	10	12	100
183	40.9398	105.16291	483741	4528496	312	5	42
184	40.93959	105.16328	483816	4528456	5	2	95
185	40.93908	105.17126	483828	4528387	152	24	242
186	40.93822	105.16122	483882	4528361	354	7	84
187	40.93809	105.16152	483904	4528340	343	7	73
188	40.93777	105.16246	483964	4523147	280	1	10
189	40.93691	105.17579	483965	4523288	355	17	85
190	40.93686	105.17068	483967	4516115	178	46	268
191	40.93676	105.17065	483995	4522903	169	37	259
192	40.9366	105.17061	483996	4521144	174	40	264
193	40.93618	105.16012	484009	4523087	2	12	92
194	40.93476	105.16038	484041	4523366	257	17	347
195	40.93476	105.16148	484041	4541359	7	9	97
196	40.93472	105.16277	484058	4522971	16	14	106
197	40.93467	105.16241	484061	4521081	301	2	31
198	40.93456	105.1621	484087	4541363	19	9	109
199	40.93441	105.16273	484089	4516177	167	8	257
200	40.93423	105.16387	484128	4521021	186	26	276
201	40.93387	105.16959	484135	4520947	159	36	249
202	40.93364	105.15921	484186	4516212	9	14	99
203	40.93363	105.16016	484199	4541269	3	11	93
204	40.93349	105.16342	484205	4520914	180	12	270

Appendix 3: Complete Bedding Attitude Data Tables (Continued)

#	Lat. °N (WGS 84)	Long. °W	m E (13N NAD 27)	m N	Strike	Dip	Dip Az
205	40.93345	105.16988	484215	4541118	174	23	264
206	40.93332	105.16125	484226	4541372	348	7	78
207	40.9333	105.15956	484230	4516217	357	8	87
208	40.93322	105.16183	484256	4520818	19	3.5	109
209	40.9332	105.16064	484273	4520869	352	8	82
210	40.93319	105.1624	484280	4541237	138	3	228
211	40.93315	105.16509	484281	4520694	195	63	285
212	40.93288	105.16348	484282	4520753	185	13	275
213	40.93288	105.16386	484293	4516279	181	22	271
214	40.93272	105.15857	484294	4541180	356	13	86
215	40.93255	105.16362	484299	4521340	171	23	261
216	40.93254	105.16424	484304	4541094	160	24	250
217	40.93253	105.1648	484312	4541020	177	21	267
218	40.93143	105.15656	484315	4516244	59	13	149
219	40.93116	105.15715	484316	4541370	357	11	87
220	40.92789	105.2158	484359	4523380	12	9	102
221	40.92717	105.14188	484382	4540581	0	13	90
222	40.92137	105.20049	484386	4521374	24	14	114
223	40.91537	105.14468	484411	4522999	4	9	94
224	40.91409	105.276	484417	4522995	10	36	100
225	40.91372	105.27429	484423	4516179	144	9	234
226	40.91311	105.27684	484469	4516138	125	5	215
227	40.91274	105.27025	484474	4533165	133	11	223
228	40.91248	105.14043	484504	4516087	8	11	98
229	40.91225	105.27144	484520	4521524	83	50	173
230	40.91169	105.27241	484535	4541391	83	10	173
231	40.91032	105.13786	484545	4540531	349	12	79
232	40.90961	105.19381	484553	4521506	220	54	310
233	40.90948	105.13784	484561	4521458	16	16	106
234	40.90944	105.19402	484571	4522706	224	55	314
235	40.90929	105.19359	484574	4517535	215	46	305
236	40.90918	105.19532	484593	4522769	268	8	358
237	40.90894	105.1927	484615	4522885	223	27	313
238	40.90882	105.19465	484650	4522920	207	57	297
239	40.90866	105.19723	484674	4517923	14	7	104
240	40.90864	105.19568	484699	4521474	218	9	308
241	40.90857	105.19659	484741	4521074	339	5	69
242	40.90849	105.19529	484754	4521529	219	41	309
243	40.90848	105.19536	484760	4540509	219	30	309
244	40.90831	105.19256	484765	4522951	249	14	339
245	40.90808	105.19191	484771	4517336	298	2	28
246	40.90789	105.19165	484775	4521190	334	7	64
247	40.90652	105.19653	484775	4521631	210	56	300
248	40.90645	105.19644	484779	4521367	206	72	296
249	40.90634	105.19735	484807	4521564	2	9	92
250	40.9058	105.13644	484831	4500413	2	13	92
251	40.90546	105.1471	484838	4517268	358	11	88
252	40.90488	105.19781	484869	4517836	298	6	28
253	40.90445	105.13692	484876	4500282	313	6	43
254	40.9031	105.13246	484922	4545701	357	9	87
255	40.9029	105.2001	484952	4521608	7	8	97

Appendix 3: Complete Bedding Attitude Data Tables (Continued)

#	Lat. °N (WGS 84)	Long. °W	m E (13N NAD 27)	m N	Strike	Dip	Dip Az
256	40.90272	105.19595	484952	4521608	197	14	287
257	40.90265	105.19894	484974	4521577	326	6	56
258	40.90257	105.19863	484980	4531916	203	15	293
259	40.90231	105.19856	484982	4517648	207	13	297
260	40.90116	105.19859	484982	4500129	204	9	294
261	40.90108	105.19803	484985	4521453	195	38	285
262	40.90099	105.19823	485017	4521402	190	55	280
263	40.90036	105.19803	485023	4521353	188	52	278
264	40.89996	105.19766	485058	4521326	187	62	277
265	40.89989	105.19745	485068	4522671	184	58	274
266	40.89973	105.19705	485083	4533439	200	43	290
267	40.89967	105.19624	485105	4534617	208	7	298
268	40.8992	105.19681	485106	4535155	208	25	298
269	40.89877	105.22721	485114	4521999	19	14	109
270	40.89856	105.21936	485136	4534941	25	8	115
271	40.89856	105.21936	485143	4533288	112	28	202
272	40.89853	105.23183	485156	4533160	126	31	216
273	40.89824	105.228	485166	4533474	70	25	160
274	40.89672	105.19703	485192	4533469	32	3	122
275	40.89637	105.19619	485210	4533482	10	7	100
276	40.89448	105.19825	485216	4533122	242	4	332
277	40.89424	105.19533	485221	4546009	17	15	107
278	40.89398	105.19566	485228	4532865	13	14	103
279	40.89382	105.19821	485246	4531558	333	6	63
280	40.89357	105.19781	485247	4533494	352	9	82
281	40.89325	105.19865	485257	4518586	298	6	28
282	40.89293	105.19706	485262	4533127	15	13	105
283	40.89284	105.20667	485272	4531983	342	10	72
284	40.89157	105.15588	485277	4533495	354	6	84
285	40.89119	105.20641	485278	4545917	327	25	57
286	40.88989	105.20584	485282	4518475	353	10	83
287	40.88883	105.2014	485291	4522537	243	13	333
288	40.88877	105.15578	485292	4545937	325	7	55
289	40.88858	105.20506	485295	4518291	343	17	73
290	40.88822	105.20403	485296	4532024	357	7	87
291	40.88802	105.20137	485296	4533486	187	41	277
292	40.88779	105.20363	485314	4534166	276	7	6
293	40.88697	105.2013	485314	4522518	187	15	277
294	40.88405	105.11552	485316	4533142	357	15	87
295	40.87472	105.20202	485323	4533503	114	11	204
296	40.87262	105.20021	485328	4522563	30	8	120
297	40.87124	105.20805	485331	4533263	69	7	159
298	40.871	105.13362	485334	4533322	37	9	127
299	40.86865	105.20583	485334	4533508	55	17	145
300	40.86853	105.20808	485335	4534069	62	8	152
301	40.86721	105.2078	485344	4522527	59	9	149
302	40.86673	105.20632	485345	4534218	66	17	156
303	40.8652	105.20233	485361	4545941	73	16	163
304	40.86446	105.20475	485363	4533506	52	22	142
305	40.86376	105.14047	485364	4522561	38	11	128
306	40.86336	105.21306	485377	4534057	69	14	159

Appendix 3: Complete Bedding Attitude Data Tables (Continued)

#	Lat. °N (WGS 84)	Long. °W	m E (13N NAD 27)	m N	Strike	Dip	Dip Az
307	40.86322	105.18613	485378	4522496	41	10	131
308	40.86309	105.1899	485382	4533193	55	11	145
309	40.86282	105.21568	485386	4534027	84	17	174
310	40.86238	105.1908	485393	4534046	120	6	210
311	40.86182	105.20912	485394	4534015	70	20	160
312	40.86168	105.21483	485403	4534005	61	24	151
313	40.86111	105.1908	485407	4533271	155	15	245
314	40.86092	105.21957	485413	4534009	44	25	134
315	40.86057	105.19027	485413	4522692	290	35	20
316	40.85979	105.1855	485417	4534268	280	56	10
317	40.85976	105.21942	485420	4534107	8	11	98
318	40.85975	105.18543	485425	4517178	292	52	22
319	40.85953	105.18968	485425	4536533	281	21	11
320	40.85936	105.1813	485426	4533993	286	41	16
321	40.85934	105.21425	485430	4534099	289	25	19
322	40.85908	105.18266	485431	4545847	290	29	20
323	40.85891	105.19043	485432	4534330	274	18	4
324	40.85876	105.18308	485433	4533148	281	25	11
325	40.85786	105.21341	485433	4534249	312	10	42
326	40.85773	105.21164	485438	4534001	330	4	60
327	40.85773	105.21664	485442	4522555	330	4	60
328	40.85772	105.18333	485442	4534212	258	20	348
329	40.85752	105.16989	485445	4534455	337	17	67
330	40.85729	105.12229	485452	4533481	28	25	118
331	40.85728	105.21303	485453	4535194	289	3	19
332	40.85723	105.16899	485453	4533986	360	28	90
333	40.85722	105.17105	485465	4534194	354	21	84
334	40.85722	105.17272	485471	4534089	345	25	75
335	40.85715	105.18359	485482	4534541	248	4	338
336	40.85704	105.1736	485487	4522712	320	31	50
337	40.85702	105.12065	485490	4517051	33	27	123
338	40.85684	105.1777	485496	4534004	261	5	351
339	40.85661	105.21295	485500	4534156	56	15	146
340	40.85661	105.21295	485519	4516871	56	15	146
341	40.85637	105.17116	485522	4534116	2	25	92
342	40.85636	105.17015	485524	4534547	9	26	99
343	40.85632	105.16969	485525	4536478	31	25	121
344	40.85588	105.17461	485534	4533426	356	19	86
345	40.85586	105.17418	485540	4536430	359	30	89
346	40.85581	105.17326	485540	4534253	348	32	78
347	40.85571	105.21298	485542	4534836	3	4	93
348	40.85564	105.17504	485549	4533144	349	12	79
349	40.85555	105.17442	485550	4534830	2	18	92
350	40.85547	105.17477	485551	4533033	322	12	52
351	40.85546	105.12139	485563	4534528	34	36	124
352	40.8554	105.2136	485566	4533206	25	13	115
353	40.85527	105.17401	485576	4517162	1	23	91
354	40.8552	105.21667	485587	4536402	358	11	88
355	40.85444	105.21336	485592	4534540	39	13	129
356	40.85399	105.12217	485594	4533831	34	33	124
357	40.85329	105.2139	485596	4534123	52	18	142

Appendix 3: Complete Bedding Attitude Data Tables (Continued)

#	Lat. °N (WGS 84)	Long. °W	m E (13N NAD 27)	m N	Strike	Dip	Dip Az
358	40.85328	105.13398	485600	4517015	41	4	131
359	40.85271	105.21516	485601	4534166	62	20	152
360	40.85265	105.12294	485609	4534776	51	54	141
361	40.85179	105.21699	485618	4534538	74	20	164
362	40.8517	105.12361	485619	4522617	41	58	131
363	40.85162	105.12506	485625	4534767	43	42	133
364	40.85079	105.17713	485628	4531798	34	21	124
365	40.85035	105.12545	485628	4522712	42	42	132
366	40.84934	105.22995	485632	4533928	257	86	347
367	40.84923	105.14006	485646	4534537	59	1	149
368	40.8492	105.14128	485647	4534749	42	1	132
369	40.8491	105.22987	485658	4516047	74	87	164
370	40.84896	105.22978	485659	4516372	59	63	149
371	40.84747	105.18114	485661	4516117	64	13	154
372	40.84727	105.17905	485665	4516727	42	31	132
373	40.84727	105.17905	485670	4516329	42	31	132
374	40.84725	105.13224	485671	4515921	40	9	130
375	40.84699	105.17878	485672	4516047	56	31	146
376	40.84696	105.13144	485673	4519089	40	14	130
377	40.84687	105.18076	485676	4534556	65	29	155
378	40.84675	105.23381	485676	4531552	64	35	154
379	40.84666	105.23608	485678	4534641	94	41	184
380	40.84655	105.18139	485679	4531541	58	35	148
381	40.8465	105.18417	485682	4531523	65	9	155
382	40.84634	105.18378	485689	4534711	70	12	160
383	40.84623	105.23238	485700	4534702	84	11	174
384	40.8461	105.23898	485704	4522616	65	68	155
385	40.84608	105.23787	485705	4535081	114	9	204
386	40.84605	105.18204	485708	4534696	59	26	149
387	40.84603	105.13066	485719	4519592	58	52	148
388	40.84593	105.12979	485725	4533080	62	74	152
389	40.84591	105.18368	485726	4522745	85	13	175
390	40.84587	105.17865	485735	4536365	53	25	143
391	40.84541	105.17827	485740	4535131	46	28	136
392	40.84515	105.18575	485741	4535013	27	33	117
393	40.8451	105.2433	485743	4522611	255	75	345
394	40.84509	105.18109	485743	4531173	61	30	151
395	40.84499	105.24332	485753	4534480	70	78	160
396	40.84497	105.1782	485768	4531220	53	28	143
397	40.84493	105.13317	485773	4534997	40	40	130
398	40.84485	105.13498	485773	4535136	54	25	144
399	40.84484	105.18678	485775	4534458	55	14	145
400	40.84473	105.17778	485792	4535532	32	39	122
401	40.84469	105.24434	485793	4535144	55	45	145
402	40.84462	105.24362	485798	4534978	61	38	151
403	40.84454	105.1454	485802	4522712	44	3	134
404	40.84429	105.13224	485807	4534439	42	40	132
405	40.84421	105.22826	485818	4534406	119	5	209
406	40.8435	105.18113	485843	4534954	65	28	155
407	40.84307	105.19037	485850	4535557	48	8	138
408	40.84256	105.14164	485852	4517103	46	3	136

Appendix 3: Complete Bedding Attitude Data Tables (Continued)

#	Lat. °N (WGS 84)	Long. °W	m E (13N NAD 27)	m N	Strike	Dip	Dip Az
409	40.8425	105.1896	485854	4532785	83	14	173
410	40.84245	105.18153	485867	4519149	64	30	154
411	40.84196	105.1888	485882	4535204	61	14	151
412	40.8413	105.18872	485891	4533487	57	28	147
413	40.841	105.18789	485891	4519168	58	28	148
414	40.84092	105.1363	485894	4515118	38	40	128
415	40.8406	105.18708	485921	4519393	60	33	150
416	40.84014	105.18728	485921	4532786	61	32	151
417	40.83955	105.18697	485943	4535638	61	33	151
418	40.83902	105.18698	485945	4536029	62	28	152
419	40.83727	105.14018	485959	4535868	55	34	145
420	40.83392	105.27791	485967	4519411	79	65	169
421	40.83381	105.27602	485976	4533394	92	43	182
422	40.83373	105.28229	485983	4532291	164	73	254
423	40.82973	105.15586	485983	4535829	79	26	169
424	40.82929	105.15663	485989	4536050	80	24	170
425	40.82912	105.1699	485995	4535091	63	10	153
426	40.82749	105.16695	486019	4519246	69	8	159
427	40.82733	105.1675	486021	4548634	294	6	24
428	40.82601	105.16634	486030	4532646	105	72	195
429	40.82574	105.1657	486039	4517150	84	49	174
430	40.8253	105.16785	486043	4535252	83	68	173
431	40.82513	105.16814	486044	4536036	43	52	133
432	40.82477	105.23528	486049	4532649	54	5	144
433	40.82459	105.17044	486072	4519216	91	34	181
434	40.82456	105.23479	486078	4533420	51	10	141
435	40.82441	105.23448	486089	4536131	48	12	138
436	40.82424	105.2343	486093	4517290	51	25	141
437	40.8242	105.23404	486124	4535396	36	33	126
438	40.82408	105.2338	486126	4536245	31	33	121
439	40.82388	105.23412	486133	4548636	31	31	121
440	40.82332	105.23531	486146	4531139	45	22	135
441	40.82325	105.236	486147	4517204	63	5	153
442	40.82303	105.23576	486148	4515020	54	17	144
443	40.82243	105.23766	486171	4531070	59	6	149
444	40.82224	105.23862	486197	4532333	61	7	151
445	40.82167	105.23847	486204	4517358	59	8	149
446	40.82148	105.23948	486212	4536505	50	10	140
447	40.82094	105.23989	486218	4531071	39	8	129
448	40.82069	105.23843	486225	4536527	53	11	143
449	40.82065	105.23854	486226	4536196	52	11	142
450	40.82065	105.23846	486237	4514934	29	14	119
451	40.82034	105.23951	486249	4531259	51	11	141
452	40.82005	105.17535	486250	4531109	63	17	153
453	40.82004	105.23925	486265	4536434	50	16	140
454	40.81995	105.24102	486269	4532105	49	6	139
455	40.81976	105.24005	486270	4531072	39	10	129
456	40.81975	105.23861	486278	4536472	170	5	260
457	40.81966	105.2401	486282	4531109	39	10	129
458	40.81962	105.23898	486287	4531177	215	11	305
459	40.81954	105.24014	486296	4517494	74	29	164

Appendix 3: Complete Bedding Attitude Data Tables (Continued)

#	Lat. °N (WGS 84)	Long. °W	m E (13N NAD 27)	m N	Strike	Dip	Dip Az
460	40.81952	105.24001	486300	4531854	43	29	133
461	40.81933	105.24153	486331	4531877	16	10	106
462	40.81905	105.17506	486336	4509690	31	16	121
463	40.81897	105.24081	486342	4531313	38	9	128
464	40.81873	105.24186	486345	4531279	26	11	116
465	40.81839	105.24175	486365	4515020	31	25	121
466	40.81799	105.24168	486369	4531652	31	34	121
467	40.81741	105.24481	486372	4531307	156	3	246
468	40.81739	105.1749	486373	4531143	344	16	74
469	40.81666	105.24354	486375	4532086	33	27	123
470	40.81663	105.24317	486394	4517586	38	33	128
471	40.81649	105.24384	486398	4531295	36	28	126
472	40.81645	105.2435	486421	4531146	38	30	128
473	40.8163	105.24365	486439	4532198	40	31	130
474	40.81618	105.24419	486446	4514976	39	33	129
475	40.81585	105.24566	486448	4531687	59	12	149
476	40.81559	105.24392	486450	4531317	33	25	123
477	40.8153	105.24485	486458	4536688	17	33	107
478	40.81406	105.18225	486470	4531157	319	9	49
479	40.81402	105.24603	486473	4531701	49	23	139
480	40.81387	105.15531	486476	4536159	315	21	45
481	40.81359	105.24635	486491	4548688	38	27	128
482	40.81347	105.2464	486506	4536097	36	24	126
483	40.81328	105.17994	486521	4531144	346	30	76
484	40.81313	105.24646	486527	4536248	32	26	122
485	40.81214	105.24743	486543	4531317	49	57	139
486	40.81159	105.17859	486553	4532014	331	18	61
487	40.81159	105.15974	486561	4531192	277	34	7
488	40.8115	105.24825	486565	4531475	55	46	145
489	40.81135	105.15836	486572	4517645	316	20	46
490	40.81112	105.24976	486588	4536558	39	17	129
491	40.81106	105.16185	486607	4517428	249	45	339
492	40.81063	105.24918	486612	4531155	34	38	124
493	40.81057	105.18343	486636	4515055	329	11	59
494	40.81028	105.24985	486641	4548795	44	46	134
495	40.81023	105.24935	486641	4531193	39	41	129
496	40.81023	105.16301	486688	4517618	224	43	314
497	40.81016	105.2495	486695	4531090	50	50	140
498	40.81016	105.24816	486708	4535767	19	5	109
499	40.81012	105.24951	486716	4535981	54	32	144
500	40.80999	105.24948	486814	4530917	31	25	121
501	40.80973	105.2497	486838	4519609	24	33	114
502	40.80964	105.15932	486864	4530947	310	18	40
503	40.809	105.1641	486867	4514634	215	55	305
504	40.80878	105.18109	486903	4519658	321	23	51
505	40.80839	105.16541	486913	4526522	206	55	296
506	40.80817	105.18029	486921	4526211	322	19	52
507	40.80761	105.16477	486928	4535690	206	47	296
508	40.80737	105.17333	486946	4517897	299	25	29
509	40.80722	105.17154	486955	4514959	298	28	28
510	40.80712	105.16605	486960	4514912	228	44	318

Appendix 3: Complete Bedding Attitude Data Tables (Continued)

#	Lat. °N (WGS 84)	Long. °W	m E (13N NAD 27)	m N	Strike	Dip	Dip Az
511	40.8067	105.16827	486966	4516603	276	34	6
512	40.80622	105.17256	486973	4516364	283	30	13
513	40.8059	105.17125	487023	4535784	271	35	1
514	40.8046	105.17221	487092	4535850	263	48	353
515	40.80436	105.14996	487102	4535553	347	15	77
516	40.80331	105.17048	487107	4535809	263	30	353
517	40.8027	105.1471	487154	4514795	318	15	48
518	40.8024	105.1463	487183	4515618	335	16	65
519	40.80221	105.15505	487210	4510884	313	13	43
520	40.80103	105.21051	487233	4549359	267	36	357
521	40.80033	105.14566	487238	4535355	342	18	72
522	40.80033	105.14566	487246	4549158	320	13	50
523	40.80025	105.15002	487351	4535381	331	19	61
524	40.80011	105.17054	487367	4510976	288	23	18
525	40.80006	105.15496	487387	4516157	314	19	44
526	40.79984	105.14816	487390	4516384	338	16	68
527	40.79972	105.17041	487396	4516841	358	16	88
528	40.79945	105.14649	487547	4516339	334	13	64
529	40.79925	105.18673	487637	4516656	270	48	0
530	40.7992	105.14457	487646	4512836	344	19	74
531	40.79893	105.18647	487656	4528063	306	57	36
532	40.79869	105.18747	487686	4510943	267	45	357
533	40.79864	105.18799	487687	4516295	255	48	345
534	40.79835	105.18519	487704	4516623	304	25	34
535	40.79832	105.18915	487758	4516393	249	43	339
536	40.7982	105.15005	487758	4516393	346	19	76
537	40.79798	105.18464	487788	4521300	325	15	55
538	40.79781	105.17051	487836	4513053	348	33	78
539	40.79776	105.19059	487846	4512842	229	43	319
540	40.79752	105.18422	487849	4516267	335	20	65
541	40.79718	105.17038	487860	4510837	340	13	70
542	40.79718	105.17054	487861	4529162	340	15	70
543	40.79624	105.22095	488099	4530472	226	30	316
544	40.79605	105.17038	488104	4521080	6	13	96
545	40.79334	105.15246	488136	4521817	351	17	81
546	40.79198	105.31876	488146	4512488	263	4	353
547	40.78967	105.27051	488147	4513104	40	16	130
548	40.78953	105.27003	488207	4523433	49	8	139
549	40.78882	105.16772	488219	4528841	135	6	225
550	40.78826	105.15893	488226	4520492	9	24	99
551	40.78794	105.16214	488239	4521820	149	15	239
552	40.78794	105.16471	488280	4513437	9	8	99
553	40.78782	105.25001	488435	4528601	355	7	85
554	40.78772	105.25098	488436	4528508	338	6	68
555	40.78757	105.25236	488513	4527949	343	6	73
556	40.78755	105.16118	488553	4528099	147	31	237
557	40.7874	105.15515	488554	4520897	5	13	95
558	40.78716	105.16365	488666	4521333	35	12	125
559	40.78698	105.15509	488752	4522269	9	16	99
560	40.78593	105.15278	488785	4524236	353	14	83
561	40.78467	105.32641	488819	4521342	25	6	115

Appendix 3: Complete Bedding Attitude Data Tables (Continued)

#	Lat. °N (WGS 84)	Long. °W	m E (13N NAD 27)	m N	Strike	Dip	Dip Az
562	40.78447	105.15618	488888	4527799	51	5	141
563	40.77371	105.13941	488897	4521271	11	15	101
564	40.77071	105.14098	488897	4521599	13	14	103
565	40.77024	105.14466	488965	4521567	13	16	103
566	40.76834	105.14454	489030	4521464	6	13	96
567	40.76829	105.14691	489104	4521452	20	14	110
568	40.76516	105.14098	489470	4521942	20	15	110
569	40.75153	105.15018	489503	4522083	22	9	112
570	40.75123	105.1464	489626	4522092	29	12	119
571	40.75069	105.15204	489682	4522197	19	12	109
572	40.75028	105.14434	489738	4522712	42	12	132
573	40.73992	105.16237	489747	4522346	16	13	106
574	40.65632	105.17997	489813	4522509	11	16	101
575	40.65514	105.17943	489876	4522682	348	17	78
576	40.65377	105.17817	490312	4525682	350	2	80

**Appendix 3: Bedding Data from Livermore Mtn, Laporte, Livermore, Virginia Dale, and Table Mtn
Maps (Braddock et al., 1988b; 1988c; 1988d; 1989b; Courtwright and Braddock, 1989)**

#	Lat. °N (WGS 84)	Long. °W	m E (13N NAD 27)	m N	Strike	Dip	Dip Az
1	40.98055	105.20517	482784	4536408	15	10	105
2	40.99638	105.17914	484978	4538161	7	12	97
3	40.98544	105.19291	483817	4536949	12	11	102
4	40.98368	105.16866	485857	4536749	26	8	116
5	40.98188	105.16514	486152	4536549	210	6	300
6	40.98088	105.16006	486579	4536437	318	5	48
7	40.98277	105.16185	486429	4536647	182	25	272
8	40.97645	105.17480	485338	4535948	12	21	102
9	40.97372	105.17195	485578	4535644	10	11	100
10	40.97154	105.17286	485500	4535402	329	7	59
11	40.97225	105.17061	485690	4535481	271	10	1
12	40.97363	105.16753	485949	4535634	222	37	312
13	40.97613	105.15862	486700	4535909	359	13	89
14	40.97338	105.15686	486847	4535604	1	15	91
15	40.97332	105.16292	486337	4535598	29	9	119
16	40.96742	105.19729	483444	4534949	350	14	80
17	40.96381	105.20745	482588	4534550	1	24	91
18	40.96101	105.19572	483575	4534238	12	15	102
19	40.95800	105.20656	482662	4533905	359	14	89
20	40.94818	105.21179	482219	4532816	18	12	108
21	40.95025	105.20193	483049	4533044	12	14	102
22	40.94016	105.21423	482011	4531926	30	14	120
23	40.96577	105.14768	487618	4534758	4	12	94
24	40.97055	105.12194	489784	4535285	38	15	128
25	40.93721	105.12941	489150	4531585	332	20	62
26	40.92970	105.13688	488521	4530752	359	26	89
27	40.93894	105.10634	491093	4531774	340	10	70
28	40.91502	105.09226	492276	4529117	10	10	100
29	40.92470	105.13717	488496	4530197	1	13	91
30	40.92175	105.14307	487998	4529870	5	13	95
31	40.91107	105.14760	487614	4528686	8	11	98
32	40.90101	105.15378	487092	4527570	336	11	66
33	40.90411	105.13284	488857	4527911	340	10	70
34	40.90330	105.14941	487460	4527823	338	10	68
35	40.88927	105.15703	486816	4526267	1	10	91
36	40.89864	105.15770	486762	4527307	5	9	95
37	40.88926	105.13789	488428	4526263	323	4	53
38	40.89380	105.12177	489787	4526765	326	10	56
39	40.88284	105.11073	490715	4525547	1	15	91
40	40.87713	105.10163	491482	4524913	17	22	107
41	40.87815	105.09773	491811	4525025	17	31	107
42	40.88275	105.11424	490420	4525537	356	14	86
43	40.87241	105.09629	491931	4524388	32	58	122
44	40.87183	105.09258	492243	4524324	29	62	119
45	40.86823	105.08937	492513	4523923	30	64	120
46	40.86529	105.08448	492925	4523597	31	35	121
47	40.86811	105.10336	491335	4523912	11	60	101
48	40.85729	105.08443	492928	4522708	328	15	58
49	40.85172	105.09597	491955	4522091	11	25	101
50	40.85469	105.10191	491455	4522421	23	52	113

Appendix 3: Bedding Data from Published USGS Maps (Continued)

#	Lat. °N (WGS 84)	Long. °W	m E (13N NAD 27)	m N	Strike	Dip	Dip Az
51	40.85742	105.08826	492606	4522724	349	22	79
52	40.93891	105.04829	495980	4531767	32	5	122
53	40.93299	105.06514	494561	4531110	53	5	143
54	40.93848	105.03354	497221	4531718	51	75	141
55	40.91443	105.00252	499833	4529048	58	9	148
56	40.92791	105.02520	497923	4530545	25	45	115
57	40.93262	105.05725	495225	4531069	21	3	111
58	40.92796	105.05474	495436	4530551	82	6	172
59	40.92492	105.05294	495587	4530214	51	29	141
60	40.92320	105.05181	495682	4530023	32	60	122
61	40.92080	105.04882	495934	4529756	28	80	118
62	40.91940	105.04469	496281	4529600	30	76	120
63	40.90820	105.04624	496150	4528358	30	65	120
64	40.91228	105.04684	496100	4528810	20	54	110
65	40.85435	105.10229	491423	4522384	9	45	99
66	40.82781	105.13815	488396	4519442	353	5	83
67	40.82461	105.14553	487773	4519088	317	17	47
68	40.81900	105.14435	487871	4518465	277	25	7
69	40.85612	105.10933	490830	4522581	41	52	131
70	40.85488	105.10119	491516	4522443	29	58	119
71	40.83956	105.09054	492412	4520741	353	12	83
72	40.81738	105.04762	496028	4518276	244	15	334
73	40.81678	105.03862	496788	4518209	328	6	58
74	40.81090	105.03233	497318	4517557	323	9	53
75	40.81297	105.03959	496705	4517786	313	7	43
76	40.79890	105.06694	494398	4516226	348	10	78
77	40.79776	105.06705	494388	4516100	346	7	76
78	40.79093	105.06735	494363	4515342	1	7	91
79	40.79942	105.05713	495225	4516283	216	16	306
80	40.79774	105.05589	495330	4516096	179	20	269
81	40.79748	105.05153	495698	4516068	329	3	59
82	40.80166	105.04323	496398	4516531	327	9	57
83	40.79360	105.03969	496696	4515637	345	10	75
84	40.80483	105.04702	496078	4516883	316	9	46
85	40.76007	105.05215	495643	4511915	168	15	258
86	40.78159	105.03794	496843	4514304	349	9	79
87	40.77550	105.04645	496125	4513627	6	8	96
88	40.76921	105.05101	495740	4512930	172	3	262
89	40.76296	105.05516	495389	4512236	176	15	266
90	40.75444	105.04789	496002	4511289	168	5	258
91	40.75436	105.03768	496864	4511281	344	15	74
92	40.76076	105.05501	495402	4511991	176	12	266
93	40.75458	105.01764	498556	4511304	343	15	73
94	40.74731	105.01303	498945	4510497	352	7	82
95	40.74000	105.06858	494254	4509689	358	7	88
96	40.74012	105.06678	494407	4509701	358	10	88
97	40.73997	105.05731	495206	4509684	142	14	232
98	40.74074	105.04950	495865	4509769	168	8	258
99	40.74248	105.06878	494238	4509963	357	11	87
100	40.73823	105.03884	496766	4509490	358	9	88
101	40.73323	105.06532	494529	4508936	358	10	88

Appendix 3: Bedding Data from Published USGS Maps (Continued)

#	Lat. °N (WGS 84)	Long. °W	m E (13N NAD 27)	m N	Strike	Dip	Dip Az
102	40.72296	105.03593	497011	4507795	1	10	91
103	40.72227	105.03122	497408	4507719	4	13	94
104	40.72524	105.03603	497002	4508048	5	10	95
105	40.72538	105.06262	494757	4508065	350	11	80
106	40.72264	105.06207	494803	4507761	350	11	80
107	40.71830	105.07017	494118	4507279	348	11	78
108	40.71685	105.06762	494334	4507118	347	12	77
109	40.71906	105.06547	494516	4507363	350	12	80
110	40.71853	105.06231	494782	4507304	355	11	85
111	40.71765	105.06116	494879	4507207	355	11	85
112	40.71743	105.05370	495509	4507182	178	12	268
113	40.71644	105.05260	495602	4507072	178	11	268
114	40.71621	105.04860	495940	4507046	176	9	266
115	40.72056	105.09285	492203	4507533	15	11	105
116	40.72201	105.08980	492461	4507693	17	11	107
117	40.72373	105.08244	493083	4507883	8	8	98
118	40.72461	105.07743	493505	4507981	169	10	259
119	40.71978	105.07302	493877	4507444	334	6	64
120	40.72142	105.07092	494055	4507626	349	9	79
121	40.72317	105.06897	494220	4507820	344	5	74
122	40.71172	105.05763	495177	4506548	0	11	90
123	40.70458	105.07442	493758	4505757	4	8	94
124	40.71193	105.06412	494629	4506572	352	15	82
125	40.71621	105.08431	492924	4507049	183	3	273
126	40.71554	105.08168	493146	4506973	211	2	301
127	40.71393	105.07960	493321	4506794	257	3	347
128	40.69453	105.06344	494685	4504641	359	14	89
129	40.69573	105.05083	495750	4504773	136	15	226
130	40.69580	105.04956	495857	4504780	136	12	226
131	40.69412	105.04617	496144	4504594	160	11	250
132	40.69415	105.04495	496247	4504598	160	11	250
133	40.69316	105.02185	498199	4504486	345	11	75
134	40.71048	105.02981	497527	4506410	353	10	83
135	40.70418	105.02736	497733	4505710	342	8	72
136	40.70175	105.02863	497626	4505440	357	10	87
137	40.70067	105.04895	495909	4505321	150	11	240
138	40.67819	105.08788	492618	4502828	280	13	10
139	40.67635	105.08104	493196	4502624	307	13	37
140	40.67405	105.07847	493413	4502368	343	5	73
141	40.67848	105.07004	494126	4502859	14	7	104
142	40.67251	105.09286	492196	4502199	310	20	40
143	40.67204	105.09040	492405	4502147	315	15	45
144	40.67161	105.09816	491749	4502099	312	17	42
145	40.67101	105.06037	494942	4502029	359	12	89
146	40.69914	105.07403	493791	4505153	356	9	86
147	40.69323	105.07577	493643	4504497	29	7	119
148	40.68869	105.07710	493530	4503993	30	3	120
149	40.69275	105.08775	492631	4504445	148	5	238
150	40.67834	105.09339	492153	4502846	300	6	30
151	40.69607	105.09274	492209	4504814	1	5	91
152	40.68603	105.04508	496236	4503696	175	15	265

Appendix 3: Bedding Data from Published USGS Maps (Continued)

#	Lat. °N (WGS 84)	Long. °W	m E (13N NAD 27)	m N	Strike	Dip	Dip Az
153	40.68548	105.04298	496413	4503635	172	15	262
154	40.68301	105.04329	496386	4503360	177	15	267
155	40.68682	105.03869	496775	4503783	150	7	240
156	40.67389	105.04772	496012	4502349	195	27	285
157	40.67357	105.04467	496270	4502312	194	10	284
158	40.67357	105.04326	496389	4502312	193	11	283
159	40.75196	105.07025	494114	4511016	359	13	89
160	40.75390	105.07447	493758	4511232	2	10	92
161	40.68156	105.05932	495032	4503201	5	15	95
162	40.66314	105.09210	492260	4501159	345	12	75
163	40.66682	105.09410	492091	4501567	332	15	62
164	40.66935	105.05860	495092	4501845	357	7	87
165	40.66738	105.05738	495195	4501627	354	15	84
166	40.66523	105.05055	495772	4501387	207	20	297
167	40.65792	105.05389	495489	4500576	199	7	289
168	40.65473	105.05724	495206	4500222	250	5	340
169	40.66440	105.04455	496279	4501295	213	8	303
170	40.64492	105.09220	492249	4499136	358	10	88
171	40.64022	105.09200	492266	4498614	356	15	86
172	40.64848	105.08292	493034	4499530	357	10	87
173	40.65007	105.08453	492899	4499707	357	12	87
174	40.63996	105.08544	492821	4498585	3	10	93
175	40.63952	105.08004	493277	4498536	358	12	88
176	40.64279	105.06795	494300	4498897	356	11	86
177	40.64335	105.05755	495179	4498959	205	9	295
178	40.64220	105.06474	494571	4498832	350	9	80
179	40.62630	105.03879	496765	4497066	3	14	93
180	40.63285	105.05618	495294	4497793	156	8	246
181	40.63085	105.05812	495130	4497571	151	14	241
182	40.62844	105.06142	494850	4497304	328	12	58
183	40.62785	105.05447	495438	4497238	144	12	234
184	40.67234	105.02191	498193	4502176	10	9	100
185	40.65273	105.02311	498091	4499999	5	11	95
186	40.63931	105.02993	497514	4498509	9	11	99
187	40.71661	105.13362	488759	4507098	30	14	120
188	40.96588	105.17155	485609	4534773	210	47	300
189	40.96658	105.17006	485735	4534851	212	32	302
190	40.96738	105.16780	485925	4534940	327	15	57
191	40.96462	105.17013	485729	4534634	348	9	78
192	40.95901	105.17456	485355	4534012	177	48	267
193	40.96208	105.16821	485890	4534352	14	13	104
194	40.95804	105.17572	485257	4533904	178	41	268
195	40.95730	105.17528	485294	4533822	184	19	274
196	40.95661	105.17801	485064	4533746	193	54	283
197	40.95612	105.17254	485524	4533690	12	8	102
198	40.95398	105.17637	485201	4533453	187	47	277
199	40.95378	105.17475	485338	4533431	110	8	200
200	40.95349	105.17163	485600	4533398	41	20	131
201	40.95154	105.17668	485175	4533182	179	31	269
202	40.95055	105.17570	485257	4533073	127	27	217
203	40.95073	105.17264	485514	4533091	38	12	128

Appendix 3: Bedding Data from Published USGS Maps (Continued)

#	Lat. °N (WGS 84)	Long. °W	m E (13N NAD 27)	m N	Strike	Dip	Dip Az
204	40.94854	105.17292	485491	4532849	105	11	195
205	40.94744	105.16995	485740	4532726	105	14	195
206	40.94787	105.16826	485883	4532773	95	7	185
207	40.94777	105.16548	486117	4532762	3	7	93
208	40.94619	105.16741	485953	4532587	135	14	225
209	40.94451	105.16579	486090	4532400	235	12	325
210	40.94536	105.16415	486228	4532494	293	7	23
211	40.94130	105.16372	486263	4532043	248	5	338
212	40.94091	105.16132	486465	4532000	304	16	34
213	40.93886	105.16514	486144	4531773	164	34	254
214	40.93739	105.16263	486354	4531609	140	2	230
215	40.94416	105.17436	485368	4532363	107	16	197
216	40.94362	105.17090	485659	4532302	88	25	178
217	40.94152	105.17895	484981	4532070	7	21	97
218	40.94140	105.17480	485331	4532057	15	17	105
219	40.94035	105.16948	485778	4531939	158	35	248
220	40.93894	105.16829	485878	4531783	164	35	254
221	40.93608	105.16551	486112	4531465	170	33	260
222	40.93533	105.16423	486219	4531381	208	21	298
223	40.93539	105.16259	486357	4531387	179	5	269
224	40.93971	105.15962	486608	4531867	342	7	72
225	40.93621	105.16017	486561	4531478	358	8	88
226	40.92853	105.16568	486095	4530627	205	32	295
227	40.92584	105.16484	486166	4530327	188	16	278
228	40.92738	105.17072	485671	4530499	203	26	293
229	40.92645	105.16993	485737	4530396	193	41	283
230	40.92634	105.17323	485459	4530385	323	14	53
231	40.92425	105.17309	485471	4530153	289	8	19
232	40.93291	105.17017	485718	4531113	179	31	269
233	40.93311	105.16813	485890	4531135	178	50	268
234	40.93127	105.16369	486263	4530930	218	2	308
235	40.92989	105.15959	486608	4530777	27	9	117
236	40.95563	105.15772	486771	4533634	344	10	74
237	40.94002	105.14871	487526	4531899	7	10	97
238	40.93762	105.14978	487436	4531633	349	13	79
239	40.91610	105.16189	486412	4529246	28	15	118
240	40.91114	105.17164	485590	4528697	0	10	90
241	40.92174	105.16229	486380	4529872	33	11	123
242	40.91470	105.16588	486076	4529091	346	4	76
243	40.91696	105.16960	485763	4529343	17	3	107
244	40.91462	105.17128	485621	4529083	48	1	138
245	40.91597	105.18727	484275	4529236	254	18	344
246	40.91629	105.18562	484414	4529271	286	16	16
247	40.91585	105.18423	484531	4529222	296	12	26
248	40.91477	105.17788	485065	4529101	287	10	17
249	40.92491	105.20790	482540	4530233	16	11	106
250	40.92248	105.20248	482996	4529961	16	16	106
251	40.92060	105.20049	483163	4529753	14	16	104
252	40.91968	105.19309	483786	4529649	15	12	105
253	40.91575	105.19757	483407	4529213	6	12	96
254	40.91285	105.20061	483151	4528892	9	15	99

Appendix 3: Bedding Data from Published USGS Maps (Continued)

#	Lat. °N (WGS 84)	Long. °W	m E (13N NAD 27)	m N	Strike	Dip	Dip Az
255	40.91921	105.21663	481804	4529601	15	13	105
256	40.91857	105.21309	482102	4529529	348	21	78
257	40.91688	105.21244	482155	4529342	306	42	36
258	40.91513	105.21477	481959	4529148	37	22	127
259	40.91465	105.21244	482155	4529094	37	22	127
260	40.91169	105.21667	481798	4528766	1	15	91
261	40.90655	105.22377	481199	4528198	341	19	71
262	40.90581	105.22051	481473	4528114	6	18	96
263	40.90614	105.21443	481986	4528150	12	13	102
264	40.90278	105.21933	481572	4527778	6	23	96
265	40.90050	105.20807	482520	4527523	10	14	100
266	40.89852	105.21311	482095	4527303	10	12	100
267	40.89776	105.21469	481961	4527219	320	21	50
268	40.89794	105.22636	480978	4527242	78	42	168
269	40.89763	105.22465	481122	4527207	78	27	168
270	40.92410	105.30517	474350	4530166	28	5	118
271	40.92407	105.28944	475674	4530159	346	3	76
272	40.92802	105.30116	474689	4530600	25	1	115
273	40.94134	105.30846	474080	4532081	142	65	232
274	40.93872	105.30684	474215	4531789	140	10	230
275	40.93079	105.29714	475028	4530906	336	55	66
276	40.91487	105.27531	476861	4529133	110	18	200
277	40.91392	105.27586	476814	4529028	19	37	109
278	40.91158	105.27663	476748	4528769	30	4	120
279	40.90569	105.27921	476529	4528116	20	2	110
280	40.90570	105.27475	476905	4528116	2	5	92
281	40.89092	105.26936	477354	4526473	351	10	81
282	40.90059	105.24032	479803	4527540	124	21	214
283	40.89957	105.23690	480091	4527426	116	23	206
284	40.89890	105.23426	480313	4527350	115	47	205
285	40.89806	105.24146	479707	4527259	79	12	169
286	40.89581	105.24018	479814	4527009	73	8	163
287	40.89146	105.24337	479543	4526526	336	3	66
288	40.89077	105.24649	479280	4526450	290	5	20
289	40.88776	105.23130	480559	4526113	295	4	25
290	40.88900	105.21300	482101	4526247	334	5	64
291	40.89454	105.19065	483985	4526857	14	13	104
292	40.89193	105.17419	485371	4526565	8	9	98
293	40.89290	105.19859	483316	4526677	278	6	8
294	40.89076	105.20069	483138	4526440	194	56	284
295	40.88642	105.20002	483194	4525958	185	34	275
296	40.89718	105.19766	483396	4527152	194	43	284
297	40.89646	105.19746	483412	4527072	198	5	288
298	40.88472	105.19790	483372	4525769	347	11	77
299	40.88509	105.19478	483635	4525809	350	19	80
300	40.88636	105.19015	484025	4525950	356	15	86
301	40.88546	105.18439	484511	4525849	345	11	75
302	40.87597	105.21035	482321	4524800	145	7	235
303	40.87631	105.20733	482575	4524837	169	2	259
304	40.87711	105.20166	483053	4524924	150	13	240
305	40.87522	105.19759	483396	4524715	27	10	117

Appendix 3: Bedding Data from Published USGS Maps (Continued)

#	Lat. °N (WGS 84)	Long. °W	m E (13N NAD 27)	m N	Strike	Dip	Dip Az
306	40.87539	105.18395	484545	4524731	34	12	124
307	40.87424	105.17768	485073	4524602	45	8	135
308	40.89856	105.19901	483282	4527306	192	58	282
309	40.87057	105.12123	489829	4524186	26	6	116
310	40.86366	105.11041	490739	4523418	41	28	131
311	40.85529	105.12096	489850	4522490	36	30	126
312	40.85815	105.22613	480986	4522825	56	15	146
313	40.85899	105.22180	481352	4522918	19	25	109
314	40.86130	105.22268	481278	4523174	40	18	130
315	40.86839	105.20809	482509	4523958	64	9	154
316	40.86603	105.20818	482501	4523696	65	14	155
317	40.86155	105.20891	482438	4523199	71	14	161
318	40.85828	105.20907	482424	4522836	323	12	53
319	40.84387	105.24464	479421	4521244	65	60	155
320	40.84631	105.23856	479935	4521514	66	70	156
321	40.84921	105.22974	480680	4521834	78	90	168
322	40.85072	105.22505	481075	4522000	72	65	162
323	40.85035	105.22385	481176	4521959	66	40	156
324	40.85341	105.21948	481545	4522298	66	25	156
325	40.83767	105.23219	480470	4520554	46	1	136
326	40.86228	105.18581	484385	4523276	42	8	132
327	40.85883	105.19028	484008	4522894	263	16	353
328	40.86005	105.18396	484541	4523028	287	35	17
329	40.85975	105.17719	485111	4522993	308	20	38
330	40.85725	105.17339	485431	4522715	338	25	68
331	40.85076	105.19863	483302	4521999	80	3	170
332	40.86679	105.19589	483537	4523779	45	12	135
333	40.86300	105.19261	483812	4523357	57	10	147
334	40.86312	105.18726	484263	4523370	31	12	121
335	40.86513	105.18744	484249	4523593	26	9	116
336	40.85701	105.17010	485708	4522688	359	28	89
337	40.84971	105.17396	485381	4521879	26	25	116
338	40.85010	105.15467	487007	4521918	60	8	150
339	40.84668	105.14584	487751	4521538	60	2	150
340	40.84297	105.13042	489050	4521124	42	70	132
341	40.84111	105.14206	488069	4520919	47	7	137
342	40.83695	105.14075	488178	4520457	45	50	135
343	40.83462	105.14142	488122	4520199	57	60	147
344	40.83325	105.14353	487943	4520047	45	60	135
345	40.82925	105.15324	487124	4519604	70	78	160
346	40.82826	105.15598	486892	4519495	50	55	140
347	40.83264	105.15835	486694	4519981	85	5	175
348	40.83054	105.16500	486132	4519749	59	5	149
349	40.82630	105.15637	486859	4519277	64	27	154
350	40.82027	105.16102	486466	4518608	355	10	85
351	40.81911	105.16054	486506	4518479	218	70	308
352	40.82197	105.15914	486625	4518797	47	20	137
353	40.82212	105.15295	487147	4518813	254	80	344
354	40.82011	105.14279	488003	4518588	218	25	308
355	40.81761	105.14392	487907	4518311	320	25	50
356	40.81423	105.15332	487114	4517937	318	13	48

Appendix 3: Bedding Data from Published USGS Maps (Continued)

#	Lat. °N (WGS 84)	Long. °W	m E (13N NAD 27)	m N	Strike	Dip	Dip Az
357	40.83252	105.17038	485680	4519970	58	3	148
358	40.82253	105.17909	484943	4518863	20	6	110
359	40.82475	105.17212	485531	4519107	50	15	140
360	40.82153	105.17344	485419	4518750	38	30	128
361	40.81748	105.17700	485118	4518301	4	14	94
362	40.81892	105.16411	486205	4518459	6	25	96
363	40.81714	105.16215	486370	4518261	234	50	324
364	40.83924	105.19434	483660	4520720	65	15	155
365	40.83243	105.22278	481261	4519970	48	25	138
366	40.81936	105.20808	482497	4518516	53	5	143
367	40.82766	105.19639	483485	4519434	2	40	92
368	40.82434	105.18521	484427	4519064	26	3	116
369	40.81494	105.20180	483026	4518024	54	8	144
370	40.79399	105.22501	481063	4515703	229	32	319
371	40.79686	105.22255	481271	4516021	230	45	320
372	40.80102	105.19267	483793	4516477	310	18	40
373	40.79787	105.19027	483994	4516127	0	0	90
374	40.79086	105.19420	483660	4515350	1	21	91
375	40.80087	105.17609	485191	4516457	283	30	13
376	40.80420	105.17649	485157	4516827	283	25	13
377	40.80566	105.17379	485386	4516989	290	30	20
378	40.80535	105.16584	486056	4516953	228	27	318
379	40.80452	105.16215	486367	4516860	196	10	286
380	40.80425	105.16129	486440	4516830	314	9	44
381	40.79913	105.16093	486470	4516262	272	22	2
382	40.80629	105.14996	487396	4517055	330	14	60
383	40.80049	105.14368	487925	4516411	340	15	70
384	40.79136	105.14185	488077	4515396	350	17	80
385	40.77297	105.12866	489188	4513354	8	12	98
386	40.76894	105.14204	488057	4512908	10	13	100
387	40.77041	105.15548	486924	4513073	10	11	100
388	40.76839	105.15007	487380	4512848	10	11	100
389	40.75701	105.15533	486934	4511586	18	13	108
390	40.75817	105.19276	483774	4511721	350	15	80
391	40.77950	105.16827	485846	4514084	359	16	89
392	40.77493	105.19438	483642	4513582	353	17	83
393	40.78489	105.17126	485595	4514682	1	15	91
394	40.78177	105.23329	480360	4514348	288	11	18
395	40.78651	105.24616	479276	4514877	247	65	337
396	40.83351	105.22849	480780	4520091	47	3	137
397	40.82724	105.22189	481335	4519394	48	2	138
398	40.82101	105.24017	479792	4518706	41	8	131
399	40.81666	105.24525	479362	4518224	55	5	145
400	40.81577	105.24446	479428	4518125	43	35	133
401	40.81380	105.24344	479514	4517907	47	30	137
402	40.81182	105.24962	478992	4517688	15	19	105
403	40.81195	105.24782	479144	4517702	36	45	126
404	40.80910	105.24926	479022	4517386	4	16	94
405	40.82876	105.29544	475134	4519581	59	46	149
406	40.83232	105.28458	476051	4519973	58	50	148
407	40.83352	105.27636	476744	4520103	75	90	165

Appendix 3: Bedding Data from Published USGS Maps (Continued)

#	Lat. °N (WGS 84)	Long. °W	m E (13N NAD 27)	m N	Strike	Dip	Dip Az
408	40.83298	105.27545	476821	4520044	75	3	165
409	40.81078	105.25277	478726	4517573	75	8	165
410	40.80799	105.25387	478632	4517263	48	30	138
411	40.80550	105.25423	478601	4516988	29	15	119
412	40.79502	105.26297	477860	4515827	323	22	53
413	40.79304	105.26771	477460	4515608	23	50	113
414	40.79262	105.26300	477857	4515560	270	10	0
415	40.79068	105.26996	477269	4515346	49	34	139
416	40.78958	105.26898	477352	4515224	224	20	314
417	40.79117	105.26636	477573	4515400	250	40	340
418	40.78412	105.25273	478720	4514614	302	75	32
419	40.77839	105.26449	477727	4513980	302	16	32
420	40.77467	105.27915	476488	4513571	306	11	36
421	40.77681	105.27317	476994	4513807	281	30	11
422	40.77376	105.31504	473459	4513481	288	15	18
423	40.77610	105.33050	472155	4513746	21	3	111
424	40.77424	105.31908	473118	4513535	286	15	16
425	40.80410	105.31684	473320	4516849	32	20	122
426	40.79818	105.30240	474535	4516188	89	1	179
427	40.79739	105.30219	474552	4516100	89	6	179
428	40.72314	105.16518	486095	4507827	10	16	100
429	40.73858	105.16065	486481	4509541	24	13	114
430	40.69521	105.17305	485424	4504729	1	20	91
431	40.68106	105.15163	487232	4503155	351	15	81
432	40.67517	105.17048	485637	4502504	1	23	91
433	40.67304	105.17270	485449	4502267	99	12	189
434	40.67046	105.17673	485108	4501982	118	18	208
435	40.67214	105.16813	485835	4502166	344	30	74
436	40.67041	105.16849	485804	4501975	355	5	85
437	40.67063	105.16615	486002	4501999	313	42	43
438	40.66577	105.16959	485710	4501459	180	70	270
439	40.65603	105.17933	484885	4500380	356	15	86
440	40.65192	105.17570	485191	4499924	208	37	298
441	40.66015	105.14491	487796	4500833	320	14	50
442	40.66642	105.14867	487479	4501529	351	16	81
443	40.66789	105.17261	485456	4501696	108	12	198
444	40.70609	105.18157	484707	4505937	5	25	95
445	40.68827	105.17661	485122	4503959	1	25	91
446	40.67447	105.17892	484923	4502427	92	35	182
447	40.67340	105.17777	485021	4502308	102	25	192
448	40.67395	105.18477	484429	4502371	355	25	85
449	40.67420	105.18733	484213	4502399	350	15	80
450	40.68408	105.20676	482573	4503499	108	83	198
451	40.66869	105.20169	482998	4501789	340	22	70
452	40.67978	105.20840	482434	4503022	338	20	68
453	40.65707	105.20919	482361	4500501	352	15	82
454	40.66480	105.19805	483304	4501358	342	25	72
455	40.65313	105.19888	483231	4500062	353	19	83
456	40.65035	105.19369	483670	4499753	345	19	75
457	40.65742	105.16858	485794	4500532	195	77	285
458	40.65173	105.17285	485432	4499902	240	80	330

Appendix 3: Bedding Data from Published USGS Maps (Continued)

#	Lat. °N (WGS 84)	Long. °W	m E (13N NAD 27)	m N	Strike	Dip	Dip Az
459	40.64395	105.17197	485505	4499039	261	20	351
460	40.64738	105.17090	485595	4499418	264	23	354
461	40.63458	105.19116	483880	4498001	339	24	69
462	40.63541	105.18235	484625	4498092	338	25	68
463	40.63651	105.17597	485165	4498214	163	88	253
464	40.63482	105.17362	485363	4498026	159	85	249
465	40.64023	105.16787	485851	4498624	1	16	91
466	40.63267	105.16690	485931	4497785	48	20	138
467	40.63453	105.16295	486265	4497991	18	20	108
468	40.63768	105.15201	487191	4498339	356	24	86
469	40.65027	105.16336	486234	4499739	303	22	33
470	40.64881	105.15240	487160	4499575	342	17	72
471	40.63627	105.14813	487518	4498182	3	24	93
472	40.63308	105.13820	488358	4497827	14	30	104